

Theoretical Study of Excitonic Phases in Strongly Correlated Electron Systems

February 2016

Chiba University
Graduate School of Science
Division of Fundamental Sciences
Department of Physics

Tatsuya Kaneko

Theoretical Study of Excitonic Phases in Strongly Correlated Electron Systems

Tatsuya Kaneko

Department of Physics, Chiba University

(February 29, 2016)

Abstract

The excitonic phases, often referred to as the excitonic insulators, are described by the quantum condensation of excitons in a small band-gap semiconductor or a small band-overlap semimetal. It is known that the exciton condensation in a semimetallic region can be described in analogy with the BCS theory of superconductivity and that in a semiconducting region can be discussed in terms of the Bose-Einstein condensation (BEC) of excitons. The excitonic phases were predicted theoretically half a century ago using free-electron-like models for weakly correlated electron systems. However, candidate materials recently reported as the excitonic insulators are mostly transition-metal compounds, which are one of the main stages of strongly correlated electron systems, and thus we need to construct any appropriate theories for such systems taking into account the spin, lattice, and orbital degrees of freedom explicitly.

In this thesis, motivated by such developments in the field, we investigate the excitonic phases in strongly correlated electron systems. First, we investigate the BCS-BEC crossover of the exciton condensation using the extended Falicov-Kimball model, which is a minimal lattice model to describe the excitonic phases in strongly correlated electron systems. In particular, we focus on an anomalous Green's function from weak to strong coupling regions and show the character of the crossover phenomena by means of exact diagonalization, density matrix renormalization group, and variational cluster approximation methods. Next, to construct the theory of the excitonic phase with spin degrees of freedom, we investigate the stability of excitonic phases in the multi-band Hubbard model. Using the variational cluster approximation, we show that the interband repulsion leads to the excitonic instability in both the spin-singlet and spin-triplet channels and that the interband exchange interaction, such as Hund's rule coupling, always stabilizes the spin-triplet excitonic phase. We also investigate the excitonic phases in the multi-band Hubbard model supplemented by the electron-phonon coupling. We show the spin-singlet excitonic phase becomes stabler than the spin-triplet excitonic phase when the electron-phonon coupling is stronger than the interband exchange interaction. Then, we elucidate the spatial structures of the spin-singlet and spin-triplet exciton condensates using the local wave functions in the tight-binding approximation, putting particular emphasis on their consequences such as the bond order and multipole formations. Finally, we discuss the electronic state and observed phase transition of Ta_2NiSe_5 , a promising candidate material for the spin-singlet excitonic insulator.

Contents

1	Introduction	1
2	Introduction of Excitonic Phases	4
2.1	Introduction	4
2.2	Excitonic Phases	4
2.2.1	Order Parameter and Gap Equation	4
2.2.2	Solution of the Gap Equation	6
2.2.3	Phase Diagram	10
2.2.4	Absence of Off-Diagonal Long-Range Order	11
2.3	Excitonic Phases with Spin Degrees of Freedom	13
2.3.1	Interband Interactions with Spin Degrees of Freedom	13
2.3.2	Ground-State Energy and Excitonic Density-Wave States	14
2.4	Summary	16
3	Numerical Methods	17
3.1	Introduction	17
3.2	Exact Diagonalization (ED)	17
3.2.1	Eigenvalue from the Lanczos Method	17
3.2.2	Eigenstate from the Inverse Iteration Method	18
3.2.3	Dynamical Functions	19
3.3	Self-energy Functional Theory (SFT)	21
3.3.1	Grand Potential and Self-energy	21
3.3.2	Luttinger-Ward Functional	21
3.3.3	Variational Principle	22
3.4	Variational Cluster Approximation (VCA)	23
3.4.1	Reference System and VCA	23
3.4.2	Spontaneous Symmetry Breaking in VCA	26
3.5	Cluster Perturbation Theory (CPT)	26
3.5.1	Green's Function of CPT	26
3.5.2	Physical Quantity from CPT	28
3.6	Summary	29
4	Excitonic Phase in the Extended Falicov-Kimball Model	30
4.1	Introduction	30
4.2	Two-Dimensional Double-Layer System	31
4.2.1	Anomalous Green's Function	32
4.2.2	Momentum Distribution Functions	33
4.2.3	Pair Coherence Length	34
4.2.4	Order Parameter and Binding Energy	34
4.2.5	Effect of Mass Asymmetry	36
4.3	One-Dimensional System	37
4.3.1	Phase Diagram	37
4.3.2	Criticality of Excitonic Insulator	39
4.3.3	BCS-BEC Crossover	39
4.4	Summary	41

5	Roles of Interband Exchange Interaction for Excitonic Phases	42
5.1	Introduction	42
5.2	Model and Method	42
5.2.1	Two-band Hubbard model	42
5.2.2	Stability of Spin-singlet and Spin-triplet Excitonic States	44
5.2.3	Variational Cluster Approximation	45
5.3	Results	45
5.3.1	Stability of Excitonic Phases	45
5.3.2	Single-particle Spectral Function	47
5.3.3	Condensation Amplitude and Coherence Length	49
5.4	Summary	50
6	Roles of Electron-Phonon Coupling for Excitonic Phases	51
6.1	Introduction	51
6.2	Model and Methods	51
6.2.1	Model Hamiltonian	51
6.2.2	Mean-Field Approximation for Phonons	52
6.2.3	Variational Cluster Approximation	53
6.3	Results	53
6.3.1	Phase of Order Parameters	53
6.3.2	Stability of Spin-singlet Excitonic Phase	54
6.3.3	Ground-state Phase Diagram	56
6.4	Discussion	57
6.5	Summary	57
7	Charge and Spin Density Distributions in Excitonic Phases	58
7.1	Introduction	58
7.2	Multi-Orbitals in a Single Ion	58
7.2.1	Charge and Spin Densities	58
7.2.2	Multipole Moments	61
7.2.3	Valence and Conduction Bands Composed of Multi-Orbitals	63
7.3	Multi-Orbitals in Different Ions	65
7.4	Summary	67
8	Theory of Ta₂NiSe₅ as an Excitonic Insulator	68
8.1	Introduction	68
8.2	Electronic Structure of Ta ₂ NiSe ₅	69
8.2.1	Crystal Structure of Ta ₂ NiSe ₅	69
8.2.2	Underestimation of the Band Gap	70
8.2.3	Effective Electronic Structure for Exciton Formation	71
8.3	Model Study of Ta ₂ NiSe ₅	72
8.3.1	Model Hamiltonian	72
8.3.2	Mean-Field Approximation	73
8.3.3	Excitonic and Structural Phase Transition	75
8.3.4	Single-particle Spectra	76
8.3.5	Heat Capacity	77
8.3.6	Elastic Constant	77
8.3.7	Ultrasonic Attenuation Rate	78
8.3.8	Nuclear Magnetic Relaxation Rate	79
8.4	Summary	79
9	Summary	81

A BCS-BEC Crossover in the Attractive Hubbard Model	84
A.1 Introduction	84
A.2 Model and Method	84
A.2.1 Attractive Hubbard Model	84
A.2.2 Variational Cluster Approximation for Superconductivity	85
A.3 Results	86
A.3.1 Order Parameter	86
A.3.2 Spectra and Momentum Distributions	88
A.3.3 Pair Coherence Length	89
A.3.4 Ground State Energy	90
A.4 Summary	91
B Description of Multipoles in Excitonic Insulators	92
Acknowledgements	97
Bibliography	98

Chapter 1

Introduction

The formation and condensation of excitonic bound states of electrons and holes in semimetallic or semiconducting systems possessing a small band overlap or band gap were predicted theoretically half a century ago [1, 2]. The excitonic phases, often referred to as the excitonic insulators, are described by the quantum condensation of such excitons triggered by the interband Coulomb interaction [1–19]. The exciton condensation in semimetallic systems can be described in analogy with the BCS theory of superconductors, and that in semiconducting systems can be discussed in terms of the Bose-Einstein condensation (BEC) of preformed excitons [20–23]. The crossover phenomena between the BCS and BEC states are then expected to produce rich physics in the field of quantum many-body systems.

Recently, a number of candidate materials for the excitonic phases have been discovered and physics of the excitonic phases has attracted renewed experimental and theoretical attention. Examples of the candidate materials are the following: Tm(Se,Te) was argued to exhibit a pressure-induced excitonic instability, where an anomalous increase in the electrical resistivity and thermal diffusivity have been reported [23, 24]. In $\text{Ca}_{1-x}\text{La}_x\text{B}_6$, the observed weak ferromagnetism was interpreted in terms of the doped spin-triplet excitons [25–27]. The charge-density-wave (CDW) state observed in $1T\text{-TiSe}_2$ was claimed to be of the excitonic origin [28–35]. Likewise, the structural phase transition observed in a layered chalcogenide Ta_2NiSe_5 has been attributed to a spin-singlet excitonic insulator [36–41]. The spin-density-wave (SDW) states of Cr [42–45] and iron-pnictide superconductors [46–59] has sometimes been argued to be of the excitonic origin as well. The condensation of spin-triplet excitons was also predicted to occur in the proximity of the spin-state transition [60], of which $\text{Pr}_{0.5}\text{Ca}_{0.5}\text{CoO}_3$ is an example [61, 62].

In this thesis, motivated by such developments in the field, we investigate the excitonic condensation in solids theoretically. The conventional theories of excitonic phases have often been based on free-electron-like models of weakly interacting electrons, but the candidate materials recently discovered as the excitonic insulators are transition-metal compounds, which are obviously among strongly correlated electron systems, and thus one needs to construct any appropriate theories for such systems. The purpose of this thesis is therefore to build the theory of excitonic phases in strongly correlated electron systems. We in particular focus on the stability of the excitonic phases in correlated lattice fermion models and consider the crossover phenomena between the weak-coupling BCS and strong-coupling BEC states. We also apply the theory of the excitonic insulators to the candidate material Ta_2NiSe_5 , of which much experimental and theoretical attention has been attracted in recent years.

This thesis is organized as follows. In Chap. 2, we briefly review the basic theory of excitonic phases. We first describe the characters of an excitonic phase using the simplest spinless model and introduce the order parameter, gap equation of the excitonic phase, and its solutions in both the semiconducting and semimetallic regions. We also discuss the difference between the excitonic phase and superconductivity in terms of the two-particle density matrix, which is often used to evaluate superfluidity of the systems. Then, we describe the excitonic phases with spin degrees freedom and discuss the effects of interband interactions and calculate the ground states in the Hartree-Fock approximation. We introduce two possible excitonic phases realized when the order parameter has the spin degrees of freedom; i.e. an excitonic CDW state realized as a condensed state of spin-singlet excitons, and an excitonic SDW state realized as a condensed state of spin-triplet excitons.

In Chap. 3, we introduce the numerical methods used in this thesis, which enables us to treat the strongly correlated electron models. First, we introduce the exact-diagonalization (ED) technique based on the Lanczos algorithm, which can solve the many-body problems in small-size systems exactly.

Next, we introduce the variational cluster approximation (VCA) based on the self-energy functional theory (SFT), where we can take into account the effects of short-range spatial electron correlations even in low-dimensional systems; the momentum dependences of physical quantities can be reproduced precisely in this method. The VCA is useful for discussing the spontaneous symmetry breaking in correlated electron systems beyond the mean-field theory. Within the framework of the VCA, we use the cluster perturbation theory (CPT) to calculate the Green's function, which is useful for evaluating the single-particle excitation spectrum and their integrated values such as the density of states, momentum distribution function, etc. Thus, the method of the CPT is also discussed in this chapter.

In Chap. 4, we investigate the exciton condensation in the extended Falicov-Kimball model (EFKM), which is a minimal theoretical model to describe the excitonic phases in strongly correlated electron systems. In particular, we focus on the BCS-BEC crossover of the exciton condensation. In Sec. 4.2, we address the problem of exciton condensation in an electron-hole double layer system described by the 2D EFKM, where we use the ED technique. We calculate the anomalous excitation spectra, condensation amplitude, and exciton momentum distribution function in the BCS, intermediate, and BEC regions. From the calculated condensation amplitude, we evaluate the pair coherence length and order parameter of the condensate. We also compare the results of the ED calculations with the results of the mean-field theory and VCA. We also discuss the effects of a mass imbalance between the holes and electrons based on the calculated pair coherence length and exciton binding energy. In Sec. 4.3, we investigate the excitonic insulator state in the 1D EFKM. First, we describe the complete ground-state phase diagram of the 1D EFKM from the large-scale density matrix renormalization group (DMRG) method [63]. In comparison with the 2D system, the excitonic phase in the 1D EFKM is a critical phase with power-law correlation decay; we thus show a critical character in the 1D system using the concept of the central charge. We also show a crossover between the BCS and BEC condensates by the exciton-exciton correlation function and exciton momentum distribution function. Following the method used in the 2D systems, we also calculate the anomalous spectral function and extract the pair coherence length and binding energy of the electron-hole pairs in the 1D EFKM. [Chap. 4 is based on T. Kaneko, S. Ejima, H. Fehske, and Y. Ohta, *Phy. Rev. B* **88**, 035312 (2013), and S. Ejima, T. Kaneko, Y. Ohta, and H. Fehske, *Phy. Rev. Lett.* **112**, 026401 (2014).]

The EFKM is the simplest model to investigate the excitonic phases, but it does not include the spin degrees of freedom. In real materials, electrons have the spin degrees of freedom, and therefore we need to investigate the excitonic phases with spinful strongly correlated electron models. In Chap. 5, we investigate the excitonic phase in the two-band Hubbard model (TBHM), which is the simplest model for discussing the excitonic phases with spin degrees of freedom. We study the stability of the excitonic phases with the spin degrees of freedom in the TBHM, where the interband interactions such as the interband Coulomb repulsion, interband exchange interaction, and pair-hopping term are taken into account in addition to the standard intraband Hubbard repulsion. We first rewrite the interband interaction part of the Hamiltonian in terms of the creation and annihilation operators of the spin-singlet and spin-triplet excitons. Then, we show that the interband repulsion actually leads to the exciton formation in both the spin-singlet and spin-triplet channels and that the interband exchange interaction always lowers the energy of the spin-triplet exciton and raises the energy of the spin-singlet exciton. The VCA is then used to study the stability of the excitonic phases in the TBHM in detail. Moreover, we examine the characteristics of these excitonic phases using a variety of physical quantities, including the single-particle spectral function, density of states, condensation amplitude, and pair coherence length. [Chap. 5 is based on T. Kaneko, and Y. Ohta, *Phy. Rev. B* **90**, 245144 (2014).]

Taking into account only the electronic interband interactions, we find that the spin-singlet excitonic phase is difficult to stabilize, which is however thought to be realized in $1T$ -TiSe₂ and Ta₂NiSe₅. On the other hand, in these materials, the importance of electron-phonon coupling was recently pointed out [31–35, 38]. Thus, in Chap. 6, to clarify how the spin-singlet excitonic condensation occurs, we investigate the TBHM with the electron-phonon coupling. The model is analyzed by the static mean-field theory for the electron-phonon coupling and by the VCA for treating the electronic correlations. We first discuss the influence of the electron-phonon coupling on the stability of the spin-singlet excitonic state. We thereby find that, incorporating the interband exchange interactions, the spin-triplet excitonic state indeed competes with the spin-singlet excitonic state. The ground-state phase diagram of the TBHM is thus determined. We moreover pay particular attention to the macroscopic phase of the order parameter, which is related to possible superfluidity of the excitonic condensation states. We thereby find that the phase of the order parameter is fixed by including the electron-phonon coupling and pair-hopping interaction and thus the superfluidity is unlikely to occur in the ground state of the excitonic condensation states. [Chap. 6 is based on T. Kaneko, B. Zenker, H. Fehske and Y. Ohta, *Phy. Rev. B*

92, 115106 (2015).]

In Chap. 7, in order to visualize the electronic structures of the excitonic phases in strongly correlated electron systems, we evaluate charge and spin densities of the spin-singlet and spin-triplet exciton condensation states from the local wave function in the tight-binding approximation. In this chapter, we first consider the charge and spin densities of the excitonic phases when the valence and conduction bands are composed of orthogonal two orbitals in a single ion. Because the energy bands are reconstructed by the hybridization of many orbitals in real materials, we also consider the electronic structure of the excitonic phases, in which the valence and conduction bands include the components of many orbitals in a single ion. In this chapter, we also illustrate the excitonic density-wave states when the valence and conduction bands are composed of the orbitals located in different ions.

In Chap. 8, we introduce a theory to elucidate the origin of the structural phase transition and associated anomalous electronic properties of Ta_2NiSe_5 , a promising candidate for an excitonic insulator. We carry out the density-functional-theory (DFT) based electronic structure calculations for the orthorhombic phase of Ta_2NiSe_5 . Based on the DFT calculation, we construct an effective three-chain Hubbard model to reproduce the three bands near the Fermi level. The phonon degrees of freedom are also taken into account in the model. We then analyze this model by the mean-field approximation and calculate its phase diagrams to clarify the origin of the structural phase transition. To reproduce the flattening of the valence band top observed in experiment, we calculate the single-particle excitation spectra. To consider the anomalous electronic properties associated with the excitonic phase transition, we also carry out the calculations of thermodynamic quantities, such as heat capacity and elastic constant, as well as the ultrasonic attenuation and nuclear-magnetic-resonance spin-lattice relaxation rates. [Chap. 8 is based on T. Kaneko, T. Toriyama, T. Konishi, and Y. Ohta, *Phy. Rev. B* **87**, 035121 (2013) and K. Sugimoto, T. Kaneko, and Y. Ohta, *Phy. Rev. B* **93**, 041105(R) (2016).]

Summary of this thesis is given in Chap. 9.

Chapter 2

Introduction of Excitonic Phases

2.1 Introduction

The formation and condensation of excitonic bound states of electrons and holes in semimetallic or semiconducting systems possessing a small band overlap or band gap were predicted theoretically half a century ago [1, 2]. The excitonic phases, often referred to as the excitonic insulator, are described by the quantum condensation of excitons triggered by the interband Coulomb interaction [1–19]. The exciton condensation in semimetallic systems can be described in analogy with the BCS theory of superconductors, and that in semiconducting systems can be discussed in terms of the Bose-Einstein condensation (BEC) of preformed excitons [20–23].

In this chapter, we introduce the excitonic phase. First, we describe basic features of excitonic phases using the simplest spinless model. Here, we show the order parameter, gap equation of an excitonic phase, and its solutions in the semiconducting and semimetallic region. After that, we discuss the general phase diagram of the excitonic phase. We also discuss the difference between the excitonic phase and superconductivity in terms of the two-particle density matrix, whereby we can evaluate superfluidity of the systems. Finally, we describe the excitonic phases with spin degrees freedom and discuss the effects of interband interactions and calculate the ground states in the Hartree-Fock approximation. We introduce two possible excitonic phases realized when the order parameter has the spin degrees of freedom; i.e. an excitonic charge-density-wave state realized as a condensed state of spin-singlet excitons, and an excitonic spin-density-wave state realized as a condensed state of spin-triplet excitons.

2.2 Excitonic Phases

2.2.1 Order Parameter and Gap Equation

The simplest model describing the excitonic phases is the two-band model with Coulomb repulsive interaction between electrons in the valence and conduction bands, which is given as

$$\mathcal{H} = \sum_{\mathbf{k}} \varepsilon_a(\mathbf{k}) a_{\mathbf{k}}^\dagger a_{\mathbf{k}} + \sum_{\mathbf{k}} \varepsilon_b(\mathbf{k}) b_{\mathbf{k}}^\dagger b_{\mathbf{k}} + \frac{1}{\Omega} \sum_{\mathbf{k}, \mathbf{k}', \mathbf{q}} V(\mathbf{q}) b_{\mathbf{k}+\mathbf{q}}^\dagger b_{\mathbf{k}} a_{\mathbf{k}'-\mathbf{q}}^\dagger a_{\mathbf{k}'}, \quad (2.1)$$

where $a_{\mathbf{k}}^\dagger$ ($a_{\mathbf{k}}$) and $b_{\mathbf{k}}^\dagger$ ($b_{\mathbf{k}}$) are the creation (annihilation) operators of the valence and conduction bands, respectively. $\varepsilon_a(\mathbf{k})$ and $\varepsilon_b(\mathbf{k})$ are the energy dispersions around the valence band maximum and conduction band minimum, respectively, which are defined as

$$\varepsilon_a(\mathbf{k}) = -\frac{\mathbf{k}^2}{2m_a} - \frac{G}{2}, \quad \varepsilon_b(\mathbf{k}) = \frac{(\mathbf{k} - \mathbf{Q})^2}{2m_b} + \frac{G}{2}, \quad (2.2)$$

where m_a and m_b are the effective masses of the valence and conduction bands, respectively, and G is the energy gap. $G > 0$ indicates a semiconductor and $G < 0$ indicates a semimetal. This energy dispersion represents that the valence band maximum and conduction band minimum are separated by the wave vector \mathbf{Q} . $V(\mathbf{q})$ is the Coulomb repulsive interaction between electrons in the valence and conduction bands defined as

$$V(\mathbf{q}) = \frac{4\pi e^2}{K(\mathbf{q})q^2}, \quad (2.3)$$

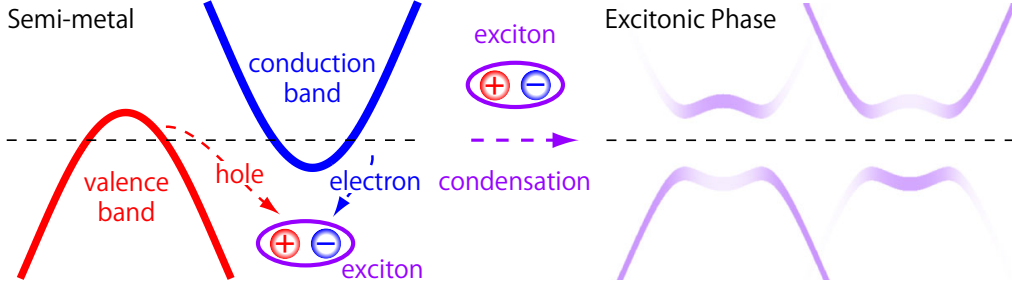


Figure 2.1: Schematic picture of excitonic phase.

where $K(\mathbf{q})$ is the effective dielectric constant¹. The Coulomb repulsive interaction between electrons in the valence and conduction bands corresponds to the Coulomb attractive interaction between a valence band hole and a conduction band electron. The interband Coulomb interaction drives the excitonic phase in a small band-overlap semimetal or a small band-gap semiconductor. In this section, in order to make a proper correspondence to the BCS theory for superconductivity, we consider a direct gap ($Q = 0$) semiconductor (or semimetal), assuming that the valence and conduction electrons have the same masses ($m_a = m_b = m$). We also ignore the spin degrees of freedom in the model (2.1), which we will discuss in the next section.

In this model, the creation operator of an exciton with momentum \mathbf{q} is given as $b_{\mathbf{k}+\mathbf{q}}^\dagger a_{\mathbf{k}}$. Exciton condensation state at $\mathbf{q} = 0$ is given by $\langle b_{\mathbf{k}}^\dagger a_{\mathbf{k}} \rangle \neq 0$. Therefore, in the theory of excitonic phases, the order parameter of the exciton condensation state is defined as²

$$\Delta(\mathbf{k}) \equiv -\frac{1}{\Omega} \sum_{\mathbf{k}'} V(\mathbf{k} - \mathbf{k}') \langle b_{\mathbf{k}'}^\dagger a_{\mathbf{k}'} \rangle. \quad (2.4)$$

Using the order parameter $\Delta(\mathbf{k})$, the mean-field Hamiltonian of Eq. (2.1) is given by

$$\tilde{\mathcal{H}} = \sum_{\mathbf{k}} \varepsilon_a(\mathbf{k}) a_{\mathbf{k}}^\dagger a_{\mathbf{k}} + \sum_{\mathbf{k}} \varepsilon_b(\mathbf{k}) b_{\mathbf{k}}^\dagger b_{\mathbf{k}} + \sum_{\mathbf{k}} \left(\Delta(\mathbf{k}) a_{\mathbf{k}}^\dagger b_{\mathbf{k}} + h.c. \right) + \varepsilon_0, \quad (2.5)$$

where the energy term ε_0 is derived from the mean-field approximation as $\varepsilon_0 = \sum_{\mathbf{k}} \Delta(\mathbf{k}) \langle a_{\mathbf{k}}^\dagger b_{\mathbf{k}} \rangle$. To diagonalize Eq. (2.5), we introduce the Bogoliubov transformation [9]

$$\alpha_{\mathbf{k}} = u_{\mathbf{k}} a_{\mathbf{k}} - v_{\mathbf{k}} b_{\mathbf{k}}, \quad (2.6)$$

$$\beta_{\mathbf{k}} = v_{\mathbf{k}}^* a_{\mathbf{k}} + u_{\mathbf{k}}^* b_{\mathbf{k}}. \quad (2.7)$$

Due to the commutation relation $[\alpha_{\mathbf{k}}, \alpha_{\mathbf{k}}^\dagger]_+ = 1$, the coefficients $u_{\mathbf{k}}$ and $v_{\mathbf{k}}$ should fulfill

$$|u_{\mathbf{k}}|^2 + |v_{\mathbf{k}}|^2 = 1. \quad (2.8)$$

To diagonalize the mean-field Hamiltonian (2.5), the off-diagonal term of the Bogoliubov transformed Hamiltonian (coefficients of $\alpha_{\mathbf{k}}^\dagger \beta_{\mathbf{k}}$ and $\beta_{\mathbf{k}}^\dagger \alpha_{\mathbf{k}}$) should be zero, and thus $u_{\mathbf{k}}$ and $v_{\mathbf{k}}$ are given by³

$$|u_{\mathbf{k}}|^2 = \frac{1}{2} \left(1 + \frac{\xi_{\mathbf{k}}}{E_{\mathbf{k}}} \right), \quad (2.9)$$

$$|v_{\mathbf{k}}|^2 = \frac{1}{2} \left(1 - \frac{\xi_{\mathbf{k}}}{E_{\mathbf{k}}} \right), \quad (2.10)$$

¹When the Coulomb interaction is screened with screening length κ^{-1} in real space, $V(\mathbf{q})$ is given as follows.

$$V(\mathbf{r}) = \frac{e^2}{K r} e^{-\kappa r} \Rightarrow V(\mathbf{q}) = \frac{4\pi e^2 / K}{q^2 + \kappa^2}$$

Here, the effective dielectric constant is given as $K(\mathbf{q}) = K(1 + \kappa^2/q^2)$.

²Using the transformation $a_{\mathbf{k}} \rightarrow c_{\mathbf{k},\uparrow}^\dagger$, $b_{\mathbf{k}}^\dagger \rightarrow c_{-\mathbf{k},\downarrow}^\dagger$, the order parameter in Eq. (2.4) becomes

$$\Delta(\mathbf{k}) = -\frac{1}{\Omega} \sum_{\mathbf{k}'} V(\mathbf{k} - \mathbf{k}') \langle c_{\mathbf{k}',\uparrow}^\dagger c_{-\mathbf{k}',\downarrow}^\dagger \rangle,$$

which is consistent with the order parameter of the s -wave superconductivity in the BCS-theory.

³The off-diagonal term is given as $(\varepsilon_a(\mathbf{k}) - \varepsilon_b(\mathbf{k}))u_{\mathbf{k}}v_{\mathbf{k}} + \Delta(\mathbf{k})u_{\mathbf{k}}^2 - \Delta^*(\mathbf{k})v_{\mathbf{k}}^2 = 0$.

where we define

$$\xi_{\mathbf{k}} \equiv \frac{\varepsilon_b(\mathbf{k}) - \varepsilon_a(\mathbf{k})}{2}, \quad E_{\mathbf{k}} \equiv \sqrt{\xi_{\mathbf{k}}^2 + |\Delta(\mathbf{k})|^2}. \quad (2.11)$$

From the Bogoliubov transformation, the diagonalized Hamiltonian becomes

$$\tilde{\mathcal{H}} = \sum_{\mathbf{k}} E_{\alpha}(\mathbf{k}) \alpha_{\mathbf{k}}^{\dagger} \alpha_{\mathbf{k}} + \sum_{\mathbf{k}} E_{\beta}(\mathbf{k}) \beta_{\mathbf{k}}^{\dagger} \beta_{\mathbf{k}} + \varepsilon_0, \quad (2.12)$$

where the energy eigenvalues $E_{\alpha}(\mathbf{k})$ and $E_{\beta}(\mathbf{k})$ are given as

$$E_{\alpha}(\mathbf{k}) = \eta_{\mathbf{k}} - E_{\mathbf{k}}, \quad E_{\beta}(\mathbf{k}) = \eta_{\mathbf{k}} + E_{\mathbf{k}} \quad \left(\eta_{\mathbf{k}} \equiv \frac{\varepsilon_b(\mathbf{k}) + \varepsilon_a(\mathbf{k})}{2} \right). \quad (2.13)$$

The expectation values of the number of the quasiparticles at finite temperature are given by $\langle \alpha_{\mathbf{k}}^{\dagger} \alpha_{\mathbf{k}} \rangle = f(E_{\alpha}(\mathbf{k}))$ and $\langle \beta_{\mathbf{k}}^{\dagger} \beta_{\mathbf{k}} \rangle = f(E_{\beta}(\mathbf{k}))$, where $f(x) = 1/(e^{\beta x} + 1)$ is Fermi distribution function and $\beta^{-1} = k_B T$. From the inverse Bogoliubov transformation⁴ and Eq. (2.4), the gap equation of the excitonic phase is given by

$$\Delta(\mathbf{k}) = \frac{1}{\Omega} \sum_{\mathbf{k}'} V(\mathbf{k} - \mathbf{k}') \frac{\Delta(\mathbf{k}')}{2E_{\mathbf{k}'}} [f(E_{\alpha}(\mathbf{k}')) - f(E_{\beta}(\mathbf{k}'))]. \quad (2.14)$$

Here, we assume $m = m_a = m_b$ for simplicity and the gap equation is finally given as⁵

$$\Delta(\mathbf{k}) = \frac{1}{\Omega} \sum_{\mathbf{k}'} V(\mathbf{k} - \mathbf{k}') \frac{\Delta(\mathbf{k}')}{2E_{\mathbf{k}'}} \tanh \frac{\beta E_{\mathbf{k}'}}{2}. \quad (2.15)$$

This formula is consistent with the gap equation of an s -wave superconductivity in the BCS theory. The gap equation (2.15) is solved self-consistently and the solution with $\Delta(\mathbf{k}) \neq 0$ indicates the presence of the excitonic phase. $\Delta(\mathbf{k})$ induces the hybridization gap between the valence and conduction bands and the system becomes insulating. Therefore, the excitonic phase is called the ‘‘excitonic insulator’’.

The wave function of the excitonic phase also has similarity with the BCS-theory of superconductivity. The normal semiconducting ground state is given as

$$|\Psi_N\rangle = \prod_{\mathbf{k}} a_{\mathbf{k}}^{\dagger} |0\rangle, \quad (2.16)$$

where $|0\rangle$ indicates the vacuum state. In the excitonic phase with $\Delta(\mathbf{k}) \neq 0$, the ground state of the excitonic phase is given as⁶

$$|\Psi_E\rangle = \prod_{\mathbf{k}} \alpha_{\mathbf{k}}^{\dagger} |0\rangle = \prod_{\mathbf{k}} (u_{\mathbf{k}}^* - v_{\mathbf{k}}^* b_{\mathbf{k}}^{\dagger} a_{\mathbf{k}}) |\Psi_N\rangle. \quad (2.17)$$

A hole in the a -band at \mathbf{k} and an electron in the b -band at \mathbf{k} are either present or absent in this state, which obviously corresponds to the ground state of the BCS theory of superconductivity [9].

2.2.2 Solution of the Gap Equation

In this section, we give solutions of the gap equation Eq. (2.15) in the two regions, (i) semiconducting region, where the exciton binding energy $|E_B|$ is close to the band gap G , and (ii) semimetal region, where the valence and conduction bands are deeply overlapped.

⁴From the inverse Bogoliubov transformation, $\langle b_{\mathbf{k}}^{\dagger} a_{\mathbf{k}} \rangle$ in Eq. (2.4) is given by

$$\langle b_{\mathbf{k}}^{\dagger} a_{\mathbf{k}} \rangle = -u_{\mathbf{k}}^* v_{\mathbf{k}} \left(\langle \alpha_{\mathbf{k}}^{\dagger} \alpha_{\mathbf{k}} \rangle - \langle \beta_{\mathbf{k}}^{\dagger} \beta_{\mathbf{k}} \rangle \right) = -\frac{\Delta(\mathbf{k})}{2E_{\mathbf{k}}} [f(E_{\alpha}(\mathbf{k})) - f(E_{\beta}(\mathbf{k}))].$$

⁵From $m = m_a = m_b$, $\varepsilon_b(\mathbf{k}) = -\varepsilon_a(\mathbf{k})$, $E_{\beta}(\mathbf{k}) = -E_{\alpha}(\mathbf{k}) = E_{\mathbf{k}}$ and $f(E_{\alpha}(\mathbf{k})) - f(E_{\beta}(\mathbf{k})) = \tanh(\beta E_{\mathbf{k}}/2)$.

⁶ $\prod_{\mathbf{k}} (u_{\mathbf{k}}^* - v_{\mathbf{k}}^* b_{\mathbf{k}}^{\dagger} a_{\mathbf{k}}) |\Psi_N\rangle = \left[\prod_{\mathbf{k}} (u_{\mathbf{k}}^* - v_{\mathbf{k}}^* b_{\mathbf{k}}^{\dagger} a_{\mathbf{k}}) \right] \left[\prod_{\mathbf{k}'} a_{\mathbf{k}'}^{\dagger} \right] |0\rangle = \prod_{\mathbf{k}} \left[(u_{\mathbf{k}}^* - v_{\mathbf{k}}^* b_{\mathbf{k}}^{\dagger} a_{\mathbf{k}}) a_{\mathbf{k}}^{\dagger} \right] |0\rangle = \prod_{\mathbf{k}} (u_{\mathbf{k}}^* a_{\mathbf{k}}^{\dagger} - v_{\mathbf{k}}^* b_{\mathbf{k}}^{\dagger}) |0\rangle = \prod_{\mathbf{k}} \alpha_{\mathbf{k}}^{\dagger} |0\rangle = |\Psi_E\rangle.$

(i) Semiconducting Region

In the semiconducting region, it is known that the gap equation Eq. (2.15) has nontrivial solution when the exciton binding energy is larger than the band gap, $|E_B| > G$. Following the study of Kozlov and Maksimov in Ref. [5], we introduce the solution of the gap equation Eq. (2.15) around $|E_B| \sim G$.

The gap equation (2.15) at $T = 0$ is given by

$$\Delta(\mathbf{k}) = \frac{1}{\Omega} \sum_{\mathbf{k}'} V(\mathbf{k} - \mathbf{k}') \frac{\Delta(\mathbf{k}')}{2E_{\mathbf{k}'}}. \quad (2.18)$$

Here, we introduce $\psi(\mathbf{k}) = \Delta(\mathbf{k})/2E_{\mathbf{k}}$ as a wave function and the gap equation can be rewritten as

$$\left[\left(\frac{\mathbf{k}^2}{m} + G \right)^2 + 4\Delta^2(\mathbf{k}) \right]^{\frac{1}{2}} \psi(\mathbf{k}) = \frac{1}{\Omega} \sum_{\mathbf{k}'} V(\mathbf{k} - \mathbf{k}') \psi(\mathbf{k}'). \quad (2.19)$$

In the semiconducting region, $\Delta(\mathbf{k}) = \Delta_0 \ll G$ around $\mathbf{k} = 0$, and we can approximate Eq. (2.19) as

$$\left[\frac{\mathbf{k}^2}{m} + G + \frac{2\Delta_0^2}{G} \right] \psi(\mathbf{k}) = \frac{1}{\Omega} \sum_{\mathbf{k}'} V(\mathbf{k} - \mathbf{k}') \psi(\mathbf{k}'). \quad (2.20)$$

On the other hand, the elementary equation for the exciton wave function in momentum space is given as⁷

$$\left[\frac{\mathbf{k}^2}{m} + |E_B| \right] \varphi(\mathbf{k}) = \frac{1}{\Omega} \sum_{\mathbf{k}'} V(\mathbf{k} - \mathbf{k}') \varphi(\mathbf{k}') \quad \left(|E_B| = \frac{m}{4} \left(\frac{e^2}{K} \right)^2 \right). \quad (2.21)$$

In comparison between Eq. (2.19) and (2.21), we confirm that $\Delta_0 = 0$ when $G > |E_B|$. We can also verify that a nontrivial solution, $\Delta_0 > 0$, exists when $G < |E_B|$. At $G \sim |E_B|$, we may approximate $G + 2\Delta_0^2/G$ in Eq. (2.20) as an exciton binding energy, i.e. $|E_B| \sim G + 2\Delta_0^2/G$. Thus, the order parameter Δ_0 at $G \lesssim |E_B|$ may be given as

$$\Delta_0 = |E_B| \sqrt{\frac{1}{2} \left(1 - \frac{G}{|E_B|} \right)}. \quad (2.22)$$

(ii) Semimetallic Region ($G < 0$)

At $G < 0$, the valence and conduction bands are overlapped and it is a semimetal. We can solve the gap equation approximately in the deeply overlapped semimetal ($|G| \gg 1$) and the results are basically

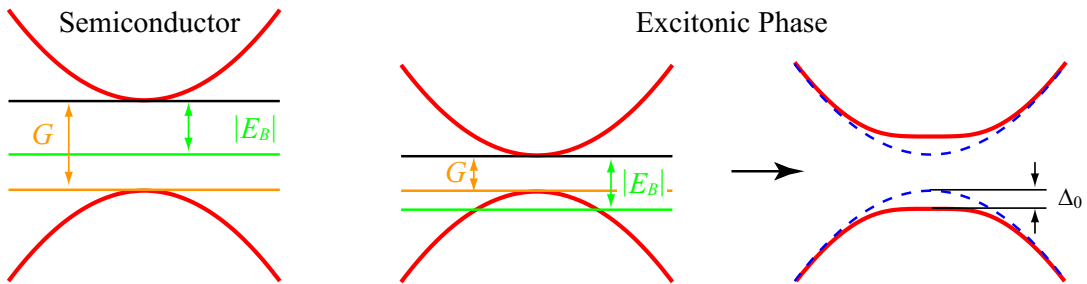


Figure 2.2: Schematic picture of the excitonic phase transition in a semiconductor, where the exciton binding energy $|E_B|$ is close to the band gap G .

⁷The Schrödinger equation for the exciton wave function is

$$\left[-\frac{\nabla^2}{2\mu} - \frac{e^2}{Kr} \right] \varphi(\mathbf{r}) = -|E_B| \varphi(\mathbf{r}) \quad \left(|E_B| = \frac{\mu}{2} \left(\frac{e^2}{K} \right)^2 \right)$$

where $1/\mu = 1/m_a + 1/m_b$ is the reduced mass. In this section, we assume $m_a = m_b = m$, and thus $1/\mu = 2/m$. Here, we also use the static dielectric constant K because the system is a semiconductor. We obtain Eq. (2.21) from the Fourier transformation of this Schrödinger equation.

consistent with the BCS theory. In the semimetal, the valence and conduction bands are crossed at $\varepsilon_a(\mathbf{k}) = \varepsilon_b(\mathbf{k})$ and Fermi momentum k_F is defined as $k_F = \sqrt{m|G|}$ [see Fig. 2.3]. Thus, the energy dispersions are given by

$$\varepsilon(\mathbf{k}) \equiv \varepsilon_b(\mathbf{k}) = -\varepsilon_a(\mathbf{k}) = \frac{\mathbf{k}^2}{2m} - \frac{k_F^2}{2m} \quad (2.23)$$

When $|G| \gg 1$, the Coulomb interaction is screened by a large number of carriers, which is given as [5]

$$V(\mathbf{k}) = \frac{4\pi e^2/K}{\mathbf{k}^2 + \kappa^2} \quad \kappa^2 = \frac{2}{\pi} m \left(\frac{e^2}{K} \right) k_F, \quad (2.24)$$

where κ is the screening parameter. Using $V(\mathbf{k})$ in Eq. (2.24), the gap equation becomes

$$\Delta(\mathbf{k}) = \frac{1}{(2\pi)^3} \int d\mathbf{k}' \frac{4\pi e^2/K}{|\mathbf{k} - \mathbf{k}'|^2 + \kappa^2} \frac{\Delta(\mathbf{k}')}{2E_{\mathbf{k}'}} \tanh \frac{\beta E_{\mathbf{k}'}}{2}. \quad (2.25)$$

In the deeply overlapped semimetal, the Coulomb interaction $V(\mathbf{k})$ is weak due to the screening, and thus the BCS-like weak electron-hole pairing is expected.

To solve the gap equation, we introduce the cut-off k_c and approximate the order parameter around the Fermi momentum k_F as

$$\Delta(\mathbf{k}) = \begin{cases} \Delta_0 & |k - k_F| < k_c \\ 0 & |k - k_F| > k_c \end{cases}, \quad (2.26)$$

where we assume $\Delta_0 \ll |G|$ due to weak interaction $V(\mathbf{k})$. Note that we have to be careful of choosing the cut-off k_c because k_c appears in the solutions. In Eq. (2.24), the spread of the Coulomb interaction in momentum space depends on the screening parameter κ , and the cut-off k_c may have the order of the screening parameter κ ⁸. Thus, in this section, we assume $k_c \sim \kappa$.

First, we estimate the order parameter at $T = 0$. From Eq. (2.25) and (2.26), the gap equation at $T = 0$ is given as

$$\begin{aligned} \Delta(\mathbf{k}) &= \frac{1}{(2\pi)^3} \int d\mathbf{k}' \frac{4\pi e^2/K}{|\mathbf{k} - \mathbf{k}'|^2 + \kappa^2} \frac{\Delta(\mathbf{k}')}{2E_{\mathbf{k}'}} \\ &\simeq \frac{4\pi e^2/K}{(2\pi)^3} \Delta_0 \int_{k_F - k_c}^{k_F + k_c} dk' \int_0^\pi d\theta \int_0^{2\pi} d\phi \frac{k'^2 \sin \theta}{k^2 + k'^2 - 2kk' \cos \theta + \kappa^2} \frac{1}{2E_{\mathbf{k}'}} \\ &= \frac{e^2/K}{2\pi k} \Delta_0 \int_{k_F - k_c}^{k_F + k_c} k' dk' \frac{1}{2E_{\mathbf{k}'}} \ln \left[\frac{(k + k')^2 + \kappa^2}{(k - k')^2 + \kappa^2} \right]. \end{aligned} \quad (2.27)$$

The integration for k' in Eq. (2.27) is analytically difficult. Here, we assume $k_c \ll k_F$ so that the range of the integration in Eq. (2.27) is narrow around $k' = k_F$. Thus, we may approximately take out the factor $\ln[\dots]$ from the integration assuming $k' = k_F$. At $k = k_F$, $\Delta(k_F) = \Delta_0$ and the gap equation becomes

$$1 = \frac{e^2/K}{2\pi k_F} \ln \left[1 + \frac{4k_F^2}{\kappa^2} \right] \int_{k_F - k_c}^{k_F + k_c} k' dk' \frac{1}{2\sqrt{\varepsilon^2(k') + \Delta_0^2}}. \quad (2.28)$$

Using $\xi = \varepsilon(k)$, we can integrate Eq. (2.28) with respect to k' , and we obtain

$$\int_{k_F - k_c}^{k_F + k_c} k' dk' \frac{1}{2\sqrt{\varepsilon^2(k') + \Delta_0^2}} = m \int_0^{\frac{k_F k_c}{m}} d\xi \frac{1}{\sqrt{\xi^2 + \Delta_0^2}} \simeq m \ln \left[\frac{2k_F k_c}{m\Delta_0} \right]. \quad (2.29)$$

Therefore, the gap equation at $T = 0$ finally becomes [5]

$$1 = \frac{me^2/K}{2\pi k_F} \ln \left[1 + \frac{4k_F^2}{\kappa^2} \right] \ln \left[\frac{2k_F k_c}{m\Delta_0} \right]. \quad (2.30)$$

Here, we note the relation

$$\frac{4k_F^2}{\kappa^2} = \frac{2\pi k_F}{me^2/K} = \pi \sqrt{\frac{|G|}{|E_B|}}, \quad (2.31)$$

⁸Kozlov and Maksimov in Ref. [5] have defined the cutoff k_c from $\Delta(k_F \pm k_c) = \Delta(k_F)/2$.

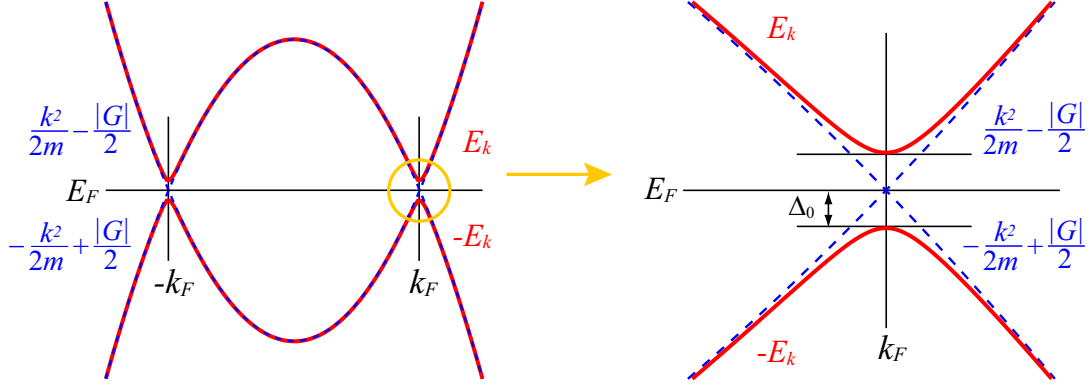


Figure 2.3: Schematic picture of transition of excitonic phase in semimetallic region.

and from Eq. (2.30) and (2.31), the order parameter at $T = 0$ is given as

$$\Delta_0 = \frac{2k_F k_c}{m} \exp\left(-\frac{\pi\sqrt{|G|/|E_B|}}{\ln\left(1 + \pi\sqrt{|G|/|E_B|}\right)}\right). \quad (2.32)$$

Next, we evaluate the order parameter around the transition temperature T_c . At $T = T_c$, we can approximate as $E_{\mathbf{k}} = \varepsilon(\mathbf{k})$ and the gap equation is given by

$$\Delta(\mathbf{k}) = \frac{1}{(2\pi)^3} \int d\mathbf{k}' \frac{4\pi e^2/K}{|\mathbf{k} - \mathbf{k}'|^2 + \kappa^2} \frac{\Delta(\mathbf{k}')}{2\varepsilon(\mathbf{k}')} \tanh\left(\frac{\beta_c \varepsilon(\mathbf{k}')}{2}\right). \quad (2.33)$$

Using the same assumption as above, the gap equation is approximately given as

$$1 = \frac{e^2/K}{2\pi k_F} \ln\left[1 + \frac{4k_F^2}{\kappa^2}\right] \int_{k_F - k_c}^{k_F + k_c} k' dk' \frac{1}{2\varepsilon(k')} \tanh\left(\frac{\beta_c \varepsilon(k')}{2}\right). \quad (2.34)$$

Using $\xi = \beta_c \varepsilon(k)/2$, we can integrate Eq. (2.34) with respect to k' as

$$\begin{aligned} \int_{k_F - k_c}^{k_F + k_c} k' dk' \frac{1}{2\varepsilon(k')} \tanh\left(\frac{\beta_c \varepsilon(k')}{2}\right) &= m \int_0^{\frac{k_F k_c}{2m} \beta_c} d\xi \frac{1}{\xi} \tanh \xi \\ &= m \left(\left[\ln \xi \tanh \xi \right]_0^{\frac{k_F k_c}{2m} \beta_c} - \int_0^{\frac{k_F k_c}{2m} \beta_c} d\xi \frac{\ln \xi}{\cosh^2 \xi} \right). \end{aligned} \quad (2.35)$$

At $|G| \gg 1$, Δ_0 decreases exponentially with $|G|$ and T_c is expected to be very low. Therefore, we can approximate as $k_F k_c \beta_c / (2m) \rightarrow \infty$ in the second term of Eq. (2.35), which is given as

$$\int_0^\infty d\xi \frac{\ln \xi}{\cosh^2 \xi} = -\ln \frac{4e^\gamma}{\pi}, \quad (2.36)$$

where $\gamma = 0.577 \dots$ is a Euler constant. From this estimation, the integration in Eq. (2.35) is given as

$$\int_0^{\frac{k_F k_c}{2m} \beta_c} d\xi \frac{1}{\xi} \tanh \xi \simeq \ln\left(\frac{2e^\gamma}{\pi} \frac{k_F k_c}{m} \beta_c\right). \quad (2.37)$$

From Eqs. (2.34), (2.35), and (2.37), the gap equation at $T = T_c$ finally becomes

$$1 = \frac{me^2/K}{2\pi k_F} \ln\left[1 + \frac{4k_F^2}{\kappa^2}\right] \ln\left[\frac{2e^\gamma}{\pi} \frac{k_F k_c}{m} \beta_c\right]. \quad (2.38)$$

From Eq. (2.38), the transition temperature T_c is given as

$$k_B T_c = \frac{2e^\gamma}{\pi} \frac{k_F k_c}{m} \exp\left(-\frac{\pi\sqrt{|G|/|E_B|}}{\ln\left(1 + \pi\sqrt{|G|/|E_B|}\right)}\right). \quad (2.39)$$

Around $T \sim T_c$, the gap equation is approximately given as

$$1 = \frac{me^2/K}{2\pi k_F} \ln \left[1 + \frac{4k_F^2}{\kappa^2} \right] \int_{-\frac{k_F k_c}{m}}^{\frac{k_F k_c}{m}} d\xi \frac{1}{2\sqrt{\xi^2 + \Delta^2}} \tanh \left(\frac{\beta\sqrt{\xi^2 + \Delta^2}}{2} \right), \quad (2.40)$$

where we assume $\Delta \neq 0$ and $\varepsilon(k) = \xi$. We expand the integrand in Eq. (2.40) with respect to Δ ($\ll 1$) and we have

$$\int_{-\frac{k_F k_c}{m}}^{\frac{k_F k_c}{m}} d\xi \frac{1}{2\sqrt{\xi^2 + \Delta^2}} \tanh \left(\frac{\beta\sqrt{\xi^2 + \Delta^2}}{2} \right) \simeq \ln \left(\frac{2e^\gamma k_F k_c \beta}{\pi m} \right) - \frac{\beta^2 \Delta^2}{\pi^2} \frac{7}{8} \zeta(3) + \mathcal{O}(\Delta^4), \quad (2.41)$$

where $\zeta(s) = \sum_{n=1}^{\infty} n^{-s}$ is the zeta function⁹. From Eqs. (2.38), (2.40) and (2.41), we have

$$\ln \left(\frac{T}{T_c} \right) = -\frac{\Delta^2(T)}{\pi^2 (k_B T_c)^2} \frac{7}{8} \zeta(3), \quad (2.42)$$

and thus the order parameter around the transition temperature is given as¹⁰

$$\Delta(T) = \pi k_B T_c \sqrt{\frac{8}{7\zeta(3)} \cdot \frac{T_c - T}{T_c}}. \quad (2.43)$$

Comparing between Eqs. (2.32) and (2.39), we find that Δ_0 and $k_B T_c$ have the same functional form. Therefore, the ratio between Δ_0 and $k_B T_c$ is a universal constant given as

$$\frac{2\Delta_0}{k_B T_c} = \frac{2\pi}{e^\gamma} \sim 3.53. \quad (2.44)$$

In the weak-coupling semimetallic region ($G < 0$ and $|G| \ll 1$), we can formally solve the gap equation just as in the BCS theory, and thus the ratio in Eq. (2.44) is consistent with the BCS theory for the s -wave superconductivity. In contrast to the BCS theory of superconductivity, where Δ_0 and T_c increase exponentially with increasing k_F ¹¹, Δ_0 and T_c in the excitonic phase given in Eqs. (2.32) and (2.39) show the exponential decrease with increasing k_F . This difference is caused by the \mathbf{k} -dependence of the interaction $V(\mathbf{k})$. In the excitonic phase, the screening of the interaction $V(\mathbf{k})$, which increases with increasing k_F , suppresses the excitonic order exponentially.

2.2.3 Phase Diagram

In this subsection, we summarize the results of the previous subsections and discuss the characteristic behaviors of the phase diagram of the excitonic phase. At $G > |E_B|$, the system is normal semiconducting. However, when $G = |E_B|$, the gap equation has a nontrivial solution and the semiconductor gives way to the excitonic phase. At $G \lesssim |E_B|$, $\Delta_0 \propto \sqrt{1 - G/|E_B|}$, indicating that the phase transition from the semiconductor to the excitonic phase is of the second-order. At $|E_B| > G > 0$, the order parameter increases with decreasing G and Δ_0 has a maximum at $G = 0$, where the valence band top touches the conduction band bottom. In the semimetallic region at $G < 0$, the Coulomb repulsive interaction becomes weak with increasing of the number of carriers, and thus Δ_0 decreases monotonically with increasing $|G|$ from the maximum value of Δ_0 at $G = 0$. In the deeply overlapped semimetal ($G < 0$ and $|G| \gg 1$), we can solve the gap equation in the BCS-like approximation and the order parameter Δ_0 decrease exponentially as in Eq. (2.32). In real materials, the valence and conduction bands have

⁹In Eq. (2.41), we have

$$\begin{aligned} & \int_{-\frac{k_F k_c}{m}}^{\frac{k_F k_c}{m}} d\xi \frac{1}{2\sqrt{\xi^2 + \Delta^2}} \tanh \left(\frac{\beta\sqrt{\xi^2 + \Delta^2}}{2} \right) \\ &= \int_{-\frac{k_F k_c}{m}}^{\frac{k_F k_c}{m}} d\xi \frac{1}{2\xi} \tanh \left(\frac{\beta\xi}{2} \right) + \int_{-\frac{k_F k_c}{m}}^{\frac{k_F k_c}{m}} d\xi \left[\frac{1}{2\sqrt{\xi^2 + \Delta^2}} \tanh \left(\frac{\beta\sqrt{\xi^2 + \Delta^2}}{2} \right) - \frac{1}{2\xi} \tanh \left(\frac{\beta\xi}{2} \right) \right]. \end{aligned}$$

The first term is consistent with the first term in Eq. (2.41). In the second term, we expand the integrand and integrate it. It is consistent with the second term of Eq. (2.41).

¹⁰At $T \sim T_c$, $\ln(T/T_c) \simeq (T - T_c)/T_c$.

¹¹In the BCS theory of superconductivity, Δ_0 and $T_c \propto \exp(-c/k_F)$, where c is a constant.

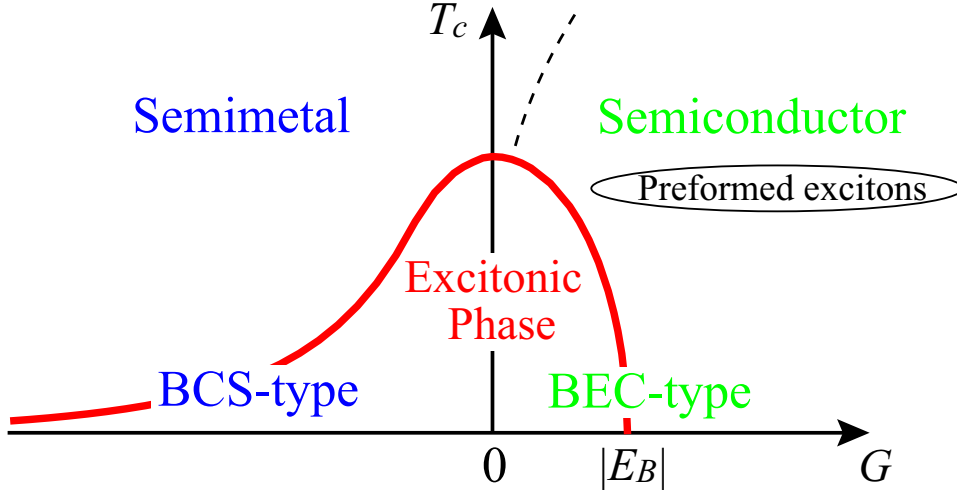


Figure 2.4: Schematic phase diagram of the excitonic phase. G is the band gap at $G > 0$ and the band overlap at $G < 0$. $|E_B|$ is the exciton binding energy.

an anisotropy of the Fermi surfaces and it is known that the anisotropy suppresses the excitonic phase and a finite boundary $|G_c|$ appears in the semimetallic region [10].

The critical temperature of the excitonic phase T_c is related to the value of the order parameter at zero temperature Δ_0 , i.e. $k_B T_c = (e^\gamma/\pi)\Delta_0$ in the semimetallic region [see Eq. (2.44)]. Schematic phase diagram of the excitonic phase is shown in Fig. 2.4. In the semiconducting region ($G > 0$), an electron and a hole make a pair and the preformed excitons exist above the critical temperature ($T > T_c$). In the semiconducting region, the Coulomb interaction is not screened by the carriers, and thus tightly bound excitons are expected to persist unlike in the semimetallic region. Therefore, the excitonic phase in the semiconducting region is described by the BEC of preformed excitons, which are hydrogen-like Bose particles. On the other hand, in the semimetallic region ($G < 0$), preformed excitons do not exist but an electron-hole plasma state is realized above the critical temperature ($T > T_c$) due to the strong screening of Coulomb interaction. We can solve the gap equation for the excitonic phase in the semimetallic region in the BCS-like approximation, and thus the condensation of weakly paired excitonic state is realized below T_c . Therefore, the phase diagram of the excitonic phase includes two different types of exciton condensation states, i.e., BEC and BCS states, and the BCS-BEC crossover is expected as a function of the energy gap G .

2.2.4 Absence of Off-Diagonal Long-Range Order

The theory of excitonic phase has a lot of similarities with the BCS theory of superconductivity. However, Jérôme *et al.* [9] have shown that the fundamental character of the order, which is related to superfluidity, is entirely different between the excitonic insulator and superconductor [9, 64]. It is known that superfluidity in a system is often characterized by the off-diagonal long-range order (ODLRO) [17, 65, 66]. The criterion for the ODLRO of composite bosons, such as Cooper pairs and excitons, is given by the two-particle density matrix, which is defined as

$$\langle \mathbf{x}' \mathbf{y}' | \rho_2 | \mathbf{x} \mathbf{y} \rangle \equiv \langle \psi^\dagger(\mathbf{y}) \psi^\dagger(\mathbf{x}) \psi(\mathbf{x}') \psi(\mathbf{y}') \rangle, \quad (2.45)$$

where $\psi(\mathbf{x})$ is a field operator. By using the two-particle density matrix, the ODLRO is defined with

$$\langle \mathbf{x}' \mathbf{y}' | \rho_2 | \mathbf{x} \mathbf{y} \rangle \neq 0 \quad \text{at} \quad |\mathbf{x} - \mathbf{x}'| \rightarrow \infty \quad \text{and} \quad \mathbf{x} \simeq \mathbf{y}, \quad \mathbf{x}' \simeq \mathbf{y}'. \quad (2.46)$$

For example, in the BCS theory of superconductivity, the two-particle density matrix is given by

$$\begin{aligned} \langle \mathbf{x}' \uparrow \mathbf{y}' \downarrow | \rho_2 | \mathbf{x} \uparrow \mathbf{y} \downarrow \rangle &\equiv \langle \psi_\downarrow^\dagger(\mathbf{y}) \psi_\downarrow^\dagger(\mathbf{x}) \psi_\uparrow(\mathbf{x}') \psi_\uparrow(\mathbf{y}') \rangle \\ &= \langle \psi_\uparrow^\dagger(\mathbf{x}) \psi_\uparrow(\mathbf{x}') \rangle \langle \psi_\downarrow^\dagger(\mathbf{y}) \psi_\downarrow(\mathbf{y}') \rangle + \langle \psi_\downarrow^\dagger(\mathbf{y}) \psi_\downarrow^\dagger(\mathbf{x}) \rangle \langle \psi_\uparrow(\mathbf{x}') \psi_\uparrow(\mathbf{y}') \rangle. \end{aligned} \quad (2.47)$$

In the limit $|\mathbf{x} - \mathbf{x}'| \rightarrow \infty$, $\mathbf{x} \simeq \mathbf{y}$ and $\mathbf{x}' \simeq \mathbf{y}'$, we have

$$\langle \mathbf{x}' \uparrow \mathbf{y}' \downarrow | \rho_2 | \mathbf{x} \uparrow \mathbf{y} \downarrow \rangle \rightarrow \langle \psi_{\downarrow}^{\dagger}(\mathbf{x}) \psi_{\downarrow}^{\dagger}(\mathbf{x}') \rangle \langle \psi_{\uparrow}(\mathbf{x}') \psi_{\uparrow}(\mathbf{x}) \rangle \neq 0, \quad (2.48)$$

and the second term in Eq. (2.47) remains finite¹². Thus, superconductivity is characterized by the ODLRO.

On the other hand, in the excitonic phase, the two-particle density matrix Eq. (2.45) in the two band model, is given with the field operator as

$$\psi(\mathbf{x}) = \frac{1}{\sqrt{\Omega}} \sum_{\mathbf{k}} [\varphi_{a\mathbf{k}}(\mathbf{x}) a_{\mathbf{k}} + \varphi_{b\mathbf{k}}(\mathbf{x}) b_{\mathbf{k}}], \quad (2.49)$$

where $\varphi_{a\mathbf{k}}(\mathbf{x})$ and $\varphi_{b\mathbf{k}}(\mathbf{x})$ are the Bloch wave function of the a and b bands at \mathbf{k} . In the mean-field (Hartree-Fock) approximation, the two-particle density matrix becomes

$$\langle \mathbf{x}' \mathbf{y}' | \rho_2 | \mathbf{x} \mathbf{y} \rangle = \langle \psi^{\dagger}(\mathbf{x}) \psi(\mathbf{x}') \rangle \langle \psi^{\dagger}(\mathbf{y}) \psi(\mathbf{y}') \rangle - \langle \psi^{\dagger}(\mathbf{x}) \psi(\mathbf{y}') \rangle \langle \psi^{\dagger}(\mathbf{y}) \psi(\mathbf{x}') \rangle. \quad (2.50)$$

By using the field operator of the two-band model in Eq. (2.49), we have

$$\langle \psi^{\dagger}(\mathbf{x}) \psi(\mathbf{x}') \rangle = g(\mathbf{x}, \mathbf{x}') - f(\mathbf{x}, \mathbf{x}') \quad (2.51)$$

with

$$g(\mathbf{x}, \mathbf{x}') = \frac{1}{\Omega} \sum_{\mathbf{k}} [|u_{\mathbf{k}}|^2 \varphi_{a\mathbf{k}}^*(\mathbf{x}) \varphi_{a\mathbf{k}}(\mathbf{x}') + |v_{\mathbf{k}}|^2 \varphi_{b\mathbf{k}}^*(\mathbf{x}) \varphi_{b\mathbf{k}}(\mathbf{x}')] \quad (2.52)$$

$$f(\mathbf{x}, \mathbf{x}') = \frac{1}{\Omega} \sum_{\mathbf{k}} [u_{\mathbf{k}}^* v_{\mathbf{k}} \varphi_{b\mathbf{k}}^*(\mathbf{x}) \varphi_{a\mathbf{k}}(\mathbf{x}') + u_{\mathbf{k}} v_{\mathbf{k}}^* \varphi_{a\mathbf{k}}^*(\mathbf{x}) \varphi_{b\mathbf{k}}(\mathbf{x}')]. \quad (2.53)$$

Both $g(\mathbf{x}, \mathbf{x}')$ and $f(\mathbf{x}, \mathbf{x}')$ vanish when $|\mathbf{x} - \mathbf{x}'| \rightarrow \infty$. Therefore, in the limit $|\mathbf{x} - \mathbf{x}'| \rightarrow \infty$, $\mathbf{x} \simeq \mathbf{y}$ and $\mathbf{x}' \simeq \mathbf{y}'$, we have

$$\langle \mathbf{x}' \mathbf{y}' | \rho_2 | \mathbf{x} \mathbf{y} \rangle \rightarrow 0, \quad (2.54)$$

and thus the ODLRO is absent in the excitonic insulator state.

It should be noted here that, Jérôme *et al.* [9] have shown that the two-particle density matrix $\langle \mathbf{x}' \mathbf{y}' | \rho_2 | \mathbf{x} \mathbf{y} \rangle$ is finite and has a periodic dependence on $|\mathbf{x} - \mathbf{y}|$ in the limit $|\mathbf{x} - \mathbf{y}| \rightarrow \infty$, $\mathbf{x} = \mathbf{x}'$ and $\mathbf{y} = \mathbf{y}'$, and thus the excitonic phase has an additional diagonal long-range order (DLRO) [9, 64]. In this section, we have assumed a direct gap ($\mathbf{Q} = 0$) for simplicity, but when there is an indirect gap with a finite \mathbf{Q} , an excitonic phase shows a new periodicity characterized by \mathbf{Q} in real space as a DLRO [9, 64].

We point out here that the absence of the ODLRO may not always indicate the absence of superfluidity [67]. Nagaoka in fact has suggested that, even though it is a DLRO, a condensate can show superfluidity in ideal and simplified systems when there is a continuous degeneracy of energy in the symmetry breaking state [67]. For example, Fröhlich has predicted superconductivity in incommensurate density waves, which are DLRO [68]. In the theory of incommensurate density waves, due to a continuous degeneracy in the phase of the order parameter, the condensate has a gapless collective mode in the excitation spectrum, indicating a translational motion of the condensate without loss of energy [68]. However, imperfections in real materials, such as impurity, lattice defects, and anisotropy, lift the continuous degeneracy and a condensate needs a finite energy for a collective motion [67, 69]. Therefore, the collective motion of DLRO is influenced by a lot of factors in real materials, leading to the absence of superfluidity in DLRO [67]. On the other hand, Keldysh [70] has pointed out that the excitonic insulator state is in a thermodynamic equilibrium state, whereas the absence of superfluidity is not justified in the case of high-density nonequilibrium excitons in semiconductors [64, 70, 71].

¹²By using the field operator of free electron $\psi_{\sigma}(\mathbf{x}) = (1/\sqrt{\Omega}) \sum_{\mathbf{k}} e^{i\mathbf{k}\cdot\mathbf{x}} c_{\mathbf{k}\sigma}$, the two-particle density matrix in the BCS theory [9] is given as $\langle \mathbf{x}' \uparrow \mathbf{y}' \downarrow | \rho_2 | \mathbf{x} \uparrow \mathbf{y} \downarrow \rangle = g(\mathbf{x}' - \mathbf{x})g(\mathbf{y}' - \mathbf{y}) + f^*(\mathbf{x} - \mathbf{y})f(\mathbf{x}' - \mathbf{y}')$, where

$$g(\mathbf{x}' - \mathbf{x}) \equiv \langle \psi_{\sigma}^{\dagger}(\mathbf{x}) \psi_{\sigma}(\mathbf{x}') \rangle = \frac{1}{\Omega} \sum_{\mathbf{k}} \langle c_{\mathbf{k}\sigma}^{\dagger} c_{\mathbf{k}\sigma} \rangle e^{-i\mathbf{k}\cdot(\mathbf{x} - \mathbf{x}')} = \frac{1}{\Omega} \sum_{\mathbf{k}} |v_{\mathbf{k}}|^2 e^{i\mathbf{k}\cdot(\mathbf{x}' - \mathbf{x})},$$

$$f(\mathbf{x} - \mathbf{y}) \equiv \langle \psi_{\uparrow}(\mathbf{x}) \psi_{\downarrow}(\mathbf{y}) \rangle = \frac{1}{\Omega} \sum_{\mathbf{k}} \langle c_{\mathbf{k}\uparrow} c_{-\mathbf{k}\downarrow} \rangle e^{i\mathbf{k}\cdot(\mathbf{x} - \mathbf{y})} = \frac{1}{\Omega} \sum_{\mathbf{k}} u_{\mathbf{k}} v_{\mathbf{k}} e^{i\mathbf{k}\cdot(\mathbf{x} - \mathbf{y})}.$$

In the limit $|\mathbf{x} - \mathbf{x}'| \rightarrow \infty$, $\mathbf{x} \simeq \mathbf{y}$ and $\mathbf{x}' \simeq \mathbf{y}'$, $g(\mathbf{x}' - \mathbf{x}) = g(\infty) = 0$ and $f(\mathbf{x} - \mathbf{y}) = f(0) \neq 0$. Thus, the two-particle density matrix in the Eq. (2.47) remains finite in this limit.

2.3 Excitonic Phases with Spin Degrees of Freedom

2.3.1 Interband Interactions with Spin Degrees of Freedom

In the previous section, we neglect the spin degrees of freedom. In this section, following a review by Halperin and Rice [14, 15], we introduce the excitonic phases with spin degrees of freedom. Here, we consider a spinful two-band model for simplicity, where the valence band a and conduction band b are separated by the wave vector \mathbf{Q} . The Coulomb interaction is generally given as

$$\mathcal{H}_{int} = \frac{1}{2} \sum_{\sigma, \sigma'} \int d\mathbf{x} d\mathbf{x}' V(\mathbf{x}, \mathbf{x}') \psi_{\sigma}^{\dagger}(\mathbf{x}) \psi_{\sigma}(\mathbf{x}) \psi_{\sigma'}^{\dagger}(\mathbf{x}') \psi_{\sigma'}(\mathbf{x}'), \quad (2.55)$$

where $V(\mathbf{x}, \mathbf{x}')$ is the Coulomb repulsive interaction and $\psi_{\sigma}(\mathbf{x})$ is a field operator. By using the Bloch wave state $\varphi_{n\mathbf{k}}(\mathbf{x})$ and the creation (annihilation) operator $c_{n,\mathbf{k},\sigma}^{\dagger}$ ($c_{n,\mathbf{k},\sigma}$) of an electron at $n = a, b$ band, the field operator is given as

$$\psi_{\sigma}(\mathbf{x}) = \frac{1}{\sqrt{\Omega}} \sum_{\mathbf{k}} \sum_{n=a,b} \varphi_{n\mathbf{k}}(\mathbf{x}) c_{n,\mathbf{k},\sigma}. \quad (2.56)$$

From Eq. (2.55) and (2.56), the Coulomb repulsive interaction becomes

$$\mathcal{H}_{int} = \frac{1}{2} \sum_{\sigma, \sigma'} \sum_{\mathbf{k}, \mathbf{k}', \mathbf{q}} \sum_{n_1, n_2, n_3, n_4} V_{\mathbf{k}, \mathbf{k}', \mathbf{q}}^{n_1 n_2 n_3 n_4} c_{n_1, \mathbf{k} + \mathbf{q}, \sigma}^{\dagger} c_{n_2, \mathbf{k}, \sigma} c_{n_3, \mathbf{k}' - \mathbf{q}, \sigma'}^{\dagger} c_{n_4, \mathbf{k}', \sigma'}. \quad (2.57)$$

$V_{\mathbf{k}, \mathbf{k}', \mathbf{q}}^{n_1 n_2 n_3 n_4}$ is the Coulomb repulsive interaction in momentum space and is given as

$$V_{\mathbf{k}, \mathbf{k}', \mathbf{q}}^{n_1 n_2 n_3 n_4} \equiv \frac{1}{\Omega} \sum_{\mathbf{G}, \mathbf{G}'} V_{\mathbf{G}\mathbf{G}'}(\mathbf{q}) [F_{-\mathbf{G}}^{n_2 n_1}(\mathbf{k}, \mathbf{k} + \mathbf{q})]^* F_{-\mathbf{G}'}^{n_3 n_4}(\mathbf{k}' - \mathbf{q}, \mathbf{k}'), \quad (2.58)$$

where \mathbf{G} is a reciprocal lattice vector, $V_{\mathbf{G}\mathbf{G}'}(\mathbf{q})$ is a Fourier transformation of $V(\mathbf{x}, \mathbf{x}')$ ¹³, and $F_{\mathbf{G}}^{n n'}(\mathbf{k} + \mathbf{q}, \mathbf{k}')$ is called the form factor [15] defined as

$$F_{\mathbf{G}}^{n n'}(\mathbf{k} + \mathbf{q}, \mathbf{k}') \equiv \int d\mathbf{x} \varphi_{n\mathbf{k} + \mathbf{q}}^*(\mathbf{x}) \varphi_{n'\mathbf{k}'}(\mathbf{x}) e^{i(\mathbf{q} + \mathbf{G}) \cdot \mathbf{x}}. \quad (2.59)$$

In order to discuss the excitonic phases, we just consider the interband interaction although the interaction in Eq. (2.57) includes the intraband interactions as well. The interaction in Eq. (2.57) has three types of interband interactions. The interaction Hamiltonian with $n_1 = n_2 = b, n_3 = n_4 = a$ gives the direct term,

$$\mathcal{H}_{int}^{\text{I}} = \sum_{\sigma, \sigma'} \sum_{\mathbf{k}, \mathbf{k}', \mathbf{q}} V_{\mathbf{k}, \mathbf{k}', \mathbf{q}}^{bbaa} b_{\mathbf{k} + \mathbf{q}, \sigma}^{\dagger} b_{\mathbf{k}, \sigma} a_{\mathbf{k}' - \mathbf{q}, \sigma'}^{\dagger} a_{\mathbf{k}', \sigma'}. \quad (2.60)$$

In the previous section discussing the spinless system, we consider this term only. The interaction Hamiltonian with $n_1 = n_4 = b, n_2 = n_3 = a$ gives the exchange term,

$$\mathcal{H}_{int}^{\text{II}} = \sum_{\sigma, \sigma'} \sum_{\mathbf{k}, \mathbf{k}', \mathbf{q}} V_{\mathbf{k}, \mathbf{k}', \mathbf{q}}^{baab} b_{\mathbf{k} + \mathbf{q}, \sigma}^{\dagger} a_{\mathbf{k}, \sigma} a_{\mathbf{k}' - \mathbf{q}, \sigma'}^{\dagger} b_{\mathbf{k}', \sigma'}. \quad (2.61)$$

The interaction Hamiltonian with $n_1 = n_3 = b, n_2 = n_4 = a$ and $n_1 = n_3 = a, n_2 = n_4 = b$ gives the pair hopping term,

$$\mathcal{H}_{int}^{\text{III}} = \frac{1}{2} \sum_{\sigma, \sigma'} \sum_{\mathbf{k}, \mathbf{k}', \mathbf{q}} \left(V_{\mathbf{k}, \mathbf{k}', \mathbf{q}}^{baba} b_{\mathbf{k} + \mathbf{q}, \sigma}^{\dagger} a_{\mathbf{k}, \sigma} b_{\mathbf{k}' - \mathbf{q}, \sigma'}^{\dagger} a_{\mathbf{k}', \sigma'} + V_{\mathbf{k}, \mathbf{k}', \mathbf{q}}^{abab} a_{\mathbf{k} + \mathbf{q}, \sigma}^{\dagger} b_{\mathbf{k}, \sigma} a_{\mathbf{k}' - \mathbf{q}, \sigma'}^{\dagger} b_{\mathbf{k}', \sigma'} \right). \quad (2.62)$$

¹³ $V_{\mathbf{G}\mathbf{G}'}(\mathbf{q})$ is given as $V(\mathbf{x}, \mathbf{x}') = (1/\Omega) \sum_{\mathbf{q}} \sum_{\mathbf{G}, \mathbf{G}'} e^{i(\mathbf{q} + \mathbf{G}) \cdot \mathbf{x}} e^{-i(\mathbf{q} + \mathbf{G}') \cdot \mathbf{x}'} V_{\mathbf{G}\mathbf{G}'}(\mathbf{q})$.

2.3.2 Ground-State Energy and Excitonic Density-Wave States

Ground-State Energy

The excitonic phases are characterized by the nonvanishing values $\langle b_{\mathbf{k}+\mathbf{Q},\sigma}^\dagger a_{\mathbf{k},\sigma'} \rangle$ in the presence of the interband interactions \mathcal{H}_{int}^I , \mathcal{H}_{int}^{II} and \mathcal{H}_{int}^{III} . In the Hartree-Fock approximation at $\langle b_{\mathbf{k}+\mathbf{Q},\sigma}^\dagger a_{\mathbf{k},\sigma'} \rangle \neq 0$, the energies (expectation values of the Hamiltonian) from the interband interactions are given as¹⁴

$$\langle \mathcal{H}_{int}^I \rangle = - \sum_{\sigma,\sigma'} \sum_{\mathbf{k},\mathbf{k}'} V_{\mathbf{k}'+\mathbf{Q},\mathbf{k},\mathbf{k}-\mathbf{k}'}^{bbaa} \langle b_{\mathbf{k}+\mathbf{Q},\sigma}^\dagger a_{\mathbf{k},\sigma'} \rangle \langle a_{\mathbf{k}',\sigma'}^\dagger b_{\mathbf{k}'+\mathbf{Q},\sigma} \rangle, \quad (2.63)$$

$$\langle \mathcal{H}_{int}^{II} \rangle = \sum_{\sigma,\sigma'} \sum_{\mathbf{k},\mathbf{k}'} V_{\mathbf{k},\mathbf{k}'+\mathbf{Q},\mathbf{Q}}^{baab} \langle b_{\mathbf{k}+\mathbf{Q},\sigma}^\dagger a_{\mathbf{k},\sigma} \rangle \langle a_{\mathbf{k}',\sigma'}^\dagger b_{\mathbf{k}'+\mathbf{Q},\sigma'} \rangle, \quad (2.64)$$

$$\begin{aligned} \langle \mathcal{H}_{int}^{III} \rangle &= \frac{1}{2} \sum_{\sigma,\sigma'} \sum_{\mathbf{k},\mathbf{k}'} \left[V_{\mathbf{k},\mathbf{k}',\mathbf{Q}}^{baba} \langle b_{\mathbf{k}+\mathbf{Q},\sigma}^\dagger a_{\mathbf{k},\sigma} \rangle \langle b_{\mathbf{k}'+\mathbf{Q},\sigma'}^\dagger a_{\mathbf{k}',\sigma'} \rangle + h.c. \right] \\ &\quad - \frac{1}{2} \sum_{\sigma,\sigma'} \sum_{\mathbf{k},\mathbf{k}'} \left[V_{\mathbf{k}',\mathbf{k},\mathbf{k}-\mathbf{k}'+\mathbf{Q}}^{baba} \langle b_{\mathbf{k}+\mathbf{Q},\sigma}^\dagger a_{\mathbf{k},\sigma} \rangle \langle b_{\mathbf{k}'+\mathbf{Q},\sigma'}^\dagger a_{\mathbf{k}',\sigma'} \rangle + h.c. \right]. \end{aligned} \quad (2.65)$$

To consider the spin degrees of freedom, we introduce the unitary matrix \hat{M} for the Bogoliubov transformation and the operators of the quasiparticles are given as

$$\alpha_{\mathbf{k},\sigma} = u_{\mathbf{k}} a_{\mathbf{k},\sigma} - v_{\mathbf{k}} \sum_{\sigma'} M_{\sigma\sigma'} b_{\mathbf{k}+\mathbf{Q},\sigma'}, \quad (2.66)$$

$$\beta_{\mathbf{k},\sigma} = v_{\mathbf{k}} a_{\mathbf{k},\sigma} + u_{\mathbf{k}} \sum_{\sigma'} M_{\sigma\sigma'} b_{\mathbf{k}+\mathbf{Q},\sigma'}, \quad (2.67)$$

where we assume that $u_{\mathbf{k}}$ and $v_{\mathbf{k}}$ are real for simplicity¹⁵. From the Bogoliubov transformation in Eqs. (2.66) and (2.67), the expectation value for the excitonic term is given by

$$\langle b_{\mathbf{k}+\mathbf{Q},\sigma}^\dagger a_{\mathbf{k},\sigma'} \rangle = - \left(f(E_{\mathbf{k}}^\alpha) - f(E_{\mathbf{k}}^\beta) \right) u_{\mathbf{k}} v_{\mathbf{k}} M_{\sigma\sigma'} \equiv g(\mathbf{k}) M_{\sigma\sigma'}, \quad (2.68)$$

where we define $g(\mathbf{k}) \equiv -(f(E_{\mathbf{k}}^\alpha) - f(E_{\mathbf{k}}^\beta)) u_{\mathbf{k}} v_{\mathbf{k}}$. From Eq. (2.68), Eqs. (2.63)-(2.65) become

$$\langle \mathcal{H}_{int}^I \rangle = -2 \sum_{\mathbf{k},\mathbf{k}'} V_{\mathbf{k}'+\mathbf{Q},\mathbf{k},\mathbf{k}-\mathbf{k}'}^{bbaa} g(\mathbf{k}) g(\mathbf{k}'), \quad (2.69)$$

$$\langle \mathcal{H}_{int}^{II} \rangle = \sum_{\mathbf{k},\mathbf{k}'} V_{\mathbf{k},\mathbf{k}'+\mathbf{Q},\mathbf{Q}}^{baab} g(\mathbf{k}) g(\mathbf{k}') \left| \text{tr} \hat{M} \right|^2, \quad (2.70)$$

$$\langle \mathcal{H}_{int}^{III} \rangle = \sum_{\mathbf{k},\mathbf{k}'} V_{\mathbf{k},\mathbf{k}',\mathbf{Q}}^{baba} g(\mathbf{k}) g(\mathbf{k}') \text{Re} \left[\left(\text{tr} \hat{M} \right)^2 \right] - \sum_{\mathbf{k},\mathbf{k}'} V_{\mathbf{k}',\mathbf{k},\mathbf{k}-\mathbf{k}'+\mathbf{Q}}^{baba} g(\mathbf{k}) g(\mathbf{k}') \text{Re} \left[\text{tr} \left(\hat{M}^2 \right) \right]. \quad (2.71)$$

In general, $\langle \mathcal{H}_{int}^I \rangle \gg \langle \mathcal{H}_{int}^{II} \rangle, \langle \mathcal{H}_{int}^{III} \rangle$, and we sometimes consider $\langle \mathcal{H}_{int}^I \rangle$ only without $\langle \mathcal{H}_{int}^{II} \rangle$ and $\langle \mathcal{H}_{int}^{III} \rangle$. This approximation is called the dominant term approximation in Ref. [15]. $\langle \mathcal{H}_{int}^I \rangle$ does not depend on the matrix \hat{M} , and thus the results of the dominant term approximation is consistent with those of the spinless model. Here, we denote the energy in the dominant term approximation as A .

Next, we consider the contributions from $\langle \mathcal{H}_{int}^{II} \rangle$ and $\langle \mathcal{H}_{int}^{III} \rangle$. The coefficient of \hat{M} in $\langle \mathcal{H}_{int}^{II} \rangle$ and the first term of $\langle \mathcal{H}_{int}^{III} \rangle$ have the same values¹⁶, and thus we define

$$B \equiv \sum_{\mathbf{k},\mathbf{k}'} V_{\mathbf{k},\mathbf{k}'+\mathbf{Q},\mathbf{Q}}^{baab} g(\mathbf{k}) g(\mathbf{k}') = \sum_{\mathbf{k},\mathbf{k}'} V_{\mathbf{k}',\mathbf{k},\mathbf{k}-\mathbf{k}'+\mathbf{Q}}^{baba} g(\mathbf{k}) g(\mathbf{k}'). \quad (2.72)$$

Note that B is basically positive if we neglect the electron-phonon coupling [15]. On the other hand, we also define the coefficient of \hat{M} in the second term of $\langle \mathcal{H}_{int}^{III} \rangle$ as

$$C \equiv \sum_{\mathbf{k},\mathbf{k}'} V_{\mathbf{k}',\mathbf{k},\mathbf{k}-\mathbf{k}'+\mathbf{Q}}^{baba} g(\mathbf{k}) g(\mathbf{k}'), \quad (2.73)$$

¹⁴In Eq. (2.65), we use $(V_{\mathbf{k},\mathbf{k}',\mathbf{q}}^{baba})^* = V_{\mathbf{k}'-\mathbf{q},\mathbf{k}+\mathbf{q},\mathbf{q}}^{abab}$.

¹⁵We can use this assumption when the order parameter $\Delta(\mathbf{k})$ is real.

¹⁶In Eq. (2.72), we use $g(-\mathbf{k}) = g(\mathbf{k})$ and $F_{-\mathbf{C}}^{ba}(\mathbf{k}-\mathbf{Q},\mathbf{k}) = F_{-\mathbf{C}}^{ab}(-\mathbf{k},-\mathbf{k}+\mathbf{Q})$.

and C is positive¹⁷.

Therefore, the ground-state energy from the interband interactions $E_{int} \equiv \langle \mathcal{H}_{int}^I \rangle + \langle \mathcal{H}_{int}^{II} \rangle + \langle \mathcal{H}_{int}^{III} \rangle$, is given as

$$E_{int} = A + B \left(\left| \text{tr} \hat{M} \right|^2 + \text{Re} \left[\left(\text{tr} \hat{M} \right)^2 \right] \right) - C \text{Re} \left[\text{tr} \left(\hat{M}^2 \right) \right], \quad (2.74)$$

which depends on the matrix \hat{M} . In the following, we show two examples of the ground states (or the choice of \hat{M}), i.e., the charge density wave (CDW) and spin density wave (SDW)¹⁸ [15].

Charge density wave

The spin-singlet excitonic phase is characterized by

$$\hat{M} = \hat{I}, \quad (2.75)$$

where \hat{I} is the unit matrix. When $\hat{M} = \hat{I}$, the energy in Eq. (2.74) is given as

$$E_{int} = A + 8B - 2C, \quad (2.76)$$

and the ordered state appears in the charge density defined as

$$\rho(\mathbf{x}) = \sum_{\sigma} \psi_{\sigma}^{\dagger}(\mathbf{x}) \psi_{\sigma}(\mathbf{x}). \quad (2.77)$$

The Fourier transformation of $\rho(\mathbf{x})$ is given by

$$\rho_{\mathbf{q}+\mathbf{G}} = \int d\mathbf{x} e^{-i(\mathbf{q}+\mathbf{G})\cdot\mathbf{x}} \rho(\mathbf{x}) = \sum_{\mathbf{k}} \sum_{\sigma} \sum_{n, n'} F_{-\mathbf{G}}^{n' n}(\mathbf{k} - \mathbf{q}, \mathbf{k}) c_{n', \mathbf{k}-\mathbf{q}, \sigma}^{\dagger} c_{n, \mathbf{k}, \sigma}, \quad (2.78)$$

where $F_{-\mathbf{G}}^{n' n}(\mathbf{k} - \mathbf{q}, \mathbf{k})$ is the form factor defined in Eq. (2.59). The excitonic phase is characterised by $\langle b_{\mathbf{k}+\mathbf{Q}, \sigma}^{\dagger} a_{\mathbf{k}, \sigma} \rangle \neq 0$ and the expectation value of the charge density at $\mathbf{q} = \mathbf{Q}$ is given as

$$\langle \rho_{\mathbf{Q}+\mathbf{G}} \rangle = 2 \sum_{\mathbf{k}} F_{-\mathbf{G}}^{ab}(\mathbf{k}, \mathbf{k} + \mathbf{Q}) g(\mathbf{k}) \text{Re} \left[\text{tr} \hat{M} \right] = 2\rho_{\mathbf{Q}+\mathbf{G}}^0 \text{Re} \left[\text{tr} \hat{M} \right] \quad (2.79)$$

where $\rho_{\mathbf{Q}+\mathbf{G}}^0 \equiv \sum_{\mathbf{k}} F_{-\mathbf{G}}^{ab}(\mathbf{k}, \mathbf{k} + \mathbf{Q}) g(\mathbf{k})$. Therefore, the excitonic phase with $\hat{M} = \hat{I}$ indicates the charge density wave with $\langle \rho_{\mathbf{Q}+\mathbf{G}} \rangle = 4\rho_{\mathbf{Q}+\mathbf{G}}^0$. Throughout the thesis, we call this state the excitonic CDW state.

Spin density wave

The spin-triplet excitonic phase is characterized by

$$\hat{M} = \mathbf{n} \cdot \hat{\boldsymbol{\sigma}}, \quad (2.80)$$

where \mathbf{n} is the unit direction vector and $\hat{\boldsymbol{\sigma}}$ is the Pauli spin matrix. When $\hat{M} = \mathbf{n} \cdot \hat{\boldsymbol{\sigma}}$, the energy in Eq. (2.74) is given as

$$E_{int} = A - 2C, \quad (2.81)$$

and the ordered state appears in the spin density defined as

$$\boldsymbol{\rho}^s(\mathbf{x}) = \sum_{\sigma, \sigma'} \psi_{\sigma}^{\dagger}(\mathbf{x}) \boldsymbol{\sigma}_{\sigma\sigma'} \psi_{\sigma'}(\mathbf{x}). \quad (2.82)$$

The Fourier transformation of $\boldsymbol{\rho}^s(\mathbf{x})$ is given by

$$\boldsymbol{\rho}_{\mathbf{q}+\mathbf{G}}^s = \int d\mathbf{x} e^{-i(\mathbf{q}+\mathbf{G})\cdot\mathbf{x}} \boldsymbol{\rho}^s(\mathbf{x}) = \sum_{\mathbf{k}} \sum_{\sigma, \sigma'} \sum_{n, n'} F_{-\mathbf{G}}^{n' n}(\mathbf{k} - \mathbf{q}, \mathbf{k}) c_{n', \mathbf{k}-\mathbf{q}, \sigma}^{\dagger} \boldsymbol{\sigma}_{\sigma, \sigma'} c_{n, \mathbf{k}, \sigma'}. \quad (2.83)$$

¹⁷ $g(\mathbf{k})$ has a large peak at $\mathbf{k} \sim 0$ and $C \simeq (\sum_{\mathbf{k}} g(\mathbf{k}))^2 V_{\mathbf{0}, \mathbf{0}, \mathbf{Q}}^{baba} > 0$.

¹⁸In Ref. [14, 15], Halperin and Rice also mentioned the other solutions, i.e., the charge current density wave and spin current density wave states. However, their energy are higher than those of the CDW and SDW states.

The excitonic phase is characterised by $\langle b_{\mathbf{k}+\mathbf{Q},\sigma}^\dagger a_{\mathbf{k},\sigma'} \rangle \neq 0$ and the expectation value of the spin density at $\mathbf{q} = \mathbf{Q}$ is given as

$$\langle \rho_{\mathbf{Q}+\mathbf{G}}^s \rangle = 2 \sum_{\mathbf{k}} F_{-\mathbf{G}}^{ab}(\mathbf{k}, \mathbf{k} + \mathbf{Q}) g(\mathbf{k}) \text{Re} \left[\text{tr} \left(\hat{\sigma} \hat{M}^\dagger \right) \right] = 2 \rho_{\mathbf{Q}+\mathbf{G}}^0 \text{Re} \left[\text{tr} \left(\hat{\sigma} \hat{M}^\dagger \right) \right]. \quad (2.84)$$

Therefore, the excitonic phase with $\hat{M} = \mathbf{n} \cdot \hat{\sigma}$ indicates the spin density wave with $\langle \rho_{\mathbf{Q}+\mathbf{G}}^s \rangle = 4 \rho_{\mathbf{Q}+\mathbf{G}}^0 \mathbf{n}$. Throughout the thesis, we call this state the excitonic SDW state.

Comparing the energies of the CDW in Eq. (2.76) and SDW in Eq. (2.81), the SDW state is lower than that of the CDW state. On the other hand, Halperin and Rice have pointed out that, if we consider electron-phonon coupling, the coefficients B can be negative [14,15], and thus the CDW can be stabilized by the strong electron-phonon coupling even though the interband Coulomb interactions exist.

2.4 Summary

In this chapter, we have reviewed the basic theory of excitonic phases. We have discussed the nature of excitonic phases using the simplest spinless model, where we have shown that a lot of similarities with the BCS theory of superconductivity exist in, e.g., the order parameter, gap equation, and its solutions. In contrast to superconductivity, however, we have discussed that the ODLRO is absent in the excitonic insulator states, indicating the difficulty in realizing superfluidity in real materials of excitonic insulators. After that, we have described the excitonic phases with spin degrees of freedom. We have introduced two types of the excitonic phases that can be realized when the order parameter has the spin degrees of freedom; i.e., the excitonic CDW and SDW states, which are the diagonal long-range orders.

Chapter 3

Numerical Methods

3.1 Introduction

In this Chapter, we introduce numerical methods used in this thesis, which enable us to treat the strongly correlated electron models. First, we introduce an exact-diagonalization (ED) technique based on the Lanczos algorithm, which can solve many-body problems in small-size systems exactly. Next, we introduce the variational cluster approximation (VCA) based on the self-energy functional theory (SFT), where we can take into account the effects of short-range spatial electron correlations even in low-dimensional systems in the thermodynamic limit. The VCA is useful for discussing the spontaneous symmetry breaking in correlated electron systems beyond the mean-field theory. Within the framework of the VCA, we use the cluster perturbation theory (CPT) to calculate the Green's function, which is useful for evaluating the single-particle excitation spectrum and their integrated values such as the density of states, momentum distribution function, etc. Thus, the method of the CPT is also discussed in this Chapter.

3.2 Exact Diagonalization (ED)

3.2.1 Eigenvalue from the Lanczos Method

The Lanczos method is one of the simplest method for calculating eigenvalues of a sparse matrix [72–74]. In the Lanczos method, we can calculate the eigenvalues efficiently with the tridiagonalized matrix, which is composed from the Lanczos basis. In comparison with other methods, the Lanczos method is suitable for calculating the maximum/minimum eigenvalue of the large sparse matrix.

The Lanczos basis is constructed from the series of the states by applying the matrix \mathcal{H} repeatedly [72, 73]. Starting from a random initial state $|\phi_0\rangle$, the next state is given as

$$|\phi_1\rangle = \mathcal{H}|\phi_0\rangle - \frac{\langle\phi_0|\mathcal{H}|\phi_0\rangle}{\langle\phi_0|\phi_0\rangle}|\phi_0\rangle, \quad (3.1)$$

where $|\phi_1\rangle$ and $|\phi_0\rangle$ are orthogonal. The next state, which is orthogonal to both $|\phi_0\rangle$ and $|\phi_1\rangle$, is given as

$$|\phi_2\rangle = \mathcal{H}|\phi_1\rangle - \frac{\langle\phi_1|\mathcal{H}|\phi_1\rangle}{\langle\phi_1|\phi_1\rangle}|\phi_1\rangle - \frac{\langle\phi_1|\phi_1\rangle}{\langle\phi_0|\phi_0\rangle}|\phi_0\rangle. \quad (3.2)$$

In the same way, the $(k+1)$ -th state is composed as

$$|\phi_{k+1}\rangle = \mathcal{H}|\phi_k\rangle - a_k|\phi_k\rangle - b_k^2|\phi_{k-1}\rangle, \quad (3.3)$$

where the coefficients are defined as

$$a_k = \frac{\langle\phi_k|\mathcal{H}|\phi_k\rangle}{\langle\phi_k|\phi_k\rangle}, \quad (3.4)$$

$$b_k^2 = \frac{\langle\phi_k|\phi_k\rangle}{\langle\phi_{k-1}|\phi_{k-1}\rangle}. \quad (3.5)$$

The basis set $\{|\phi_0\rangle, \dots, |\phi_{N-1}\rangle\}$ is called the Lanczos basis. By using the Lanczos basis, the Hamiltonian becomes the tridiagonalized matrix given as

$$\tilde{\mathcal{H}}_N = \begin{pmatrix} a_0 & b_1 & 0 & & & \\ b_1 & a_1 & b_2 & 0 & & \\ 0 & b_2 & a_2 & b_3 & \ddots & \\ & 0 & b_3 & a_3 & \ddots & 0 \\ & & \ddots & \ddots & \ddots & b_{N-1} \\ & & & 0 & b_{N-1} & a_{N-1} \end{pmatrix}. \quad (3.6)$$

To obtain the exact eigenvalue, we need to diagonalize the tridiagonal matrix with the same Hilbert space dimension. However, the Lanczos basis spans the Krylov subspace and the component of the largest/smallest eigenvalue is enhanced with increasing the Lanczos step N ¹. When the eigenvalue converges within an allowable error, we can stop the step at a small N . We can thus calculate the largest/smallest eigenvalue from the matrix $\tilde{\mathcal{H}}_N$ easily. The Lanczos method is therefore suitable for calculating the ground state energy of our models.

3.2.2 Eigenstate from the Inverse Iteration Method

The inverse iteration method is suitable for calculating the eigenstate if the ground state energy is found by the Lanczos method [73]. Here, we introduce $E'_0 = E_0 - \delta$, where E_0 is the ground state energy calculated from the Lanczos method and δ is a very small value. We also assume that $|\psi_i\rangle$ is the eigenstate belonging to the eigenenergy E_i , i.e. $\mathcal{H}|\psi_i\rangle = E_i|\psi_i\rangle$. By subtracting E'_0 from both sides of the equation, i.e., $(\mathcal{H} - E'_0)|\psi_i\rangle = (E_i - E'_0)|\psi_i\rangle$, and multiplying $(\mathcal{H} - E'_0)^{-1}$ to both sides, we obtain

$$(\mathcal{H} - E'_0)^{-1}|\psi_i\rangle = \frac{1}{E_i - E'_0}|\psi_i\rangle, \quad (3.7)$$

and thus we can regard $(E_i - E'_0)^{-1}$ as the eigenvalue of $(\mathcal{H} - E'_0)^{-1}$.

In the inverse iteration method, we configure the new state as

$$|u_n\rangle = (\mathcal{H} - E'_0)^{-1}|u_{n-1}\rangle. \quad (3.8)$$

Here, we introduce the initial vector $|u_0\rangle$ and expand it with the eigenstates $|\psi_i\rangle$, i.e.,

$$|u_0\rangle = \sum_i C_i |\psi_i\rangle. \quad (3.9)$$

From Eqs. (3.7) and (3.9), we have

$$|u_n\rangle = \sum_i \frac{C_i}{(E_i - E'_0)^n} |\psi_i\rangle. \quad (3.10)$$

When $i \neq 0$ and $E_i - E'_0 > E_0 - E'_0 = \delta$, we can approximate Eq. (3.10) as

$$|u_n\rangle = \frac{C_0}{(E_0 - E'_0)^n} \left(|\psi_0\rangle + \sum_{i \neq 0} \frac{C_i}{C_0} \left(\frac{E_0 - E'_0}{E_i - E'_0} \right)^n |\psi_i\rangle \right) \simeq \frac{C_0}{(E_0 - E'_0)^n} |\psi_0\rangle, \quad (3.11)$$

with a large enough value of n . By normalizing $|u_n\rangle$ and noting $C_0/(E_0 - E'_0)^n \simeq 1$ for a large enough value of n , we can obtain the ground state as $|\psi_0\rangle \simeq |u_n\rangle$.

¹Starting from an initial state $|u_0\rangle$, we construct the state $|u_n\rangle = \mathcal{H}^n|u_0\rangle$ by applying the matrix \mathcal{H} repeatedly. Expand $|u_0\rangle$ with respect to the eigenstates $|i\rangle$ (belonging to the eigenvalue E_i) of the matrix \mathcal{H} , we have

$$|u_n\rangle = \mathcal{H}^n|u_0\rangle = \mathcal{H}^n \sum_i C_i |i\rangle = \sum_i C_i E_i^n |i\rangle = C_0 E_0^n \left(|0\rangle + \sum_{i \neq 0} \frac{C_i}{C_0} \left(\frac{E_i}{E_0} \right)^n |i\rangle \right),$$

where $|0\rangle$ is the eigenstate belonging to the largest eigenvalue $|E_0| > |E_i|$. With increasing n , the weight of $|0\rangle$ is enhanced and we can approximate as $|u_n\rangle = C_0 E_0^n |0\rangle$ within an allowable error. $\{|u_0\rangle, \mathcal{H}|u_0\rangle, \mathcal{H}^2|u_0\rangle, \dots, \mathcal{H}^n|u_0\rangle\}$ is called the Krylov subspace.

To calculate $|u_n\rangle$, we have to evaluate $(\mathcal{H} - E_{\text{GS}})^{-1}$, but the matrix inversion in a large dimension is time-consuming. Here, we solve a simultaneous equation

$$(\mathcal{H} - E'_0)|u_n\rangle = |u_{n-1}\rangle \quad (3.12)$$

and we generate the new state $|u_n\rangle$. By using the conjugate gradient method, we can solve the simultaneous equations (3.12) for a large sparse matrix efficiently. In our numerical calculation, we use the conjugate gradient method to solve Eq. (3.12).

3.2.3 Dynamical Functions

In the ED technique, the calculations of the dynamical functions, such as correlation functions and single-particle spectral functions, are comparatively easy [72, 73]. Here, we consider the dynamical function defined as

$$C(t) = \langle \psi_0 | \mathcal{O}^\dagger(t) \mathcal{O}(0) | \psi_0 \rangle, \quad (3.13)$$

where $|\psi_0\rangle$ is the ground state of the system and $\mathcal{O}(t) = e^{i\mathcal{H}t} \mathcal{O} e^{-i\mathcal{H}t}$. In practice, we estimate the Fourier transformed dynamical function given as

$$\begin{aligned} C(\omega) &= \int_{-\infty}^{\infty} dt e^{i\omega t} \langle \psi_0 | \mathcal{O}^\dagger(t) \mathcal{O}(0) | \psi_0 \rangle \\ &= \sum_n |\langle \psi_n | \mathcal{O} | \psi_0 \rangle|^2 \delta(\omega - (E_n - E_0)), \end{aligned} \quad (3.14)$$

where $\mathcal{H}|\psi_n\rangle = E_n|\psi_n\rangle$ and $|\psi_n\rangle$ ($n \neq 0$) is the excited state. To calculate the excited states $|\psi_n\rangle$, we need a perfect diagonalization, which is time-consuming. Thus, we introduce the continued fraction expansion method. In this method, we introduce

$$G(z) = \langle \psi_0 | \mathcal{O}^\dagger \frac{1}{z - \mathcal{H}} \mathcal{O} | \psi_0 \rangle. \quad (3.15)$$

When $z = \omega + E_0 + i\eta$, $G(z)$ is given as

$$G(\omega + E_0 + i\eta) = \sum_n |\langle \psi_n | \mathcal{O} | \psi_0 \rangle|^2 \frac{1}{\omega - (E_n - E_0) + i\eta}. \quad (3.16)$$

From Eqs. (3.14) and (3.16), we can find the relation²

$$C(\omega) = -\frac{1}{\pi} \lim_{\eta \rightarrow +0} \text{Im} G(\omega + E_0 + i\eta). \quad (3.17)$$

Thus, we have to calculate the function $G(z)$ to evaluate the dynamical function $C(\omega)$.

In the Lanczos method, we can calculate $G(z)$ as follows. First, we introduce the initial vector defined as

$$|f_0\rangle = \frac{\mathcal{O}|\psi_0\rangle}{\sqrt{\langle \psi_0 | \mathcal{O}^\dagger \mathcal{O} | \psi_0 \rangle}}. \quad (3.18)$$

By using $|f_0\rangle$, the function $G(z)$ becomes

$$G(z) = \langle \psi_0 | \mathcal{O}^\dagger \mathcal{O} | \psi_0 \rangle \langle f_0 | \frac{1}{z - \mathcal{H}} | f_0 \rangle, \quad (3.19)$$

so that we have to calculate $\langle f_0 | (z - \mathcal{H})^{-1} | f_0 \rangle$. In the Lanczos method, we generate the states in order as³

$$|f_{k+1}\rangle = \mathcal{H}|f_k\rangle - \alpha_k|f_k\rangle - \beta_k^2|f_{k-1}\rangle, \quad (3.20)$$

²Here, we use

$$\frac{1}{x + i\eta} = P \frac{1}{x} - i\pi\delta(x).$$

³At $k = 1$, $|f_1\rangle = \mathcal{H}|f_0\rangle - \alpha_0|f_0\rangle$.

where the coefficients are defined as

$$\alpha_k = \frac{\langle f_k | \mathcal{H} | f_k \rangle}{\langle f_k | f_k \rangle}, \quad (3.21)$$

$$\beta_k^2 = \frac{\langle f_k | f_k \rangle}{\langle f_{k-1} | f_{k-1} \rangle}. \quad (3.22)$$

From the bases $|f_0\rangle, |f_1\rangle, |f_2\rangle \dots$, the matrix representation of $z - \mathcal{H}$ is given by

$$z - \mathcal{H} = \begin{pmatrix} z - \alpha_0 & -\beta_1 & & & \\ -\beta_1 & z - \alpha_1 & -\beta_2 & & \\ & & -\beta_2 & z - \alpha_2 & \ddots \\ & & & \ddots & \ddots \\ & & & & \ddots & \ddots \end{pmatrix}. \quad (3.23)$$

$\langle f_0 | (z - \mathcal{H})^{-1} | f_0 \rangle$ is given by the (0,0)-element in the inverse matrix of Eq. (3.23). From the Cramer's rule, we have

$$\langle f_0 | \frac{1}{z - \mathcal{H}} | f_0 \rangle = ((z - \mathcal{H})^{-1})_{00} = \frac{\text{adj}(z - \mathcal{H})_{00}}{\det(z - \mathcal{H})}, \quad (3.24)$$

where $\text{adj}(z - \mathcal{H})$ is the adjugate matrix and $\det(z - \mathcal{H})$ is the determinant. Here, we introduce the determinant

$$D_i \equiv \begin{vmatrix} z - \alpha_i & -\beta_{i+1} & & & \\ -\beta_{i+1} & z - \alpha_{i+1} & -\beta_{i+2} & & \\ & & -\beta_{i+2} & z - \alpha_{i+2} & \ddots \\ & & & \ddots & \ddots \\ & & & & \ddots & \ddots \end{vmatrix}. \quad (3.25)$$

By using D_i , the determinant and the (0,0)-element of the adjugate matrix of Eq. (3.23) are given by

$$D_0 = \det(z - \mathcal{H}), \quad (3.26)$$

$$D_1 = \text{adj}(z - \mathcal{H})_{00}, \quad (3.27)$$

respectively. Thus, $\langle f_0 | (z - \mathcal{H})^{-1} | f_0 \rangle = D_1/D_0$. From Eq. (3.25), we also find the recurrence relation

$$D_i = (z - \alpha_i)D_{i+1} - \beta_{i+1}^2 D_{i+2}. \quad (3.28)$$

From the Eq. (3.28), we have

$$D_i/D_{i+1} = z - \alpha_i - \frac{\beta_{i+1}^2}{D_{i+1}/D_{i+2}}. \quad (3.29)$$

Using the relation Eq. (3.29) repeatedly, we obtain

$$\langle f_0 | \frac{1}{z - \mathcal{H}} | f_0 \rangle = \frac{1}{D_0/D_1} = \frac{1}{z - \alpha_0 - \frac{\beta_1^2}{D_1/D_2}} = \frac{1}{z - \alpha_0 - \frac{\beta_1^2}{z - \alpha_1 - \frac{\beta_2^2}{D_2/D_3}}} = \dots \quad (3.30)$$

Therefore, from Eqs. (3.19) and (3.30), the function $G(z)$ is given by the continued fraction expansion,

$$G(z) = \frac{\langle \psi_0 | \mathcal{O}^\dagger \mathcal{O} | \psi_0 \rangle}{z - \alpha_0 - \frac{\beta_1^2}{z - \alpha_1 - \frac{\beta_2^2}{z - \alpha_2 - \dots}}}. \quad (3.31)$$

From the relation Eq. (3.17) and the continued fraction expansion Eq. (3.31), we can calculate the dynamical function $C(\omega)$. In practice, we can cut the continued fraction expansion in a finite step within an allowable error.

3.3 Self-energy Functional Theory (SFT)

3.3.1 Grand Potential and Self-energy

In the SFT, we consider the grand canonical system with the chemical potential μ and temperature T ($= 1/\beta$) [75]. The Hamiltonian consisting of the noninteracting one-body term \mathbf{t} and interaction term \mathbf{U} is given as

$$\mathcal{H} = \mathcal{H}_{\mathbf{t},\mathbf{U}} = \mathcal{H}_{\mathbf{t}} + \mathcal{H}_{\mathbf{U}}, \quad (3.32)$$

$$\mathcal{H}_{\mathbf{t}} = \sum_{\alpha\beta} t_{\alpha\beta} c_{\alpha}^{\dagger} c_{\beta}, \quad (3.33)$$

$$\mathcal{H}_{\mathbf{U}} = \frac{1}{2} \sum_{\alpha\beta\gamma\delta} U_{\alpha\beta\gamma\delta} c_{\alpha}^{\dagger} c_{\beta}^{\dagger} c_{\gamma} c_{\delta}, \quad (3.34)$$

where c_{α}^{\dagger} (c_{α}) is the creation (annihilation) operator of a fermion. In the grand canonical system, the grand potential of the system is given by the partition function:

$$\Omega_{\mathbf{t},\mathbf{U}} = -\frac{1}{\beta} \ln Z_{\mathbf{t},\mathbf{U}}, \quad (3.35)$$

$$Z_{\mathbf{t},\mathbf{U}} = \text{tr} [\exp(-\beta(\mathcal{H}_{\mathbf{t},\mathbf{U}} - \mu N))]. \quad (3.36)$$

The one-particle Green's function $G_{\alpha\beta} \equiv \langle\langle c_{\alpha}; c_{\beta}^{\dagger} \rangle\rangle$ is given by the thermal average, so that the Green's function depends on \mathbf{t} and \mathbf{U} , i.e., $G_{\mathbf{t},\mathbf{U},\alpha\beta}$. In this section, we write the matrix representation of $G_{\mathbf{t},\mathbf{U},\alpha\beta}$ as $\mathbf{G}_{\mathbf{t},\mathbf{U}}$. At $\mathbf{U} = 0$, the free Green's function $\mathbf{G}_{\mathbf{t},0}$ is given as

$$G_{\mathbf{t},0,\alpha\beta}(i\omega_n) = [(i\omega_n + \mu)\delta_{\alpha\beta} - t_{\alpha\beta}]^{-1}, \quad (3.37)$$

where $i\omega_n \equiv i(2n+1)\pi/\beta$ is the fermion Matsubara frequency. Introducing the self-energy $\Sigma_{\mathbf{t},\mathbf{U}}$, which includes the many-body effects, the Green's function of the interacting system $\mathbf{G}_{\mathbf{t},\mathbf{U}}$ is given from the Dyson's equation as

$$\mathbf{G}_{\mathbf{t},\mathbf{U}}^{-1} = \mathbf{G}_{\mathbf{t},0}^{-1} - \Sigma_{\mathbf{t},\mathbf{U}}. \quad (3.38)$$

Conversely, we can evaluate the self-energy from the Green's functions: $\Sigma_{\mathbf{t},\mathbf{U}} = \mathbf{G}_{\mathbf{t},0}^{-1} - \mathbf{G}_{\mathbf{t},\mathbf{U}}^{-1}$.

3.3.2 Luttinger-Ward Functional

In the interacting system, the grand potential is given by the Luttinger-Ward (LW) functional $\hat{\Phi}_{\mathbf{U}}[\mathbf{G}]$ ⁴ [75–79]. The LW functional plays an important role in the SFT. In this section, we therefore introduce the LW functional in some detail. The LW functional has the following properties.

(I) The domain of the LW function is given by the space of the Green's function \mathbf{G} [75, 76]. The LW functional is constructed by the skeleton diagrams shown in Fig.3.1 [75, 76]. It is also known that the LW functional can be formulated in the path integral method [75, 77–79]. In the non-interacting limit ($\mathbf{U} = 0$), the LW functional vanishes, i.e., $\hat{\Phi}_{\mathbf{U}}[\mathbf{G}_{\mathbf{t},\mathbf{U}}] = 0$.

(II) When the Green's function is exact in the system with Hamiltonian $H_{\mathbf{t},\mathbf{U}}$, i.e., $\mathbf{G} = \mathbf{G}_{\mathbf{t},\mathbf{U}}$, the LW functional gives the exact quantity

$$\hat{\Phi}_{\mathbf{U}}[\mathbf{G}_{\mathbf{t},\mathbf{U}}] = \Phi_{\mathbf{t},\mathbf{U}}, \quad (3.39)$$

and the grand potential of the system is given by

$$\Omega_{\mathbf{t},\mathbf{U}}[\mathbf{G}_{\mathbf{t},\mathbf{U}}] = \Phi_{\mathbf{t},\mathbf{U}} + \text{Tr} \ln \mathbf{G}_{\mathbf{t},\mathbf{U}} - \text{Tr}(\Sigma_{\mathbf{t},\mathbf{U}} \mathbf{G}_{\mathbf{t},\mathbf{U}}), \quad (3.40)$$

where $\text{Tr} \mathbf{X} = T \sum_{\omega_n} \sum_{\mathbf{k}} \sum_{\alpha} e^{i\omega_n 0^+} \text{tr} X_{\alpha\alpha}(i\omega_n)$ and $\Sigma_{\mathbf{t},\mathbf{U}}$ is the exact self-energy given by the Dyson's equation (3.38) [75].

⁴In this section, we indicate functionals as $\hat{X}[\dots]$ with a hat, which should be distinguished from physical quantities A [75].

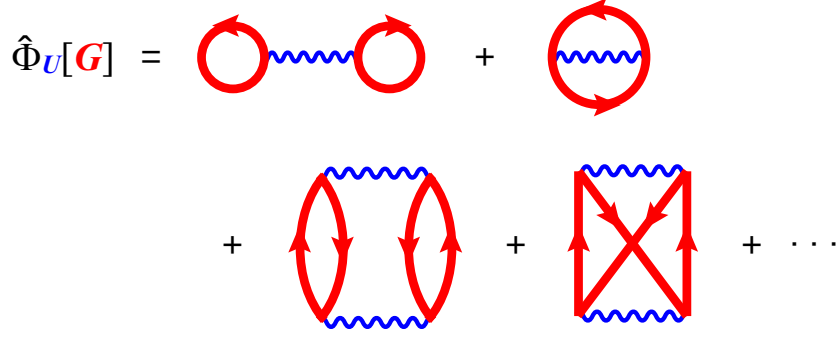


Figure 3.1: Skeleton diagrams of the Luttinger-Ward functional $\hat{\Phi}_U[\mathbf{G}]$. Red arrows and blue wave lines represent the Green's function \mathbf{G} and interaction \mathbf{U} , respectively.

(III) The functional derivative of the LW functional $\hat{\Phi}_U[\mathbf{G}]$ with respect to the Green's function \mathbf{G} gives

$$\frac{1}{T} \frac{\delta \hat{\Phi}_U[\mathbf{G}]}{\delta \mathbf{G}} = \hat{\Sigma}_U[\mathbf{G}], \quad (3.41)$$

and the functional $\hat{\Sigma}_U[\mathbf{G}]$ corresponds to the self-energy. For the exact Green's function $\mathbf{G}_{t,U}$, this gives the exact self-energy: [75]

$$\hat{\Sigma}_U[\mathbf{G}_{t,U}] = \Sigma_{t,U}. \quad (3.42)$$

(IV) The functional relation of $\hat{\Phi}_U[\dots]$ explicitly depends on the interaction \mathbf{U} , but it does not depend on \mathbf{t} . In other words, when two systems have the same interaction \mathbf{U} but different one-body term \mathbf{t} , the systems are described by the same LW functional. From Eq. (3.41), $\hat{\Sigma}_U[\dots]$ does not depend on \mathbf{t} either. Therefore, the LW functional is a universal functional [75, 76].

3.3.3 Variational Principle

In the SFT, the grand potential is described as a functional of Σ [75, 77, 78]. Although the LW functional $\hat{\Phi}_U[\mathbf{G}]$ is given by a functional of \mathbf{G} , we can introduce another functional of Σ by using the Legendre transformation, which is given as

$$\hat{F}_U[\Sigma] = \hat{\Phi}_U[\hat{\mathbf{G}}_U[\Sigma]] - \text{Tr}(\Sigma \hat{\mathbf{G}}_U[\Sigma]). \quad (3.43)$$

Here, $\hat{\mathbf{G}}_U[\hat{\Sigma}[\mathbf{G}]] = \mathbf{G}$. From Eqs. (3.41) and (3.43), the functional derivative of $\hat{F}_U[\Sigma]$ with respect to Σ gives the following relation⁵

$$\frac{1}{T} \frac{\delta \hat{F}_U[\Sigma]}{\delta \Sigma} = -\hat{\mathbf{G}}_U[\Sigma]. \quad (3.44)$$

With the functional $\hat{F}_U[\Sigma]$ and Eq. (3.40), we can define the grand potential functional, which is given as

$$\hat{\Omega}_{t,U}[\Sigma] = \text{Tr} \ln (\mathbf{G}_{t,0}^{-1} - \Sigma)^{-1} + \hat{F}_U[\Sigma]. \quad (3.45)$$

The functional derivative of Eq. (3.45) with respect to Σ gives

$$\frac{1}{T} \frac{\delta \hat{\Omega}_{t,U}[\Sigma]}{\delta \Sigma} = \frac{1}{\mathbf{G}_{t,0}^{-1} - \Sigma} - \hat{\mathbf{G}}_U[\Sigma]. \quad (3.46)$$

5

$$\begin{aligned} \frac{1}{T} \frac{\delta \hat{F}_U[\Sigma]}{\delta \Sigma_{\alpha\beta}} &= \frac{1}{T} \sum_{\gamma,\delta} \frac{\delta \hat{\Phi}_U[\hat{\mathbf{G}}_U[\Sigma]]}{\delta \hat{\mathbf{G}}_{U,\gamma\delta}[\Sigma]} \frac{\delta \hat{\mathbf{G}}_{U,\gamma\delta}[\Sigma]}{\delta \Sigma_{\alpha\beta}} - \frac{\delta}{\delta \Sigma_{\alpha\beta}} \left(\sum_{\gamma,\delta} \Sigma_{\delta\gamma} \hat{\mathbf{G}}_{U,\gamma\delta}[\Sigma] \right) \\ &= \sum_{\gamma,\delta} \Sigma_{\delta\gamma} \frac{\delta \hat{\mathbf{G}}_{U,\gamma\delta}[\Sigma]}{\delta \Sigma_{\alpha\beta}} - \sum_{\gamma,\delta} \left(\delta_{\alpha,\delta} \delta_{\beta,\gamma} \hat{\mathbf{G}}_{U,\gamma\delta}[\Sigma] + \Sigma_{\delta\gamma} \frac{\delta \hat{\mathbf{G}}_{U,\gamma\delta}[\Sigma]}{\delta \Sigma_{\alpha\beta}} \right) = -\hat{\mathbf{G}}_{U,\beta\alpha}[\Sigma] \end{aligned}$$

When the self-energy is exact ($\Sigma = \Sigma_{t,U}$), the functional $\hat{G}_U[\Sigma_{t,U}] = G_{t,U}$ becomes the exact Green's function $G_{t,U}$, where we find

$$\hat{G}_U[\Sigma_{t,U}] = G_{t,U} = \frac{1}{G_{t,0}^{-1} - \Sigma_{t,U}} \quad (3.47)$$

from the Dyson's equation (3.38). From Eqs. (3.46) and (3.47), we find the following relation when $\Sigma = \Sigma_{t,U}$:

$$\frac{\delta \hat{\Omega}_{t,U}[\Sigma_{t,U}]}{\delta \Sigma_{t,U}} = 0. \quad (3.48)$$

In other words, we may regard Eq. (3.48) as the variational equation for a trial self-energy Σ , i.e.,

$$\frac{\delta \hat{\Omega}_{t,U}[\Sigma]}{\delta \Sigma} = 0, \quad (3.49)$$

whereby we can determine the exact self-energy $\Sigma_{t,U}$ from the variational equation Eq. (3.49). Therefore, the problem of seeking for the exact ground state in the interacting systems is consistent with the problem of seeking for the stationary point of the Grand potential functional $\hat{\Omega}_{t,U}[\Sigma]$.

3.4 Variational Cluster Approximation (VCA)

3.4.1 Reference System and VCA

In the SFT, we need to calculate the grand potential $\hat{\Omega}_{t,U}[\Sigma]$. However, the calculation of the functional $\hat{F}_U[\Sigma]$ is difficult in general. The idea of VCA is based on the universality of the LW functional, i.e., $\hat{F}_U[\Sigma]$ is unknown but explicitly depends only on U .

From Eq. (3.45), the grand potential functional of the original system [see Fig. 3.2 (a)] is given by

$$\hat{\Omega}_{t,U}[\Sigma] = \text{Tr} \ln (G_{t,0}^{-1} - \Sigma)^{-1} + \hat{F}_U[\Sigma]. \quad (3.50)$$

Let us introduce the reference system here, whose example is shown in Fig. 3.2 (b). In the reference system, the one-body parts t' are only valid in the cluster and inter-cluster hopping parameters are zero. The grand potential functional of the reference system is given as

$$\hat{\Omega}_{t',U}[\Sigma] = \text{Tr} \ln (G_{t',0}^{-1} - \Sigma)^{-1} + \hat{F}_U[\Sigma]. \quad (3.51)$$

Owing to the universality of the functional $\hat{F}_U[\Sigma]$, we find that Eqs. (3.50) and (3.51) have the same functional $\hat{F}_U[\Sigma]$ even though the original and reference systems have the different one-body terms.

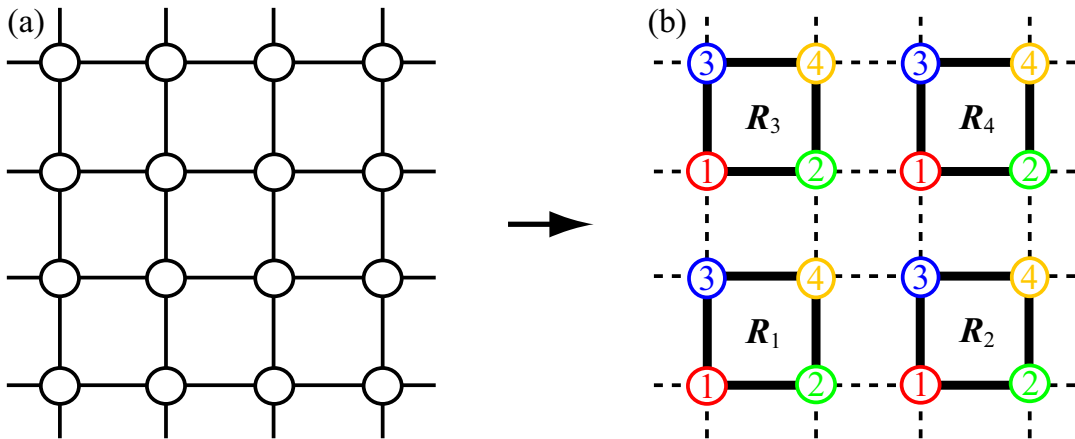


Figure 3.2: (a) Original lattice system and (b) reference system based on $2 \times 2 = 4$ site clusters.

From Eqs. (3.50) and (3.51), we can eliminate the unknown functional $\hat{F}_U[\Sigma]$ and then the grand potential functional of the original system is given by

$$\hat{\Omega}_{t,U}[\Sigma] = \hat{\Omega}_{t',U}[\Sigma] + \text{Tr} \ln (\mathbf{G}_{t,0}^{-1} - \Sigma)^{-1} - \text{Tr} \ln (\mathbf{G}_{t',0}^{-1} - \Sigma)^{-1}. \quad (3.52)$$

Up to here, the formalism of Eq. (3.52) does not include any approximation. Adopting the exact self-energy of the reference system, i.e., $\Sigma = \Sigma_{t',U}$, the first and third term of r.h.s. of Eq. (3.52) becomes $\hat{\Omega}_{t',U}[\Sigma_{t',U}] = \Omega_{t',U}$ and $\mathbf{G}_{t,0}^{-1} - \Sigma_{t',U} = \mathbf{G}_{t',U}^{-1}$, respectively. Thus, using $\Sigma = \Sigma_{t',U}$, Eq. (3.52) becomes

$$\hat{\Omega}_{t,U}[\Sigma_{t',U}] = \Omega_{t',U} + \text{Tr} \ln (\mathbf{G}_{t,0}^{-1} - \Sigma_{t',U})^{-1} - \text{Tr} \ln \mathbf{G}_{t',U}. \quad (3.53)$$

Introducing the reference system, where we solve the many-body problem exactly in each cluster, we can calculate all the terms of r.h.s of Eq. (3.53), and thus we can evaluate $\hat{\Omega}_{t,U}[\Sigma]$ approximately. Nothing that $\hat{\Omega}_{t,U}[\Sigma_{t',U}]$ is a function of the variational parameters t' , we use the notation $\Omega(t') \equiv \hat{\Omega}_{t,U}[\Sigma_{t',U}]$ hereafter.

The grand potential $\Omega(t')$ includes approximation, but using the variational principle,

$$\frac{\partial \Omega(t')}{\partial t'} = 0, \quad (3.54)$$

we can optimize $\Omega(t')$ with respect to t' , so that we can evaluate the accurate ground state⁶ [75, 77–81].

Grand potential for numerical calculations

For our numerical calculations, we rewrite the grand potential (3.53) as follows. First, introducing $\mathbf{V} \equiv H_t - H_{t'}$, we rewrite the second term of r.h.s of Eq. (3.53) as⁷

$$\mathbf{G}_{t,0}^{-1} - \Sigma_{t',U} = \mathbf{G}_{t',U}^{-1} - \mathbf{V}. \quad (3.55)$$

Using \mathbf{V} , the grand potential (3.53) becomes

$$\begin{aligned} \Omega(t') &= \Omega_{t',U} + \text{Tr} \ln (\mathbf{G}_{t',U}^{-1} - \mathbf{V})^{-1} - \text{Tr} \ln \mathbf{G}_{t',U} \\ &= \Omega_{t',U} - \text{Tr} \ln (\mathbf{1} - \mathbf{V} \mathbf{G}_{t',U}). \end{aligned} \quad (3.56)$$

Next, let us discuss the quantity of \mathbf{V} in detail. Here, we label each cluster in the reference system as \mathbf{R} and the site in the cluster as \mathbf{r}_a [see Fig. 3.4 (a)]. Then, using \mathbf{R} and \mathbf{r}_a , the site of the original lattice system is given by

$$\mathbf{r}_i = \mathbf{R} + \mathbf{r}_a. \quad (3.57)$$

Noting that the one-body parts of the reference system are only valid in the cluster, the Hamiltonian $H_{t'}$ is given with \mathbf{R} and \mathbf{r}_a as

$$H_{t'} = \sum_{ij} t'_{ij} c_i^\dagger c_j = \sum_{\mathbf{R}\mathbf{R}'} \sum_{ab} \delta_{\mathbf{R},\mathbf{R}'} t'_{ab} c_{\mathbf{R}a}^\dagger c_{\mathbf{R}'b}. \quad (3.58)$$

Using \mathbf{R} and \mathbf{r}_a , \mathbf{V} is then given by

$$\mathbf{V} = \sum_{ij} (t_{ij} - t'_{ij}) c_i^\dagger c_j = \sum_{\mathbf{R}\mathbf{R}'} \sum_{ab} (t_{ab}^{\mathbf{R}\mathbf{R}'} - \delta_{\mathbf{R},\mathbf{R}'} t'_{ab}) c_{\mathbf{R}a}^\dagger c_{\mathbf{R}'b} \equiv \sum_{\mathbf{R}\mathbf{R}'} \sum_{ab} V_{ab}^{\mathbf{R}\mathbf{R}'} c_{\mathbf{R}a}^\dagger c_{\mathbf{R}'b}. \quad (3.59)$$

⁶In the VCA, we calculate the grand potential directly and seek for the stationary point. On the other hand, from Eq. (3.54), we can derive the following Euler equation,

$$\frac{\partial \Sigma_{t',U}}{\partial t'} \frac{\delta \hat{\Omega}_{t,U}[\Sigma_{t',U}]}{\delta \Sigma_{t',U}} = T \frac{\partial \Sigma_{t',U}}{\partial t'} \left(\frac{1}{\mathbf{G}_{t,0}^{-1} - \Sigma_{t',U}} - \mathbf{G}_{t',U} \right) = 0.$$

We can solve the Euler equation self-consistently, which is consistent with the self-energy optimization in the dynamical mean-field theory.

⁷Free Green's function of the original lattice system is give as $\mathbf{G}_{t,0}(z) = (z + \mu - H_t)^{-1}$ and

$$\mathbf{G}_{t,0}^{-1} - \Sigma_{t',U} = (z + \mu - H_t - \Sigma_{t',U}) - (H_t - H_{t'}) = \mathbf{G}_{t',U}^{-1} - \mathbf{V}$$

In the reference system, \mathbf{V} does not maintain the translation symmetry of the original lattice system but keeps the translation symmetry of the superlattice constructed by the small clusters. The Fourier transformation for the superlattice is defined as

$$c_{\mathbf{R}a}^\dagger = \frac{1}{\sqrt{N}} \sum_{\mathbf{Q}} c_{\mathbf{Q}a}^\dagger e^{i\mathbf{Q}\cdot\mathbf{R}}, \quad (3.60)$$

where N is the number of the clusters in the reference system. Using the Fourier transformation for the superlattice thus defined, we have

$$\mathbf{V} = \sum_{\mathbf{Q}} \sum_{ab} \left(\sum_{\mathbf{R}} V_{ab}^{0\mathbf{R}} e^{i\mathbf{Q}\cdot\mathbf{R}} \right) c_{\mathbf{Q}a}^\dagger c_{\mathbf{Q}b} \equiv \sum_{\mathbf{Q}} \sum_{ab} V_{ab}(\mathbf{Q}) c_{\mathbf{Q}a}^\dagger c_{\mathbf{Q}b}, \quad (3.61)$$

where \mathbf{V} is diagonal with respect to \mathbf{Q} . Defining

$$V_{ab}(\mathbf{Q}) \equiv \sum_{\mathbf{R}} V_{ab}^{0\mathbf{R}} e^{i\mathbf{Q}\cdot\mathbf{R}} = \sum_{\mathbf{R}} t_{ab}^{0\mathbf{R}} e^{i\mathbf{Q}\cdot\mathbf{R}} - t'_{ab}, \quad (3.62)$$

we obtain the grand potential (3.53) as⁸

$$\Omega(\mathbf{t}') = \Omega_{\mathbf{t}',U} - T \sum_{\omega_n} \sum_{\mathbf{Q}} \sum_{\sigma} \ln \det(\mathbf{1} - \mathbf{V}(\mathbf{Q}) \mathbf{G}_{\mathbf{t}',U}(i\omega_n)). \quad (3.63)$$

In our practical calculations, we usually use the ED method to solve the many-body problem in each cluster, which is suitable for calculating quantities at zero temperature. Therefore, we introduce the formalism of the grand potential at zero temperature. Using the residue theorem⁹, the second term of r.h.s. of Eq. (3.63) is given by

$$\begin{aligned} I &\equiv T \sum_{\omega_n} \sum_{\mathbf{Q}} \sum_{\sigma} \ln \det(\mathbf{1} - \mathbf{V}(\mathbf{Q}) \mathbf{G}_{\mathbf{t}',U}(i\omega_n)) \\ &= \sum_{\sigma} \oint_{\Gamma} \frac{dz}{2\pi i} f(z) \sum_{\mathbf{Q}} \ln \det(\mathbf{1} - \mathbf{V}(\mathbf{Q}) \mathbf{G}_{\mathbf{t}',U}(z)), \end{aligned} \quad (3.64)$$

where $f(z)$ is the Fermi distribution function and Γ is the contour around the Matsubara frequency $i\omega_n$. At zero temperature, the Fermi distribution function becomes a step function, and thus Γ becomes C , the contour of the frequency integral that encloses the negative real axis. Thus, the integral I at $T = 0$ is given as¹⁰,

$$\begin{aligned} I &= \sum_{\sigma} \oint_C \frac{dz}{2\pi i} \sum_{\mathbf{Q}} \ln \det(\mathbf{1} - \mathbf{V}(\mathbf{Q}) \mathbf{G}_{\mathbf{t}',U}(z)) \\ &= \sum_{\sigma} \left(\int_0^{\infty} \frac{dx}{\pi} \sum_{\mathbf{Q}} \ln |\det(\mathbf{1} - \mathbf{V}(\mathbf{Q}) \mathbf{G}_{\mathbf{t}'U}(ix))| - \sum_{\mathbf{Q}} \frac{\text{tr} \mathbf{V}(\mathbf{Q})}{2} \right). \end{aligned} \quad (3.65)$$

We can also calculate $\Omega_{\mathbf{t}',U}$ in Eq. (3.63) from the ED. With the ground state energy E'_0 and the number of particles N' in the reference system, the grand potential of the reference system is given by

$$\Omega_{\mathbf{t}'U} = \frac{1}{L} (E'_0 - \mu N'), \quad (3.66)$$

⁸In Eq. (3.63), we use the definition $\text{Tr} = T \sum_{\omega_n} \sum_{\mathbf{k}} \sum_{\sigma} e^{i\omega_n 0^+} \text{tr}$ and the relation $\text{tr} \ln \mathbf{A} = \ln \det \mathbf{A}$. From Eq. (3.74) given below, we find that $\mathbf{G}_{\mathbf{t}',U}(i\omega_n)$ does not depend on \mathbf{Q} .

⁹The Fermi distribution function $f(z) = 1/(e^{\beta z} + 1)$ has poles of order one at the Matsubara frequency $i\omega_n$ and

$$\lim_{z \rightarrow i\omega_n} \frac{z - i\omega_n}{e^{\beta z} + 1} = -T.$$

Thus, from the residue theorem, the following relation holds:

$$T \sum_n g(i\omega_n) = \oint_{\Gamma} \frac{dz}{2\pi i} f(z) g(z).$$

¹⁰The details of the calculation of Eq. (3.65) is given in Ref. [79].

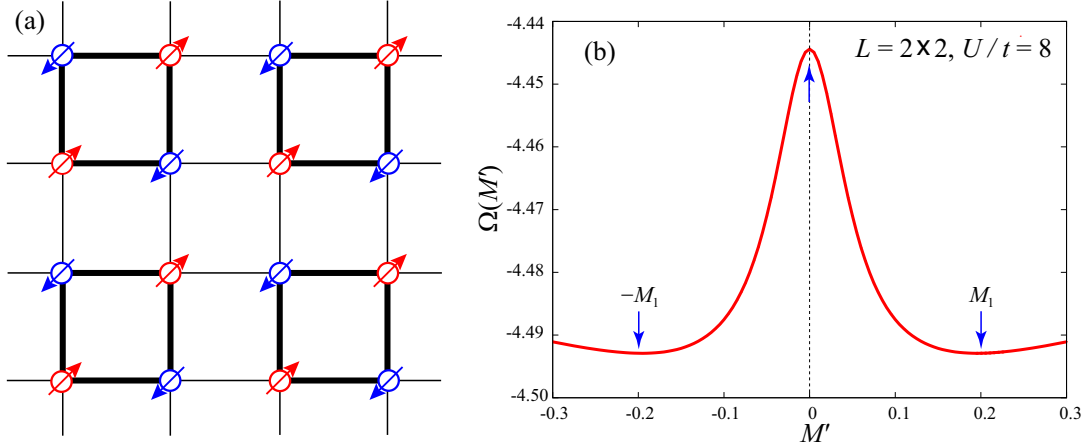


Figure 3.3: (a) Antiferromagnetic state in the reference system with $L = 2 \times 2 = 4$ sites cluster and (b) the calculated grand potential as a function of the Weiss field M' with the 4 site cluster at $U/t = 8$.

where L is the number of sites in the cluster. From Eqs. (3.63), (3.65) and (3.66), the grand potential at zero temperature is given by

$$\Omega(\mathbf{t}') = \frac{1}{L}(E'_0 - \mu N') - \frac{1}{NL} \sum_{\sigma} \left(\int_0^{\infty} \frac{dx}{\pi} \sum_{\mathbf{Q}} \ln |\det(\mathbf{1} - \mathbf{V}(\mathbf{Q})\mathbf{G}_{\mathbf{t}',U}(ix))| - \sum_{\mathbf{Q}} \frac{\text{tr}\mathbf{V}(\mathbf{Q})}{2} \right), \quad (3.67)$$

where we divide $\Omega(\mathbf{t}')$ by NL . We can calculate E'_0 and $\mathbf{G}_{\mathbf{t}',U}(z)$ from the ED and estimate $\mathbf{V}(\mathbf{Q})$ from Eq. (3.62). In our calculation, we use the double exponential formula for the integration in Eq. (3.67).

3.4.2 Spontaneous Symmetry Breaking in VCA

Within the VCA, we can take into account the spontaneous symmetry breakings just by adding appropriate Weiss fields to the reference system [82], adopting the fields as the variational parameters. In this section, as an example of the spontaneous symmetry breaking treated in the VCA, we show the antiferromagnetic (AF) ordered state in the two-dimensional square-lattice Hubbard model. The Hubbard Hamiltonian is defined as

$$\mathcal{H} = - \sum_{i,j,\sigma} t_{ij} c_{i,\sigma}^{\dagger} c_{j,\sigma} + U \sum_i n_{i,\uparrow} n_{i,\downarrow}. \quad (3.68)$$

The ground state of the Hubbard model on the square lattice is known to be the AF state. Here, we introduce the Weiss field for the AF order, which is given as

$$\mathcal{H}_{\text{AF}} = M' \sum_{i,\sigma} e^{i\mathbf{Q} \cdot \mathbf{r}_i} (n_{i,\uparrow} - n_{i,\downarrow}), \quad (3.69)$$

where $\mathbf{Q} = (\pi, \pi)$ and the AF state is shown in Fig. 3.3 (a). To discuss the stability of the AF state, we add the Weiss field (3.69) to the Hubbard Hamiltonian (3.68), i.e. $\mathcal{H}' = \mathcal{H} + \mathcal{H}_{\text{AF}}$. We calculate the grand potential (3.67) for the Hamiltonian of the reference system \mathcal{H}' and search the most stable stationary point as a function of the variational parameter M' .

In Fig. 3.3 (b), we show the calculated grand potential $\Omega(M')$ obtained using the $L = 2 \times 2 = 4$ site cluster at $U/t = 8$. The calculated grand potential has three stationary points, which are at $M' = 0$ and $M' = \pm M_1 \neq 0$. Noting $\Omega(M_1) < \Omega(0)$, the stationary point at M_1 is the most stable, which indicates that the AF state is stabler than the normal state.

3.5 Cluster Perturbation Theory (CPT)

3.5.1 Green's Function of CPT

In this section, we introduce the CPT [81,83,84]. In the VCA, we calculate the grand potential using the self-energy of the reference system $\Sigma_{\mathbf{t}',U}$. From Eq. (3.47) and (3.55), using the the self-energy $\Sigma_{\mathbf{t}',U}$,

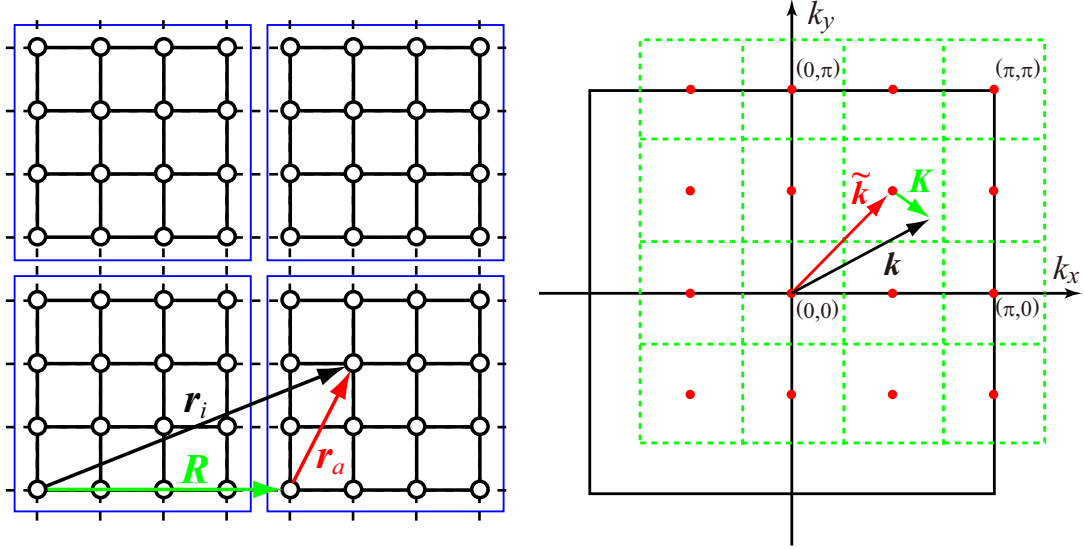


Figure 3.4: (a) Reference system with 16 site clusters and (b) Brillouin zone of the reference system.

the Green's function of the original lattice system is given by

$$\mathcal{G}(z) \equiv \hat{G}_U[\Sigma_{t',U}] = (\mathbf{G}_{t',U}^{-1} - \mathbf{V})^{-1}. \quad (3.70)$$

Using the index of the reference system ($\mathbf{r}_i = \mathbf{R} + \mathbf{r}_a$), we write $\mathcal{G}_{ij}(z) = \mathcal{G}_{ab}^{\mathbf{R}\mathbf{R}'}(z)$ and the Fourier transformation of $\mathcal{G}(z)$ is given by

$$\mathcal{G}(\mathbf{k}, \mathbf{k}', z) = \frac{1}{NL} \sum_{\mathbf{R}\mathbf{R}'ab} \mathcal{G}_{ab}^{\mathbf{R}\mathbf{R}'}(z) e^{-i\mathbf{k}\cdot(\mathbf{R}+\mathbf{r}_a)} e^{i\mathbf{k}'\cdot(\mathbf{R}'+\mathbf{r}_b)}. \quad (3.71)$$

The Green's function $\mathcal{G}(z)$ keeps the translation symmetry of the superlattice, which is diagonal with respect to the momentum of superlattice \mathbf{Q} . Here, we consider the Fourier transformed Green's function $\mathcal{G}_{ab}(\mathbf{Q}, z)$ defined as

$$\mathcal{G}_{ij}(z) = \mathcal{G}_{ab}^{\mathbf{R}\mathbf{R}'}(z) = \frac{1}{N} \sum_{\mathbf{Q}} \mathcal{G}_{ab}(\mathbf{Q}, z) e^{i\mathbf{Q}\cdot(\mathbf{R}-\mathbf{R}')}. \quad (3.72)$$

The Green's function of the reference system is valid in the cluster, i.e.,

$$G_{t',U,ij}(z) = \delta_{\mathbf{R},\mathbf{R}'} G_{t',U,ab}(z). \quad (3.73)$$

From the Fourier transformation of the Green's function of the reference system,

$$G_{t',U,ab}(\mathbf{Q}, z) = \sum_{\mathbf{R}} \delta_{\mathbf{0},\mathbf{R}} G_{t',U,ab}(z) e^{i\mathbf{Q}\cdot\mathbf{R}} = G_{t',U,ab}(z), \quad (3.74)$$

we find that the Green's function of the reference system does not depend on \mathbf{Q} . Also, from Eq. (3.62), \mathbf{V} depends only on \mathbf{Q} . Therefore, we have

$$\mathcal{G}_{ab}(\mathbf{Q}, z) = (\mathbf{G}_{t',U}^{-1}(z) - \mathbf{V}(\mathbf{Q}))_{ab}^{-1} = \left(\frac{\mathbf{G}_{t',U}(z)}{\mathbf{I} - \mathbf{V}(\mathbf{Q})\mathbf{G}_{t',U}(z)} \right)_{ab}. \quad (3.75)$$

From $\mathcal{G}_{ab}(\mathbf{Q}, z)$ and Eq. (3.71), we have¹¹

$$\mathcal{G}(\mathbf{k}, \mathbf{k}', z) = \frac{1}{L} \sum_{ab} \sum_{\mathbf{Q}} \mathcal{G}_{ab}(\mathbf{Q}, z) e^{-i\mathbf{k}\cdot\mathbf{r}_a} e^{i\mathbf{k}'\cdot\mathbf{r}_b} \delta_{\mathbf{Q}, \mathbf{k} - \tilde{\mathbf{k}}} \delta_{\mathbf{Q}, \mathbf{k}' - \tilde{\mathbf{k}'}} \quad (3.76)$$

where $\tilde{\mathbf{k}}$ and $\tilde{\mathbf{k}'}$ are the reciprocal lattice vector of the superlattice ($e^{i\tilde{\mathbf{k}}\cdot\mathbf{R}} = 1$). Defining $\mathbf{k} - \tilde{\mathbf{k}} = \mathbf{K}$ and $\mathbf{k}' - \tilde{\mathbf{k}'} = \mathbf{K}'$ [see Fig. 3.4] and using (3.76), we have

$$\mathcal{G}(\mathbf{k}, \mathbf{k}', z) = \frac{1}{L} \sum_{ab} \mathcal{G}_{ab}(\mathbf{K}, z) e^{-i\mathbf{k}\cdot\mathbf{r}_a} e^{i\mathbf{k}'\cdot\mathbf{r}_b} \delta_{\mathbf{K}, \mathbf{K}'}. \quad (3.77)$$

Because $\tilde{\mathbf{k}}$ is the reciprocal lattice vector of the superlattice ($e^{i\tilde{\mathbf{k}}\cdot\mathbf{R}} = 1$), we have

$$V_{ab}(\mathbf{K}) = \sum_{\mathbf{R}} V_{ab}^{0\mathbf{R}} e^{i(\mathbf{k} - \tilde{\mathbf{k}})\cdot\mathbf{R}} = \sum_{\mathbf{R}} V_{ab}^{0\mathbf{R}} e^{i\mathbf{k}\cdot\mathbf{R}} = V_{ab}(\mathbf{k}), \quad (3.78)$$

and thus V_{ab} depends only on \mathbf{k} . The momentum dependence of \mathcal{G}_{ab} is given in V_{ab} , and thus \mathcal{G}_{ab} depends only on \mathbf{k} , i.e.,

$$\mathcal{G}_{ab}(\mathbf{K}, z) = \mathcal{G}_{ab}(\mathbf{k}, z). \quad (3.79)$$

$\mathcal{G}_{ab}(\mathbf{K}, z)$ does not include $\tilde{\mathbf{k}}$ but $\delta_{\mathbf{K}, \mathbf{K}'}$ still have the dependence of $\tilde{\mathbf{k}}$. Introducing $\tilde{\mathbf{k}} - \tilde{\mathbf{k}'} \equiv \mathbf{q}_s$, we find that the number of \mathbf{q}_s is L in the first Brillouin zone of the original system [see Fig. 3.4]. The delta function in Eq. (3.79) becomes

$$\delta_{\mathbf{K}, \mathbf{K}'} = \sum_{s=1}^L \delta_{\mathbf{k}, \mathbf{k}' + \mathbf{q}_s}, \quad (3.80)$$

and thus the Green's function of the original lattice system is give by

$$\mathcal{G}(\mathbf{k}, \mathbf{k}', z) = \frac{1}{L} \sum_{ab} \mathcal{G}_{ab}(\mathbf{k}, z) e^{-i\mathbf{k}\cdot\mathbf{r}_a} e^{i\mathbf{k}'\cdot\mathbf{r}_b} \left(\sum_{s=1}^L \delta_{\mathbf{k}, \mathbf{k}' + \mathbf{q}_s} \right). \quad (3.81)$$

We introduce the reference system, which keeps the translation symmetry of the superlattice, but it breaks the translation symmetry of the original lattice system. Therefore, \mathcal{G} is not diagonal with respect to \mathbf{k} and the final form includes $\mathbf{q}_s = \tilde{\mathbf{k}} - \tilde{\mathbf{k}'}$. In the CPT, we use the approximation, neglecting the off-diagonal term $\mathbf{q}_s \neq 0$, we finally obtain the CPT Green's function as

$$\mathcal{G}_{\text{CPT}}(\mathbf{k}, z) = \frac{1}{L} \sum_{a,b=1}^L \mathcal{G}_{ab}(\mathbf{k}, z) e^{-i\mathbf{k}\cdot(\mathbf{r}_a - \mathbf{r}_b)}. \quad (3.82)$$

3.5.2 Physical Quantity from CPT

Using the CPT Green's function $\mathcal{G}_{\text{CPT}}(\mathbf{k}, \omega)$, we can evaluate the single particle excitation spectrum $A(\mathbf{k}, \omega)$ defined as

$$A(\mathbf{k}, \omega) = -\frac{1}{\pi} \lim_{\eta \rightarrow 0} \text{Im} \mathcal{G}_{\text{CPT}}(\mathbf{k}, \omega + i\eta), \quad (3.83)$$

¹¹

$$\begin{aligned} \mathcal{G}(\mathbf{k}, \mathbf{k}', z) &= \frac{1}{NL} \sum_{\mathbf{R}\mathbf{R}'ab} \left(\frac{1}{N} \sum_{\mathbf{Q}} \mathcal{G}_{ab}(\mathbf{Q}, z) e^{i\mathbf{Q}\cdot(\mathbf{R}-\mathbf{R}')} \right) e^{-i\mathbf{k}\cdot(\mathbf{R}+\mathbf{r}_a)} e^{i\mathbf{k}'\cdot(\mathbf{R}'+\mathbf{r}_b)} \\ &= \frac{1}{L} \sum_{ab} \sum_{\mathbf{Q}} \mathcal{G}_{ab}(\mathbf{Q}, z) e^{-i\mathbf{k}\cdot\mathbf{r}_a} e^{i\mathbf{k}'\cdot\mathbf{r}_b} \left(\frac{1}{N} \sum_{\mathbf{R}} e^{i(\mathbf{Q}-\mathbf{k})\cdot\mathbf{R}} \right) \left(\frac{1}{N} \sum_{\mathbf{R}'} e^{-i(\mathbf{Q}-\mathbf{k}')\cdot\mathbf{R}'} \right) \end{aligned}$$

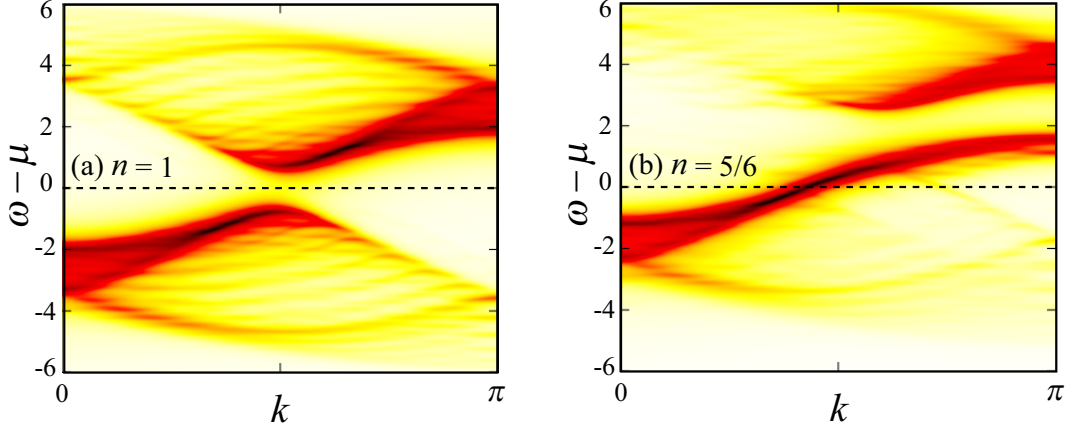


Figure 3.5: Single-particle excitation spectrum $A(\mathbf{k}, \omega)$ of the one-dimensional Hubbard chain at (a) $n = 1$ and (b) $n = 5/6$.

where η gives broadening to the spectrum. In Fig. 3.5, we show the calculated result for $A(\mathbf{k}, \omega)$ for the one-dimensional Hubbard chain. Summing up $A(\mathbf{k}, \omega)$ over momentum \mathbf{k} , we can evaluate the density of states $\rho(\omega)$ defined as

$$\rho(\omega) = \sum_{\mathbf{k} \in \text{BZ}} A(\mathbf{k}, \omega) = -\frac{1}{\pi} \lim_{\eta \rightarrow 0} \sum_{\mathbf{k} \in \text{BZ}} \text{Im} \mathcal{G}_{\text{CPT}}(\mathbf{k}, \omega + i\eta). \quad (3.84)$$

On the other hand, integrating $A(\mathbf{k}, \omega)$ with respect to frequency ω , we can evaluate the momentum distribution function $n(\mathbf{k})$ defined as

$$n(\mathbf{k}) = \oint_C \frac{dz}{2\pi i} \mathcal{G}_{\text{CPT}}(\mathbf{k}, z). \quad (3.85)$$

We can also evaluate the expectation values of the one-body parameter \mathcal{O} as

$$\langle \mathcal{O} \rangle = \frac{1}{NL} \sum_{\alpha\beta} \mathcal{O}_{\alpha\beta} \langle c_{\alpha}^{\dagger} c_{\beta} \rangle. \quad (3.86)$$

From the Green's function \mathcal{G} in Eq. (3.77), the expectation value of \mathcal{O} is given by

$$\langle \mathcal{O} \rangle = \frac{1}{NL} \text{Tr} \mathcal{O} \mathcal{G} = \frac{1}{NL} \oint_C \frac{dz}{2\pi i} \sum_{\mathbf{Q}} \text{tr}[\mathcal{O} \mathcal{G}(\mathbf{Q}, z)]. \quad (3.87)$$

Note that we sum up over momenta in the reduced Brillouin zone for the superlattice \mathbf{Q} in Eq. (3.87). For example, the expectation value of the number of particles $n = \langle n_i \rangle$ is given, setting $\mathcal{O} = \mathbf{1}$, as

$$n = \frac{1}{NL} \sum_i \langle n_i \rangle = \frac{1}{NL} \oint_C \frac{dz}{2\pi i} \sum_{\mathbf{Q}} \text{tr}[\mathcal{G}(\mathbf{Q}, z)]. \quad (3.88)$$

Note that, within the framework of the VCA, we use the optimized one-body parameter \mathbf{t}_{OPT} for the CPT calculations.

3.6 Summary

In this Chapter, we have reviewed the numerical methods used in this thesis. First, we have introduced the ED technique based on the Lanczos algorithm, which can solve the many-body problems in finite-size systems exactly. We have also introduced the method for calculating dynamical correlation functions with the ED technique. Next, we have introduced the VCA based on the SFT, where we can take into account the effects of short-range spatial correlations even in low-dimensional systems in the thermodynamic limit and can discuss the spontaneous symmetry breakings of correlated electron systems beyond the mean-field theory. We have also introduced the CPT, which is useful for evaluating the single-particle excitation spectrum and their integrated values such as the density of states and momentum distribution function in the thermodynamic limit.

Chapter 4

Excitonic Phase in the Extended Falicov-Kimball Model

4.1 Introduction

The minimal theoretical model to investigate the excitonic condensation states in lattice systems is the Falicov-Kimball type model [85]. The original Falicov-Kimball model describes localized f electrons interacting via a local Coulomb repulsion with itinerant c electrons if they reside at the same site [85,86]. An extended version of the model takes into account the direct nearest-neighbor f -electron hopping [87]. The Hamiltonian of the extended Falicov-Kimball model (EFKM) is given as

$$\begin{aligned} \mathcal{H} &= -t_f \sum_{\langle i,j \rangle} f_i^\dagger f_j + \varepsilon_f \sum_i n_i^f - t_c \sum_{\langle i,j \rangle} c_i^\dagger c_j + \varepsilon_c \sum_i n_i^c + U \sum_i n_i^f n_i^c \\ &= \sum_{\mathbf{k}} \varepsilon_{\mathbf{k}}^f f_{\mathbf{k}}^\dagger f_{\mathbf{k}} + \sum_{\mathbf{k}} \varepsilon_{\mathbf{k}}^c c_{\mathbf{k}}^\dagger c_{\mathbf{k}} + \frac{U}{L} \sum_{\mathbf{k}, \mathbf{k}', \mathbf{q}} f_{\mathbf{k}+\mathbf{q}}^\dagger f_{\mathbf{k}} c_{\mathbf{k}'-\mathbf{q}}^\dagger c_{\mathbf{k}'}, \end{aligned} \quad (4.1)$$

where α_i^\dagger ($\alpha_{\mathbf{k}}^\dagger$) denotes the creation operator of a spinless electron α ($= f, c$) at site i (momentum \mathbf{k}). Schematic picture of the EFKM is shown in Fig. 4.1(a). t_α and ε_α are the electron hopping integral on the neighboring sites and the energy level of an electron α , respectively. L is the number of sites. $\varepsilon_{\mathbf{k}}^\alpha$ is the energy band dispersion in \mathbf{k} space of the band α . In this chapter, we assume $\varepsilon_f < 0$ and $\varepsilon_c > 0$, so that the f and c bands correspond to the valence and conduction bands, respectively. The noninteracting band structure is shown in Fig. 4.1(b); a small gap semiconducting or small overlapped semimetallic state can be realized by tuning the on-site energy difference $\varepsilon_c - \varepsilon_f$. U (> 0) is the interband Coulomb repulsive interaction, which parametrizes the interband Coulomb attraction between f -holes and c -electrons. The Hamiltonian Eq. (4.1) is consistent with Eq. (2.1) in Sec. 2.2.1. Therefore, the interband interaction U induces excitonic instability in the system.

The EFKM has been studied in the context of exciton condensation (as well as electronic ferroelectricity [87–91]), where Hartree Fock (mean-field) approximation [89–92], slave boson approach [93–95], random phase approximation [92,96], projection-based renormalization method [97,98], and variational

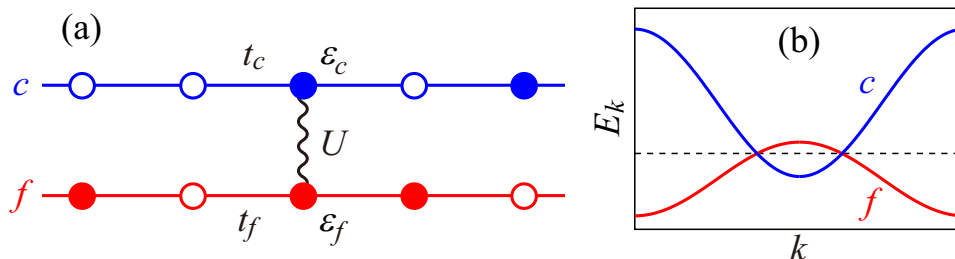


Figure 4.1: (a) Schematic representation of the extended Falicov-Kimball model (EFKM). (b) Non-interacting band structure of the EFKM.

cluster approach [99] have been used. At half-filling, it is known that the EFKM shows the three phases; i.e., staggered orbital ordered (SOO) phase, exciton condensed (excitonic insulator, EI) phase and band insulator (BI) phase. If the energy levels of the f and c electrons are located close to each other ($\varepsilon_f \sim \varepsilon_c$), the SOO phase characterized by the periodic staggered modulation of the partial density of f and c electrons appears. In the opposite limit, where the energy level splitting between the f and c electrons is large ($\varepsilon_f \ll \varepsilon_c$), the BI state characterized by the completely filled f band appears. Between the SOO and BI phases, the EI state is stabilized. The EI state is characterized by the spontaneous hybridization between the c and f electrons induced by the interband interaction U . In the EI phase, the finite temperature phase diagram in the system with the spatial dimension larger than three corresponds to the phase diagram shown in Fig. 2.4¹ [92]. Starting from the noninteracting semimetallic state, the EFKM can describe the smooth crossover of the exciton condensation state from the weak-coupling BCS state to the strong-coupling BEC state with increasing U . Therefore, the EFKM is a simple spinless model and suitable for discussing the BCS-BEC crossover of the exciton condensation state. Recently, the EFKM is applied to the candidate materials of the EI such as $1T$ -TiSe₂ [33] and Ta₂NiSe₅ [39] to explain the experimental results.

In this Chapter, we investigate the exciton condensation state in the EFKM using unbiased numerical techniques. Especially, we focus on the BCS-BEC crossover of the exciton condensation state in the two-dimensional (2D) and one-dimensional (1D) lattice systems.

In Sec. 4.2, we address the problem of exciton condensation in an electron-hole double layer system described by the 2D EFKM, where we use the exact-diagonalization (ED) technique². We calculate the anomalous excitation spectra, condensation amplitudes and exciton momentum distribution function in the BCS, intermediate, and BEC regions. From the calculated condensation amplitude, we evaluate the pair coherence length and order parameter of the condensate as a function of U . We also compare the results of the ED with the results of the mean-field (MF) theory and variational cluster approximation (VCA) at mass-symmetric case ($t_f = t_c$). Finally, we investigate the effects of a mass imbalance between the f holes and c electrons based on the pair coherence length and exciton binding energy.

In Sec. 4.3, we investigate the EI state in the 1D EFKM³. First, we determine the phase boundary of the SOO-EI and EI-BI transitions and describe the complete ground-state phase diagram of the 1D EFKM from the large-scale density matrix renormalization group (DMRG) method [63]. In comparison with the 2D system, the EI state in the 1D EFKM is critical. Then, we show a critical character of the excitonic state in the 1D system by the central charge. We also show a crossover between the BCS and BEC condensates by the exciton-exciton correlation and exciton momentum distribution functions. Following the method used in the 2D systems, we also study the anomalous spectral function and extract the pair coherence length and binding energy of the electron-hole pairs. This allows us to comment on the nature of the excitonic bound states occurring in the condensation process and to discuss the effect of a mass imbalance between the c -electrons and f -holes.

4.2 Two-Dimensional Double-Layer System

In this section, we discuss the BCS-BEC crossover of the exciton condensation state in the two-dimensional double-layered system. Here, we assume that the energy level ε_α are taken as a chemical potentials of each layer μ_α . In practice, we adjust the chemical potentials μ_f and μ_c to maintain the numbers of electrons in the f and c layers independently. Without loss of generality, the f layer is assigned to the hole (or valence-band) layer and the c layer to the electron (or conduction-band) layer. This mimics the generic situation in semiconductor electron-hole double quantum wells [100–102], and double-monolayer [103, 104] or double-bilayer graphene systems [105]. We furthermore assume that the excited electrons and holes have infinite lifetime and that the number of excited electrons is equal to the number of excited holes. This is in accordance with the experimental situations in the majority of cases [100, 104, 106–113].

To discuss the BCS-BEC crossover of the exciton condensation state, we use the Lanczos ED method. In the ED investigation of the double-layer EFKM, we use finite-size square lattice of $L_c = 4 \times 4 = 16$

¹The interband interaction U induces the Hartree shift, which enhances the energy level splitting between f and c electrons. Thus, the semimetallic EI state becomes the semiconducting EI or BI states with increasing U . In comparison with the phase diagram in Fig. 2.4, the EFKM does not include the screening effect that changes the size of the band gap or overlap.

²Sec. 4.2 is based on T. Kaneko, S. Ejima, H. Fehske, and Y. Ohta, *Phys. Rev. B* **88**, 035312 (2013) and *JPS Conf. Proc.* **3**, 017006 (2014).

³Sec. 4.3 is based on S. Ejima, T. Kaneko, Y. Ohta, and H. Fehske, *Phys. Rev. Lett.* **112**, 026401 (2014).

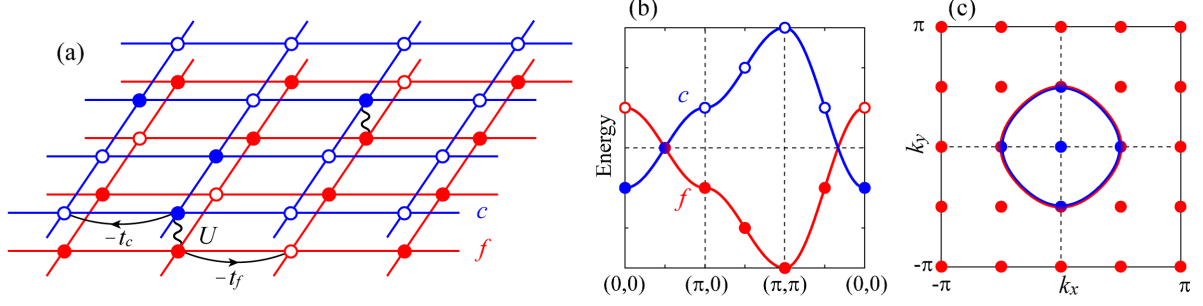


Figure 4.2: (a) Schematic representation of the 2D EFKM cluster model with $N_s = 16$ sites (32 orbitals). (b) Non-interacting tight-binding band structure and (c) square lattice Brillouin zone. Dots indicate the allowed momenta of the 4×4 lattice with periodic boundary condition. Throughout this work, we assume filling factors $n^f = 0.75$ and $n^c = 0.25$, i.e., $(N_f, N_c) = (12, 4)$ which means $n^h = n^e = 0.25$, irrespective of U . The red and blue lines in (c) show the perfectly matching hole and electron Fermi surfaces, respectively, with finite-lattice Fermi momenta \mathbf{k}_F located at $\mathbf{k} = (\pm\pi/2, 0)$ and $(0, \pm\pi/2)$ [114].

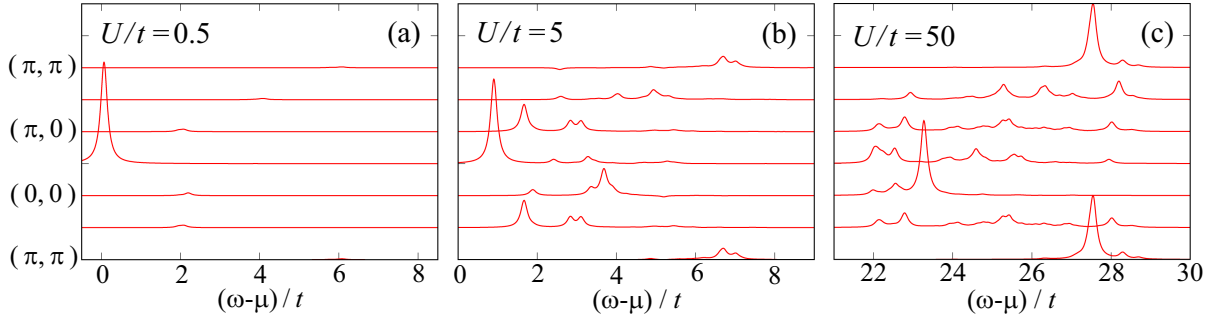


Figure 4.3: Anomalous spectral function $F(\mathbf{k}, \omega)$ in the mass-symmetric 2D EFKM with $U/t = 0.5$ (left), 5 (middle), and 50 (right). We use a Lorentzian broadening of $\eta/t = 0.1$.

sites (32 orbitals) with periodic boundary condition (PBC). We show the schematic representation of the 2D EFKM cluster model in Fig. 4.2. Here, we assume a band structure with a direct band gap ($t_c t_f < 0$). The particle densities are fixed to be $n_f = 0.75$ and $n_c = 0.25$, i.e., $(N_f, N_c) = (12, 4)$, which realizes a quarter-filled electron and hole band: $n^e = n^h = 0.25$. For the 4×4 lattice with $(N_f, N_c) = (12, 4)$ considered, the Fermi momenta are located at $\mathbf{k}_F = (\pm\pi/2, 0)$ and $\mathbf{k}_F = (0, \pm\pi/2)$ at $U = 0$ [see Fig. 4.2 (c)].

4.2.1 Anomalous Green's Function

Let us first discuss the anomalous Green's function. Using the ED technique, the anomalous Green's function is obtained from

$$G^{cf}(\mathbf{k}, \omega) = \langle N_f - 1, N_c + 1 | c_{\mathbf{k}}^\dagger \frac{1}{\omega + i\eta - \mathcal{H} + E_0} f_{\mathbf{k}} | N_f, N_c \rangle, \quad (4.2)$$

where $|N_f, N_c\rangle$ is the ground state of the EFKM with fixed numbers of c and f electrons. In Eq. (4.2), E_0 is the average energy of the states $|N_f, N_c\rangle$ and $|N_f - 1, N_c + 1\rangle$ [114–116]. From $G^{cf}(\mathbf{k}, \omega)$, we can immediately deduce the anomalous spectral function: $F(\mathbf{k}, \omega) = -\frac{1}{\pi} \text{Im} G^{cf}(\mathbf{k}, \omega)$. Note that, if $|t_f| = t_c$, $F(\mathbf{k}, \omega > 0)$ and the inverse function $F(\mathbf{k}, -\omega)$ is symmetrical with respect to $\omega = 0$. However, for the mass-asymmetric case $|t_f| \neq t_c$, $F(\mathbf{k}, \omega)$ is not consistent with $F(\mathbf{k}, -\omega)$, and thus we need to calculate the inverse function.

Figure 4.3 gives an intensity plot of $F(\mathbf{k}, \omega)$ in the square-lattice Brillouin zone with $|t_f| = t_c = t$. In the weak-coupling regime [see Fig. 4.3 (a)], $F(\mathbf{k}, \omega)$ has a sharp peak at the Fermi momentum $\mathbf{k}_F = (\pi/2, 0)$, whose intensity goes almost to zero as soon as the momentum deviates from \mathbf{k}_F . With increasing U/t , the lowermost peak of $F(\mathbf{k}, \omega)$ shifts to higher energies, indicating an enhancement of the exciton's binding energy $|E_B|$, which may also be evaluated from the ground-state energies [see

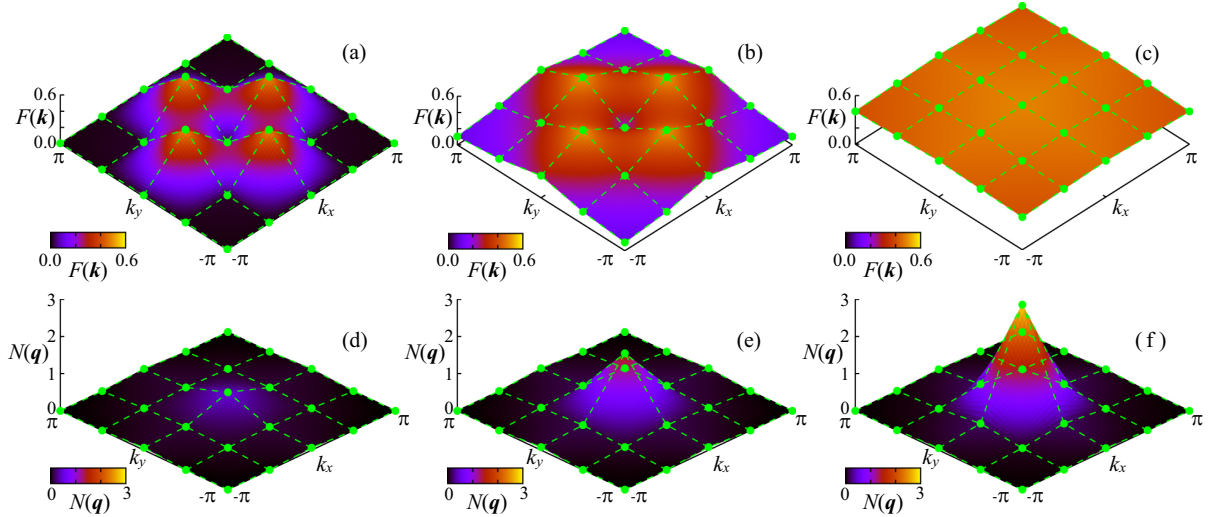


Figure 4.4: Condensation amplitude $F(\mathbf{k})$ (upper panels) and momentum distribution function $N(\mathbf{q})$ of excitons (lower panels) in the mass-symmetric 2D EFKM at $U/t = 0.5$ (left), 5 (middle), and 50 (right) [114].

below]. For $U/t = 5$ [see Fig. 4.3(b)], $F(\mathbf{k}, \omega)$ still exhibits pronounced peak around \mathbf{k}_F , but to compare with the spectrum at $U/t = 0.5$, $F(\mathbf{k}, \omega)$ acquires substantial weight at momenta away from \mathbf{k}_F . In the strong-coupling limit [see Fig. 4.3(c)], the spectral weight of $F(\mathbf{k}, \omega)$ is redistributed to higher energies and spread over the entire Brillouin zone. If the effective mass of the c electron is equal to that of the f hole (or $|t_f| = t_c = t$), the exciton condensation state in the double-layer EFKM can be mapped onto the superconducting (superfluid) state in the attractive Hubbard model. The behavior of $F(\mathbf{k}, \omega)$ for the exciton condensation state in the EFKM using the ED is consistent with that of the anomalous spectral function for the superconducting state in the attractive Hubbard model obtained by the VCA [117]; see also Appendix A.

4.2.2 Momentum Distribution Functions

To elucidate the nature of exciton condensation in momentum space, we now consider the condensation amplitude $F(\mathbf{k})$ and the exciton momentum distribution $N(\mathbf{q})$. Within the ED, the condensation amplitude can be directly calculated from

$$F(\mathbf{k}) = \langle N_f - 1, N_c + 1 | c_{\mathbf{k}}^\dagger f_{\mathbf{k}} | N_f, N_c \rangle. \quad (4.3)$$

Introducing a creation operator $b_{\mathbf{q}}^\dagger = (1/\sqrt{N_s}) \sum_{\mathbf{k}} c_{\mathbf{k}+\mathbf{q}}^\dagger f_{\mathbf{k}}$ of an excitonic quasiparticle with momentum \mathbf{q} , the momentum distribution function of excitons can be obtained from

$$N(\mathbf{q}) = \langle N_f, N_c | b_{\mathbf{q}}^\dagger b_{\mathbf{q}} | N_f, N_c \rangle. \quad (4.4)$$

Figure 4.4 shows the corresponding data for the condensation amplitude $F(\mathbf{k})$ and exciton momentum distribution $N(\mathbf{q})$ in the mass-symmetric case ($|t_f| = t_c = t$) in a wide parameter range of U . In the weak-coupling regime [panels (a) and (d)], $F(\mathbf{k})$ exhibits pronounced maxima at the Fermi momenta $\mathbf{k}_F = (\pm\pi/2, 0)$, $(0, \pm\pi/2)$ where $|F(\mathbf{k}_F)| \simeq 0.5$ and decreases rapidly away from the ‘Fermi surface’, pointing towards a BCS-type instability of weakly bound electron-hole pairs with s -wave symmetry. The sharply peaked $F(\mathbf{k})$ in momentum space indicates that the radius of the exciton is large in real space, i.e., we observe a weakly bound electron-hole pair. In the weak coupling region, $N(\mathbf{q})$ has a weak peak at $\mathbf{q} = 0$. As U increases, $F(\mathbf{k})$ broadens in momentum space [see Fig. 4.4 (b)], indicating that the radius of the bound electron-hole objects becomes smaller in real space. Accordingly, $N(\mathbf{q})$ is enhanced at momentum $\mathbf{q} = (0, 0)$ [see Fig. 4.4 (e)]. In the strong-coupling regime [see Fig. 4.4 (c) and (f)], $F(\mathbf{k})$ is homogeneously spread over the entire Brillouin zone, whereas $N(\mathbf{q})$ is sharply peaked at $\mathbf{q} = (0, 0)$, which is a sign of a BEC of tightly bound excitons. That is to say, as the attraction between electrons and holes increases in the EFKM, we get evidence for a BCS-BEC crossover. In Appendix A, we show the condensation amplitude for the Cooper pairs in the attractive Hubbard model, where we find that

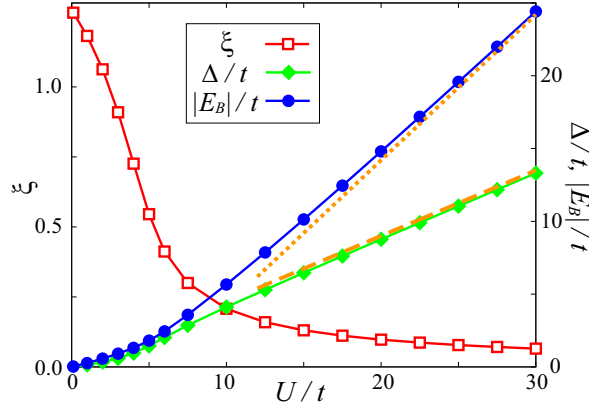


Figure 4.5: Coherence length ξ (squares), order parameter Δ (diamonds), and exciton binding energy E_B (circles) for the mass-symmetric 2D EFKM as functions of U/t . For comparison, the asymptotics in the strong-coupling limit $\Delta \propto 0.45U$ (dashed line) and $|E_B| \propto U$ (dotted line) have been inserted [114].

the behavior of $F(\mathbf{k})$ is consistent with that for the superconducting state in the attractive Hubbard model.

4.2.3 Pair Coherence Length

The pair coherence length ξ gives valuable information as to the nature of the exciton condensate. Using $F(\mathbf{k})$, this quantity may be defined as

$$\xi^2 = \frac{\sum_{\mathbf{r}} r^2 |F(\mathbf{r})|^2}{\sum_{\mathbf{r}} |F(\mathbf{r})|^2} = \frac{\sum_{\mathbf{k}} |\nabla_{\mathbf{k}} F(\mathbf{k})|^2}{\sum_{\mathbf{k}} |F(\mathbf{k})|^2}, \quad (4.5)$$

where $F(\mathbf{r}) = \frac{1}{\sqrt{L}} \sum_{\mathbf{r}'} \langle c_{\mathbf{r}'+\mathbf{r}}^\dagger f_{\mathbf{r}'} \rangle$ is the condensation amplitude in real space for the electron-hole pairs with distance \mathbf{r} [99, 114, 116, 117]. Here, we assume the lattice constant $a = 1$.

The behavior of the coherence length with $|t_f| = t_c = t$ is shown in Fig. 4.5. At small U/t , the coherence length is larger than the lattice constant, as a consequence of the weakly bound electron-hole pairs [see the behavior of $F(\mathbf{k})$ shown in Fig. 4.4 (a)]. This is the BCS limit. Increasing U , ξ decreases and first becomes comparable with, and finally becomes much smaller than the lattice constant. As a result, the excitons become BEC-like tightly bound pairs at large U . Altogether, we observe a smooth crossover from a BCS state of weakly paired electrons and holes ($\xi \gg 1$) to a BEC state of tightly bound pairs ($\xi \ll 1$). This crossover behavior is consistent with the calculated spectral and momentum distribution properties of the system shown in Fig. 4.3 and Fig. 4.4.

At mass-symmetric case ($|t_f| = t_c = t$), the exciton condensation state in the double-layer EFKM can be mapped onto the superconducting (superfluid) state in the attractive Hubbard model [117, 118], and thus we compare the coherence length calculated by the ED with results calculated by the VCA and MF. The results obtained by the ED, VCA, and MF are shown in Fig. 4.6 (a). In contrast to the coherence length obtained by the VCA and MF, ξ calculated by the ED stays finite as $U/t \rightarrow 0$. This is clearly a finite-size effect caused by the small number of available momenta in the Brillouin zone. In the VCA and MF, we can treat the large number of momenta in the Brillouin zone, so that ξ diverges as $U/t \rightarrow 0$. In the intermediate-to-strong coupling regime, the coherence lengths calculated by the ED, VCA, and MF are in quantitative agreement.

4.2.4 Order Parameter and Binding Energy

Let us discuss the order parameter for exciton condensation and binding energy of an electron and a hole. The order parameter again can be obtained from the condensation amplitude as

$$\Delta = \frac{U}{L} \sum_{\mathbf{k}} \langle c_{\mathbf{k}}^\dagger f_{\mathbf{k}} \rangle = \frac{U}{L} \sum_{\mathbf{k}} F(\mathbf{k}), \quad (4.6)$$

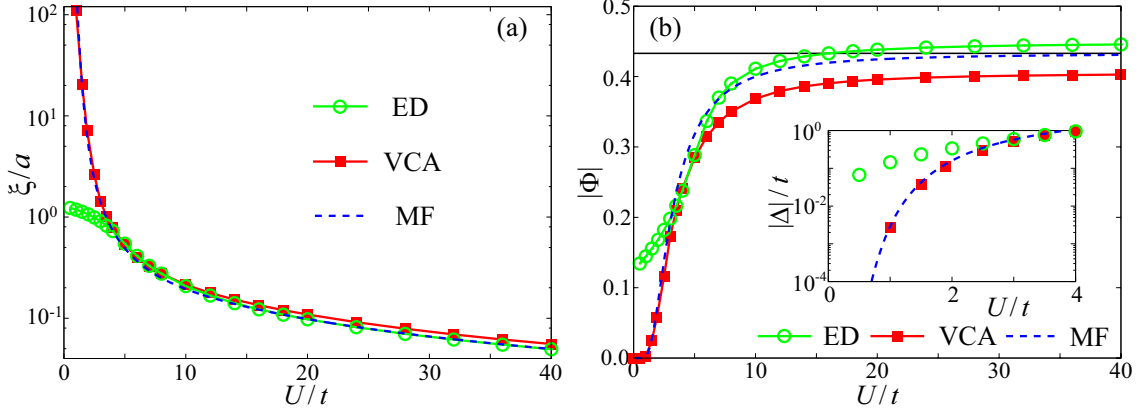


Figure 4.6: (a) Coherence length ξ in unit of the lattice constant a and (b) anomalous expectation value Φ for the 2D EFKM, obtained by ED (open green circles), VCA (full red squares), and MF (dashed blue lines). In (b), the horizontal line indicates $|\Phi| = \sqrt{3}/4$ and the inset gives the order parameter $\Delta = U\Phi$ in the weak-coupling regime [114, 117, 118].

where we also define the anomalous expectation value $\Phi = \sum_{\mathbf{k}} \langle c_{\mathbf{k}}^{\dagger} f_{\mathbf{k}} \rangle / L = \Delta / U$. Within our finite-cluster approach, the exciton binding energy E_B may be obtained as follow. Representing the f - c flavor by electron-hole variables, i.e., $f_i^{\dagger} \rightarrow h_i$ and $c_i^{\dagger} \rightarrow e_i^{\dagger}$, the interaction term of the EFKM takes the form $U \sum_i n_i^f n_i^c \rightarrow -U \sum_i n_i^e n_i^h + U \sum_i n_i^e$. We find that, in addition to the attractive electron-hole interaction, an extra on-site energy term appears. Due to this term, we should first determine the energy for the addition and removal of an electron:

$$E_B^+ = E_0(N_f - 1, N_c + 1) + E_0(N_f, N_c) - 2E_0(N_f, N_c + 1) + U, \quad (4.7)$$

$$E_B^- = E_0(N_f - 1, N_c + 1) + E_0(N_f, N_c) - 2E_0(N_f - 1, N_c) - U, \quad (4.8)$$

where $E_0(N_f, N_c)$ is the ground-state energy of the system with (N_f, N_c) electrons. Then, if $|t_f| = t_c$, the exciton binding energy E_B equals $E_B^+ = E_B^-$. For the mass-asymmetric case $|t_f| \neq t_c$, however, $E_B^+ \neq E_B^-$ because $E_0(N_f, N_c + 1) - U \neq E_0(N_f - 1, N_c)$. Hence, E_B should be defined as the average of E_B^+ and E_B^- , i.e., in general, the exciton binding energy is given by

$$E_B = E_0(N_f - 1, N_c + 1) + E_0(N_f, N_c) - E_0(N_f - 1, N_c) - E_0(N_f, N_c + 1). \quad (4.9)$$

Figure 4.5 displays the U dependence of both the exciton order parameter and exciton binding energy at $|t_f| = t_c = t$. The binding energy of an exciton, E_B , is equal to twice of the order parameter Δ in the weak-coupling limit and deviate largely from this value in the strong-coupling regime. The results may be compared with those of the BCS mean-field theory [22, 119], which gives Δ and E_B as a solution of the self-consistent equations

$$1 = \frac{U}{2N_s} \sum_{\mathbf{k}} \frac{1}{\sqrt{(\varepsilon_{\mathbf{k}} - \bar{\mu})^2 + \Delta^2}}, \quad (4.10)$$

$$2n = 1 - \frac{1}{N_s} \sum_{\mathbf{k}} \frac{\varepsilon_{\mathbf{k}} - \bar{\mu}}{\sqrt{(\varepsilon_{\mathbf{k}} - \bar{\mu})^2 + \Delta^2}}, \quad (4.11)$$

where $\varepsilon_{\mathbf{k}} = 2t(\cos k_x + \cos k_y)$, $n = n^e = n^h$, $\bar{\mu} = \mu - U(n - 1/2)$, and $\mu_f = -\mu_c = \mu$. In the weak-coupling limit, we should recover the usual BCS picture. Δ should therefore increase exponentially with U : $\Delta \propto \exp(-1/\rho(\varepsilon_F)U)$, thereby satisfying the relation $|E_B| = 2\Delta$ with $\rho(\varepsilon_F)$ being the density of states at the Fermi level. In the strong-coupling limit, on the other hand, the BCS equations yield the asymptotic behavior: $\Delta = U\sqrt{n(1-n)} = \sqrt{3}U/4 \simeq 0.433U$ and $|E_B| = 2\sqrt{\bar{\mu}^2 + \Delta^2} = U$. The numerical results obtained for Δ and $|E_B|$ show that we find the BCS relation $|E_B| = 2\Delta$ at weak couplings. In the strong-coupling limit, Δ and $|E_B|$ are found to be $\propto 0.45U$ and $\propto U$, respectively, which matches the BEC of composite bosons, where $\Delta = 0.433U$ and $|E_B| = U$ for $U/t \rightarrow \infty$.

In Fig. 4.6 (b), we also compare the results of the ED, MF and VCA. In the weak-coupling region, the ED obviously fails in reproducing the BCS mean-field-like behavior: Φ calculated by the ED stays

finite as $U/t \rightarrow 0$ and Δ evaluated by the ED does not show the exponential increase at $U/t \gtrsim 0$. Clearly, this can be attributed to finite-size effects within our small cluster calculation. Remarkably, the VCA yields the exponential increase expected in the weak-coupling limit [see inset of Fig. 4.6 (b)]. We furthermore note that Φ obtained by the VCA is in qualitative accordance with the ED and MF results in the intermediate to strong coupling regime. For $U/t \gtrsim 5$, Φ obtained by the VCA is reduced in comparison to the MF result. This may be due to the effects of quantum fluctuations of exciton condensation included in the VCA but not in the MF. Note that the calculations of the ED include quantum fluctuations in the cluster, but the ED calculations tend to overestimate the order parameter due to finite size effect. Due to quantum fluctuations, Φ calculated by the VCA is suppressed in comparison with the result of the MF theory, $\Phi \sim 0.405 < 0.433$ at $U \rightarrow \infty$.

4.2.5 Effect of Mass Asymmetry

In this section, we address the effects of a mass imbalance between f holes and c electrons. Since $|t_f| \neq t_c$ it makes sense to use U as the unit of energy and determine the exciton binding energy E_B and coherence length ξ in dependence on $|t_f|/U$. Figure 4.7 shows the results for $t_c/U = 1$ in comparison to the mass-symmetric case where a BCS-to-BEC crossover occurs with decreasing $|t_f|/U$. By contrast, ξ is not reflective of such a crossover for $t_c \neq |t_f|$, and the exciton binding energy even weakens at strong couplings $|t_f|/U \ll 1$.

In the strong-coupling region, where both $|t_f|/U$ and t_c/U are small, the EFKM can be mapped onto the XXZ quantum spin-1/2 model in a magnetic field [87],

$$\begin{aligned} \mathcal{H}_{\text{XXZ}} &= J \sum_{\langle i,j \rangle} (S_i^x S_j^x + S_i^y S_j^y + \Delta S_i^z S_j^z) - h \sum_i S_i^z \\ &= J \sum_{\langle i,j \rangle} [\mathbf{S}_i \cdot \mathbf{S}_j + \delta S_i^z S_j^z] - h \sum_i S_i^z, \end{aligned} \quad (4.12)$$

where $\mathbf{S}_i = (1/2) \sum_{\alpha,\beta} \alpha_i^\dagger \boldsymbol{\sigma}_{\alpha\beta} \beta_i$ ($\alpha, \beta = f, c$; $\boldsymbol{\sigma}$ is the vector of Pauli matrices), $J = 4|t_f|t_c/U$, $\Delta = (t_f^2 + t_c^2)/(2|t_f|t_c)$, and $\delta = (|t_f| - t_c)^2/(2|t_f|t_c)$. $h = 2\mu$ is determined in order to maintain $\sum_i S_i^z = 1/4$. The effective model is isotropic in spin space for the case of $|t_f| = t_c$, and exhibits antiferromagnetic order in the x - y plane at zero temperature. This long-range ordered state corresponds to an exciton condensate in the original EFKM. Different hopping parameters $t_c \neq |t_f|$ give rise to an Ising anisotropy Δ (or δ), which tends to suppress the x - y antiferromagnetic order. Accordingly, the exciton binding energy $|E_B|$ (excitonic condensate) is suppressed as $|t_f|/U \rightarrow 0$.

Figure 4.8 compiles our E_B (left panel) and ξ (right panel) data by two contour plots in the t_c/U - $|t_f|/U$ plane. For the mass-symmetric case $t_c = |t_f|$, i.e., on the diagonals of Fig. 4.8, both $|E_B|/U$ and ξ indicate a smooth crossover from BCS to BEC as U increases. On the other hand, at sufficiently

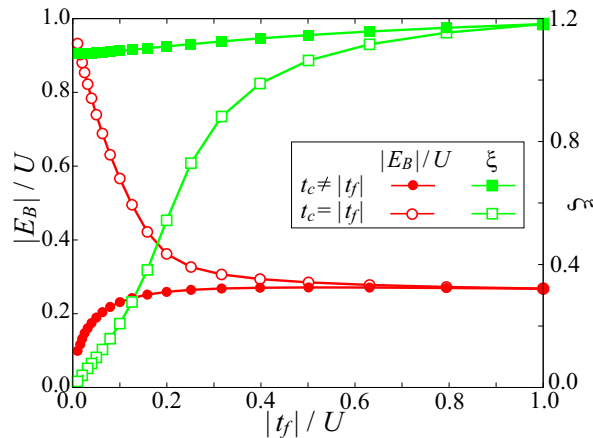


Figure 4.7: Binding energy E_B/U (left ordinate) and coherence length ξ (right ordinate) for the mass-asymmetric (filled symbols) and mass-symmetric (open symbols) 2D EFKM as functions of $|t_f|/U$ at $t_c/U = 1$ [114].

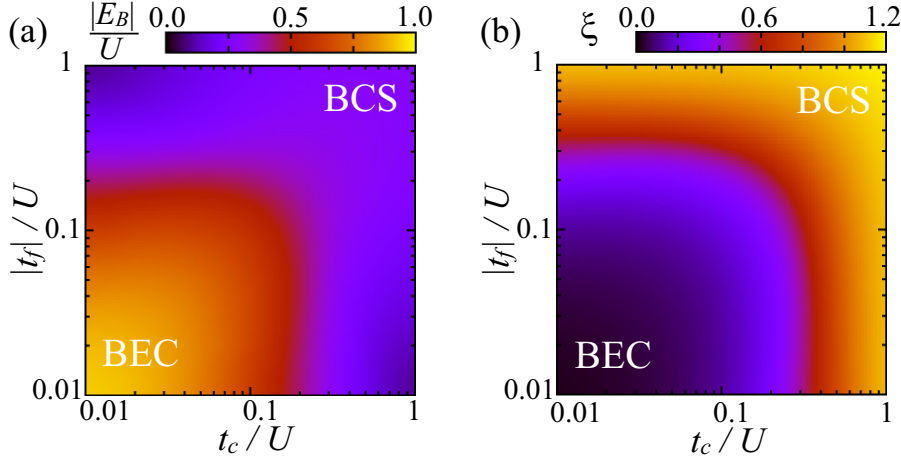


Figure 4.8: (a) Exciton binding energy E_B/U and (b) coherence length ξ of the 2D EFKM in the t_c/U - $|t_f|/U$ plane [114].

weak Coulomb interactions, $t_c/U \gtrsim 0.3$, we stay in the BCS-like state as $|t_f|/U$ is varied by changing the absolute value of t_f/t_c . Note that a strong mass imbalance between electrons and holes acts in a ‘pair-breaking’ way in both the BCS [23] and BEC [120] limits.

4.3 One-Dimensional System

In this section, we investigate the exciton condensation state in one-dimensional system. Here, we assume the energy levels ε_α as a level splitting between the f and c electrons; $\varepsilon_c = -\varepsilon_f = D/2$. In comparison with the previous section, we do not tune the number of electrons in the f and c chain independently, which indicates the number of electron of each chain can not be maintained by changing D and U . Note that we assume the half filling; the total number of electrons is constant with $n_f + n_c = 1$. This situation may correspond to the ground state of candidates materials as excitonic insulators.

To discuss the EI state in the 1D EFKM, we mainly use the large-scale DMRG [63] method⁴. In the DMRG calculation, we keep at least $m = 3200$ density-matrix eigenstates which ensure a discarded weight smaller than 1×10^{-6} . We also use the ED to calculate the dynamical Green’s function defined in Eq. (4.2). In the ED calculation, we use $L = 16$ site (32-orbitals) cluster. Note that, in our 1D setting, we use the term ‘condensate’ to indicate a critical phase with power-law correlation decay. In this section, we assume $t_c = t = 1$ as a unit energy.

4.3.1 Phase Diagram

First, we describe the phase diagram of the 1D EFKM in the U - D plane. To investigate the EI state in the one-dimensional system, the strong-coupling (large- U) limit gives a first hint of which phases might be realized in the 1D EFKM. At the strong coupling regime, the 1D EFKM can be mapped onto the exactly solvable spin-1/2 XXZ-Heisenberg model in a magnetic field $h = D$ aligned in the z -direction [121] (see Eq. (4.12)). The XXZ model exhibits three phases in the 1D chain system: the gapped antiferromagnetic (AF) phase, the critical gapless XY phase, which is discussed below, and the ferromagnetic (FM) phase. Transition lines, between the AF and XY phases ($h_{c_1} = D_{c_1}^{\text{XXZ}}$), and between the XY and FM phases ($h_{c_2} = D_{c_2}^{\text{XXZ}}$), are given from the Bethe ansatz [122, 123]:

$$h_{c_1} = D_{c_1}^{\text{XXZ}} = \frac{2\pi J \sinh \phi}{\phi} \sum_{m=0}^{\infty} \frac{1}{\cosh[(2m+1)\pi^2/2\phi]}, \quad (4.13)$$

$$h_{c_2} = D_{c_2}^{\text{XXZ}} = J(1 + \Delta), \quad (4.14)$$

where $\phi = \cosh^{-1} \Delta$ and $\Delta = (|t_f|^2 + t_c^2)/(2|t_f|t_c)$ in Eq. (4.12).

⁴DMRG calculations were performed by Dr. S. Ejima.

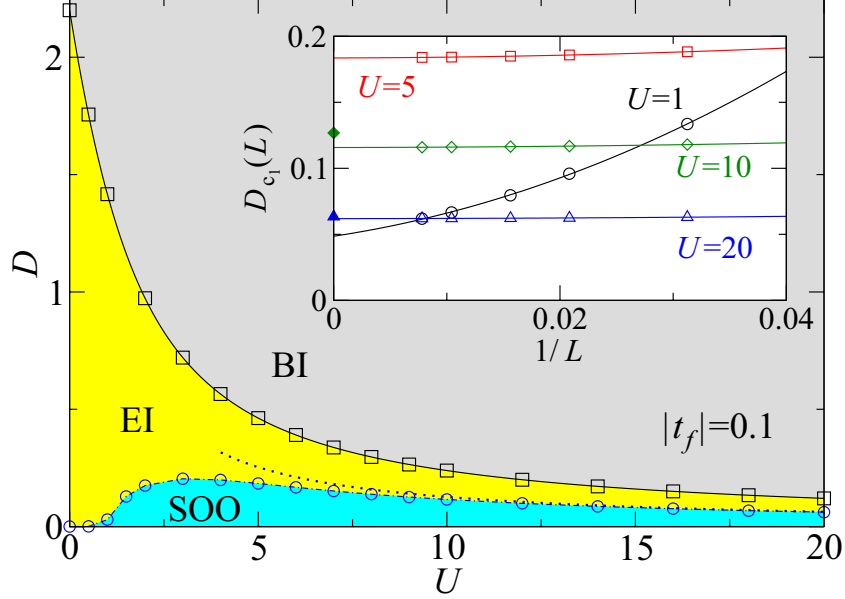


Figure 4.9: Ground-state phase diagram of the half-filled 1D EFKM with $|t_f| = 0.1$. Here and in what follows, we take t_c as the unit of energy. Squares (circles) denote the EI-BI (EI-SOO) transition points D_{c_2} (D_{c_1}) obtained by DMRG method with up to $L = 128$ sites and OBC. The solid line gives the analytical solution (4.15) for the EI-BI boundary; the dotted line shows the strong-coupling result for the EI-SOO boundary. The finite-size scaling of $D_{c_1}(L)$ is illustrated by the inset (open symbols), here the corresponding strong-coupling data are given by filled symbols [125].

Correspondingly, increasing the magnitude of the f - c level splitting D in the EFKM, we expect to find the following sequence of phases: (i) the SOO phase that matches the Ising-like AF phase in the XXZ model, (ii) an intermediate critical EI phase, which is consistent with the critical XY phase in the XXZ model, and (iii) a BI state, which is characterized by a filled (empty) f (c) band and related to the FM phase of the XXZ model. The phase boundary separating the EI and BI states in the EFKM is exactly known to be [124]

$$D_{c_2} = \sqrt{4(|t_f| + |t_c|)^2 + U^2} - U. \quad (4.15)$$

In the finite-size system, the transition points of the SOO-EI (AF-XY) and EI-BI (XY-FM) in the EFKM are given by

$$D_{c_1}(L) = E_0(L/2 + 1, L/2 - 1) - E_0(L/2, L/2), \quad (4.16)$$

$$D_{c_2}(L) = E_0(L, 0) - E_0(L - 1, 1), \quad (4.17)$$

respectively, corresponding to the XXZ model. Here, $E_0(N_f, N_c)$ denotes the ground-state energy for a system with N_f and N_c at $D = 0$.

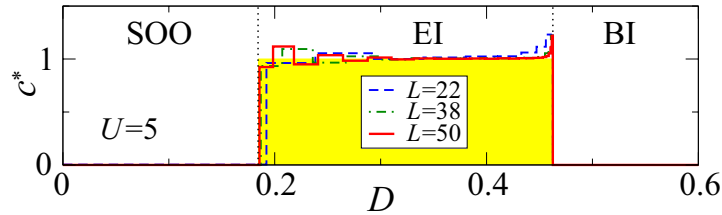


Figure 4.10: Central charge obtained at $U = 5$ for various L and PBC. Criticality, $c^* \sim 1$, is observed for the EI [125].

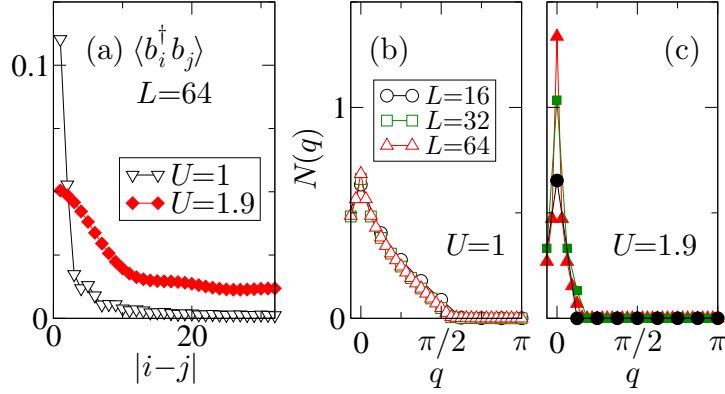


Figure 4.11: (a) Exciton-exciton correlation function $\langle b_i^\dagger b_j \rangle$ and (b) excitonic momentum distribution $N(q)$ at $U = 1$ and (c) 1.9 for $t_f = -0.1$, $D = 1$. Data are obtained by the DMRG for 1D L -site lattices with PBC [125].

The complete phase diagram of the 1D EFKM is presented in Fig. 4.9. Symbols denote the DMRG BI-EI and EI-SOO transition points, which can be obtained from Eq. (4.16) and Eq. (4.17), respectively, in the course of a finite-size scaling analysis up to $L = 128$ (see the inset). Note that Eq. (4.17) holds for both open and periodic boundary conditions (OBC/PBC), whereas Eq. (4.16) has to be evaluated with PBC (if OBC were used here, an extra factor 2 results: $D_{c_1}^{\text{OBC}} = 2D_{c_1}$). The $D_{c_2}(L \rightarrow \infty)$ values demonstrate the accuracy of our DMRG calculations. Exact results for $D_{c_1}(L \rightarrow \infty)$ can only be obtained numerically, where a comparison with the dotted line reveals the limits of the strong-coupling approach. Even if we assume indirect gap with $t_f t_c > 0$, we can get exactly the same phase diagram.

4.3.2 Criticality of Excitonic Insulator

Next, we discuss the criticality of the EI phase in the 1D EFKM. Corresponding to the critical XY phase in the XXZ model, the EI state in the 1D EFKM should be characterized by the central charge $c = 1$. The central charge can be confirmed by the von Neumann entanglement entropy $S_L(\ell) = -\text{Tr}_\ell(\rho_\ell \ln \rho_\ell)$ (with reduced density matrix $\rho_\ell = \text{Tr}_{L-\ell}(\rho)$). Numerically, the central charge is best estimated from the entropy difference [126, 127]:

$$c^*(L) \equiv \frac{3[S_L(L/2 - 1) - S_L(L/2)]}{\ln[\cos(\pi/L)]}. \quad (4.18)$$

The results from DMRG calculation are shown in the Fig. 4.10 for $|t_f| = 0.1$ at $U = 5$. It give clear evidence that $c^* \rightarrow 1$ in the EI, whereas we find $c^* = 0$ in the BI and SOO phases.

We also discuss the nature of the EI state with the correlation function. As a signature of an excitonic Bose-Einstein condensate in 1D, one expects (i) a power-law decay of the correlations $\langle b_i^\dagger b_j \rangle$ with $b_i^\dagger = c_i^\dagger f_i$ and (ii) a divergence of the excitonic momentum distribution $N(q) = \langle b_q^\dagger b_q \rangle$ with $b_q^\dagger = (1/\sqrt{L}) \sum_k c_{k+q}^\dagger f_k$ for the state with the lowest possible energy (in the direct gap case at $q = 0$) due to the absence of true long-range order. In Fig. 4.11, we show the correlation function calculated by DMRG. Calculated results support these expectations: Whereas in the weak-coupling BCS regime ($U = 1$), $\langle b_i^\dagger b_j \rangle$ decays almost exponentially (see Fig. 4.11(a)) and $N(q)$ shows only a marginal system-size dependence for all momenta (see Fig. 4.11(b)), in the strong-coupling BEC regime close to the EI-BI transition ($U = 1.9$), $\langle b_i^\dagger b_j \rangle$ exhibits a rather slow algebraic decay of the excitonic correlations (see Fig. 4.11(a)) and $N(q = 0)$ becomes divergent as $L \rightarrow \infty$ (see Fig. 4.11(c)).

4.3.3 BCS-BEC Crossover

Following the previous section, we discuss the excitonic BCS-BEC crossover using the anomalous Green's function $G^{cf}(k, \omega)$ in Eq. (4.2). Figures 4.12(a) and 4.12(b) show the anomalous spectral function $F(k, \omega)$ calculated by the ED method in the weak-coupling ($U = 1$) and strong-coupling ($U = 1.9$) regimes, respectively, at $D = 1$. At $U = 1$, EI arises from a semimetallic phase and the most of the spectral weight of the quasiparticle excitations is located around the Fermi points $k = \pm k_F$. The

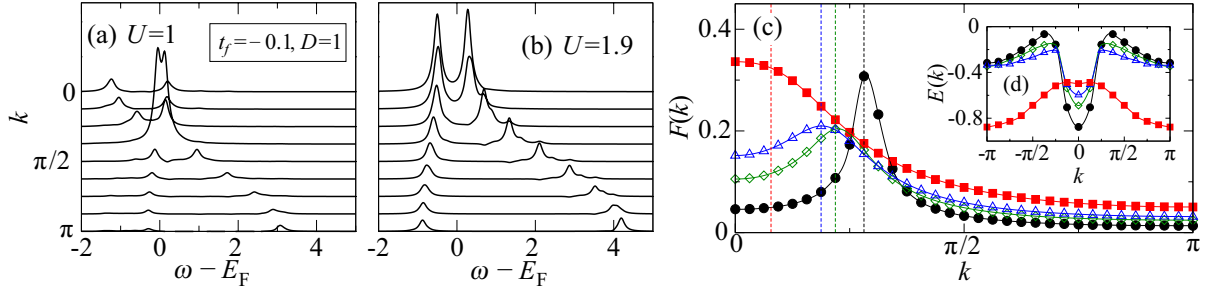


Figure 4.12: Anomalous spectral function $F(k, \omega)$ in the 1D EFKM with $U = 1$ (a) and $U = 1.9$ (b), where $t_f = -0.1$, $D = 1$. Data are obtained by ED using $\eta = 0.1$, $L = 16$, and PBC. Numerical results for $F(k)$ (c) and $E(k)$ (d) are shown for $U = 1$ (circles), 1.5 (diamonds), 1.7 (triangles), and 1.9 (squares). $F(k)$ is determined by the DMRG for $L = 64$ (PBC), whereas $E(k)$ is extracted from the lowest peaks of single-particle spectra $A(k, \omega)$ calculated by ED for $L = 16$ (PBC). Dashed lines in the panel (c) mark the corresponding Fermi momenta $k_F = \pi N_c / L$ in the noninteracting limit [125].

sharply peak around the Fermi points $k = \pm k_F$ in momentum space indicates that the radius of the exciton is large in real space, indicating a weak BCS-type pairing of electrons and holes. Fermi surface effects play no role at $U = 1.9$ where the Hartree shift drives the system to the semiconducting regime. Here, the $F(k, \omega)$ has a large peak at $k = 0$ and the peaks become larger in the entire momentum space in comparison with the weak coupling region. Spreading out of $F(k, \omega)$ in momentum space indicates the radius of electron-hole pairs becomes small in real space. The gap between the lowest energy peaks observed in $F(k, \omega)$ is equal to the binding energy E_B given by Eq. (4.9), and it enhances with increasing U .

To investigate the nature of excitons in momentum space in detail, we evaluate the condensation amplitude $F(k)$ with large size DMRG calculation. In Fig. 4.12(c), we display $F(k)$ calculated by DMRG with $L = 64$. At $U = 1$, $F(k)$ exhibits a sharp peak at the Fermi momentum, corresponding to $F(k, \omega)$. Increasing U , $F(k)$ becomes broad in momentum space and the peak shifts to smaller momenta. Close to the EI-BI transition point $U = 1.9 \lesssim U_{c_2} = 1.92$, $F(k)$ has a maximum at $k = 0$ but is spread out in momentum space, indicating a strong BEC-type pairing of electrons and holes.

In Fig. 4.12(d), we also show the quasiparticle dispersion $E(k)$ derived from single-particle excitation spectrum $A(k, \omega)$ by the ED method. Driving the BCS-BEC crossover by increasing U , the peaks around $k = \pm k_F$ disappear as well as the notch around $k = 0$. Instead a valence band with a flat top around $k = 0$ develops, just as observed e.g. in quasi-1D Ta_2NiSe_5 [36].

Figure 4.13 shows the calculated binding energy E_B defined in Eq. (4.9) and the coherence length ξ defined in Eq. (4.5) in the EI phase of the 1D EFKM with $|t_f| = 1$ (left panels) and 0.1 (right panels) by the DMRG. At small U , E_B is rather small, but increases exponentially with U , indicating a BCS pairing mechanism [see Fig. 4.13 (a) and (b)]. On the other hand, corresponding to $F(k)$, the excitonic state is composed of electron-hole pairs having large spatial extension, leading to large values of ξ [see Fig. 4.13 (c) and (d)]. At large U , the binding energy E_B increases linearly with U . Here, small values of ξ indicates tightly bound spatially confined excitons in a Bose-Einstein condensation process.

We address the influence of a mass imbalance between f - and c -band quasiparticles. In the mass-symmetric case $|t_f| = t_c$, EFKM is consistent with the 1D Hubbard model at $D = 0$. Here, we cannot distinguish between the AF (with vanishing spin gap) and EI phases, because both phases are critical. Therefore, in this limit, we have examined the 1D EFKM for $N_f > L/2$. To this end, both the U and D axes in Fig. 4.13 have been rescaled by $(|t_f| + t_c)$, as suggested by the EI-BI transition lines Eq.(4.15). Indeed, we find that EI phase shrinks as $|t_f|$ decreases. That is, the mass anisotropy gets stronger, which is simply a bandwidth effect, however, leading to a stronger Ising anisotropy. This, on their part, enlarges the SOO region at small D region, while the EI-BI phase boundary basically is unaffected. Importantly, the location of the BCS-BEC crossover, which can be derived from the intensity plots for E_B and ξ , does not change in this presentation.

To expose correlation effects, we include in Fig. 4.13 the semimetallic-to-semiconducting transition line assuming that the EI phase is absent. $U_{\text{BI}}(D)$ can be obtained from the band gap Δ_c that depends linearly on U for fixed D : $\Delta_c(D) = U + 2(|t_f| + t_c) + U_{\text{BI}}(D)$ [i.e., $U_{\text{BI}}(D)$ scales again with $|t_f| + t_c$]. Apparently, in the BCS-BEC crossover regime, a strong renormalization of the band structure due to

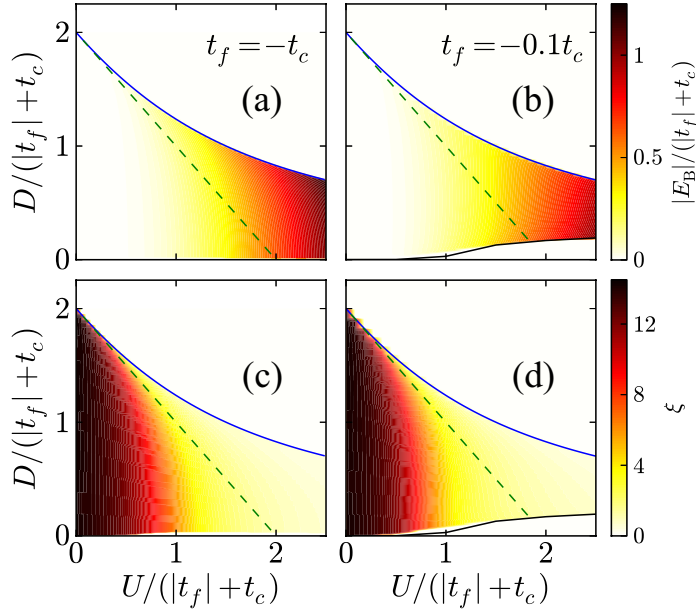


Figure 4.13: Intensity plots of the binding energy E_B (upper panels; $L = 128$, OBC) and the coherence length ξ (lower panels; $L = 64$, PBC) in the rescaled $U/(|t_f|+t_c)-D/(|t_f|+t_c)$ plane. Data were obtained by the DMRG for $N_f > L/2$ (to avoid the AF state in the Hubbard model limit $|t_f| = 1, D = 0$). Solid lines denote the SOO-EI and EI-BI transition points in the thermodynamic limit (in the lower panels the small uncolored slot just above the SOO-EI appears because $|E_B|$ and ξ are obtained here for a fixed finite system size). The dashed line $[U_{BI}(D)]$ would separate the semimetallic and semiconducting phases if the EI is assumed to be absent [125].

the incipient f - c hybridization takes place.

4.4 Summary

In this Chapter, we have investigated the exciton condensation state in the EFKM and the nature of the BCS-BEC crossover of the condensation by using the ED and DMRG. In Sec. 4.2, we have investigated the formation and condensation of excitons in the double-layer EFKM on the square lattice by using ED technique. We have analyzed the nature of excitonic condensation states on the basis of the interband interaction U dependence of the anomalous excitation spectrum, condensation amplitude, coherence length, exciton binding energy, and order parameter. We have compared the results of the ED with the results of the VCA and MF at the mass-symmetric case; in this respect, the VCA turns out to be especially advantageous in the weak-to-intermediate coupling regime. We have also investigated the effect of the mass asymmetry of electrons and holes. We found that a mass asymmetry between electrons and holes suppresses the condensation of excitons.

In Sec. 4.3, we have examined the one-dimensional EFKM by using the numerically exact DMRG technique and proved that the EI state is critical in contrast to the higher dimensional systems. The phase boundary between the BI, EI, and SOO was determined with high accuracy and the complete ground-state phase diagram was derived. The related anomalous spectral function clearly showed the different nature of the electron-hole pairing and condensation process at the weak and strong couplings. At fixed level splitting, the binding energy between c electrons and f holes is exponentially small in the weak-coupling regime and strongly increases as the Coulomb attraction increases. Concomitantly, the coherence length of the electron-hole pair condensate shortens. This unambiguously demonstrates a crossover from the BCS-like electron-hole pairing to the BEC of preformed excitons.

Chapter 5

Roles of Interband Exchange Interaction for Excitonic Phases

5.1 Introduction

In the previous Chapter, we investigated the excitonic phase in the extended Falicov-Kimball model (EFKM). The EFKM is the simplest model to study the excitonic phase, but the EFKM does not include the spin degrees of freedom. In real materials, electron has spin degrees of freedom, and thus we need to investigate the excitonic phase with spinful model. The simplest model to discuss the excitonic phases with spin degrees of freedom is the two-band Hubbard model (TBHM). In the TBHM, the excitonic phases are characterized by an order parameter $\langle c_{\mathbf{k}+\mathbf{Q}\sigma}^\dagger f_{\mathbf{k}\sigma'} \rangle$, where $c_{\mathbf{k}\sigma}^\dagger$ and $f_{\mathbf{k}\sigma}^\dagger$ are the creation operators of an electron with spin σ in the conduction and valence bands, respectively. If the valence-band top and conduction-band bottom are separated by the wave vector \mathbf{Q} , the system shows the density wave with modulation \mathbf{Q} [14, 15]. When the order parameter has spin degrees of freedom, two possible excitonic phases can be realized, i.e. excitonic charge density wave (CDW) state, which is a spin-singlet excitonic state, and excitonic spin density wave (SDW) state, which is a spin-triplet excitonic state.

In this section, we study the stability of the excitonic density-wave states in the TBHM with the interband exchange interaction¹. It is known that the interband Coulomb repulsion induces the excitonic instability in the system [57, 128], but the condensations of the spin-singlet and spin-triplet excitons are exactly degenerate unless interband exchange interaction or electron-phonon coupling are taken into account. Thus, in this section, we study the roles of the interband exchange and pair-hopping interactions played in the excitonic density wave formation. We first rewrite the interband interaction terms of the Hamiltonian in terms of the creation and annihilation operators of the spin-singlet and spin-triplet excitons. We then show that the interband repulsion U' actually leads to the exciton formation in both the spin-singlet and spin-triplet channels and that the interband exchange interaction J always lowers the energy of the spin-triplet exciton and raises the energy of the spin-singlet exciton. The variational cluster approximation (VCA) [80, 82] is then used to study the TBHM in detail, and we show that the interband exchange and pair-hopping interactions always stabilize the excitonic SDW state and destabilize the excitonic CDW state. The characteristics of these excitonic density-wave states will moreover be examined using a variety of physical quantities, including the single-particle spectral function, density of states (DOS), condensation amplitude, and pair coherence length.

5.2 Model and Method

5.2.1 Two-band Hubbard model

We consider the TBHM with interband exchange and pair-hopping terms,

$$\mathcal{H} = \mathcal{H}_e + \mathcal{H}_{e-e}^U + \mathcal{H}_{e-e}^{U'} + \mathcal{H}_{e-e}^J + \mathcal{H}_{e-e}^{J'}, \quad (5.1)$$

defined on a two-dimensional square lattice.

¹Chap. 5 is based on T. Kaneko, and Y. Ohta, *Phy. Rev. B* **90**, 245144 (2014).

The noninteracting f and c band electrons are described by

$$\begin{aligned}\mathcal{H}_e &= -t_f \sum_{\langle i,j \rangle} \sum_{\sigma} f_{i\sigma}^{\dagger} f_{j\sigma} + \varepsilon_f \sum_i n_i^f - t_c \sum_{\langle i,j \rangle} \sum_{\sigma} c_{i\sigma}^{\dagger} c_{j\sigma} + \varepsilon_c \sum_i n_i^c \\ &= \sum_{\mathbf{k}} \sum_{\sigma} \varepsilon_{\mathbf{k}}^f f_{\mathbf{k}\sigma}^{\dagger} f_{\mathbf{k}\sigma} + \sum_{\mathbf{k}} \sum_{\sigma} \varepsilon_{\mathbf{k}}^c c_{\mathbf{k}\sigma}^{\dagger} c_{\mathbf{k}\sigma},\end{aligned}\quad (5.2)$$

where $\alpha_{i\sigma}^{\dagger}$ ($\alpha_{\mathbf{k}\sigma}^{\dagger}$) denotes the creation operator of an electron at site i (momentum \mathbf{k}) and spin σ ($=\uparrow, \downarrow$) in the α ($=f, c$) band and $n_i^{\alpha} = n_{i\uparrow}^{\alpha} + n_{i\downarrow}^{\alpha} = \alpha_{i\uparrow}^{\dagger} \alpha_{i\uparrow} + \alpha_{i\downarrow}^{\dagger} \alpha_{i\downarrow}$ is the number operator at site i in the α band. t_{α} is the electron hopping integral between the neighboring sites and ε_{α} is the energy level of the α band. On the two-dimensional square lattice, the dispersion of the band α is given by $\varepsilon_{\mathbf{k}}^{\alpha} = -2t_{\alpha}(\cos k_x + \cos k_y) + \varepsilon_{\alpha}$. The chemical potential μ is fixed to ensure a filling of two electrons per site (half filling), i.e., $\langle n_i^f \rangle + \langle n_i^c \rangle = 2$. In this section, we fix the hopping parameters as $t_f = t_c = t$ and use t as the unit of energy. Furthermore, we set $\varepsilon_c = -\varepsilon_f = D > 0$, so that the f and c bands correspond to the valence and conduction bands, respectively. The conduction-band bottom at $\mathbf{k} = (0, 0)$ gives rise to an electron pocket, while the valence-band top produces a hole pocket at $\mathbf{k} = (\pi, \pi)$, resulting in the modulation vector of the density wave $\mathbf{Q} = (\pi, \pi)$. Figure 5.1(a) and 5.1(b) show the band dispersions and Fermi surfaces in the Brillouin zone of the square lattice.

The intraband Coulomb interaction takes the form

$$\begin{aligned}\mathcal{H}_{e-e}^U &= U_f \sum_i n_{i\uparrow}^f n_{i\downarrow}^f + U_c \sum_i n_{i\uparrow}^c n_{i\downarrow}^c \\ &= \frac{U_f}{N} \sum_{\mathbf{k}, \mathbf{k}', \mathbf{q}} f_{\mathbf{k}+\mathbf{q}\uparrow}^{\dagger} f_{\mathbf{k}\uparrow} f_{\mathbf{k}'-\mathbf{q}\downarrow}^{\dagger} f_{\mathbf{k}'\downarrow} + \frac{U_c}{N} \sum_{\mathbf{k}, \mathbf{k}', \mathbf{q}} c_{\mathbf{k}+\mathbf{q}\uparrow}^{\dagger} c_{\mathbf{k}\uparrow} c_{\mathbf{k}'-\mathbf{q}\downarrow}^{\dagger} c_{\mathbf{k}'\downarrow},\end{aligned}\quad (5.3)$$

where U_{α} (> 0) is Coulomb interaction between electrons in the α band. In this study, we assume $U_f = U_c = U$ for simplicity. The interband Coulomb interaction takes the form

$$\begin{aligned}\mathcal{H}_{e-e}^{U'} &= U' \sum_i n_i^f n_i^c \\ &= \frac{U'}{N} \sum_{\mathbf{k}, \mathbf{k}', \mathbf{q}} \sum_{\sigma, \sigma'} f_{\mathbf{k}+\mathbf{q}\sigma}^{\dagger} f_{\mathbf{k}\sigma} c_{\mathbf{k}'-\mathbf{q}\sigma'}^{\dagger} c_{\mathbf{k}'\sigma'},\end{aligned}\quad (5.4)$$

where U' (> 0) gives the Coulomb interaction between the interband electrons, which is responsible for an effective electron-hole attraction, leading eventually to an excitonic instability in the system. This Hamiltonian $\mathcal{H}_{e-e}^{U'}$ is a dominant term discussed in Ref. [14] and is consistent with Eq. (2.60) in Sec. 2.3.1. The interband exchange interaction such as Hund's rule coupling, is defined by

$$\begin{aligned}\mathcal{H}_{e-e}^J &= -2J \sum_i (\mathbf{S}_i^f \cdot \mathbf{S}_i^c + \frac{1}{4} n_i^f n_i^c) \\ &= \frac{J}{N} \sum_{\mathbf{k}, \mathbf{k}', \mathbf{q}} \sum_{\sigma, \sigma'} f_{\mathbf{k}+\mathbf{q}\sigma}^{\dagger} f_{\mathbf{k}\sigma} c_{\mathbf{k}'-\mathbf{q}\sigma'}^{\dagger} f_{\mathbf{k}'\sigma'},\end{aligned}\quad (5.5)$$

where $\mathbf{S}_i^{\alpha} = \sum_{\sigma, \sigma'} \alpha_{i\sigma}^{\dagger} \boldsymbol{\sigma}_{\sigma\sigma'} \alpha_{i\sigma'}/2$ and $\boldsymbol{\sigma}$ is the vector of Pauli matrices. J (> 0) is the strengths of the interband exchange interaction. This Hamiltonian \mathcal{H}_{e-e}^J is consistent with Eq. (2.61) in Sec. 2.3.1. The pair-hopping interaction is defined by

$$\begin{aligned}\mathcal{H}_{e-e}^{J'} &= -J' \sum_i \left(c_{i\uparrow}^{\dagger} c_{i\downarrow}^{\dagger} f_{i\uparrow} f_{i\downarrow} + f_{i\uparrow}^{\dagger} f_{i\downarrow}^{\dagger} c_{i\uparrow} c_{i\downarrow} \right) \\ &= \frac{J'}{N} \sum_{\mathbf{k}, \mathbf{k}', \mathbf{q}} \left(c_{\mathbf{k}+\mathbf{q}\uparrow}^{\dagger} c_{\mathbf{k}'-\mathbf{q}\downarrow}^{\dagger} f_{\mathbf{k}'\downarrow} f_{\mathbf{k}\uparrow} + f_{\mathbf{k}+\mathbf{q}\downarrow}^{\dagger} f_{\mathbf{k}'-\mathbf{q}\uparrow}^{\dagger} c_{\mathbf{k}'\uparrow} c_{\mathbf{k}\downarrow} \right),\end{aligned}\quad (5.6)$$

where J' (> 0) is the strengths of the pair-hopping interaction. This Hamiltonian $\mathcal{H}_{e-e}^{J'}$ is consistent with Eq. (2.62) in Sec. 2.3.1.

The Hamiltonian (5.1) in the spinless case with $U = J = J' = 0$ is equivalent to the extended Falicov-Kimball model with dispersive c and f electrons, of which the excitonic insulator state has been

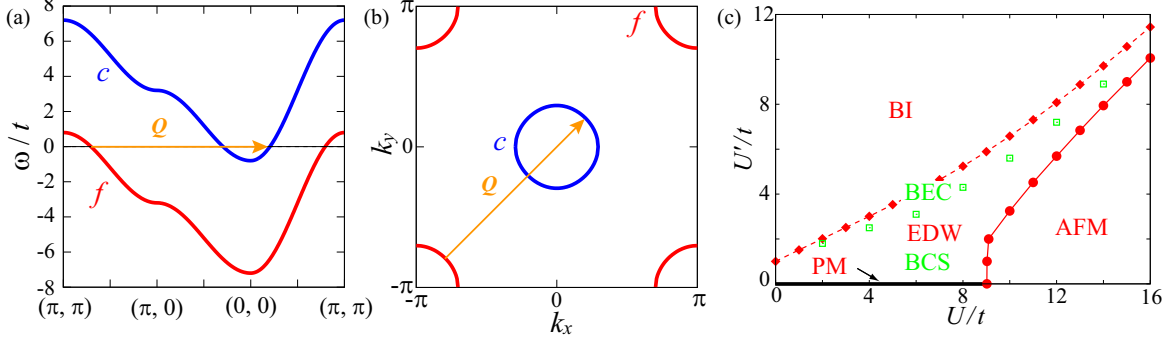


Figure 5.1: (a) Noninteracting band structure and (b) Fermi surface of the two-dimensional square lattice at half-filling and $D/t = 3.2$. The electron and hole pockets are located at $\mathbf{k} = (0, 0)$ and $\mathbf{k} = (\pi, \pi)$, respectively, and the nesting vector is give by $\mathbf{Q} = (\pi, \pi)$. (c) The phase diagram of the TBHM without the exchange interactions ($J = J' = 0$) at $D/t = 3$ [128].

studied much in detail [87, 96, 99, 114, 125]. The excitonic phases in the TBHM without the interband exchange and pair-hopping terms ($J = J' = 0$) have also been studied [57, 128], where it was shown that the model exhibits three ground-state phases: (i) the band insulator (at $U', D \gg U, J$), where $\langle n_f \rangle = 2$ and $\langle n_c \rangle = 0$, (ii) the antiferromagnetic Mott insulator (at $U, J \gg U', D$), where $\langle n_f \rangle = \langle n_c \rangle = 1$, and (iii) the excitonic density-wave state between the above two phases, where $2 > \langle n_f \rangle > 1 > \langle n_c \rangle > 0$ [see Fig. 5.1(c)].

5.2.2 Stability of Spin-singlet and Spin-triplet Excitonic States

To see the stability of the spin-singlet and spin-triplet excitons, let us first introduce the creation operators of the spin-singlet and spin-triplet excitons, which are defined respectively as²

$$A_i^{0\dagger} = \frac{1}{\sqrt{2}} \sum_{\sigma} c_{i\sigma}^{\dagger} f_{i\sigma}, \quad (5.7)$$

$$\mathbf{A}_i^{\dagger} = \frac{1}{\sqrt{2}} \sum_{\sigma\sigma'} c_{i\sigma}^{\dagger} \boldsymbol{\sigma}_{\sigma\sigma'} f_{i\sigma'}. \quad (5.8)$$

Using the spin-singlet and spin-triplet exciton operators thus defined, the interband Coulomb repulsion term in Eq. (5.4) can be divided exactly into the spin-singlet and spin-triplet terms as

$$U' n_{if} n_{ic} = -U' A_i^{0\dagger} A_i^0 - U' \mathbf{A}_i^{\dagger} \cdot \mathbf{A}_i. \quad (5.9)$$

Therefore, the formation of excitons lowers the energy of the system in both the spin-singlet and the spin-triplet channels by the same amount. The interband exchange and pair-hopping interactions in Eq. (5.5) and (5.6) can also be rewritten exactly as

$$-J \mathbf{S}_{if} \cdot \mathbf{S}_{ic} = \frac{3J}{4} A_i^{0\dagger} A_i^0 - \frac{J}{4} \mathbf{A}_i^{\dagger} \cdot \mathbf{A}_i, \quad (5.10)$$

$$-J' c_{i\uparrow}^{\dagger} c_{i\downarrow}^{\dagger} f_{i\uparrow} f_{i\downarrow} = \frac{J'}{4} A_i^{0\dagger} A_i^0 - \frac{J'}{4} \mathbf{A}_i^{\dagger} \cdot \mathbf{A}_i. \quad (5.11)$$

Therefore, due to the interband exchange interaction J , the formation of the spin-triplet (spin-singlet) excitons always lowers (raises) the energy of the system, thus lifting the degeneracy that occurs at $J = J' = 0$. The pair-hopping term J' can also be divided into the spin-singlet and spin-triplet terms as in Eq. (5.11), which are of the off-diagonal form.

²When we use the electron-electron operator, spin-singlet state is given as $\frac{1}{\sqrt{2}}(c_{\uparrow}^{\dagger} f_{\downarrow}^{\dagger} - c_{\downarrow}^{\dagger} f_{\uparrow}^{\dagger})|0\rangle$. However, in Eq. (5.7), we use electron-hole operator, so that the spin-singlet state is given as $\frac{1}{\sqrt{2}}(c_{\uparrow}^{\dagger} f_{\downarrow}^{\dagger} - c_{\downarrow}^{\dagger} f_{\uparrow}^{\dagger})|0\rangle = \frac{1}{\sqrt{2}}(c_{\uparrow}^{\dagger} f_{\uparrow} + c_{\downarrow}^{\dagger} f_{\downarrow})[f_{\uparrow}^{\dagger} f_{\downarrow}^{\dagger}|0\rangle]$.

5.2.3 Variational Cluster Approximation

We use the VCA [80, 82], which is a quantum cluster method based on the self-energy functional theory (SFT) [77, 78], and we solve the quantum many-body problem defined in Eq. (5.1). Details of the SFT and VCA have been written in Sec. 3.3 and Sec. 3.4. To study the symmetry-broken phases in the VCA, we introduce the Weiss fields as variational parameters. The variational Hamiltonian for the excitonic CDW (spin-singlet) and SDW (spin-triplet) states are then defined as

$$\mathcal{H}'_{\text{CDW}} = \Delta'_0 \sum_{\mathbf{k}, \sigma} c_{\mathbf{k}+\mathbf{Q}\sigma}^\dagger f_{\mathbf{k}\sigma} + \text{H.c.} = \Delta'_0 \sum_{i, \sigma} e^{i\mathbf{Q}\cdot\mathbf{r}_i} c_{i\sigma}^\dagger f_{i\sigma} + \text{H.c.}, \quad (5.12)$$

$$\mathcal{H}'_{\text{SDW}} = \Delta'_z \sum_{\mathbf{k}, \sigma} \sigma c_{\mathbf{k}+\mathbf{Q}\sigma}^\dagger f_{\mathbf{k}\sigma} + \text{H.c.} = \Delta'_z \sum_{i, \sigma} \sigma e^{i\mathbf{Q}\cdot\mathbf{r}_i} c_{i\sigma}^\dagger f_{i\sigma} + \text{H.c.}, \quad (5.13)$$

respectively, where Δ'_0 is the Weiss field for condensation of the spin-singlet excitons and Δ'_z is the z component of the Weiss field for condensation of the spin-triplet excitons. The variational parameters Δ'_0 and Δ'_z are optimized on the basis of the variational principle, i.e., $\partial\Omega/\partial\Delta'_0 = 0$ for the excitonic CDW state and $\partial\Omega/\partial\Delta'_z = 0$ for the excitonic SDW state. The solutions with $\Delta'_0 \neq 0$ and $\Delta'_z \neq 0$ correspond to the excitonic CDW and SDW states, respectively.

We solve the eigenvalue problem $\mathcal{H}'|\psi_0\rangle = E_0|\psi_0\rangle$ of a finite-size (L_c sites) cluster to obtain the ground state, and we calculate the trial Green's function of the reference system by the Lanczos exact-diagonalization method. Using the basis $\Psi_i^\dagger = (f_{i\sigma}^\dagger, c_{i\sigma}^\dagger)$, the Green's-function matrix \hat{G}'_σ may be written as

$$\hat{G}'_\sigma(\omega) = \begin{pmatrix} \hat{G}'_{\sigma}{}^{ff}(\omega) & \hat{G}'_{\sigma}{}^{fc}(\omega) \\ \hat{G}'_{\sigma}{}^{cf}(\omega) & \hat{G}'_{\sigma}{}^{cc}(\omega) \end{pmatrix}, \quad (5.14)$$

where $\hat{G}'_{\sigma}{}^{\alpha\beta}$ is an $L_c \times L_c$ matrix and the matrices are indicated by a hat hereafter. In our VCA calculation, we assume the two-dimensional square lattice and use an $L_c = 2 \times 2 = 4$ site (eight-orbital) cluster as the reference system.

5.3 Results

5.3.1 Stability of Excitonic Phases

First, let us examine the stability of the excitonic CDW and SDW states using the grand potential. In Fig. 5.2(a), we show the calculated grand potentials of the excitonic CDW and SDW states as a function of the variational parameter Δ' , which are obtained using the atomic-limit relation $U' = U - 2J$ [130–132]. We find that the grand potential has the stationary points at $\Delta' = 0$ and $\Delta' \neq 0$, and the latter is lower in energy, indicating that the excitonic density-wave states are thermodynamically stable. Figure 5.2(a) clearly shows that the SDW is stabler than the CDW.

However, if we assume the atomic-limit relation $U' = U - 2J$, the change in the parameter values, e.g., J , leads to the change in the overlap of the valence and conduction bands and hence to the change in the number of conduction-band electrons (and valence-band holes) as shown in Fig. 5.2 (b). The reason for the change in the overlap of the valence and conduction bands can be seen in the mean-field approximation. In the mean-field theory applied to our model Eq. (5.1), the diagonal terms of the mean-field Hamiltonian are given by $\varepsilon_f(\mathbf{k}) = -\varepsilon_c(\mathbf{k}) = -2t \sum_i^d \cos k_i - D + n(U/2 - U' + J/2)$ with $n = \langle n_{if\sigma} \rangle - \langle n_{ic\sigma} \rangle$, and thus the Hartree shift $n(U/2 - U' + J/2)$ that changes the band overlap appears in this expression [38]. Depending on the values of U , U' and J , we therefore find, e.g., the Mott-insulator state at $U' \ll (U + J)/2$ and the band-insulator state at $U' \gg (U + J)/2$ [57, 128], which are due simply to the effect of the Hartree shift. The change in the depth of band overlap (or the change in the number of carriers) affects the stability of the excitonic phases [128] and this gives an additional complexity to our calculations because in this study we just want to focus on the relative stability of the excitonic CDW and SDW states in the presence of the interband exchange and pair-hopping interactions. The effects of this Hartree shift can be suppressed completely if we assume the relation $U' = (U + J)/2$. Hereafter, unless we mention otherwise, we assume the relation $U = 2U' - J$ to suppress the Hartree shift, and we use the value $U/t = 8$ and $D/t = 3.2$ at which the excitonic density-wave state is stabilized between the band-insulator and the Mott-insulator states [128].

In Fig. 5.2 (c), we show the calculated grand potentials of the excitonic CDW and SDW states as a function of the variational parameter Δ' , which are obtained using the relation $U = 2U' - J$ and changing

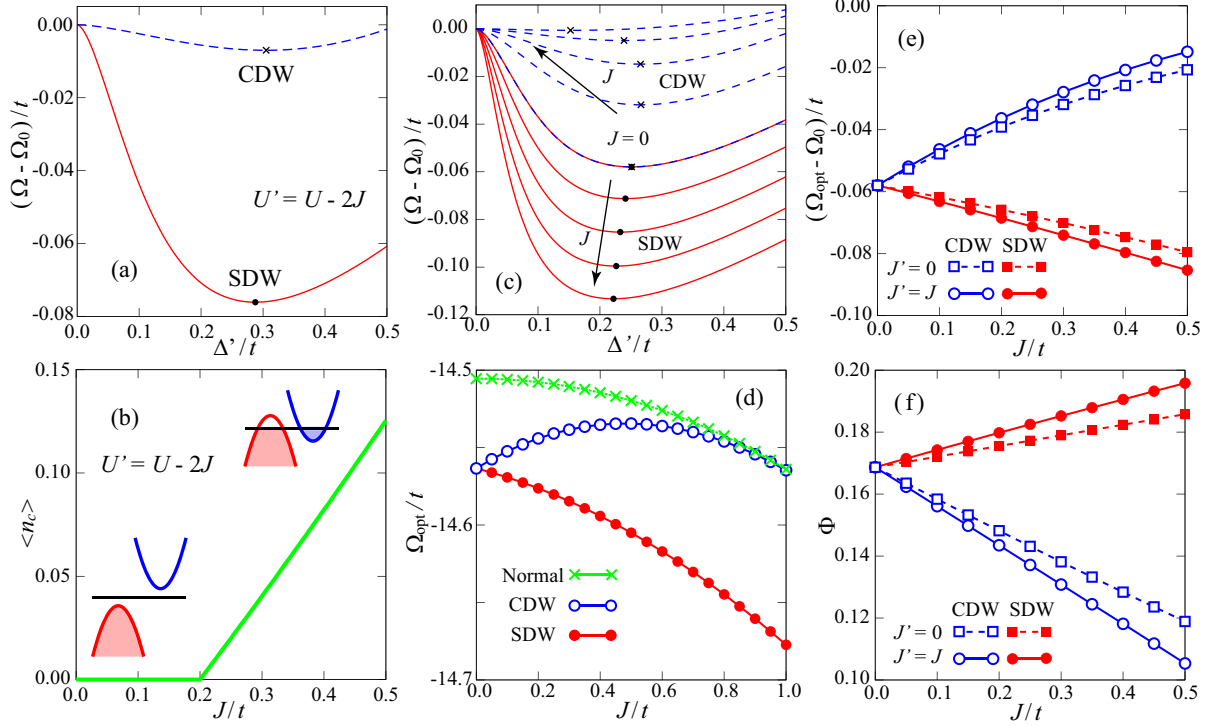


Figure 5.2: (a) Calculated grand potentials of the excitonic CDW and SDW states as a function of the variational parameter $\Delta' (= \Delta'_0, \Delta'_z)$, which are obtained using the atomic-limit relation $U' = U - 2J$ with $U/t = 5$, $J/t = J'/t = 0.5$ and $D/t = 2$. The crosses and circles indicate the stationary points for the excitonic CDW and SDW states, respectively. (b) The number of the conduction-band electrons $\langle n_c \rangle$ (or the valence-band holes) as a function of J/t in the normal state (or $\Delta' = 0$), which is obtained using the atomic-limit relation $U' = U - 2J$ with $U/t = 5$, $D/t = 2$, and $J' = 0$. (c) Calculated grand potentials for the excitonic CDW and SDW states as a function of the variational parameter $\Delta' (= \Delta'_0, \Delta'_z)$, which are obtained using the relation $U' = (U + J)/2$ and $U/t = 8$ and $D/t = 3.2$, at $J/t = J'/t = 0, 0.25, 0.5, 0.75$, and 1 . Ω_0 is the grand potential in the normal (semimetallic) state. The crosses and dots indicate the stationary points of the excitonic CDW and SDW states, respectively. (d) $J (= J')$ dependence of the grand potential at the stationary point for the normal (or semimetallic), excitonic CDW, and SDW states. (e) Optimized values of the grand potentials in the presence ($J' = J$) and absence ($J' = 0$) of the pair-hopping term. (f) J dependence of the order parameters of the excitonic CDW and SDW states in the presence ($J' = J$) and absence ($J' = 0$) of the pair-hopping term [129].

the exchange interaction J . At $J = J' = 0$, the grand potentials of the excitonic CDW and SDW states are exactly degenerate [see Fig. 5.2(a)], but J and J' lift this degeneracy. The optimized values of the grand potential as a function of $J (= J')$ are shown in Fig. 5.2(d), where we find that, with increasing J (and J'), the energy of the excitonic SDW state decreases, but the energy of the excitonic CDW state increases and approaches the energy of the normal semimetallic state. Therefore, the excitonic SDW (CDW) state is stabilized (destabilized) by J and J' . In Fig. 5.2(e), we show the optimized values of the grand potentials in the presence ($J' = J$) and absence ($J' = 0$) of the pair-hopping term, where we find that the stability of the excitonic SDW (CDW) state is enhanced (suppressed) by the pair-hopping term J' .

We also calculate the order parameters of the excitonic CDW and SDW states. Here, we introduce the quantities Φ_0 and Φ_z for the excitonic CDW and SDW order parameters, respectively, which are defined as

$$\Phi_0 = \frac{1}{2N} \sum_{\mathbf{k}} \sum_{\sigma} \langle c_{\mathbf{k}+\mathbf{Q}\sigma}^\dagger f_{\mathbf{k}\sigma} \rangle, \quad (5.15)$$

$$\Phi_z = \frac{1}{2N} \sum_{\mathbf{k}} \sum_{\sigma} \sigma \langle c_{\mathbf{k}+\mathbf{Q}\sigma}^\dagger f_{\mathbf{k}\sigma} \rangle. \quad (5.16)$$

The calculated results for Φ_0 and Φ_z are shown in Fig. 5.2(f) in the presence ($J' = J$) and absence ($J' = 0$) of the pair-hopping term. We find that Φ_z is enhanced with J (and J') and Φ_0 is suppressed with J (and J'), which are in accordance with the stability of the excitonic CDW and SDW states evaluated from the behaviors of the calculated grand potentials. Thus, we may state that the interband exchange interaction stabilizes the excitonic SDW state and destabilizes the excitonic CDW state. As seen in Figs. 5.2(e) and 5.2(f), we may moreover state that the pair-hopping term enhances the stability of the excitonic SDW state and suppresses the stability of the excitonic CDW state.

5.3.2 Single-particle Spectral Function

Next, let us calculate the Green's function at the optimized values of the variational parameters using the cluster perturbation theory (CPT) [83]. The Green's function is defined as

$$\hat{G}_\sigma(\mathbf{k}, \mathbf{k}', \omega) = \frac{1}{L_c} \sum_{i,j=1}^{L_c} \hat{G}_{ij,\sigma}^{\text{CPT}}(\mathbf{k}, \omega) e^{-i\mathbf{k}\cdot\mathbf{r}_i + i\mathbf{k}'\cdot\mathbf{r}_j}, \quad (5.17)$$

where $\hat{G}_\sigma^{\text{CPT}}(\mathbf{k}, \omega) = [\hat{G}'_{\sigma}{}^{-1}(\omega) - \hat{V}_\sigma(\mathbf{k})]^{-1}$. Using this Green's function, the single-particle spectral function is defined as

$$A(\mathbf{k}, \omega) = -\frac{1}{\pi} \sum_{\alpha,\sigma} \text{Im} \mathcal{G}_\sigma^{\alpha\alpha}(\mathbf{k}, \omega + i\eta), \quad (5.18)$$

where η gives the artificial Lorentzian broadening to the spectrum. We also calculate the DOS for the α ($= f, c$) band, which is defined as

$$N_\alpha(\omega) = -\frac{1}{\pi N} \sum_{\mathbf{k}} \sum_{\sigma} \text{Im} \mathcal{G}_\sigma^{\alpha\alpha}(\mathbf{k}, \omega + i\eta). \quad (5.19)$$

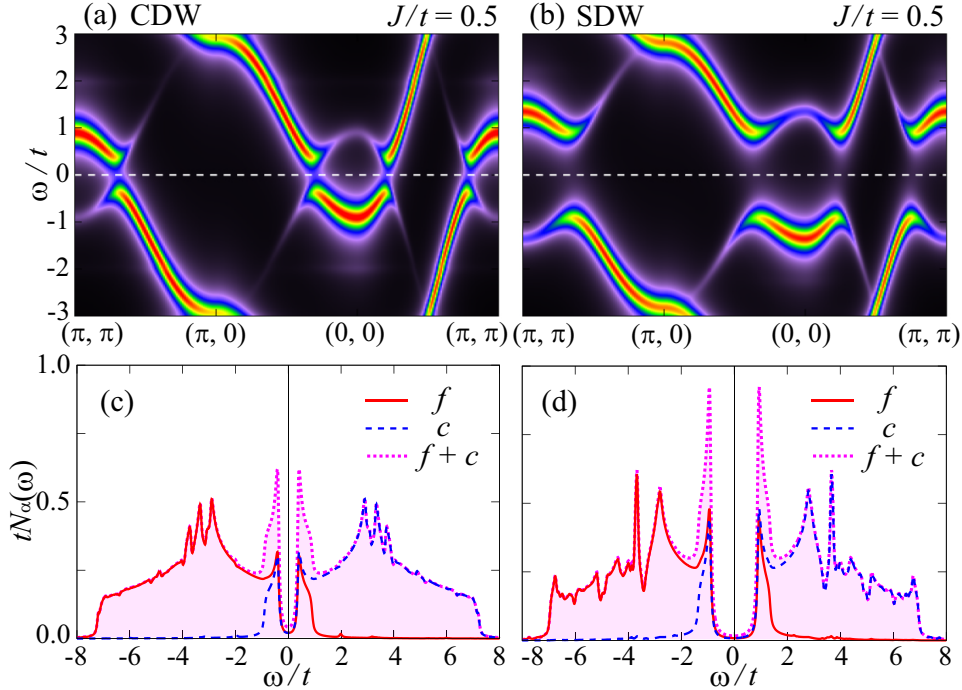


Figure 5.3: Single-particle spectral function $A(\mathbf{k}, \omega)$ and DOS $N_\alpha(\omega)$ calculated by CPT at $U/t = 8$, $D/t = 3.2$, and $J/t = J'/t = 0.5$. We show the results for the excitonic CDW state (metastable) in (a) and (c) and for the excitonic SDW state (stable) in (b) and (d). In (c) and (d), the solid, dashed, and dotted lines indicate the f orbital, c orbital, and total DOSs, respectively. The artificial Lorentzian broadening of $\eta/t = 0.15$ is used for $A(\mathbf{k}, \omega)$ and $\eta/t = 0.05$ is used for $N_\alpha(\omega)$. The Fermi level is located at $\omega = 0$ [129].

In Fig. 5.3, we show the calculated single-particle spectral function $A(\mathbf{k}, \omega)$ and DOS $N_\alpha(\omega)$; the results for the metastable CDW state [see Figs. 5.3(a) and 5.3(c)] and stable SDW state [see Figs. 5.3(b) and 5.3(d)] obtained at $J/t = J'/t = 0.5$ are shown. We find that, although a semimetallic state with a small band overlap is assumed as the noninteracting band structure at $D/t = 3.2$, the valence band around $\mathbf{k} = (\pi, \pi)$ is hybridized with the conduction band around $\mathbf{k} = (0, 0)$ due to the spontaneous c - f hybridization (or exciton condensation), leading to the opening of the band gap at the Fermi level. At $J = J' = 0$, the single-particle excitation gap Δ_g is estimated to be $\Delta_g/t = 1.47$. We find that, in agreement with the change in the order parameters, the single-particle gap in the excitonic CDW state, e.g., $\Delta_g/t = 0.76$ at $J/t = J'/t = 0.5$, is suppressed in comparison with the $J = J' = 0$ case [see Figs. 5.3(a) and 5.3(c)]. We also find that the single-particle gap in the excitonic SDW state, e.g., $\Delta_g/t = 1.81$ at $J/t = J'/t = 0.5$, is enhanced in comparison with the $J = J' = 0$ case [see Figs. 5.3(b) and 5.3(d)]. We moreover find in Figs. 5.3 (c) and 5.3(d) that the sharp coherence peak appears at the edges of the gap and that the coherence peak of the excitonic SDW state is sharper than that of the excitonic CDW state, indicating that the spontaneous c - f hybridization in the excitonic SDW (CDW) state is enhanced (suppressed) by the interband exchange and pair-hopping interactions. We note that no significant differences are found in the behaviors of $N_\alpha(\omega)$ discussed above, even if we switch off J' , retaining only J .

In order to see the character of the density oscillation in the real space, we calculate the DOS of the A and B sublattices. In general, the local Green's function is given by

$$G_\sigma(\mathbf{r}, \omega) = \frac{1}{N} \sum_{\alpha, \beta} \sum_{\mathbf{k}} \varphi_{\alpha\mathbf{k}}(\mathbf{r}) \varphi_{\beta\mathbf{k}}^*(\mathbf{r}) G_\sigma^{\alpha\beta}(\mathbf{k}, \omega), \quad (5.20)$$

where $\varphi_{\alpha\mathbf{k}}(\mathbf{r})$ is the Bloch wave function of α band [19]. Due to \mathbf{r} -dependence of the wave function $\varphi_{\alpha\mathbf{k}}(\mathbf{r})$, the local Green's function depends on the spatial position \mathbf{r} in a unit cell, and thus the charge and spin density distributions of the excitonic phases in the real space are somewhat complicated [52]. Details of the electronic distribution of the excitonic phases will be discussed in Chap. 7. In this section, we assume that the Bloch wave function is constant, i.e., independent of \mathbf{r} , for simplicity [33, 52, 57] and calculate the DOS of the A and B sublattices. Using the CPT, the sublattice Green's function is given by

$$\hat{G}_{X\sigma}(\mathbf{k}, \omega) = \frac{2}{L_c} \sum_{i, j \in X} \hat{G}_{ij, \sigma}^{\text{CPT}}(\mathbf{k}, \omega) e^{-i\mathbf{k} \cdot (\mathbf{r}_i - \mathbf{r}_j)} \quad (5.21)$$

with $X = \text{A or B}$. Assuming the constant Bloch wave functions, the DOS of the A or B sublattices is given by

$$N_{X\sigma}(\omega) = -\frac{1}{\pi N} \sum_{\mathbf{k}} \sum_{\alpha, \beta} \text{Im} \mathcal{G}_{X\sigma}^{\alpha\beta}(\mathbf{k}, \omega + i\eta). \quad (5.22)$$

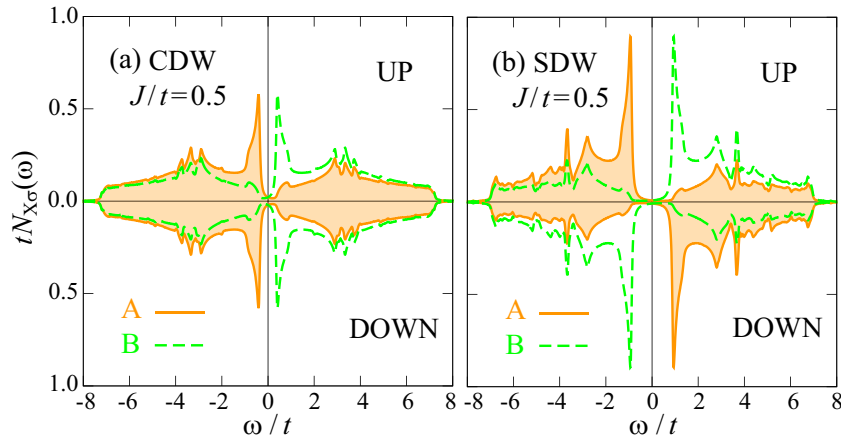


Figure 5.4: Calculated DOSs for the (a) excitonic CDW state and (b) excitonic SDW state at $J/t = J'/t = 0.5$. Solid and dashed lines indicate the DOSs of the A and B sublattices, respectively. The Lorentzian broadening of $\eta/t = 0.05$ is used. The vertical line indicates the Fermi level [129].

Note that the following results correspond to the local DOS $N_\sigma(\mathbf{r}, \omega)$ at a some position \mathbf{r} in each unit cell and do not directly represent the total charge or net magnetization in the unit cell.

In Fig. 5.4(a), we show the calculated DOS for the excitonic CDW state at $J/t = J'/t = 0.5$. We find that $N_{A\uparrow}(\omega) = N_{A\downarrow}(\omega) > N_{B\uparrow}(\omega) = N_{B\downarrow}(\omega)$ below the Fermi level ($\omega < 0$). Note that the local charge density deviation at the position \mathbf{r} in each unit cell is given by $\delta n_i(\mathbf{r}) = \delta n_{i\uparrow}(\mathbf{r}) + \delta n_{i\downarrow}(\mathbf{r}) \propto \Phi_0 \cos \mathbf{Q} \cdot \mathbf{r}_i$ with the order parameter Φ_0 , where we write $\delta n_{i\sigma}(\mathbf{r}) = \delta n_{i\sigma}(\mathbf{r} - \mathbf{r}_i)$ for simplicity. On the other hand, in Fig. 5.4(b), we show the calculated DOS for the excitonic SDW state at $J/t = J'/t = 0.5$. We find that $N_{A\uparrow}(\omega) = N_{B\downarrow}(\omega) > N_{A\downarrow}(\omega) = N_{B\uparrow}(\omega)$ below Fermi level. Note again that the local magnetization at the position \mathbf{r} in each unit cell is given by $m_i(\mathbf{r}) = \delta n_{i\uparrow}(\mathbf{r}) - \delta n_{i\downarrow}(\mathbf{r}) \propto \Phi_z \cos \mathbf{Q} \cdot \mathbf{r}_i$ with the order parameter Φ_z . We thus find that, due to the effect of the exchange interactions, Φ_z (Φ_0) is enhanced (suppressed), where $\Phi_z = 0.20$ and $\Phi_0 = 0.11$ at $J/t = J'/t = 0.5$; i.e., the excitonic SDW (CDW) modulation in real space becomes rather strong (weak). We also find that, in the excitonic CDW state, $N_{A\sigma}(\omega) \simeq N_{B\sigma}(\omega)$ far away from the Fermi level and that the coherence peak appears in the DOS of the A sublattice just below the Fermi level, where $N_{A\sigma}(\omega) > N_{B\sigma}(\omega)$. On the other hand, the DOS of excitonic SDW state has a large gap and a sharp coherence peak appears at the edge of the DOS.

5.3.3 Condensation Amplitude and Coherence Length

In order to see the character of the exciton condensation in momentum space, we calculate the condensation amplitude (or the anomalous momentum distribution function). Using the off-diagonal (or anomalous) Green's function given in Eq. (5.17), the condensation amplitudes for the spin-singlet and spin-triplet excitons are defined as

$$F_0(\mathbf{k}) = \frac{1}{2} \sum_{\sigma} \oint_C \frac{dz}{2\pi i} \mathcal{G}_{\sigma}^{cf}(\mathbf{k}, \mathbf{k} + \mathbf{Q}, z), \quad (5.23)$$

$$F_z(\mathbf{k}) = \frac{1}{2} \sum_{\sigma} \sigma \oint_C \frac{dz}{2\pi i} \mathcal{G}_{\sigma}^{cf}(\mathbf{k}, \mathbf{k} + \mathbf{Q}, z), \quad (5.24)$$

respectively. Note that we here use the term ‘‘anomalous’’ to indicate that the number of electrons on each of the c and f bands is not conserved due to the excitonic condensation, although the total number of electrons is conserved.

We show the calculated results in Fig. 5.5 for the excitonic CDW and SDW states. We find that, with increasing J ($= J'$), the peak of $F_0(\mathbf{k})$ at the Fermi momentum \mathbf{k}_F becomes sharper in the CDW state [see Fig. 5.5(a)] and that the peak of $F_z(\mathbf{k})$ at \mathbf{k}_F becomes broader in momentum space in the SDW state [see Fig. 5.5(c)]. The sharp (broad) peak of $F(\mathbf{k})$ [$= F_0(\mathbf{k})$ or $F_z(\mathbf{k})$] in momentum space indicates that the spatial extension of the electron-hole pair becomes large (small) in real space. We note that no significant differences are found in the behavior of $F(\mathbf{k})$ even if we set $J' = 0$ retaining only J .

Using $F(\mathbf{k})$, we evaluate the pair coherence length ξ , which corresponds to the spatial size of the electron-hole pair and may be defined by [99, 114, 125]

$$\xi^2 = \frac{\sum_{\mathbf{k}} |\nabla_{\mathbf{k}} F(\mathbf{k})|^2}{\sum_{\mathbf{k}} |F(\mathbf{k})|^2}. \quad (5.25)$$

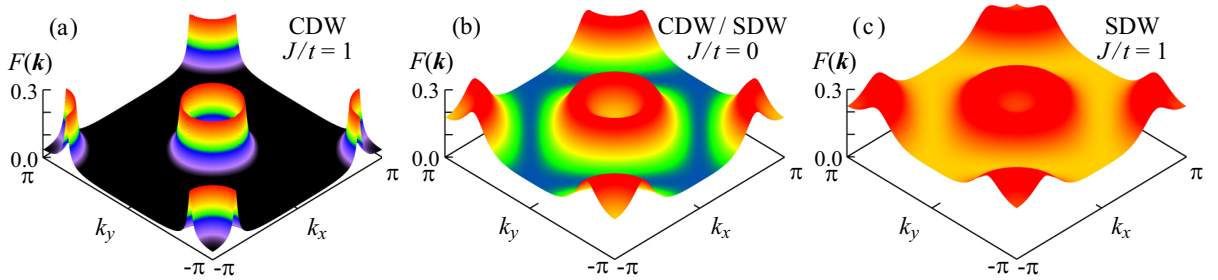


Figure 5.5: Condensation amplitude $F(\mathbf{k})$ [$= F_0(\mathbf{k})$ or $F_z(\mathbf{k})$] calculated by CPT. We show the results for (a) the excitonic CDW state at $J/t = J'/t = 1.0$ (metastable), (b) the excitonic CDW/SDW states at $J = J' = 0$ (degenerate), and (c) the excitonic SDW state at $J/t = J'/t = 1.0$ (stable) [129].

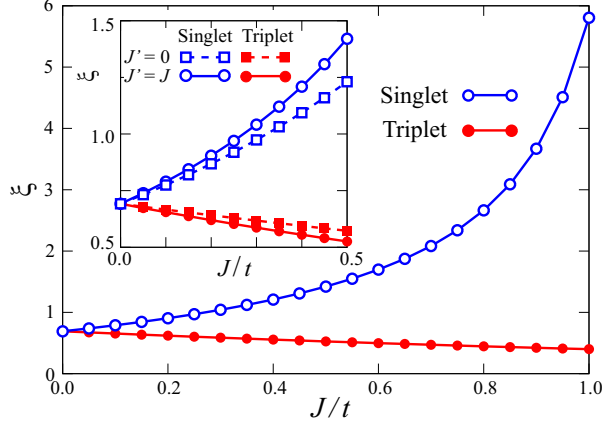


Figure 5.6: Calculated pair coherence length ξ in units of the lattice constant. J ($= J'$) dependence of ξ is shown for the spin-singlet (open circles) and spin-triplet (solid circles) exciton condensations. The inset shows the results in the absence of the pair-hopping term $J' = 0$ (open and solid squares), which are compared with the results in the presence of the pair-hopping term $J' = J$ (open and solid circles) [129].

In Fig. 5.6, we show the calculated results for the spin-singlet excitons (ξ_0) and spin-triplet excitons (ξ_z) as a function of J . We find that, with increasing J ($= J'$), ξ for the spin-singlet (triplet) excitons increases (decreases) monotonically. Thus, the size of the spin-singlet exciton becomes larger than the lattice constant ($\xi_0 > 1$) for larger J values, indicating the crossover from the tightly paired BEC state to the weakly paired BCS state. The spin-triplet excitons, on the other hand, are paired more tightly, and the size is always smaller than the lattice constant in the parameter space examined. We also find in the inset of Fig. 5.6 that the above tendencies induced by J are again enhanced by J' .

5.4 Summary

To summarize, we have studied the stability of the excitonic density-wave states in the TBHM with the interband Coulomb interaction U' , interband exchange interaction J , pair-hopping term J' , as well as the intraband Hubbard interaction U . We have rewritten the interband interactions of the Hamiltonian in terms of the creation and annihilation operators of the spin-singlet and spin-triplet excitons and examined the roles of these interactions. We have thereby shown that the U' term drives the formation of excitons in both the spin-singlet and the spin-triplet channels, and the J term stabilizes (destabilizes) the formation of the spin-triplet (spin-singlet) excitons. Using the VCA to calculate the grand potential of the system in the thermodynamic limit, we have moreover shown that the exchange interaction always stabilizes the excitonic SDW state and destabilizes the excitonic CDW state, of which the tendencies are enhanced by the pair-hopping term. A variety of physical quantities have also been calculated, which include the single-particle spectral function, density of states, anomalous Green's functions, condensation amplitude, and pair-coherence length.

Chapter 6

Roles of Electron-Phonon Coupling for Excitonic Phases

6.1 Introduction

In the previous Chapter, we discussed excitonic phases in spinful systems in the framework of the two-band Hubbard model (TBHM). We showed there that the interband exchange interaction stabilizes the spin-triplet excitonic phase in the otherwise degenerate spin-singlet and spin-triplet excitonic phases [57, 60–62, 128, 129]. On the other hand, we showed in our previous Chapter that, taking into account electronic interactions only, a spin-singlet excitonic phase cannot be stabilized, which may however be realized in $1T$ -TiSe₂ and Ta₂NiSe₅. In these materials, the importance of electron-phonon coupling was recently pointed out [31–35, 38]. Although the spin-singlet excitonic state has been investigated in the spinless multiband model with electron-phonon coupling [33, 133, 134], not much is known about the role of the electron-phonon coupling played in the excitonic density wave states in the spinful multiband Hubbard model.

In this Chapter we will thoroughly investigate the stability of the excitonic density wave states in the TBHM, paying particular attention to the electron-phonon coupling¹. The model is analyzed by the static mean-field theory for the electron-phonon coupling and the variational cluster approximation (VCA) for the electronic correlations. We will first show that the interband Coulomb interaction U' and electron-phonon interaction λ cooperatively stabilize the CDW and that a smooth crossover occurs between “excitonic” CDW and “phononic” CDW states, just by increasing the ratio λ/U' . Then, incorporating the interband exchange interaction J , an excitonic SDW state competes with the excitonic CDW state. The ground-state phase diagram of the extended TBHM is determined in the J - λ plane. We will moreover pay particular attention to the phase of the order parameter and show that both the electron-phonon coupling and pair-hopping terms fix the phase of the excitonic order parameters, thereby preventing the system from realizing a superfluid state. Finally, the implications for exciton condensation in real materials will be discussed.

6.2 Model and Methods

6.2.1 Model Hamiltonian

We consider the TBHM, supplemented by electron-phonon coupling,

$$\mathcal{H} = \mathcal{H}_e + \mathcal{H}_{e-e}^U + \mathcal{H}_{e-e}^{U'} + \mathcal{H}_{e-e}^J + \mathcal{H}_{e-e}^{J'} + \mathcal{H}_{ph} + \mathcal{H}_{e-ph}, \quad (6.1)$$

defined on a two-dimensional square lattice. We use the same Hamiltonian consisting of the non-interacting term \mathcal{H}_e and electron-electron interaction terms \mathcal{H}_{e-e}^U , $\mathcal{H}_{e-e}^{U'}$, \mathcal{H}_{e-e}^J and $\mathcal{H}_{e-e}^{J'}$, which have been defined in the previous Chapter [see Eqs. (5.2)-(5.6) in Sec. 5.2.1].

In Eq. (6.1), we also included the phonon degrees of freedom because the lattice displacements play an important role in the materials under consideration. The electron-phonon coupling becomes particularly

¹Chap. 6 is based on T. Kaneko, B. Zenker, H. Fehske and Y. Ohta, *Phy. Rev. B* **92**, 115106 (2015).

important when we address the spin-singlet electron-hole excitations. In the harmonic approximation, the phonon part of the Hamiltonian is given by

$$\mathcal{H}_{ph} = \sum_{\mathbf{q}} \omega_{\mathbf{q}} b_{\mathbf{q}}^{\dagger} b_{\mathbf{q}}, \quad (6.2)$$

where the bosonic operator $b_{\mathbf{q}}^{\dagger}$ creates a phonon with momentum \mathbf{q} and frequency $\omega_{\mathbf{q}}$ (we set $\hbar = 1$). The dominant electron-phonon coupling term between a c - f (electron-hole) excitation and lattice displacement is assumed to be

$$\mathcal{H}_{e-ph} = \frac{1}{\sqrt{N}} \sum_{\mathbf{k}, \mathbf{q}} \sum_{\sigma} g_{\mathbf{q}} (b_{\mathbf{q}} + b_{-\mathbf{q}}^{\dagger}) c_{\mathbf{k}+\mathbf{q}\sigma}^{\dagger} f_{\mathbf{k}\sigma} + \text{H.c.}, \quad (6.3)$$

with a coupling constant $g_{\mathbf{q}}$ [33, 35, 133, 134].

In this section, we fix the hopping parameters $t_f = t_c = t$ and use t as the unit of energy. Furthermore, we set $\varepsilon_c/t = -\varepsilon_f/t = 3.2$, so that the noninteracting band structure represents a semimetal with a small band overlap. The conduction-band bottom at $\mathbf{k} = (0, 0)$ gives rise to an electron pocket, while the valence-band top produces a hole pocket at $\mathbf{k} = (\pi, \pi)$, resulting in the modulation vector of the density wave $\mathbf{Q} = (\pi, \pi)$; see Fig. 5.1 for the band dispersions and Fermi surfaces in the Brillouin zone of the square lattice. Following the previous chapter, we assume $U_f = U_c = U$ and employ $U = 2U' - J$ to suppress the Hartree shift for simplicity. In this choice, the excitonic insulator state is stabilized between the band-insulator and Mott-insulator states [128, 129]. Moreover, we consider a dispersionless Einstein phonon $\omega_{\mathbf{q}} = \omega$ and a momentum-independent electron-phonon coupling constant $g_{\mathbf{q}} = g$. Since the strength of the electron-phonon coupling appears in the form $\lambda = g^2/\omega$ in the mean-field approximation used below, we take λ as the electron-phonon coupling parameter in what follows.

6.2.2 Mean-Field Approximation for Phonons

We treat the electron-phonon interaction term \mathcal{H}_{e-ph} in the mean-field (frozen-phonon) approximation. Introducing the expectation values of the c - f hybridization $\langle c^{\dagger} f \rangle$ and lattice displacement $\langle b \rangle$, the operators in Eq. (6.3) are approximated as $b_{\mathbf{q}} c_{\mathbf{k}+\mathbf{q}\sigma}^{\dagger} f_{\mathbf{k}\sigma} \sim [\langle b_{\mathbf{q}} \rangle c_{\mathbf{k}+\mathbf{q}\sigma}^{\dagger} f_{\mathbf{k}\sigma} + b_{\mathbf{q}} \langle c_{\mathbf{k}+\mathbf{q}\sigma}^{\dagger} f_{\mathbf{k}\sigma} \rangle] \delta_{\mathbf{q}, \mathbf{Q}} - \langle b_{\mathbf{q}} \rangle \langle c_{\mathbf{k}+\mathbf{q}\sigma}^{\dagger} f_{\mathbf{k}\sigma} \rangle \delta_{\mathbf{q}, \mathbf{Q}}$. Since in our model the nesting vector $\mathbf{Q} = (\pi, \pi)$ is commensurate with the lattice periodicity, i.e., $e^{2i\mathbf{Q} \cdot \mathbf{r}_i} = 1$ for lattice vectors \mathbf{r}_i , we have $b_{\mathbf{Q}} = b_{-\mathbf{Q}}$ ($b_{\mathbf{Q}}^{\dagger} = b_{-\mathbf{Q}}^{\dagger}$) [33], where $b_{\mathbf{Q}}$ and $b_{-\mathbf{Q}}$ ($b_{\mathbf{Q}}^{\dagger}$ and $b_{-\mathbf{Q}}^{\dagger}$) annihilate (create) the same phonon. This implies $\langle b_{\mathbf{Q}} \rangle = \langle b_{-\mathbf{Q}} \rangle = \langle b_{\mathbf{Q}}^{\dagger} \rangle$, and therefore $\langle b_{\mathbf{Q}} \rangle$ becomes a real number. In view of $\langle c_{\mathbf{k}+\mathbf{Q}\sigma}^{\dagger} f_{\mathbf{k}\sigma} \rangle = \langle f_{\mathbf{k}\sigma}^{\dagger} c_{\mathbf{k}+\mathbf{Q}\sigma} \rangle^* \neq 0$, we define the complex order parameter of the excitonic CDW as

$$\Phi_c = |\Phi_c| e^{i\theta_c} = \frac{1}{2N} \sum_{\mathbf{k}, \sigma} \langle c_{\mathbf{k}+\mathbf{Q}\sigma}^{\dagger} f_{\mathbf{k}\sigma} \rangle, \quad (6.4)$$

where $|\Phi_c|$ and θ_c are the amplitude and phase of the order parameter, respectively. Then the electron-phonon part in the mean-field approximation is given by

$$\mathcal{H}_{e-ph}^{\text{MF}} = \frac{2g}{\sqrt{N}} \langle b_{\mathbf{Q}} \rangle \sum_{\mathbf{k}, \sigma} \left(c_{\mathbf{k}+\mathbf{Q}\sigma}^{\dagger} f_{\mathbf{k}\sigma} + f_{\mathbf{k}\sigma}^{\dagger} c_{\mathbf{k}+\mathbf{Q}\sigma} \right) + 4g\sqrt{N} (b_{\mathbf{Q}}^{\dagger} + b_{\mathbf{Q}}) |\Phi_c| \cos \theta_c - 8g\sqrt{N} \langle b_{\mathbf{Q}} \rangle |\Phi_c| \cos \theta_c. \quad (6.5)$$

Introducing $B_{\mathbf{q}} = b_{\mathbf{q}} + \delta_{\mathbf{q}, \mathbf{Q}} (4g\sqrt{N}/\omega) |\Phi_c| \cos \theta_c$, the phonon Hamiltonian \mathcal{H}_{ph} together with the second term of the r.h.s. of Eq. (6.5) can be diagonalized, yielding $\omega \sum_{\mathbf{q}} B_{\mathbf{q}}^{\dagger} B_{\mathbf{q}} - 16\lambda N |\Phi_c|^2 \cos^2 \theta_c$. Hence, from $\langle B_{\mathbf{Q}} \rangle = \langle B_{\mathbf{Q}}^{\dagger} \rangle = 0$, we find

$$\langle b_{\mathbf{Q}} \rangle = \langle b_{\mathbf{Q}}^{\dagger} \rangle = -\frac{4g\sqrt{N}}{\omega} |\Phi_c| \cos \theta_c. \quad (6.6)$$

Substituting this expression into Eq. (6.5), we finally obtain the mean-field electron-phonon Hamiltonian,

$$\mathcal{H}_{e-ph}^{\text{MF}} = \Delta_p \cos \theta_c \sum_{\mathbf{k}, \sigma} f_{\mathbf{k}\sigma}^{\dagger} c_{\mathbf{k}+\mathbf{Q}\sigma} + \text{H.c.} + \frac{N\Delta_p^2}{4\lambda} \cos^2 \theta_c \quad (6.7)$$

with $\Delta_p = -8\lambda|\Phi_c|$. Using Eq. (6.7), we will minimize the grand potential of the system with respect to Δ_p and θ_c as shown below.

We define the complex order parameter of the excitonic SDW as

$$\Phi_s = |\Phi_s|e^{i\theta_s} = \frac{1}{2N} \sum_{\mathbf{k},\sigma} \sigma \langle c_{\mathbf{k}+\mathbf{Q}\sigma}^\dagger f_{\mathbf{k}\sigma} \rangle, \quad (6.8)$$

where $|\Phi_s|$ and θ_s are the amplitude and phase of the order parameter, respectively. Because we assume an excitonic SDW state with modulation vector $\mathbf{Q} = (\pi, \pi)$, where the expectation value $\langle c_{i\uparrow}^\dagger f_{i\uparrow} \rangle$ is in antiphase compared to $\langle c_{i\downarrow}^\dagger f_{i\downarrow} \rangle$ regarding the spatial variation, these two expectation values have opposite signs on the same site. In momentum space, this reads $\sum_{\mathbf{k}} \langle c_{\mathbf{k}+\mathbf{Q}\uparrow}^\dagger f_{\mathbf{k}\uparrow} \rangle = -\sum_{\mathbf{k}} \langle c_{\mathbf{k}+\mathbf{Q}\downarrow}^\dagger f_{\mathbf{k}\downarrow} \rangle$. We then find, from Eqs. (6.4) and (6.7), that $\langle b_{\mathbf{Q}} \rangle = \langle b_{\mathbf{Q}}^\dagger \rangle \propto \sum_{\mathbf{k},\sigma} \langle c_{\mathbf{k}+\mathbf{Q}\sigma}^\dagger f_{\mathbf{k}\sigma} \rangle = 0$, which means that the spin-triplet condensate will not couple to the phonons.

6.2.3 Variational Cluster Approximation

In order to take electron correlation effects into account, we treat the electronic interactions in Eq. (6.1) within the VCA [80,82], which is a quantum cluster method based on the self-energy functional theory [77,78]. In our VCA calculation, we take an $L_c = 2 \times 2 = 4$ site (eight-orbital) cluster as the reference system and we use exact diagonalization to solve the corresponding quantum many-body problem in the cluster. Within VCA, we can take into account spontaneous symmetry breakings just by adding appropriate Weiss fields to the reference system [82], and take these fields as variational parameters. The Weiss fields for excitonic CDW and SDW states, which are defined by the order parameter Φ_c [in Eq. (6.4)] and Φ_s [in Eq. (6.7)], respectively, may be written as

$$\mathcal{H}_c^{\text{WF}} = \Delta'_0 e^{i\theta_c} \sum_{\mathbf{k},\sigma} f_{\mathbf{k}\sigma}^\dagger c_{\mathbf{k}+\mathbf{Q}\sigma} + \text{H.c.}, \quad (6.9)$$

$$\mathcal{H}_s^{\text{WF}} = \Delta'_s e^{i\theta_s} \sum_{\mathbf{k},\sigma} \sigma f_{\mathbf{k}\sigma}^\dagger c_{\mathbf{k}+\mathbf{Q}\sigma} + \text{H.c.}. \quad (6.10)$$

Here, Δ'_0 and Δ'_s are the strengths of the Weiss fields for the excitonic CDW and SDW states generated by $\mathcal{H}_{e-e}^{U'}$, \mathcal{H}_{e-e}^J and $\mathcal{H}_{e-e}^{J'}$.

According to Eq. (6.6), we take into account the contribution of the phonons in the mean-field approximation as a one-particle term in the original system. Then, the Hamiltonian describing an excitonic CDW state in the reference system is given by

$$\mathcal{H}'_c = \mathcal{H}_e + \mathcal{H}_{e-e}^U + \mathcal{H}_{e-e}^{U'} + \mathcal{H}_{e-e}^J + \mathcal{H}_{e-e}^{J'} + \mathcal{H}_{e-ph}^{\text{MF}} + \mathcal{H}_c^{\text{WF}}, \quad (6.11)$$

where we note that $\mathcal{H}_e + \mathcal{H}_{e-e}^U + \mathcal{H}_{e-e}^{U'} + \mathcal{H}_{e-e}^J + \mathcal{H}_{e-e}^{J'} + \mathcal{H}_{e-ph}^{\text{MF}}$ is the Hamiltonian of the original system and the Weiss field $\mathcal{H}_c^{\text{WF}}$ is added in the reference system. Using \mathcal{H}'_c , we calculate the grand potential Ω and optimize the variational parameters Δ'_0 , Δ_p , and θ_c . The most stable solution with $(\Delta'_0, \Delta_p) \neq (0, 0)$ corresponds to the excitonic CDW state. Note that we determine the parameters Δ_p and θ_c via the minimization of the grand potential rather than solving the self-consistent equation. Both procedures are equivalent, however, since the order parameter Φ_c calculated, using the Green's function with Δ_p and θ_c optimized via the grand potential calculation in VCA, exactly satisfies the self-consistent condition $\Delta_p = 8\lambda\Phi_c$.

Since the spin-triplet term does not couple to the lattice degrees of freedom within our mean-field approach, the phonons will not affect the excitonic SDW state. Then, the Hamiltonian of the reference system describing an excitonic SDW is

$$\mathcal{H}'_s = \mathcal{H}_e + \mathcal{H}_{e-e}^U + \mathcal{H}_{e-e}^{U'} + \mathcal{H}_{e-e}^J + \mathcal{H}_{e-e}^{J'} + \mathcal{H}_s^{\text{WF}}. \quad (6.12)$$

Again we calculate the grand potential Ω from the reference Hamiltonian \mathcal{H}'_s and optimize Δ'_s and θ_s , where the most stable solution with $\Delta'_s \neq 0$ corresponds to the excitonic SDW state.

6.3 Results

6.3.1 Phase of Order Parameters

We first discuss the phase of the different order parameters entering the grand potential. In the spin-singlet excitonic state, the system forms an excitonic CDW at any finite U' and λ due to the

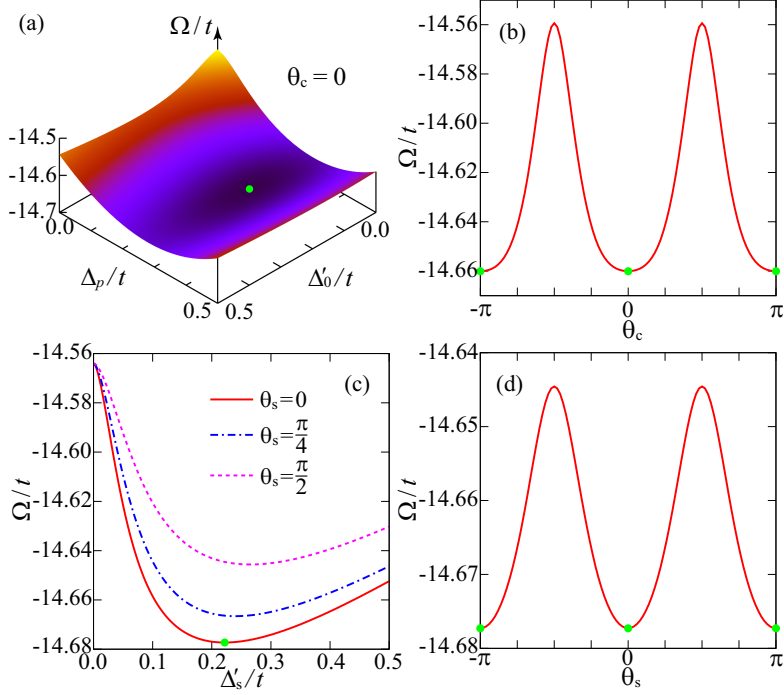


Figure 6.1: (a) Grand potential Ω as a function of the variational parameters Δ'_0 and Δ_p for $U'/t = 4$ and $\lambda/t = 0.15$. (b) θ_c dependence of Ω for the values of Δ'_0 and Δ_p optimized at $\theta_c = 0$. (c) Grand potential Ω as a function of the variational parameter Δ'_s at $U'/t = 4$ and $J/t = J'/t = 1$. (d) θ_s dependence of Ω obtained using the value of Δ'_s optimized at $\theta_s = 0$. Dots mark stable stationary points [135].

perfect nesting of the Fermi surface. Figure 6.1(a) shows the calculated grand potential Ω as a function of the variational parameters Δ'_0 and Δ_p . Obviously, the grand potential has a stationary point at $(\Delta'_0, \Delta_p) \neq (0, 0)$, signaling a CDW ordering. Without electron-phonon coupling, Ω is independent of the phase θ_c , i.e., $\Omega(\theta_c) = \Omega(\theta'_c)$. Accordingly, the excitonic CDW state reveals a gapless acoustic phase mode in its excitation spectrum [134]. If, however, the electron-phonon coupling comes into play, the grand potential manifests a dependence on the phase of the (complex) order parameter. In Fig. 6.1(b), we display the θ_c dependence of Ω ; the grand potential takes its minimum at $\theta_c = 0, \pi$. This phase fixation may be expected looking at Eq. (6.6). In our mean-field approximation, the single-particle gap caused by λ is given as $\Delta_p \cos \theta_c$ and is maximized at $\theta_c = 0$. When θ_c is fixed by the electron-phonon coupling, the collective phase mode in the spin-singlet excitonic state becomes massive (see the discussion of the spinless model in Ref. [134]).

In the case of the spin-triplet excitonic state, the excitonic SDW and CDW states are degenerate if the electron-phonon and exchange couplings are neglected. The exchange terms $\propto J$ and $\propto J'$ lift this degeneracy and stabilize the excitonic SDW state. Note that the θ_s dependence of the grand potential behaves differently in the presence or absence of the pair-hopping term J' : For $J' = 0$, the grand potential of the excitonic SDW state does not depend on θ_s , i.e., $\Omega(\theta_s) = \Omega(\theta'_s)$, whereas Ω depends on θ_s at any finite J' . Again the independence of Φ_s on the phase value θ_s accounts for a gapless excitation spectrum, i.e., an acoustic phase mode. Figure 6.1(c) and 6.1(d) gives the calculated grand potential Ω as a function of the phase θ_s in the presence of the pair-hopping term J' . Indeed we find that Ω has two minima, at $\theta_s = 0, \pi$, which fixes the phase θ_s of Φ_s . It is known that the energy in the presence of the pair-hopping-type exchange interaction shows a phase dependence $\cos 2\theta_s$ [136]. This is why the pair-hopping term J' fixes θ_s and in that way destroys the gapless acoustic phase mode in the spin-triplet excitonic state.

6.3.2 Stability of Spin-singlet Excitonic Phase

Now let us analyze the stability of the CDW state in the presence of the electron-phonon coupling in more detail. In Fig. 6.2, we present the results for both the optimized grand potential Ω_{opt} and the

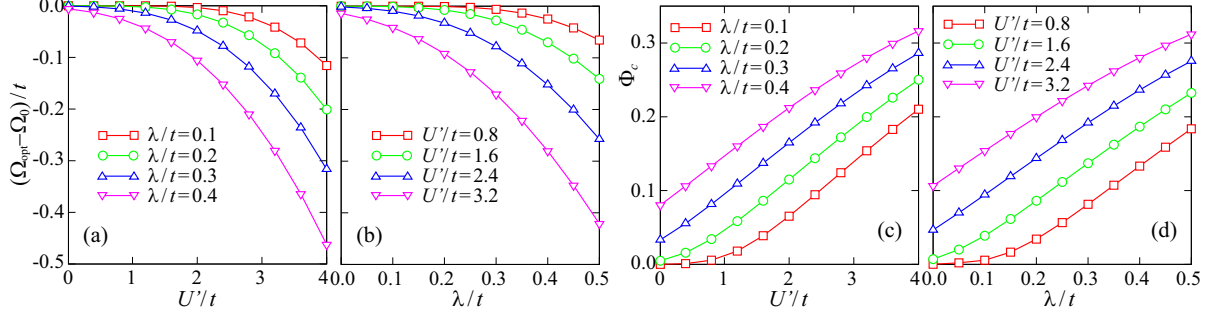


Figure 6.2: Optimized values of the grand potential Ω_{opt} as a function of (a) U'/t and (b) λ/t . Here, Ω_0 is the grand potential in the normal (semimetallic) state. Order parameter Φ_c for the excitonic CDW state as a function of (c) U'/t and (d) λ/t [135].

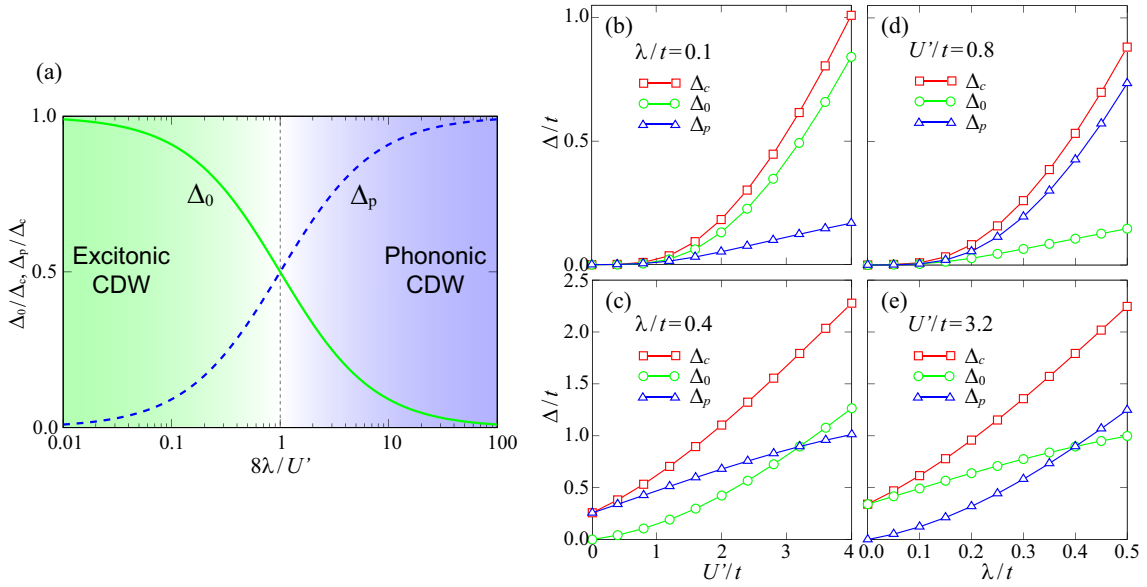


Figure 6.3: (a) Excitonic gap parameter Δ_0 (solid line) and phononic gap parameter Δ_p (dashed line) divided by the total gap $\Delta_c = \Delta_0 + \Delta_p$. Δ_c , Δ_0 , and Δ_p are separately plotted as a function of (b),(c) U'/t and (d),(e) λ/t [135].

order parameter Φ_c when the interband Coulomb interaction U' and the electron-phonon coupling λ are varied. Ω_{opt} indicates that (i) the symmetry-broken CDW state is lower in energy than the normal state and (ii) the stability of the CDW state is enhanced if U' and λ are increased; see Figs. 6.2(a) and 6.2(b). This is corroborated by the behavior of the order parameter Φ_c displayed in Figs. 6.2(c) and 6.2(d). We see that the interband Coulomb interaction U' induces and boosts the excitonic CDW state while the electron-phonon coupling λ rather promotes a phononic CDW state (see below). Both, however, cooperatively stabilize a charge-ordered state. In this connection, the electron-phonon coupling lifts the degeneracy of excitonic CDW and SDW that exists for $\lambda = 0$.

In the mean-field approximation, the gap parameter of the CDW state, $\Delta_c = (U' + 8\lambda)\Phi_c$, can be separated into two contributions: the excitonic (or interband Coulomb driven) part $\Delta_0 = U'\Phi_c$ and the phononic (or electron-phonon driven) part $\Delta_p = 8\lambda\Phi_c$. Figure 6.3(a) illustrates the relative magnitude of Δ_0 and Δ_p as a function of the ratio $8\lambda/U'$. At $8\lambda/U' \ll 1$, $\Delta_c \simeq \Delta_0 \gg \Delta_p$ and the CDW state, stabilized by the interband Coulomb interaction U' , is excitonic by its nature. Increasing $8\lambda/U'$, Δ_0 decreases while Δ_p increases, indicating a smooth crossover to a phononic CDW, which fully develops at $8\lambda/U' \gg 1$, where $\Delta_c \simeq \Delta_p \gg \Delta_0$. In the crossover region $8\lambda/U' \simeq 1$, both excitonic and phononic contributions are equally important.

In Figs. 6.3(b)–6.3(e), we show the behavior of the different contributions to the gap parameter

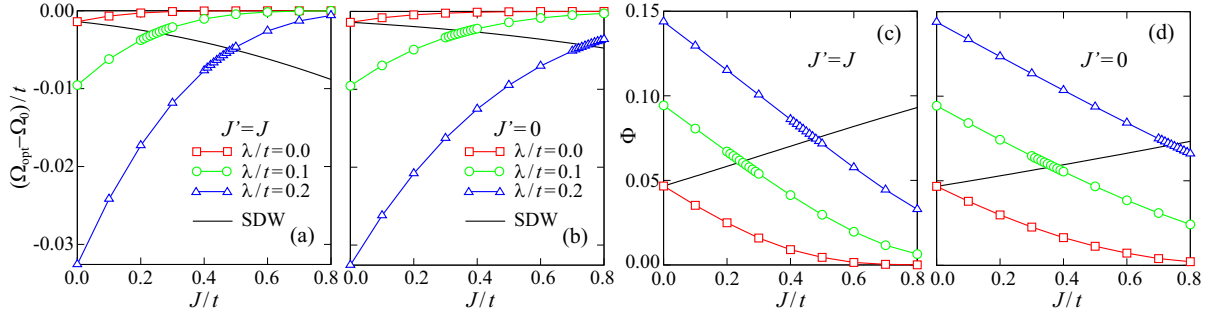


Figure 6.4: J dependence of the grand potential Ω_{opt} and the order parameter Φ in the excitonic CDW (symbols) and SDW (solid line) states (a),(c) with ($J' = J$) and (b),(d) without ($J' = 0$) the pair-hopping term, where $U'/t = 2.4$ is assumed. Ω_0 is the grand potential of the normal semimetallic state [135].

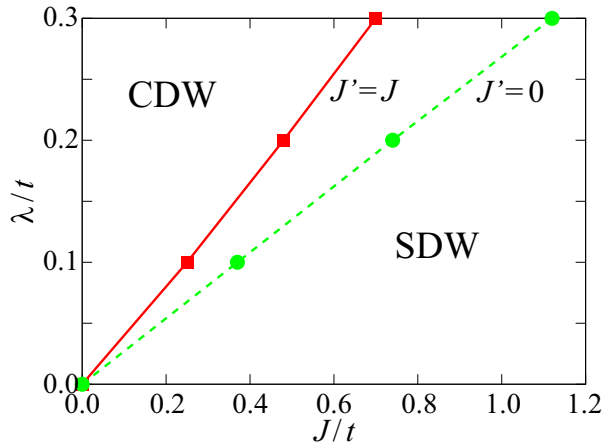


Figure 6.5: Ground-state phase diagram of the TBHM with electron-phonon and interband exchange interaction for a two-dimensional (square) lattice at half filling, showing the stability regions of excitonic CDW and SDW phases. Results are obtained by combining the mean-field and VCA approaches, in the presence ($J' = J$) and absence ($J' = 0$) of the pair-hopping term at $U'/t = 2.4$ [135].

Δ_c when U' and λ are varied separately. Data are obtained by VCA. Enhancing U'/t (λ/t) at weak λ/t (small U'/t) leads to an increase in Δ_p (Δ_0) as well, since both interactions couple to the same operator-product expectation value $\langle c_{\mathbf{k}+\mathbf{Q}\sigma}^\dagger f_{\mathbf{k}\sigma} \rangle$; see Figs. 6.3(b) and 6.3(d). The crossover between excitonic and phononic CDWs can be seen in Figs. 6.3(c) and 6.3(e), where a crossing between Δ_p and Δ_0 appears when $U' \simeq 8\lambda$.

6.3.3 Ground-state Phase Diagram

We now study the influence of the interband exchange and pair-hopping interactions on the nature of the excitonic phase and also when an additional electron-phonon coupling acts in the system. Evidently, excitonic CDW and SDW states are degenerate at $J = J' = 0$ and $\lambda = 0$ [128,129]. Any finite J and/or λ lifts this degeneracy. Figure 6.4 clearly shows that by increasing J , the optimized grand potential Ω_{opt} for the excitonic SDW (CDW) state monotonically decreases (increases); accordingly, the order parameter for the excitonic SDW (CDW) phase is enhanced (suppressed). This holds for both $J' > 0$ and $J' = 0$. Clearly the excitonic SDW state is stable as soon as $\Omega_{\text{opt}}^{\text{SDW}}$ becomes less than $\Omega_{\text{opt}}^{\text{CDW}}$. A finite pair-hopping term $\propto J'$ amplifies the tendency towards excitonic SDW formation [129].

The competition between the electron-phonon and interband exchange interaction leads to the ground-state phase diagram of the model Eq. (6.1) presented in Fig. 6.5. Obviously, λ and J tend to establish CDW and SDW phases, respectively, on top of an excitonic state enforced by U' . A finite J' increases the region in the J - λ plane where the excitonic SDW is the ground state. We note that the

SDW-CDW transition is a first-order transition in our approximations.

6.4 Discussion

First, let us discuss implications of our findings on materials aspects. The transition-metal chalcogenides $1T$ -TiSe₂ and Ta₂NiSe₅ have recently been discussed in terms of the spin-singlet excitonic insulator. In these systems, the valence and conduction bands are formed by orbitals located on different atoms. For example, in $1T$ -TiSe₂, the $4p$ orbitals of Se ions account for the valence bands and the $3d$ orbitals of Ti ions account for the conduction bands [28–35]. Also in Ta₂NiSe₅, the $3d$ orbitals of Ni ions form the valence bands and the $5d$ orbitals of Ta ions form the conduction bands [36–39]. The interband exchange interaction such as Hund’s rule coupling, acting between electrons on different orbitals of a single ion and favoring the spin-triplet excitons, is therefore negligible. Rather, in these materials, the electron-phonon coupling is at play and will stabilize a spin-singlet excitonic insulator state. The interband Coulomb interaction and electron-phonon interaction, which are inherently interrelated in these materials, will cooperatively stabilize the excitonic CDW, which is predominantly phononic or excitonic depending on the importance of electron-phonon or Coulomb effects. By contrast, in the iron-pnictide superconductors [51, 52, 57] and Co oxides [60–62], the valence and conduction bands are formed by the d orbitals on the (same) transition-metal ions, so that the Hund’s rule coupling is expected to be strong. Hence, in these materials, the SDW phase, if really excitonic in origin, is rather triggered by the Hund’s rule coupling than by electron-phonon coupling. Then, as our phase diagram suggests, the condensation of spin-triplet excitons will play a major role.

Second, let us comment on the phase of the excitonic order parameters. On the one hand, as we have shown in the preceding section, the electron-phonon interaction stabilizes the spin-singlet excitonic condensate, whereas exchange interactions such as the Hund’s rule couplings stabilize a spin-triplet excitonic condensate in the otherwise degenerate excitonic density-wave states. On the other hand, these interactions, in particular the electron-phonon and pair-hopping interactions, will fix the phase of the order parameter of the excitonic state; see Sec. 6.3.1. Because the spatial modulations of the excitonic CDW and SDW are given by $\cos(\mathbf{Q} \cdot \mathbf{r}_i + \theta)$, the phase θ may lead to a translational motion of the condensate as a whole [137]. If the energy of the condensate is independent of the phase, maintaining the continuous symmetry of the system with respect to the phase, a gapless acoustic phase mode may appear in the excitation spectrum, allowing for a translational motion of the condensate without loss of energy (i.e., superfluidity), as predicted by Fröhlich in his theory of incommensurate density waves [68]. In real materials, however, excitonic condensation will be influenced by the lattice degrees of freedom or affected by the pair-hopping term. Then, the phase of the condensate is fixed and a gap opens for the collective phase mode. This makes realization of excitonic superfluidity in real materials unlikely.

6.5 Summary

To summarize, we have studied the stability of the excitonic states with charge and spin density modulations in terms of the TBHM, supplemented by electron-phonon and interband exchange interactions, where the static mean-field theory is employed for coupling to the lattice degrees of freedom and the variational cluster approximations for the electron correlations. We have shown that both the interband Coulomb interaction U' and the electron-phonon coupling λ tend to stabilize an excitonic CDW state. While at $\lambda = 0$ the excitonic insulator exhibits an acoustic phase mode, any finite λ fixes the phase of the order parameter and therefore eliminates such a gapless excitation related to supertransport properties. The CDW typifies a predominantly excitonic and phononic state for small and large ratios λ/U' , respectively. The interband exchange interaction J , on the other hand, promotes an excitonic SDW phase, which is further stabilized by pair-hopping processes, which also fixes the phase of the order parameter. These results obtained for a generic microscopic model Hamiltonian should contribute to a better understanding of exciton condensation in several material classes with strong electronic correlations.

Chapter 7

Charge and Spin Density Distributions in Excitonic Phases

7.1 Introduction

In the previous Chapter, we discussed the stability of excitonic phases in the multi-band model. It is indubitable that the excitonic phases become a long-range density-wave state with modulation vector \mathbf{Q} when the valence and conduction bands are separated by \mathbf{Q} [14,15]. Then, what is the difference between the excitonic density-wave states in the multi-band systems and the conventional charge-density-wave (CDW) and spin-density-wave (SDW) states in the single-band systems?

In this Chapter, we evaluate charge and spin density distributions of the excitonic CDW and SDW states from the local wave functions in the tight-binding approximation. First, we consider the charge and spin densities of the excitonic phases when the valence and conduction bands are composed of orthogonal orbitals in a single ion. In the real materials, the energy bands are reconstructed by the hybridization of many orbitals. Thus, we next consider the electronic structure of the excitonic phases, in which the valence and conduction bands include the components of many orbitals in a single ion. Finally, we briefly discuss the excitonic density-wave states when the valence and conduction bands are composed of orbitals in different ions.

7.2 Multi-Orbitals in a Single Ion

7.2.1 Charge and Spin Densities

First, we consider the charge and spin densities of excitonic phases, in which the valence and conduction bands are composed of orthogonal orbitals in a single ion. In this case, the field operator in the tight-binding approximation is given by

$$\Psi_{\sigma}(\mathbf{r}) = \sum_i \sum_{\alpha} \phi_{\alpha}(\mathbf{r} - \mathbf{R}_i) c_{i\alpha\sigma}, \quad (7.1)$$

where $\phi_{\alpha}(\mathbf{r})$ is the Wannier function of the α -orbital, \mathbf{R}_i is the lattice vector, and $c_{i\alpha\sigma}$ ($c_{i\alpha\sigma}^{\dagger}$) is the annihilation (creation) operator of an electron at site i and spin σ ($=\uparrow, \downarrow$) in the α -orbital [60, 138]. From the field operator, the charge and spin densities are given by

$$\rho(\mathbf{r}) = \sum_{\sigma} \langle \Psi_{\sigma}^{\dagger}(\mathbf{r}) \Psi_{\sigma}(\mathbf{r}) \rangle, \quad (7.2)$$

$$\mathbf{s}(\mathbf{r}) = \frac{1}{2} \sum_{\sigma, \sigma'} \langle \Psi_{\sigma}^{\dagger}(\mathbf{r}) \boldsymbol{\sigma}_{\sigma\sigma'} \Psi_{\sigma'}(\mathbf{r}) \rangle, \quad (7.3)$$

respectively, where $\boldsymbol{\sigma} = (\sigma^x, \sigma^y, \sigma^z)$ is the Pauli matrix.

In this subsection, we assume a two-orbital model for simplicity and evaluate charge and spin densities in a unit cell. Using the orbitals of the valence (a) and conduction (b) bands, the field operator in the i -th unit cell is given as

$$\Psi_{i\sigma}(\mathbf{r}) = \phi_a(\mathbf{r}) c_{ia\sigma} + \phi_b(\mathbf{r}) c_{ib\sigma}, \quad (7.4)$$

where we write $\phi_\alpha(\mathbf{r} - \mathbf{R}_i) = \phi_\alpha(\mathbf{r})$ for simplicity [60,138]. We assume that $\phi_\alpha(\mathbf{r})$ is real [60,138], which may be reasonable when we neglect the spin-orbit coupling.

From the field operator in Eq. (7.4), the local charge density in the i -th unit cell is given by

$$\rho_i(\mathbf{r}) = \sum_{\sigma} \langle \Psi_{i\sigma}^{\dagger}(\mathbf{r}) \Psi_{i\sigma}(\mathbf{r}) \rangle = \sum_{\sigma} \sum_{\alpha, \beta} \phi_{\alpha}(\mathbf{r}) \phi_{\beta}(\mathbf{r}) \langle c_{i\alpha\sigma}^{\dagger} c_{i\beta\sigma} \rangle. \quad (7.5)$$

When the spin-singlet condensation state with vector \mathbf{Q} is realized, the orbital off-diagonal order parameter for the excitonic CDW is given by

$$\sum_{\sigma} \langle c_{i\beta\sigma}^{\dagger} c_{i\alpha\sigma} \rangle = \Phi_s e^{i\mathbf{Q} \cdot \mathbf{R}_i}, \quad (7.6)$$

where we set the phase of the order parameter to be zero and assume the real order parameter. Using Φ_s , the local charge density in the excitonic CDW state in Eq. (7.5) becomes

$$\rho_i(\mathbf{r}) = \phi_a^2(\mathbf{r}) n_{ia} + \phi_b^2(\mathbf{r}) n_{ib} + 2\phi_a(\mathbf{r}) \phi_b(\mathbf{r}) \Phi_s \cos \mathbf{Q} \cdot \mathbf{R}_i, \quad (7.7)$$

where we define $n_{i\alpha} \equiv \sum_{\sigma} \langle c_{i\alpha\sigma}^{\dagger} c_{i\alpha\sigma} \rangle$. From Eq. (7.7), we confirm that the local charge density has the modulation with \mathbf{Q} in the excitonic CDW state.

On the other hand, the local spin density in the i -th unit cell is given by

$$\mathbf{s}_i(\mathbf{r}) = \frac{1}{2} \sum_{\sigma, \sigma'} \langle \Psi_{i\sigma}^{\dagger}(\mathbf{r}) \boldsymbol{\sigma}_{\sigma\sigma'} \Psi_{i\sigma'}(\mathbf{r}) \rangle = \frac{1}{2} \sum_{\sigma, \sigma'} \sum_{\alpha, \beta} \phi_{\alpha}(\mathbf{r}) \phi_{\beta}(\mathbf{r}) \langle c_{i\alpha\sigma}^{\dagger} \boldsymbol{\sigma}_{\sigma, \sigma'} c_{i\beta\sigma'} \rangle. \quad (7.8)$$

When the spin-triplet condensation state with vector \mathbf{Q} is realized, the orbital off-diagonal order parameter for the excitonic SDW is given by

$$\frac{1}{2} \sum_{\sigma, \sigma'} \langle c_{i\beta\sigma}^{\dagger} \boldsymbol{\sigma}_{\sigma\sigma'} c_{i\alpha\sigma'} \rangle = \Phi_t e^{i\mathbf{Q} \cdot \mathbf{R}_i}. \quad (7.9)$$

Using Φ_t , the local spin density in the excitonic SDW state in Eq. (7.8) becomes

$$\mathbf{s}_i(\mathbf{r}) = \phi_a^2(\mathbf{r}) \mathbf{m}_{ia} + \phi_b^2(\mathbf{r}) \mathbf{m}_{ib} + 2\phi_a(\mathbf{r}) \phi_b(\mathbf{r}) \Phi_t \cos \mathbf{Q} \cdot \mathbf{R}_i, \quad (7.10)$$

where we define $\mathbf{m}_{i\alpha} \equiv \sum_{\sigma, \sigma'} \langle c_{i\alpha\sigma}^{\dagger} \boldsymbol{\sigma}_{\sigma\sigma'} c_{i\alpha\sigma'} \rangle / 2$. From Eq. (7.10), we confirm that the local spin density has the modulation with \mathbf{Q} in the excitonic SDW state.

When the excitonic phases are realized in strongly correlated electron systems, an important factor in the charge and spin density is

$$F(\mathbf{r}) = \phi_a(\mathbf{r}) \phi_b(\mathbf{r}). \quad (7.11)$$

$F(\mathbf{r})$ is given by the product of the wave functions of the a and b orbitals, which has either positive or negative part as a function of \mathbf{r} . Therefore, due to $F(\mathbf{r})$, it is expected that the charge and spin densities are spatially varying and show a variety of electronic clouds in the unit cell. In general, when parities of the wave functions $\phi_a(\mathbf{r})$ and $\phi_b(\mathbf{r})$ are the same, the parity of $F(\mathbf{r})$ becomes even. On the other hand, the wave functions $\phi_a(\mathbf{r})$ and $\phi_b(\mathbf{r})$ have different parities, their product $F(\mathbf{r})$ has odd parity and breaks the space inversion symmetry in the unit cell. Electronic ferroelectricity, which is derived from the broken inversion symmetry of $F(\mathbf{r})$, has been suggested in the extended Falicov-Kimball model [87].

Here, we consider a simple example where the valence band a and conduction band b are composed of the s -orbital and p_z -orbital, respectively [see Fig. 7.1(a)]. In this example, the orbital off-diagonal orders for the excitonic density waves are realized with $n_{is} = n_s$, $n_{ip_z} = n_{p_z}$, $\mathbf{m}_{is} = \mathbf{m}_{ip_z} = 0$, corresponding to the results in Chap. 5. In this case, the local charge density (7.7) in the excitonic CDW state is given by

$$\rho_i(\mathbf{r}) = \phi_s^2(\mathbf{r}) n_s + \phi_{p_z}^2(\mathbf{r}) n_{p_z} + 2\phi_s(\mathbf{r}) \phi_{p_z}(\mathbf{r}) \Phi_s \cos \mathbf{Q} \cdot \mathbf{R}_i \quad (7.12)$$

and the local spin density (7.10) in the excitonic SDW state is given by

$$\mathbf{s}_i(\mathbf{r}) = 2\phi_s(\mathbf{r}) \phi_{p_z}(\mathbf{r}) \Phi_t \cos \mathbf{Q} \cdot \mathbf{R}_i. \quad (7.13)$$

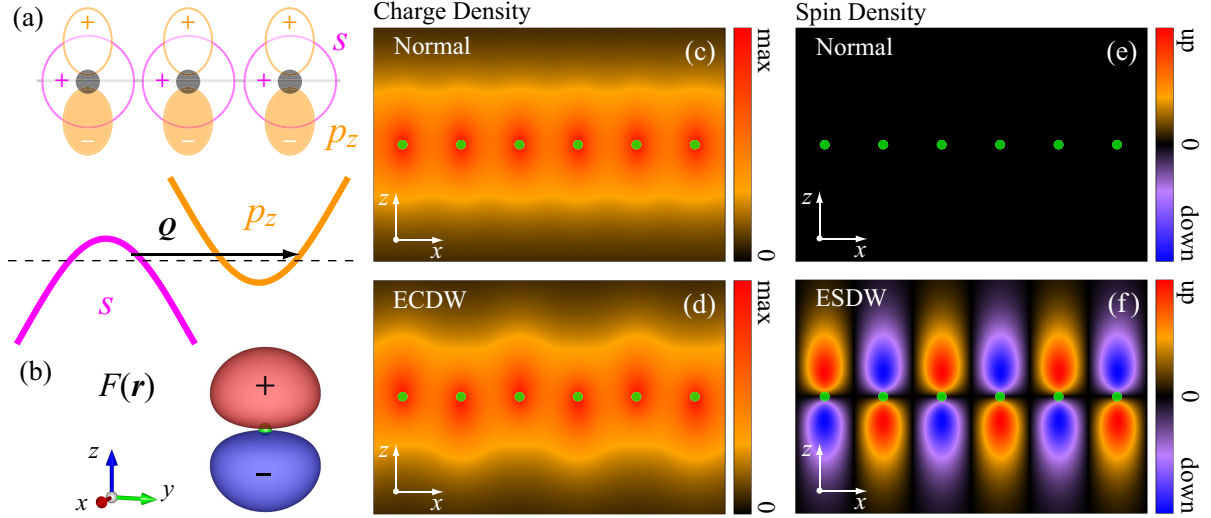


Figure 7.1: (a) Schematic picture of the example when the valence and conduction bands are composed of the s and p_z orbitals, respectively. (b) Isosurface of $F(\mathbf{r}) = \phi_s(\mathbf{r})\phi_{p_z}(\mathbf{r})$. Red and blue indicates positive and negative parts of $F(\mathbf{r})$, respectively. Illustrated are the charge density of (c) the normal state and (d) ECDW (excitonic charge-density wave) state with $Q = \pi$, and the spin density of (e) the normal state and (f) ESDW (excitonic spin-density wave) state with $Q = \pi$.

In Fig. 7.1(b), we show the function $F(\mathbf{r}) = \phi_s(\mathbf{r})\phi_{p_z}(\mathbf{r})$. The wave functions $\phi_s(\mathbf{r})$ and $\phi_{p_z}(\mathbf{r})$ have even and odd parities, respectively, and thus their product $F(\mathbf{r})$ has odd parity, which breaks the space inversion symmetry in the unit cell. In Figs. 7.1(c)-7.1(f), we show the charge and spin densities in the normal state ($\Phi_s = 0$, $\Phi_t = 0$), the charge density in the excitonic CDW state ($\Phi_s \neq 0$), and the spin density in the excitonic SDW state ($\Phi_t \neq 0$) with $Q = \pi$ ¹. The charge density in the normal state is uniform as in Fig. 7.1(c). When the excitonic CDW state is realized ($\Phi_s \neq 0$), the charge density is deviated towards the $+z$ direction, corresponding to $F(\mathbf{r})$, in the i -th site and towards the $-z$ direction in the neighboring sites, and thus the charge density has the density wave with twice period ($Q = \pi$) in the system [see Fig. 7.1(d)]. In Fig. 7.1(e) and 7.1(f), we find that there are no spin polarizations in the normal state, but in the excitonic SDW state ($\Phi_t \neq 0$), the spin polarization, which corresponds to $F(\mathbf{r})$, appears. Corresponding to $Q = \pi$, the spin polarization inverts alternately over the unit cells and the spin density has the density wave with twice period [see Fig. 7.1(f)]. From the above, we confirm that the local charge and spin densities have the density waves corresponding to Q in the excitonic insulator state. In this example, the local charge and spin densities are modulated, but we also have to emphasize that the total charge in the unit cell (or in the atom) does not change as shown in Fig. 7.1(d) and the net magnetization in the unit cell (or in the atom) is zero as shown in Fig. 7.1(f).

In comparison with the s and p orbitals in the above example, the wave functions $\phi_\alpha(\mathbf{r})$ of the d and f orbitals, which are the main stage of strongly correlated electron systems, have complex shapes. In Fig. 7.2, we show the function $F(\mathbf{r})$ and spin density when the spin-triplet excitonic condensation state is realized from the d_{xy} and $d_{x^2-y^2}$ orbitals. In this example, the hopping integral of the d_{xy} orbital has the opposite sign to that of the $d_{x^2-y^2}$ orbital, $t_{xy}t_{x^2-y^2} < 0$, and the direct gap system is realized [see Fig. 7.2(a)]. Thus, the excitonic state becomes a ferro state with $Q = 0$, which are realized in direct gap systems [see Fig. 7.2(c)]. From the formula of the spin density in Eq. (7.13), we understand that the spin density makes the density wave with Q , but from Fig. 7.2, we find that the excitonic SDW state is significantly different from the conventional SDW state that corresponds to an antiferromagnetic order. The excitonic density-wave state is the order with the charge and spin densities distributed anisotropically in each unit cell (or in the atom). Thus, it may be suitable to describe an excitonic order as a multipole order in these cases.

¹To illustrate the densities in Figs. 7.1(c)-7.1(f), we use the spherical harmonics of s and p_z orbitals for angular part (θ, φ). However, in order to exaggerate the electronic structure, we broaden the radial distribution function of the $1s$ orbital. Thus, Figs. 7.1(c)-7.1(f) are not exact but a schematic picture.

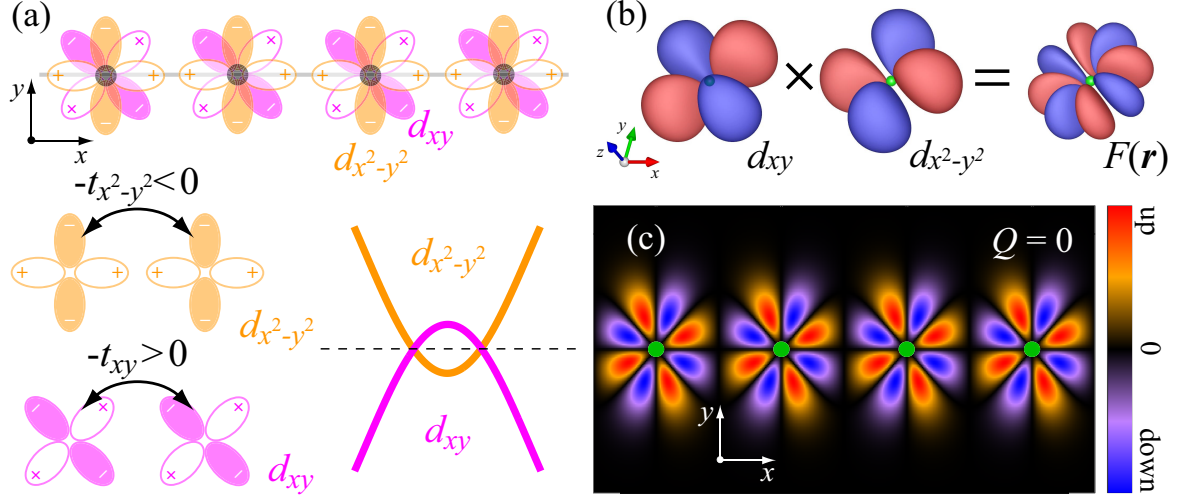


Figure 7.2: (a) Schematic picture of the example when the valence and conduction bands are composed of the s and p_z orbitals, respectively. (b) Isosurface of the wave function of d_{xy} and $d_{x^2-y^2}$ orbitals and their product $F(\mathbf{r})$. Red and blue indicates positive and negative parts of $F(\mathbf{r})$, respectively. (c) The spin density of the spin-triplet excitonic condensation state with $F(\mathbf{r})$.

7.2.2 Multipole Moments

In this subsection, we describe the character of the excitonic phases in terms of the multipole moments. Here, we consider the previous example, where the valence s -orbital and conduction p_z -orbital are hybridized due to excitonic ordering. First, we evaluate an electric monopole moment, which corresponds to the total charge in each unit cell. The electric monopole moment is defined as

$$Q_0 \equiv \int d\mathbf{r} \rho_i(\mathbf{r}) = \sum_{\sigma} \sum_{\alpha, \beta} \left[\int d\mathbf{r} \phi_{\alpha}(\mathbf{r}) \phi_{\beta}(\mathbf{r}) \right] \langle c_{i\alpha\sigma}^{\dagger} c_{i\beta\sigma} \rangle. \quad (7.14)$$

From the orthogonality of the wave function of orbitals

$$\int d\mathbf{r} \phi_{\alpha}(\mathbf{r}) \phi_{\beta}(\mathbf{r}) = \delta_{\alpha, \beta}, \quad (7.15)$$

Q_0 in Eq. (7.14) becomes

$$Q_0 = \sum_{\sigma} \sum_{\alpha} \langle c_{i\alpha\sigma}^{\dagger} c_{i\alpha\sigma} \rangle = \sum_{\alpha} n_{i\alpha}, \quad (7.16)$$

which is given simply by $n_{i\alpha}$. In the same way, a magnetic dipole moment, which corresponds to the net magnetization in each unit cell, is given as

$$\mathbf{M}_0 \equiv 2 \int d\mathbf{r} \mathbf{s}_i(\mathbf{r}) = \sum_{\sigma, \sigma'} \sum_{\alpha, \beta} \left[\int d\mathbf{r} \phi_{\alpha}(\mathbf{r}) \phi_{\beta}(\mathbf{r}) \right] \langle c_{i\alpha\sigma}^{\dagger} \boldsymbol{\sigma}_{\sigma\sigma'} c_{i\beta\sigma'} \rangle = 2 \sum_{\alpha} \mathbf{m}_{i\alpha}, \quad (7.17)$$

where $\mathbf{M}_0 = (M_0^x, M_0^y, M_0^z)$. In the example with the s and p_z orbitals, the electric monopole moment (total charge) Q_0 remains unchanged and the magnetic dipole moment (net magnetization) \mathbf{M}_0 vanishes when the excitonic density-wave states are realized with $\langle c_{ip_z\sigma}^{\dagger} c_{i\sigma} \rangle \neq 0$, $n_{i\alpha} = n_{\alpha}$ and $\mathbf{m}_{i\alpha} = 0$.

Next, we discuss the higher rank multipole moments, which are determined by the excitonic order with $\langle c_{ip_z\sigma}^{\dagger} c_{i\sigma} \rangle \neq 0$. In the same example, we evaluate an electric dipole moment in the excitonic CDW state. The electric dipole moment of z -direction is defined as

$$Q_z \equiv \int d\mathbf{r} z \rho_i(\mathbf{r}) = \sum_{\sigma} \sum_{\alpha, \beta} \left[\int d\mathbf{r} z \phi_{\alpha}(\mathbf{r}) \phi_{\beta}(\mathbf{r}) \right] \langle c_{i\alpha\sigma}^{\dagger} c_{i\beta\sigma} \rangle. \quad (7.18)$$

Here, the integral parts in Eq. (7.18) are

$$\int d\mathbf{r} z \phi_\alpha(\mathbf{r}) \phi_\alpha(\mathbf{r}) = 0, \quad \int d\mathbf{r} z \phi_s(\mathbf{r}) \phi_{p_z}(\mathbf{r}) \neq 0. \quad (7.19)$$

Therefore, the electric dipole moment becomes

$$Q_z = \sum_\sigma \left[\int d\mathbf{r} z \phi_s(\mathbf{r}) \phi_{p_z}(\mathbf{r}) \right] \left[\langle c_{is\sigma}^\dagger c_{ip_z\sigma} \rangle + \langle c_{ip_z\sigma}^\dagger c_{is\sigma} \rangle \right]. \quad (7.20)$$

When the excitonic CDW state is realized with $\sum_\sigma \langle c_{ip_z\sigma}^\dagger c_{is\sigma} \rangle \neq 0$, the electric dipole moment of z -direction becomes finite. When we calculate the electric dipole moment of x - and y -directions, the integral parts of the wave function become zero and thus $Q_x = Q_y = 0$. Therefore, depending on the shape of the wave functions of the valence and conduction bands, the electric dipole moment of z -direction becomes finite but that of the other directions becomes zero. In the same way, the magnetic quadrupole moment, which is characterized by the product of the integral part of the wave functions with the dipole distribution for z -direction and the spin polarization (magnetic dipole) $\langle c_{is\sigma}^\dagger \boldsymbol{\sigma}_{\sigma\sigma'} c_{ip_z\sigma'} \rangle$, is given as

$$\mathbf{M}_z \equiv 2 \int d\mathbf{r} z \mathbf{s}_i(\mathbf{r}) = \sum_{\sigma, \sigma'} \left[\int d\mathbf{r} z \phi_s(\mathbf{r}) \phi_{p_z}(\mathbf{r}) \right] \left[\langle c_{is\sigma}^\dagger \boldsymbol{\sigma}_{\sigma\sigma'} c_{ip_z\sigma'} \rangle + \langle c_{ip_z\sigma}^\dagger \boldsymbol{\sigma}_{\sigma\sigma'} c_{is\sigma'} \rangle \right], \quad (7.21)$$

where $\mathbf{M}_z = (M_z^x, M_z^y, M_z^z)$. When the excitonic SDW state is realized with $\sum_{\sigma, \sigma'} \langle c_{ip_z\sigma}^\dagger \boldsymbol{\sigma}_{\sigma\sigma'} c_{is\sigma'} \rangle \neq 0$, the magnetic quadrupole moment \mathbf{M}_z becomes finite.

In the excitonic phase, depending on the wave functions of the valence and conduction bands, the finite multipole moments are different because the charge and spin density distributions in real space are different. As in Fig. 7.2, when the spin-triplet excitonic order is realized from the d_{xy} and $d_{x^2-y^2}$ orbitals, the higher rank multipole moment becomes finite. In general, the multipole moments are characterized by the projection onto the spherical harmonics [139–141]. Using the spherical harmonics, the electric multipole moment is defined as

$$Q_{lm} \equiv \int d\mathbf{r} [r^l Z_{lm}(\hat{\mathbf{r}})] \rho_i(\mathbf{r}) = \sum_\sigma \sum_{\alpha, \beta} \left[\int d\mathbf{r} r^l Z_{lm}(\hat{\mathbf{r}}) \phi_\alpha(\mathbf{r}) \phi_\beta(\mathbf{r}) \right] \langle c_{i\alpha\sigma}^\dagger c_{i\beta\sigma} \rangle, \quad (7.22)$$

where $\hat{\mathbf{r}} = (\theta, \varphi)$ indicates the angular component, and we define $Z_{lm}(\hat{\mathbf{r}}) \equiv \sqrt{4\pi/(2l+1)} Y_{lm}(\hat{\mathbf{r}})$. Here, we assume the real spherical harmonics, which are sometimes called the tesseral harmonics². In practice, the electric multipole moments in Eq. (7.22) are given by $Q_{00} = Q_0$, $Q_{10} = Q_z$, $Q_{11}^{(c)} = Q_x$, $Q_{11}^{(s)} = Q_y$, \dots . l is the rank of the electric multipole moments, and the moments of each rank is called the electric monopole ($l = 0$), dipole ($l = 1$), quadrupole ($l = 2$), octupole ($l = 3$), hexadecapole ($l = 4$), etc. As in the charge density, we define the multipole moment for the spin density as³

$$\mathbf{M}_{lm} \equiv 2 \int d\mathbf{r} [r^l Z_{lm}(\hat{\mathbf{r}})] \mathbf{s}_i(\mathbf{r}) = \sum_{\sigma, \sigma'} \sum_{\alpha, \beta} \left[\int d\mathbf{r} r^l Z_{lm}(\hat{\mathbf{r}}) \phi_\alpha(\mathbf{r}) \phi_\beta(\mathbf{r}) \right] \langle c_{i\alpha\sigma}^\dagger \boldsymbol{\sigma}_{\sigma\sigma'} c_{i\beta\sigma'} \rangle, \quad (7.23)$$

where $\mathbf{M}_{lm} = (M_{lm}^x, M_{lm}^y, M_{lm}^z)$. The multipole moment in Eq. (7.23) is characterized by the product of the integral part of the l -th rank multipole distribution and the spin polarization (magnetic dipole). In this sense, we may call the multipole moments in Eq. (7.23) starting from $l = 0$ magnetic multipole moments, where $l = 0$ corresponds to the magnetic dipole.

²The spherical harmonics with $m = 0$ are real. For $|m| > 0$, the spherical harmonics can be taken to be real with the following relations.

$$Y_{l|m|}^{(c)}(\hat{\mathbf{r}}) = \frac{1}{\sqrt{2}} [Y_{l-|m|}(\hat{\mathbf{r}}) + (-1)^m Y_{l|m|}(\hat{\mathbf{r}})], \quad Y_{l|m|}^{(s)}(\hat{\mathbf{r}}) = \frac{i}{\sqrt{2}} [Y_{l-|m|}(\hat{\mathbf{r}}) - (-1)^m Y_{l|m|}(\hat{\mathbf{r}})].$$

³In the definition of the multipole moments for the spin density in Eq. (7.23), we divide the multipole moment into the integral part of the wave functions and the spin polarization, corresponding to the definition of the electric multipole moments in Eq. (7.22). In this definition, (l, m) in Eq. (7.22) is characterized by the integral part. On the other hand, the magnetic multipole moments are often defined as $M_{lm} \equiv 2 \int d\mathbf{r} \nabla [r^l Z_{lm}(\hat{\mathbf{r}})] \cdot \mathbf{s}(\mathbf{r})$ [139, 141]. We also have to consider orbital magnetism when the wave functions of valence and conduction bands and order parameter of excitonic state are imaginary. In this case, we may need to improve the definition of the magnetic multipole moment in Eq. (7.23).

From the above discussion, we find that, when the excitonic CDW or SDW state is realized from the valence and conduction bands composed of the orthogonal orbitals, the charge or spin density distributions change in each unit cell and higher rank electric or magnetic moments become finite, depending on the wave functions of the valence and conduction bands. Therefore, we may interpret that the waves in the charge and spin densities are given by the ordered multipole moments with modulation vector \mathbf{Q} in the excitonic insulator states. In this sense, the excitonic CDW and SDW states should be called the electric multipole density-wave state and magnetic multipole density-wave state, respectively. We may point out that the accurate electronic structure of the excitonic phase is rather difficult to detect experimentally when higher rank multipole moments become finite due to exciton condensation.

7.2.3 Valence and Conduction Bands Composed of Multi-Orbitals

In the previous examples, we have mentioned that the net magnetization (magnetic dipole moment) in the unit cell (or in the atom) does not appear when the orthogonal bands are hybridized as an excitonic order. However, the SDW state in Cr [42–45] and iron-based superconductors [46–59] are sometimes regarded as excitonic orderings. In these studies, we note that the excitonic SDW state has the antiferromagnetic order (conventional SDW), which has a net magnetization in each site. Why does this difference arise?

In the previous subsection, we assumed that the valence and conduction bands are composed of the pure orthogonal atomic orbitals without hybridization between different orbitals. However, in the real materials, although orbitals are orthogonal in the same site, the different orbitals can hybridize via the hoppings between the neighboring sites and the energy bands are reconstructed by the hybridization of many orbitals.

Here, we consider the example, where the valence and conduction band are composed of the s -orbital and $d_{x^2-y^2}$ -orbital on the one-dimensional chain [see Fig. 7.3(a)]. In contrast to the previous examples with the s and p_z orbitals, the s and $d_{x^2-y^2}$ orbitals hybridize via the hoppings between the neighboring sites t_{sd} [see Fig. 7.3(a)]. Hereafter, we use d as the $d_{x^2-y^2}$ orbital for simplicity. The noninteracting tight-binding Hamiltonian is given as

$$\begin{aligned} \mathcal{H}_e &= \sum_{\alpha=s,d} \left(\varepsilon_\alpha \sum_{i,\sigma} c_{i\alpha\sigma}^\dagger c_{i\alpha\sigma} - t_\alpha \sum_{\langle i,j \rangle, \sigma} c_{i\alpha\sigma}^\dagger c_{j\alpha\sigma} \right) - t_{sd} \sum_{\langle i,j \rangle, \sigma} \left(c_{is\sigma}^\dagger c_{jd\sigma} + c_{id\sigma}^\dagger c_{js\sigma} \right) \\ &= \sum_{k,\sigma} \begin{pmatrix} c_{ks\sigma}^\dagger & c_{kd\sigma}^\dagger \end{pmatrix} \begin{pmatrix} \varepsilon_s(k) & t_{sd}(k) \\ t_{sd}(k) & \varepsilon_d(k) \end{pmatrix} \begin{pmatrix} c_{ks\sigma} \\ c_{kd\sigma} \end{pmatrix}, \end{aligned} \quad (7.24)$$

where ε_α and t_α are the energy level and the hopping integral between the α orbitals in the neighboring sites, respectively. The orbital diagonal and off-diagonal dispersions in momentum space are given by $\varepsilon_\alpha(k) = \varepsilon_\alpha - 2t_\alpha \cos k$ and $t_{sd}(k) = -2t_{sd} \cos k$, respectively. We assume $\varepsilon_s < \varepsilon_d$, indicating that the valence (conduction) band includes large component of s ($d_{x^2-y^2}$) orbital. We can obtain the diagonalized energy dispersions with the unitary transformation connecting between the band μ and orbital α , $\gamma_{k\mu\sigma} = \sum_\alpha \zeta_{\mu\alpha}(k, \sigma) c_{k\alpha\sigma}$. In the Hamiltonian (7.24), the energy dispersion of the valence band $E_v(k)$ and conduction band $E_c(k)$ are given by

$$E_{v(c)}(k) = \eta(k) - (+) \sqrt{\xi^2(k) + t_{sd}^2(k)} \quad (7.25)$$

with $2\eta(k) = \varepsilon_d(k) + \varepsilon_s(k)$, $2\xi(k) = \varepsilon_d(k) - \varepsilon_s(k)$. Here, the unitary transformation connecting between the band μ ($=v, c$) and orbital α ($=s, d$) is given by

$$\begin{pmatrix} \gamma_{kv\sigma} \\ \gamma_{kc\sigma} \end{pmatrix} = \begin{pmatrix} \sqrt{1 - \nu^2(k)} & -\nu(k) \\ \nu(k) & \sqrt{1 - \nu^2(k)} \end{pmatrix} \begin{pmatrix} c_{ks\sigma} \\ c_{kd\sigma} \end{pmatrix}, \quad (7.26)$$

where the off-diagonal term of the unitary transformation $\nu(k)$ is given by

$$\nu^2(k) = \frac{1}{2} \left(1 - \frac{\xi(k)}{\sqrt{\xi^2(k) + t_{sd}^2(k)}} \right). \quad (7.27)$$

We assume $\varepsilon_s < \varepsilon_d$ and the valence (conduction) band is mainly composed of the s ($d_{x^2-y^2}$) orbital. However, due to t_{sd} , the conduction (valence) band includes the component of the s ($d_{x^2-y^2}$) orbital. $\nu(k)$ indicates the weight of a component of the s ($d_{x^2-y^2}$) orbital in the conduction (valence) band. In

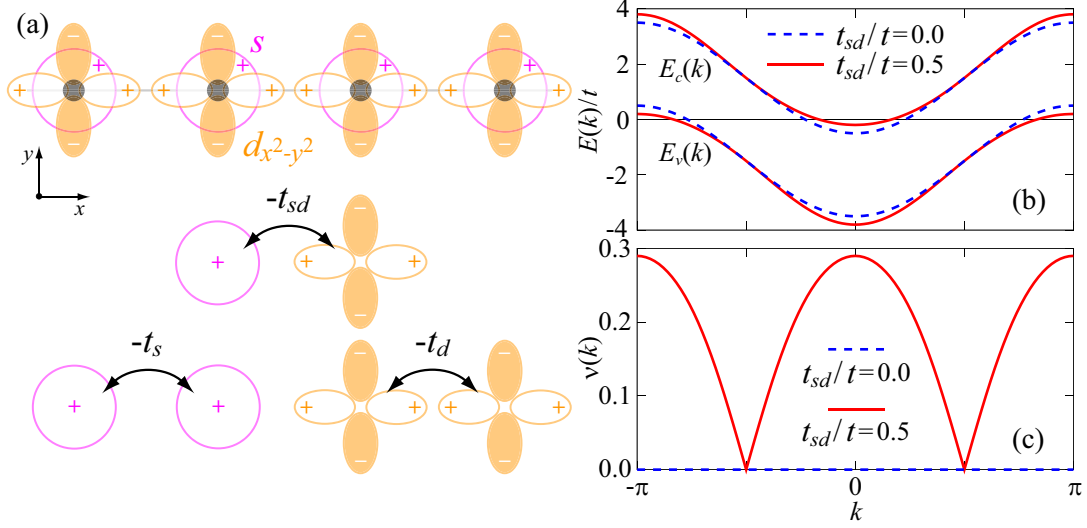


Figure 7.3: (a) Schematic picture of the example where the valence and conduction band are composed of the s and $d_{x^2-y^2}$ orbitals. The s and $d_{x^2-y^2}$ orbitals between the neighboring sites have the hopping integral t_{sd} . (b) Energy band dispersions and (c) the off-diagonal term of the coefficient in the unitary transformation $\nu(k)$ at $t_{sd}/t = 0.0$ (dashed line) and 0.5 (solid line), where we use $t_s = t_d = t$ and $(\varepsilon_d - \varepsilon_s)/t = 3$.

Figs. 7.3(b) and 7.3(c), we show the band dispersion and $\nu(k)$ with the hopping t_{sd} , where we assume $t_s = t_d = t$ and $(\varepsilon_d - \varepsilon_s)/t = 3$. We find that, even when t_{sd} is finite, the valence band top and conduction band bottom are located at $k = \pm\pi$ and $k = 0$, respectively, and thus the band structure has excitonic instability with $Q = \pi$. At $t_{sd} = 0$, where $\nu(k) = 0$, the valence (conduction) band is solely composed of the component of the s ($d_{x^2-y^2}$) orbital. When t_{sd} becomes finite, $\nu(k)$ has the large values around $k = 0, \pm\pi$, but $\nu(k) = 0$ at $k = \pm\pi/2$, due to $t_{sd}(k) = -2t_{sd} \cos k$. Due to $\nu(k)$, the component of the s ($d_{x^2-y^2}$) orbital around the conduction band bottom at $k = 0$ (valence band top at $k = \pm\pi$) is enhanced with increasing t_{sd} . Therefore, both the valence band around $k = \pm\pi$ and conduction band around $k = 0$ include the component of the same orbital at $t_{sd} > 0$ and the intraorbital Coulomb interaction may become effective as an interband Coulomb interaction.

To investigate the magnetization in this band dispersion, we apply the Hartree-Fock mean-field approximation for the two-band Hubbard model, which are given by the intraorbital Coulomb (\mathcal{H}_{e-e}^U), interorbital Coulomb ($\mathcal{H}_{e-e}^{U'}$), interorbital exchange (\mathcal{H}_{e-e}^J), and pair-hopping ($\mathcal{H}_{e-e}^{J'}$) interactions defined in Eqs. (5.3)-(5.6). Here, we evaluate the spin-triplet orbital diagonal and off-diagonal states given by $m_\alpha^z = \sum_{i,\sigma} \sigma \langle c_{i\alpha\sigma}^\dagger c_{i\alpha\sigma} \rangle e^{iQR_i} / 2N = \sum_{k,\sigma} \sigma \langle c_{k+Q\alpha\sigma}^\dagger c_{k\alpha\sigma} \rangle / 2N$ and $\Phi_t^z = \sum_{i,\sigma} \sigma \langle c_{id\sigma}^\dagger c_{is\sigma} \rangle e^{iQR_i} / 2N = \sum_{k,\sigma} \sigma \langle c_{k+Qd\sigma}^\dagger c_{ks\sigma} \rangle / 2N$, respectively. To solve the self-consistent problem, we use the antiferromagnetic Brillouin zone and expand the 2×2 Hamiltonian in Eq. (7.24) into 4×4 matrix. In Fig. 7.4(a), we show the calculated Φ_t^z and m_α^z as a function of t_{sd} , where we use $t_s = t_d = t$, $(\varepsilon_d - \varepsilon_s)/t = 3$, $U_s/t = U_d/t = 2$, $U'/t = 1$, $J/t = J'/t = 0.5$. At $t_{sd} = 0$, we obtain the solution with $\Phi_t^z > 0$ and $m_\alpha^z = 0$, which is consistent with the previous results in Chap. 5. However, we find that m_α becomes finite at $t_{sd} \neq 0$ and Φ_t^z and m_α^z are enhanced with increasing t_{sd} , where we obtain the solution with $m_s^z = m_d^z$ due to $U_s/t_s = U_d/t_d$, and Φ_t^z and m_α^z have the opposite sign. Therefore, when both the valence and conduction bands include the component of the same orbital due to t_{sd} , the net magnetization (magnetic dipole moment) in each unit cell, $M_0^z = 2m_s^z + 2m_d^z$, becomes finite, which is consistent with the conventional SDW states.

Using the solution $m_\alpha^z \neq 0$ and $\Phi_t^z \neq 0$, the local spin density in the i -th unit cell is given by

$$s_i^z(\mathbf{r}) = [\phi_s^2(\mathbf{r})m_s^z + \phi_d^2(\mathbf{r})m_d^z + 2\phi_s(\mathbf{r})\phi_d(\mathbf{r})\Phi_t^z] \cos Q \cdot R_i. \quad (7.28)$$

In Figs. 7.4(b)-7.4(d), we illustrate the local spin density distribution given by Eq (7.28)⁴. When $m_\alpha^z = 0$ at $t_{sd} = 0$ [see Fig. 7.4(b)], the formalism of the spin density in Eq. (7.28) corresponds to the formalism

⁴In the same way as in Figs. 7.1(c)-7.1(f), we broaden the radial distribution function of the $1s$ orbital in order to exaggerate the electronic structure, and thus Figs. 7.4(b)-7.4(d) are schematic pictures.

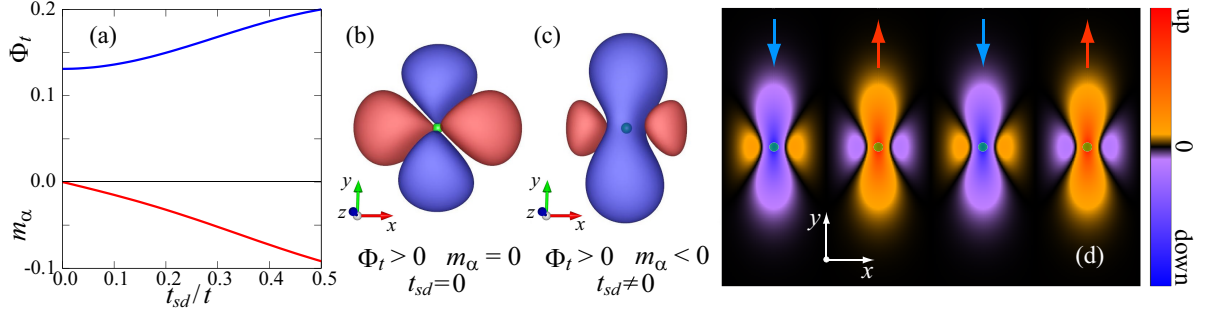


Figure 7.4: (a) The spin-triplet orbital diagonal and off-diagonal order parameters as a function of t_{sd} calculated by the Hartree-Fock mean-field approximation for the two-band Hubbard model. Here, we use $t_s = t_d = t$, $(\varepsilon_d - \varepsilon_s)/t = 3$, $U_s/t = U_d/t = 2$, $U'/t = 1$, $J/t = J'/t = 0.5$. Due to $U_s/t_s = U_d/t_d$, we find $m_\alpha = m_s = m_d$. Isosurface of the spin density in the unit cell at $R_i = 0$ when (b) $\Phi_t > 0$ and $m_\alpha = 0$ at $t_{sd} = 0$ and (c) $\Phi_t > 0$ and $m_\alpha < 0$ at $t_{sd} \neq 0$. Red and blue indicates positive and negative parts of the spin density, respectively. (d) Illustrated is the spin density distribution with $\Phi_t > 0$ and $m_\alpha < 0$ at $t_{sd} \neq 0$.

of the examples in the previous subsections. In this case, using the s -orbital and $d_{x^2-y^2}$ -orbital, the magnetic octupole moment is finite but the magnetic dipole moment is absent. However, when m_α^z becomes finite at $t_{sd} \neq 0$, the spin density is affected by $\phi_\alpha^2(\mathbf{r})m_\alpha^z$ as in Eq. (7.28). In Fig. 7.4(c), the negative part is enhanced along y -axis and the positive part is reduced at $\pm x$. The negative part is larger than the positive part in the unit cell, and thus the net magnetization appears in total. In this state, the magnetic dipole and octupole moments are finite in each unit cell. Corresponding to $Q = \pi$, the spin polarization inverts alternately over the unit cells and the magnetization oscillates with twice period [see Fig. 7.4(d)]. In contrast to the conventional SDW state in the single-orbital Hubbard system, in which all part of the spin density in a unit cell is polarized along the same direction, we find that some part of the spin density is polarized along the opposite direction to the direction of the total magnetization in a unit cell due to finite multipole moments in the excitonic SDW state in the multi-orbital system.

In this subsection, using the simple example, we show that the net magnetization (magnetic dipole moment) in each unit cell, $\mathbf{M}_0 = 2 \sum_\alpha \mathbf{m}_\alpha$, becomes finite when both the valence and conduction bands include the component of the same orbital due to the hybridization of different orbitals via the hopping between the neighboring sites. This is consistent with the SDW state discussed in Cr and iron-based superconductors. In contrast to the conventional SDW state in the single-orbital system, the complicated density wave states with the higher rank multipole moments can be realized in the local spin density $\mathbf{s}_i(\mathbf{r})$, which cannot be seen in \mathbf{m}_α . In this subsection, we have considered the one-dimensional system as an example for simplicity, but, in higher dimensions, we should be more careful with the spatial distributions of the wave functions of orbitals and hoppings between neighboring sites.

7.3 Multi-Orbitals in Different Ions

In the previous section, we have discussed the excitonic phases, in which the valence and conduction bands are composed of orbitals in a single ion. In this section, we consider the case where the valence and conduction bands are composed of orbitals in *different* ions. We note for example that the valence and conduction bands in the candidate materials of excitonic insulators, TiSe_2 and Ta_2NiSe_5 , are composed of orbitals in different ions [38,142,143]. In this chapter, we therefore discuss the electronic distributions in the excitonic phases, in which the valence and conduction bands are composed of orbitals in different ions.

When there are several ions in a unit cell, we have to consider the position of the α -orbital \mathbf{r}_α . Therefore, the field operator is given by

$$\Psi_\sigma(\mathbf{r}) = \sum_i \sum_\alpha \phi_\alpha(\mathbf{r} - \mathbf{r}_\alpha - \mathbf{R}_i) c_{i\alpha\sigma}. \quad (7.29)$$

Using the field operator in Eq. (7.29), we can evaluate the charge and spin densities of excitonic state from Eqs. (7.2) and (7.3).

In this section, we assume that the valence and conduction bands are composed of two orbitals located in different ions for simplicity. Using the orbitals of the valence (a) and conduction (b) bands, the field operator in the i -th unit cell is given as

$$\Psi_{i\sigma}(\mathbf{r}) = \phi_a(\mathbf{r} - \mathbf{r}_a)c_{ia\sigma} + \phi_b(\mathbf{r} - \mathbf{r}_b)c_{ib\sigma}, \quad (7.30)$$

where we write $\phi_\alpha(\mathbf{r} - \mathbf{r}_\alpha - \mathbf{R}_i) = \phi_\alpha(\mathbf{r} - \mathbf{r}_\alpha)$ for simplicity. Using the field operator in Eq. (7.30), the density of electrons of spin σ is given by

$$\begin{aligned} \rho_{i\sigma}(\mathbf{r}) = \langle \Psi_{i\sigma}^\dagger(\mathbf{r})\Psi_{i\sigma}(\mathbf{r}) \rangle = & \phi_a^2(\mathbf{r} - \mathbf{r}_a)\langle c_{ia\sigma}^\dagger c_{ia\sigma} \rangle + \phi_b^2(\mathbf{r} - \mathbf{r}_b)\langle c_{ib\sigma}^\dagger c_{ib\sigma} \rangle \\ & + \phi_a(\mathbf{r} - \mathbf{r}_a)\phi_b(\mathbf{r} - \mathbf{r}_b) \left[\langle c_{ib\sigma}^\dagger c_{ia\sigma} \rangle + \langle c_{ia\sigma}^\dagger c_{ib\sigma} \rangle \right], \end{aligned} \quad (7.31)$$

where the charge density is given by $\rho_i(\mathbf{r}) = \rho_{i\uparrow}(\mathbf{r}) + \rho_{i\downarrow}(\mathbf{r})$ and the spin density of the z -direction is given by $2s_i^z(\mathbf{r}) = \rho_{i\uparrow}(\mathbf{r}) - \rho_{i\downarrow}(\mathbf{r})$.

When $\langle c_{ib\sigma}^\dagger c_{ia\sigma} \rangle$ is modulated due to excitonic phase transition, the change in the density distribution of electrons is given by the third term in Eq. (7.31). Here, $\phi_a(\mathbf{r} - \mathbf{r}_a)\phi_b(\mathbf{r} - \mathbf{r}_b)\langle c_{ib\sigma}^\dagger c_{ia\sigma} \rangle$ indicates the density of electrons between the ions. When the excitonic density wave is given as $\langle c_{ib\sigma}^\dagger c_{ia\sigma} \rangle = \langle c_{ia\sigma}^\dagger c_{ib\sigma} \rangle = A_\sigma \cos \mathbf{Q} \cdot \mathbf{R}_i + C_\sigma$, the density of electrons between the ions is enhanced (making a bonding orbital) at some site and is reduced (making an antibonding orbital) at the neighboring sites. Therefore, when the excitonic phase is stabilized, in which the valence and conduction bands are composed of orbitals in different ions, the strength of the electronic bonding between the ions are modulated and the bond density wave is realized. Note that the third term in Eq. (7.31) includes the product of the wave functions of a and b orbitals $\phi_a(\mathbf{r} - \mathbf{r}_a)\phi_b(\mathbf{r} - \mathbf{r}_b)$, and thus the electron distribution depends on the sign of the wave functions. If $\langle c_{ib\sigma}^\dagger c_{ia\sigma} \rangle$ is enhanced due to excitonic ordering, the ions make the bonding (anti-bonding) orbital at the positive (negative) part of the product of the wave functions $\phi_a(\mathbf{r} - \mathbf{r}_a)\phi_b(\mathbf{r} - \mathbf{r}_b)$.

In contrast to the excitonic phases formed from the orbitals in a single ion, the interorbital exchange interaction that arranges the spins ferromagnetically like Hund's rule coupling is weak between orbitals in different ions, and thus the spin-triplet exciton condensation state is difficult to be stabilized [14, 15, 129, 135]. Moreover, when the density of electrons between ions is enhanced due to excitonic ordering, the enhancement of the charge density tends to shorten the distance between the ions. Therefore, in this case, the electrons couple with the lattice degrees of freedom and the spin-singlet excitonic condensation state is most likely to be stabilized with the lattice distortion [135].

In Fig. 7.5, we show an example of the excitonic phase, where the valence and conduction bands are composed of the s and p_z orbitals in different ions. Here, we assume that the ions locate along z -direction in a unit cell [see Fig. 7.5(a)]. We show the charge density of the normal state and excitonic CDW state with $Q = \pi$ in Fig. 7.5(b) and 7.5(c), respectively. In the normal state, the charge density is uniform [see Fig. 7.5(b)]. In the excitonic CDW state, the charge density is enhanced and the ions make an electronic bonding at the part with $\phi_a(\mathbf{r} - \mathbf{r}_a)\phi_b(\mathbf{r} - \mathbf{r}_b)\langle c_{ib\sigma}^\dagger c_{ia\sigma} \rangle > 0$, but the ions make an antibonding at the neighboring sites. Corresponding to the charge density, the electrons couple with

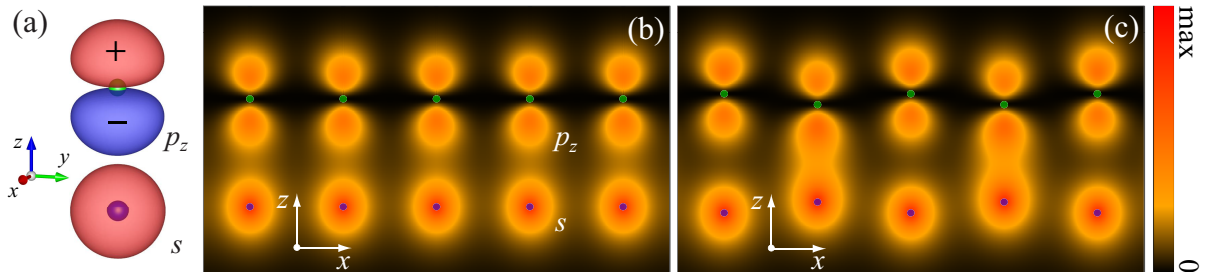


Figure 7.5: Illustrated excitonic phase where the valence and conduction bands are composed of the s and p_z orbitals in different ions. (a) The position of the wave function of the s and p_z orbitals in a unit cell. Red and blue indicates positive and negative parts of the wave function, respectively. Illustrated are the charge density of (b) the normal state and (c) excitonic CDW state with $Q = \pi$. In (c), we assume the lattice distortion with $Q = \pi$ as well.

the lattice degrees of freedom and the lattice distortion is usually induced like in Fig. 7.5(c). Therefore, when the valence and conduction bands are composed of orbitals in different ions, the bonding and antibonding orbitals alternate over the unit cells and the bond charge-density-wave state is realized [see Fig. 7.5(c)] when the excitonic ordering occurs.

7.4 Summary

In this Chapter, we have evaluated the charge and spin densities in the excitonic CDW and SDW state from the local wave functions in the tight-binding approximation. First, we have discussed the charge and spin densities of excitonic phases when the valence and conduction bands are composed of orthogonal orbitals in a single ion. We have shown that the charge or spin density distributes anisotropically in each unit cell and higher rank electric or magnetic multipole moment becomes finite, depending on the wave functions of the valence and conduction bands. In this case, the excitonic density-wave state is consistent with the multipole density-wave state. In contrast to the conventional CDW and SDW state, the modulation of the total charge (electric monopole moment) and net magnetization (magnetic dipole moment) in the unit cell does not appear when the orthogonal two orbitals are hybridized via a spin-singlet or spin-triplet excitonic condensation. However, in the real materials, the energy bands are constructed by the hybridization of many orbitals in a single ion. In this case, we have shown that, if both the conduction and valence bands include the component of the same orbitals, the modulation of the net magnetization in each unit cell appears like a conventional SDW (antiferromagnetic) state. Finally, we have discussed the density of electrons in the excitonic phases when the valence and conduction bands are composed of orbitals in different ions. In this case, we have shown that the exciton condensation enhances the electronic density between ions and the excitonic density-wave state corresponds to the bond density-wave state.

Chapter 8

Theory of Ta_2NiSe_5 as an Excitonic Insulator

8.1 Introduction

Recently, a transition-metal chalcogenide Ta_2NiSe_5 has been studied experimentally as a candidate for an excitonic insulator (EI) [36,37]. This material has a layered structure stacked loosely by a weak van der Waals interaction, and in each layer, Ni single chains and Ta double chains are running along the a -axis of the lattice to form a quasi-one-dimensional (1D) chain structure [144]. The observed resistivity shows a semiconducting behavior over a wide temperature range with a quasi-1D anisotropic electron conduction at high temperatures [145]. Then, an anomaly in the resistivity appears at 328K, which is associated with a second-order-like structural phase transition from orthorhombic to monoclinic phase [145]. The magnetic susceptibility exhibits diamagnetism in a wide temperature range (4.2 – 900 K) and shows a sudden drop (being more negative) below the structural transition temperature (328 K) [145]. The system was thus suggested to be a small band-gap semiconductor with oxidation states of Ni^{0+} ($3d^{10}$) and Ta^{5+} ($5d^0$), rather than a magnetic or Mott insulator [145,146]. However, a recent X-ray photoemission spectroscopy (XPS) experiment, together with a cluster-model calculation, showed that Ni ions have a $3d^9\bar{L}$ character (\bar{L} is a Se $4p$ hole) and consequently Ta ions have a $5d^1$ character [36]. Moreover, the angle-resolved photoemission spectroscopy (ARPES) experiment [36,37] showed that the spectra are strongly temperature dependent; i.e., at 40 K the flatness of the top of the valence band is extremely enhanced and the size of the band gap becomes wider. It was thereby suggested that the EI state is realized as the ground state of this material, where the spin-singlet excitons between the Ni $3d$ -Se $4p$ holes and Ta $5d$ electrons are presumed [36].

In this Chapter, we introduce a theory to elucidate the origin of the structural phase transition and associated anomalous electronic properties of Ta_2NiSe_5 ¹. First, we carry out the density-functional-theory (DFT) based electronic structure calculations for the orthorhombic phase of Ta_2NiSe_5 . Based on the DFT calculation, we construct an effective three-chain Hubbard model to reproduce the three bands near the Fermi level with the phonon degrees of freedom. We analyze this model by the mean-field approximation and calculate its phase diagrams to clarify the origin of the structural phase transition. We show that the interband Coulomb interaction and electron-lattice coupling cooperatively induce an excitonic and structural phase transition in Ta_2NiSe_5 . To reproduce the flattening of the valence band top in the ARPES results, we also calculate the single-particle excitation spectra. We also carry out the calculations of thermodynamic quantities, such as heat capacity and elastic constant, and show that a jump is observed in the specific heat at the phase transition and that the elastic softening relating to the structural phase transition is observed in the elastic shear constant. Finally, we calculate the temperature dependence of the ultrasonic attenuation and nuclear-magnetic-resonance (NMR) spin-lattice relaxation rates and demonstrate that the coherence peak appears in the ultrasonic attenuation rate, while there occurs a rapid decrease in the NMR relaxation rate.

¹Chap. 8 is based on T. Kaneko, T. Toriyama, T. Konishi, and Y. Ohta, *Phys. Rev. B* **87**, 035121 (2013) and K. Sugimoto, T. Kaneko, and Y. Ohta, *Phys. Rev. B* **93**, 041105(R) (2016).

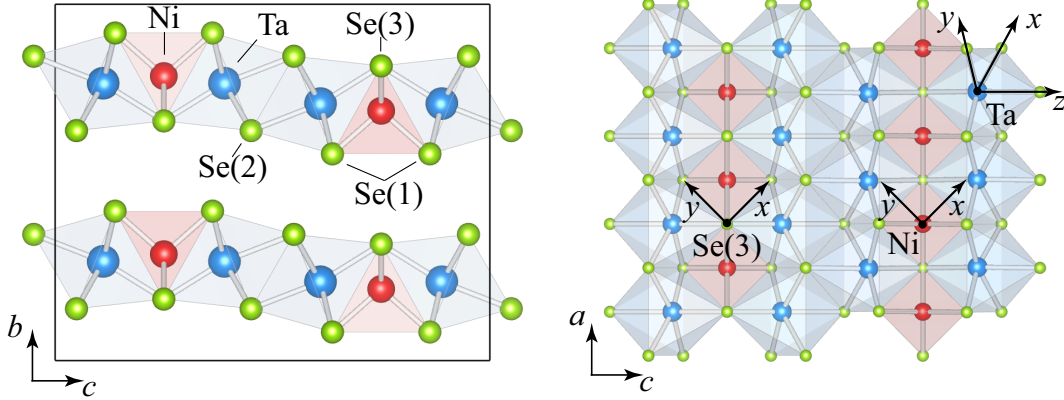


Figure 8.1: Crystal structure of Ta_2NiSe_5 [144]. Blue, red, and green spheres indicate Ta, Ni, and Se ions, respectively. All the Ta ions and Ni ions are crystallographically equivalent but there are three inequivalent Se ions, Se(1), Se(2), and Se(3). In the right panel, we define the local coordinate axes x , y , z for the orbitals on Ta, Ni, and Se(3) ions.

atom	x	y	z
Ta	-0.007931	0.221349	0.110442
Ni	0	0.701132	1/4
Se(1)	0.505303	0.080385	0.137979
Se(2)	-0.005133	0.145648	0.950866
Se(3)	0	0.327141	1/4

atom	x	y	z
Ta	0	0.222447	0.108098
Ni	0	0.702224	1/4
Se(1)	1/2	0.079970	0.139183
Se(2)	0	0.142111	0.951164
Se(3)	0	0.328012	1/4

Table 8.1: Left panel: experimental atomic coordinates of the monoclinic phase of Ta_2NiSe_5 given in Ref. [144]. Right panel: optimized atomic coordinates of the orthorhombic phase of Ta_2NiSe_5 . Definition of the coordinates (x, y, z) is given in Ref. [144].

8.2 Electronic Structure of Ta_2NiSe_5

In this section, we carry out the band structure calculations employing the WIEN2k code [147] based on the full-potential linearized augmented-plane-wave method, where we use the generalized gradient approximation for electron correlations with the exchange-correlation potential of Ref. [148].

8.2.1 Crystal Structure of Ta_2NiSe_5

We show the crystal structure of Ta_2NiSe_5 in Fig. 8.1. The primitive unit cell contains four Ta ions, two Ni ion, and ten Se ions. All the Ta ions and Ni ions are crystallographically equivalent but there are three inequivalent Se ions, Se(1), Se(2), and Se(3). This material has a layered structure stacked loosely by a weak van der Waals interaction. In each layer, Ni single chains and Ta double chains are running along the a -axis and aligned alternately along the c -axis of the crystal structure. Se ions are coordinated around the Ta ions octahedrally and around the Ni ions tetrahedrally. In the right panel of Fig. 8.1, we define the local coordinate axes x , y , z for the orbitals on Ta, Ni, and Se(3) ions. In Fig. 8.2, we show schematic pictures of the local orbitals on Ta and Ni ions, and we use these definition in this Chapter.

Because the crystal structure of the high-temperature orthorhombic phase of Ta_2NiSe_5 is not known, we make the structural optimization to determine the internal coordinates of the ions in the orthorhombic phase. Assuming the orthorhombic structure (space group $Cmcm$) and keeping the experimental lattice constants of the monoclinic phase ($a = 3.496$, $b = 12.829$, and $c = 15.641$ in units of \AA), we optimize the internal coordinates of all the ions. In the self-consistent calculations, we use 9 k -points in the irreducible part of the Brillouin zone, assuming the muffin-tin radii (R_{MT}) of 2.41, 2.21, and 1.96 Bohr for Ta, Ni, and Se ions, respectively, and the plane-wave cutoff of $K_{\text{max}} = 7.0/R_{\text{MT}}$. The determined atomic coordinates are listed in Table 8.1.

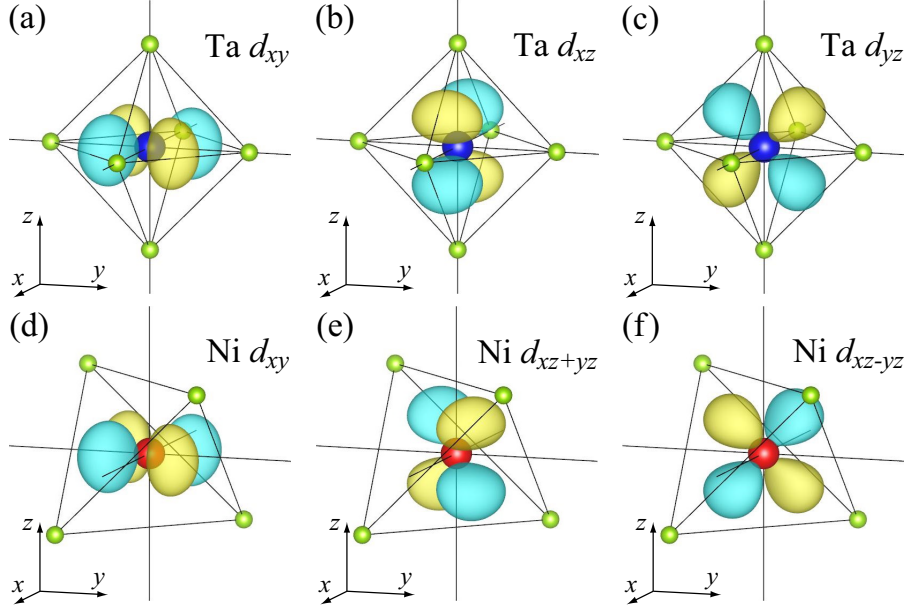


Figure 8.2: Schematic pictures of the local orbitals on (a)-(c) Ta and (d)-(f) Ni ions in Ta_2NiSe_5 . Blue, red, and green spheres indicate Ta, Ni, and Se ions, respectively. The local coordinate axes x , y , z on Ta and Ni ions are defined in Fig. 8.1.

8.2.2 Underestimation of the Band Gap

The band structure for the orthorhombic phase of Ta_2NiSe_5 is calculated for this optimized crystal structure, where we use 468 k -points in the irreducible part of the Brillouin zone in the self-consistent calculations, assuming the muffin-tin radii of 2.50, 2.33, and 2.06 Bohr for Ta, Ni, and Se ions, respectively, and the plane-wave cutoff of $K_{\max} = 7.0/R_{MT}$. The results for the band dispersion and density of states (DOS) are shown in Figs. 8.3(a) and 8.3(b), respectively. We find that the results predict a metallic state, which is in contrast to the experimental data that the electric resistivity shows a clear insulating behavior and the ARPES observes a well-defined band gap even above the structural transition temperature. It is well-known that the DFT-based band calculations often cause this problem, where the band gap in semiconductors is underestimated. In the present case, a small band overlap appears between the bottom of the conduction bands coming from the $5d$ orbitals of Ta and top of the conduction bands coming from the $3d$ orbitals of Ni hybridized with the $4p$ orbitals of Se.

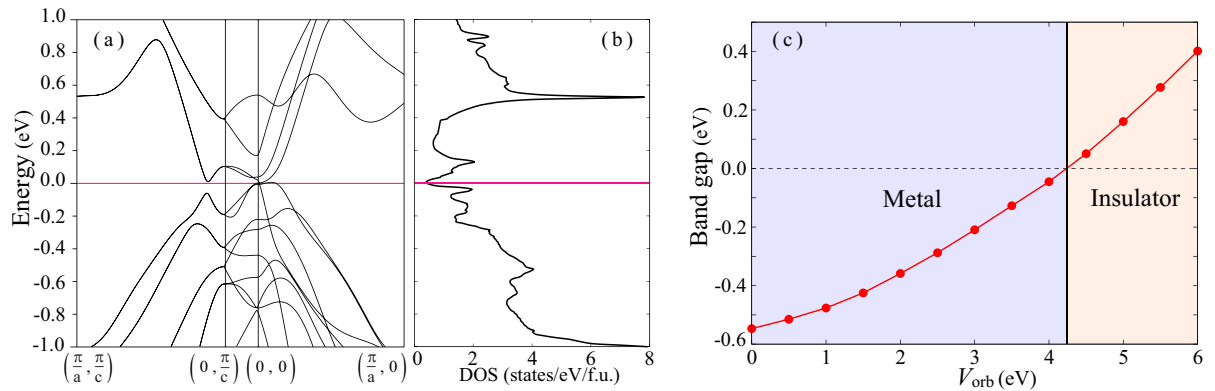


Figure 8.3: (a) Calculated band dispersions of the orthorhombic phase of Ta_2NiSe_5 , where we assume $k_y = 0$. (b) DOS of the orthorhombic phase of Ta_2NiSe_5 . In (c), we show the calculated band gap as a function of the potential V_{orb} , where the band gap is defined as the energy of the bottom of the conduction band measured from the energy of the top of the valence band [38].

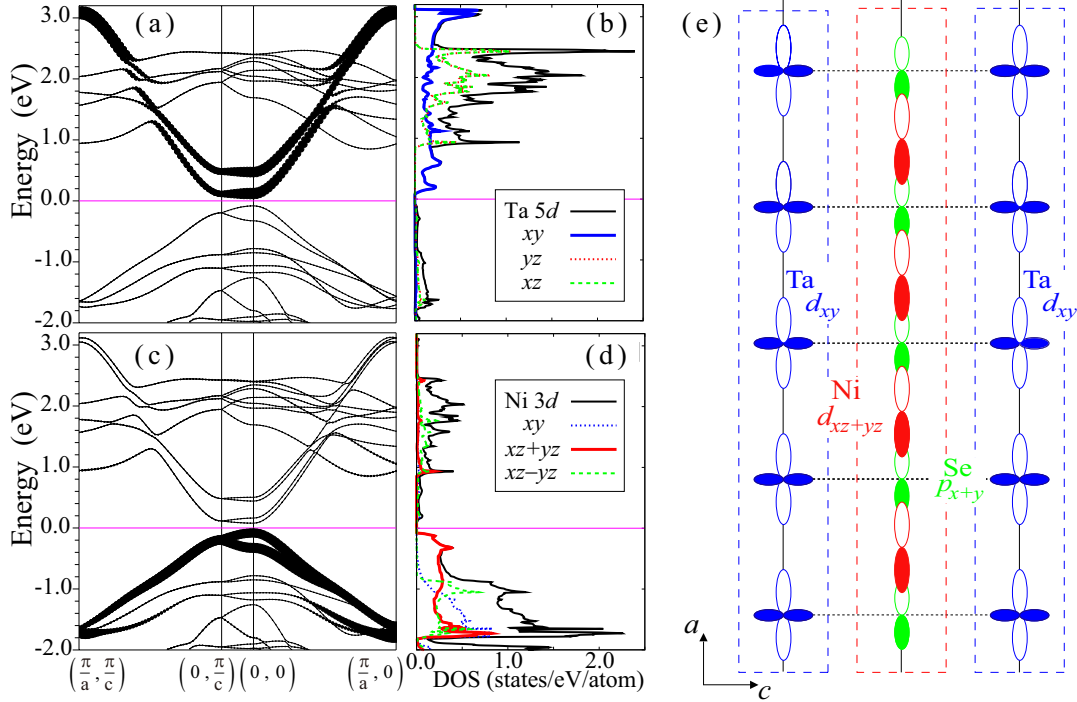


Figure 8.4: Calculated band dispersion and PDOS of the orthorhombic phase of Ta₂NiSe₅. (a) The weighted band dispersions, where the width of the curves is in proportion to the weight of the Ta 5d_{xy} orbital, and (c) that of the Ni 3d_{xz+yz} orbital, (b) PDOS for the Ta 5d *t*_{2g} orbitals and (d) PDOS for the Ni 3d *t*₂ orbitals [38]. (e) Schematic picture of the orbitals for the electronic structure near the Fermi level. Here, the local orbitals defined in Fig. 8.2 is used.

In order to solve this problem, we introduce a standard procedure [149], where the conduction (valence) bands are shifted upward (downward) by adding (subtracting) an orbital-dependent potential V_{orb} into the Hamiltonian so as to open the gap in the band dispersions. Here, we add the potentials V_{orb} to the energy of the 5d orbitals of Ta and $-V_{\text{orb}}$ to the energy of the 3d orbitals of Ni and 4p orbitals of Se. The band gap thus calculated is shown in Fig. 8.3(c) as a function of V_{orb} , where we find that the band gap actually opens for $V_{\text{orb}} \gtrsim 4.2$ eV. Note that the bands do not shift rigidly by V_{orb} due to the hybridization between the 5d orbitals of Ta and the 3d and 4p orbitals of Ni and Se, just as it has been pointed out in Ref. [149] for a variety of materials. A similar situation has also been noticed in Ref. [150] for a transition-metal oxide TiO₂.

8.2.3 Effective Electronic Structure for Exciton Formation

The results for the partial densities of states (PDOS) and band dispersions obtained are shown in Fig. 8.4. Here, we use the value $V_{\text{orb}} = 5$ eV, so that we have the band gap of 0.2 eV and band structure where the top of the valence band and bottom of the conduction band are both located at the Γ point of the Brillouin zone with the direct band gap, which is in good agreement with the experiment [36, 145]. In Fig. 8.4(b), we show the calculated PDOS for the Ta *t*_{2g} orbitals. We find that the Ta 5d_{xy} component has the largest weight and is approximately equal to the PDOS of the total Ta 5d orbitals near the Fermi level, indicating that the conduction band bottom is only composed of the Ta 5d_{xy} band. In Fig. 8.4(d), we show the calculated PDOS for the Ni *t*₂ orbitals. We find that the Ni 3d_{xz+yz} component has the largest weight near the Fermi level and the valence band top is only composed of the 3d_{xz+yz} orbital. We also find that the Se 4p_{x+y} component has the largest weight in the valence band top although not shown here.

In Figs. 8.4(a) and 8.4(c), we show the band dispersions with the weight of the Ta 5d_{xy} and Ni 3d_{xz+yz} orbitals, respectively. We find that the band structure near the Fermi level is rather simple; the conduction band has a cosine-like quasi-1D band dispersion coming from the 5d_{xy} orbitals of Ta ions arranged along the chain, whereas the top of the valence band has a quasi-1D dispersion coming from

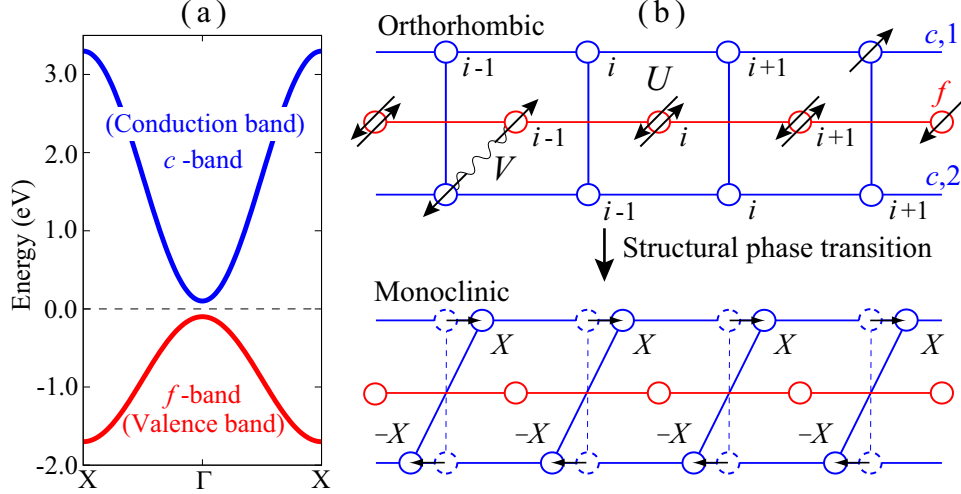


Figure 8.5: (a) Noninteracting band dispersion of our model Eq. (8.1). The conduction band is doubly degenerate. The Fermi level is indicated by a horizontal line. (b) Schematic representations of the three-chain Hubbard model for the 1D structural unit consisting of the two chains of the Ta $5d_{xy}$ orbitals yielding the c -bands and one chain of the Ni $3d_{xz+yz}$ and Se $4p_{x+y}$ orbitals of Ta₂NiSe₅ yielding the f -band. The lattice distortion of the chain corresponding to the orthorhombic-to-monoclinic phase transition is schematically illustrated [38].

the Ni $3d_{xz+yz}$ (and Se $4p_{x+y}$) orbitals arranged along the chain, and no hybridization occurs between the top of the valence band and bottom of the conduction band. We show the schematic picture of the relevant orbitals near the Fermi level in Fig. 8.4(e).

8.3 Model Study of Ta₂NiSe₅

8.3.1 Model Hamiltonian

Based on the results, we make the effective three-chain model containing the nondegenerate valence f -band coming from the hybridized Ni $3d_{xz+yz}$ and Se $4p_{x+y}$ orbitals and the doubly degenerate conduction c -bands coming from the Ta $5d_{xy}$ orbitals, to which the Hubbard-type onsite and interchain repulsive interactions are added (see Fig. 8.5). We also introduce the electron-lattice coupling assuming a uniform shear distortion of the chain (see Fig. 8.5) corresponding to the structural transition from the orthorhombic to monoclinic phase [151]. The Hamiltonian of our model is written as

$$\mathcal{H} = \mathcal{H}_0 + \mathcal{H}_{e-e} + \mathcal{H}_{\text{lat}}, \quad (8.1)$$

where \mathcal{H}_0 is a noninteracting band dispersion term, \mathcal{H}_{e-e} is an electron-electron interaction term, and \mathcal{H}_{lat} is a lattice-distortion term relating to the structural phase transition in Ta₂NiSe₅.

The noninteracting band dispersion term is written as

$$\mathcal{H}_0 = \sum_{k,\alpha,\sigma} \varepsilon_c(k) c_{k,\alpha,\sigma}^\dagger c_{k,\alpha,\sigma} + \sum_{k,\sigma} \varepsilon_f(k) f_{k,\sigma}^\dagger f_{k,\sigma}, \quad (8.2)$$

where $c_{k,\alpha,\sigma}^\dagger$ and $f_{k,\sigma}^\dagger$ are the Fourier transforms of $c_{i,\alpha,\sigma}^\dagger$ that creates an electron with spin σ ($=\uparrow, \downarrow$) at site i on the c -orbital of the chain α ($= 1, 2$) and $f_{i,\sigma}^\dagger$ that creates an electron at site i of the f -orbital, respectively. The noninteracting band dispersions are given as $\varepsilon_c(k) = 2t_c(\cos k - 1) + D/2 - \mu$ and $\varepsilon_f(k) = 2t_f(\cos k - 1) - D/2 - \mu$ with the hopping parameters t_c and t_f and the band gap D .

The electron-electron interaction term is given as

$$\begin{aligned} \mathcal{H}_{e-e} = & U_c \sum_{i,\alpha} n_{i,\alpha,\uparrow}^c n_{i,\alpha,\downarrow}^c + U_f \sum_i n_{i,\uparrow}^f n_{i,\downarrow}^f \\ & + V \sum_{i,\alpha,\sigma,\sigma'} n_{i,\alpha,\sigma}^c n_{i,\sigma'}^f + V \sum_{i,\sigma,\sigma'} (n_{i+1,1,\sigma}^c + n_{i-1,2,\sigma}^c) n_{i,\sigma'}^f, \end{aligned} \quad (8.3)$$

where $n_{i,\alpha,\sigma}^c$ and $n_{i,\sigma}^f$ are the electron number operators on the c - and f -orbitals, respectively. U_c and U_f are the on-site Coulomb interaction of the c and f band electrons. V is the intersite interaction between f and c electrons, which drives the excitonic instability in the system.

The lattice-distortion term consists of a term of harmonic oscillators for the Ta atoms and a hybridization term between conduction and valence band electrons caused by the lattice distortion, which is written as

$$\mathcal{H}_{\text{lat}} = \frac{K}{2} \sum_{i,\alpha} X_{i,\alpha}^2 - \sum_{i,\alpha,\sigma} \gamma_\alpha X_{i,\alpha} \left(c_{i,\alpha,\sigma}^\dagger f_{i,\sigma} + f_{i,\sigma}^\dagger c_{i,\alpha,\sigma} \right), \quad (8.4)$$

where $X_{i,\alpha}$ is the displacement of a Ta atom at site i in the α -th chain measured from its equilibrium position, and K is a spring constant of the harmonic oscillators. γ_α is the strength of hybridization between f and c electrons caused by the lattice distortion.

We use the values $t_c = -0.8$, $t_f = 0.4$, and $D = 0.2$ in units of eV obtained from the fitting to the calculated band dispersions. We assume $U_c = U_f (= U)$ for simplicity and choose $V = U/4$ in order to minimize the Hartree shift in the mean-field approximation. We also assume $\gamma_1 = \gamma$ and $\gamma_2 = -\gamma$ and make use of the parameter $\lambda = \gamma^2/2K$ for the strength of the electron-lattice coupling in the following discussions. L is the number of the unit cells in the system, where the unit cell contains an f - and two c -orbitals. We restrict ourselves to the filling of two electrons per unit cell.

8.3.2 Mean-Field Approximation

To investigate the excitonic and structural phase transition of the model (8.1), we apply the mean-field approximation

$$n_{i,\uparrow} n_{i,\downarrow} \approx \langle n_{i,\uparrow} \rangle n_{i,\downarrow} + n_{i,\uparrow} \langle n_{i,\downarrow} \rangle, \quad (8.5)$$

for the onsite terms of both orbitals and

$$\begin{aligned} n_{i,\alpha,\sigma}^c n_{i,\sigma'}^f &\approx \langle n_{i,\alpha,\sigma}^c \rangle n_{i,\sigma'}^f + n_{i,\alpha,\sigma}^c \langle n_{i,\sigma'}^f \rangle - \langle n_{i,\alpha,\sigma}^c \rangle \langle n_{i,\sigma'}^f \rangle \\ &\quad - \langle f_{i,\sigma}^\dagger c_{i,\alpha,\sigma} \rangle c_{i,\alpha,\sigma}^\dagger f_{i,\sigma} - f_{i,\sigma}^\dagger c_{i,\alpha,\sigma} \langle c_{i,\alpha,\sigma}^\dagger f_{i,\sigma} \rangle + \langle f_{i,\sigma}^\dagger c_{i,\alpha,\sigma} \rangle \langle c_{i,\alpha,\sigma}^\dagger f_{i,\sigma} \rangle, \end{aligned} \quad (8.6)$$

for the formation of spin-singlet excitons. Assuming the uniform electron distribution, the numbers of electrons per c and f site may be written, respectively, as

$$\langle n_{i,\alpha,\sigma}^c \rangle = n, \quad \langle n_{i,\sigma}^f \rangle = 1 - 2n. \quad (8.7)$$

The excitonic order parameters (or excitonic gap functions) may be defined by

$$\begin{aligned} \Delta_{1,1} &= V \langle c_{i,1,\sigma}^\dagger f_{i,\sigma} \rangle, & \Delta_{1,2} &= V \langle c_{i+1,1,\sigma}^\dagger f_{i,\sigma} \rangle, \\ \Delta_{2,1} &= V \langle c_{i,2,\sigma}^\dagger f_{i,\sigma} \rangle, & \Delta_{2,2} &= V \langle c_{i-1,2,\sigma}^\dagger f_{i,\sigma} \rangle, \end{aligned} \quad (8.8)$$

and the order parameter of the uniform lattice distortion may be defined by

$$\delta_\alpha = \gamma_\alpha X_{i,\alpha}. \quad (8.9)$$

Using the approximations, we obtain the mean-field Hamiltonian

$$\mathcal{H}^{\text{MF}} = \sum_{k,\sigma} \begin{pmatrix} c_{k,1,\sigma}^\dagger & c_{k,2,\sigma}^\dagger & f_{k,\sigma}^\dagger \end{pmatrix} \begin{pmatrix} \tilde{\varepsilon}_c(k) & 0 & -\tilde{\Delta}_1^*(k) \\ 0 & \tilde{\varepsilon}_c(k) & -\tilde{\Delta}_2^*(k) \\ -\tilde{\Delta}_1(k) & -\tilde{\Delta}_2(k) & \tilde{\varepsilon}_f(k) \end{pmatrix} \begin{pmatrix} c_{k,1,\sigma} \\ c_{k,2,\sigma} \\ f_{k,\sigma} \end{pmatrix} + L\varepsilon_0, \quad (8.10)$$

with

$$\tilde{\varepsilon}_c(k) = 2t_c(\cos k - 1) + \frac{1}{2}(D - 4nV) - \mu_0, \quad \tilde{\varepsilon}_f(k) = 2t_f(\cos k - 1) - \frac{1}{2}(D - 4nV) - \mu_0, \quad (8.11)$$

where we define μ_0 as $\mu = \mu_0 + 4V(1 - n/2)$,

$$\tilde{\Delta}_1(k) = \Delta_{1,1} + \Delta_{1,2}e^{ik} + \delta_1, \quad \tilde{\Delta}_2(k) = \Delta_{2,1} + \Delta_{2,2}e^{-ik} + \delta_2, \quad (8.12)$$

and

$$\varepsilon_0 = -4V(1 - 2n^2) + \frac{2}{V} \sum_{\alpha,\beta} |\Delta_{\alpha,\beta}|^2 + \frac{1}{4\lambda} \sum_{\alpha} \delta_{\alpha}^2. \quad (8.13)$$

Diagonalizing the mean-field Hamiltonian given in Eq. (8.10), we obtain

$$\mathcal{H}^{\text{MF}} = \sum_{k,\sigma} \sum_{\epsilon=c,\pm} E_{k,\epsilon} \gamma_{k,\epsilon,\sigma}^{\dagger} \gamma_{k,\epsilon,\sigma} + L\varepsilon_0, \quad (8.14)$$

where

$$E_{k,c} = \tilde{\varepsilon}_c(k), \quad E_{k,\pm} = \eta_k \pm E_k \quad (8.15)$$

with

$$\eta_k = \frac{\tilde{\varepsilon}_c(k) + \tilde{\varepsilon}_f(k)}{2}, \quad \xi_k = \frac{\tilde{\varepsilon}_c(k) - \tilde{\varepsilon}_f(k)}{2}, \quad E_k = \sqrt{\xi_k^2 + |\tilde{\Delta}_1(k)|^2 + |\tilde{\Delta}_2(k)|^2}. \quad (8.16)$$

$\gamma_{k,\epsilon,\sigma}$ ($\gamma_{k,\epsilon,\sigma}^{\dagger}$) is the annihilation (creation) operator of the quasiparticle. The quasiparticle operators satisfy the relation $c_{k,\mu,\sigma} = \sum_{\epsilon} \psi_{k,\sigma;\mu,\epsilon} \gamma_{k,\epsilon,\sigma}$, where $\psi_{k,\sigma;\mu,\epsilon}$ is the Bogoliubov transformation coefficient and $f_{k,\sigma} = c_{k,3,\sigma}$. The coefficients $\psi_{k,\sigma;\mu,\epsilon}$ are determined as

$$\begin{pmatrix} c_{k,1,\sigma} \\ c_{k,2,\sigma} \\ f_{k,\sigma} \end{pmatrix} = \begin{pmatrix} \frac{|\tilde{\Delta}_2|}{|\tilde{\Delta}_1|} w_{k,1}^* & -u_k w_{k,1}^* & v_k w_{k,1}^* \\ -\frac{|\tilde{\Delta}_1|}{|\tilde{\Delta}_2|} w_{k,2}^* & -u_k w_{k,2}^* & v_k w_{k,2}^* \\ 0 & v_k & u_k \end{pmatrix} \begin{pmatrix} \gamma_{k,c,\sigma} \\ \gamma_{k,+,\sigma} \\ \gamma_{k,-,\sigma} \end{pmatrix} \quad (8.17)$$

with

$$u_k = \sqrt{\frac{1}{2} \left(1 + \frac{\xi_k}{E_k} \right)}, \quad v_k = \sqrt{\frac{1}{2} \left(1 - \frac{\xi_k}{E_k} \right)}, \quad w_{k,\alpha} = \frac{\tilde{\Delta}_{\alpha}(k)}{\sqrt{|\tilde{\Delta}_1(k)|^2 + |\tilde{\Delta}_2(k)|^2}}. \quad (8.18)$$

The self-consistent equations for n , $\Delta_{\alpha,\beta}$, and δ_{α} are determined to minimize the free energy²

$$F = -k_{\text{B}}T \sum_{k,\epsilon,\sigma} \ln(1 + e^{-\beta E_{k,\epsilon}}) + L\varepsilon_0. \quad (8.19)$$

Writing the parameter as x , the minimization satisfies the equation $\partial F/\partial x = 0$. This equation reads

$$\sum_{k,\epsilon,\sigma} \frac{\partial E_{k,\epsilon}}{\partial x} f(E_{k,\epsilon}) + L \frac{\partial \varepsilon_0}{\partial x} = 0, \quad (8.20)$$

where $f(E) = 1/(e^{\beta E} + 1)$ is the Fermi distribution function. For the number of conduction electrons n , we obtain

$$n = \frac{1}{2L} \sum_k \{f(E_{k,c}) + u_k^2 f(E_{k,+}) + v_k^2 f(E_{k,-})\}. \quad (8.21)$$

For the excitonic order parameters $\Delta_{\alpha,1}$ and $\Delta_{\alpha,2}$, we obtain

$$\Delta_{\alpha,1} = -\frac{V}{2L} \sum_k \frac{\tilde{\Delta}_{\alpha}(k)}{E_k} (f(E_{k,+}) - f(E_{k,-})), \quad (8.22)$$

$$\Delta_{\alpha,2} = -\frac{V}{2L} \sum_k e^{\mp ik} \frac{\tilde{\Delta}_{\alpha}(k)}{E_k} (f(E_{k,+}) - f(E_{k,-})), \quad (8.23)$$

²The free energy is given as

$$F = \langle \mathcal{H}^{\text{MF}} \rangle - TS = \sum_{k,\sigma,\epsilon} E_{k,\epsilon} f(E_{k,\epsilon}) + L\varepsilon_0 + \frac{1}{\beta} \sum_{k,\sigma,\epsilon} \{(1 - f(E_{k,\epsilon})) \ln(1 - f(E_{k,\epsilon})) + f(E_{k,\epsilon}) \ln f(E_{k,\epsilon})\}$$

and for the displacement δ_α we have

$$\delta_\alpha = -\frac{4\lambda}{L} \sum_k \frac{\text{Re}[\tilde{\Delta}_\alpha(k)]}{E_k} (f(E_{k,+}) - f(E_{k,-})). \quad (8.24)$$

We solve these equations self-consistently to obtain the order parameters. Corresponding to the lattice distortion with $\delta_1 = \delta_2$, we find the solution with $\Delta_{1,1} = \Delta_{2,1}$ and $\Delta_{1,2} = \Delta_{2,2}$. Note that the definition of the excitonic gap functions is slightly generalized from the previous study [38] but the calculated results do not change significantly.

8.3.3 Excitonic and Structural Phase Transition

The calculated results for the ground-state and finite-temperature phase diagrams are shown in Fig. 8.6. Note that, in this calculation, we assume $\Delta_{1,1} = \Delta_{2,1} = \Delta_{1,2} = \Delta_{2,2} = \Delta$ and $\delta_1 = \delta_2 = \delta$ for simplicity [38]. As for the ground state, we clearly see in Figs. 8.6(a)-8.6(c) that when V and λ are small the system is the band insulator (BI) with $\Delta = \delta = 0$ but when V and λ are large the EI state $\Delta > 0$ with the shear distortion of the chain $\delta > 0$ appears in the ground state. The EI state occurs simultaneously and cooperatively with the lattice distortion except at the lines $\lambda = 0$ and $V = 0$. We emphasize here that even if λ is small the structural phase transition occurs with the help of the exciton condensation: i.e., the interaction V drives the EI-state formation $\Delta > 0$, which leads to the spontaneous c - f hybridization, and as a consequence, the structural distortion $\delta > 0$ occurs even if λ is small. The spontaneous c - f hybridization stabilizes the lattice distortion, leading to the orthorhombic-to-monoclinic phase transition. This is consistent with the situation in the real material Ta₂NiSe₅, where the monoclinic distortion of the angle $0.5^\circ - 1^\circ$ (or the atomic displacement $0.02 - 0.04 \text{ \AA}$) is very small [145]; a rough estimation may be $\delta \sim 0.02 - 0.04 \text{ eV}$, which corresponds to $\lambda \sim 0.02 - 0.05 \text{ eV}$ ³. The oxidation states of Ni²⁺ and Ta⁴⁺ observed in the XPS experiment [36] are also consistent with the nonzero value of n induced by the spontaneous c - f hybridization in the EI phase (see Fig. 8.6(c)).

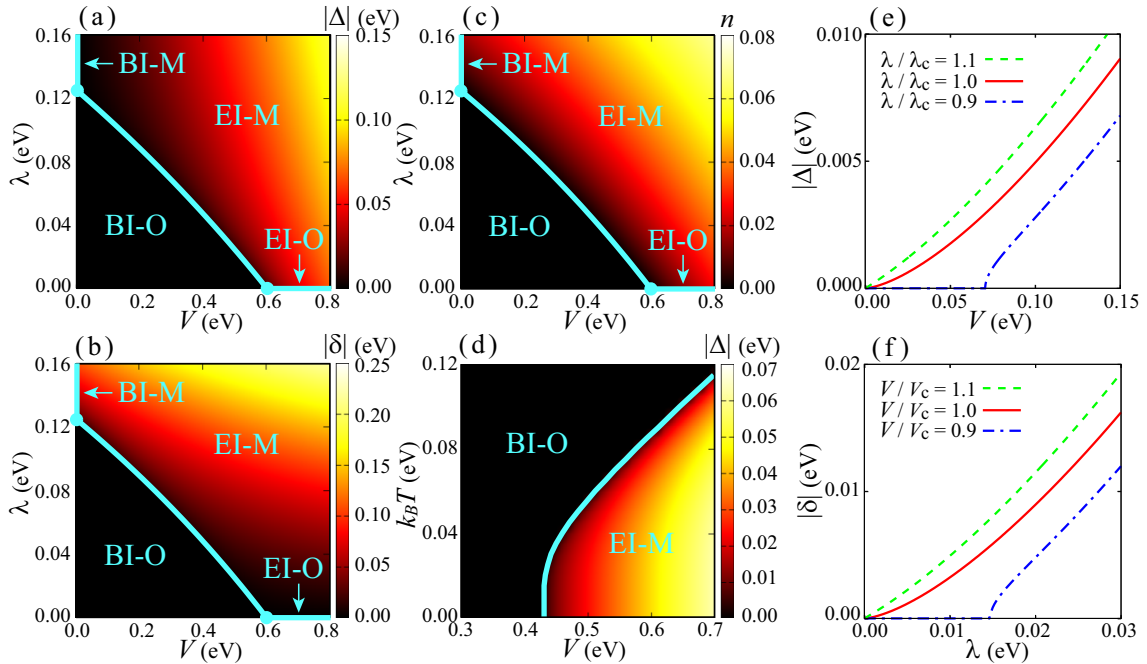


Figure 8.6: Ground-state phase diagram with the order parameters (a) Δ , (b) δ , and (c) n , in the parameter space (V, λ) . (d) Finite-temperature phase diagram with the order parameter Δ as a function of V at $\lambda = 0.04 \text{ eV}$. Also shown are (e) the V dependence of Δ and (f) λ dependence of δ at $T = 0 \text{ K}$ with $\lambda_c = 0.125 \text{ eV}$ and $V_c = 0.6 \text{ eV}$. Abbreviations are BI (band insulator), EI (excitonic insulator), O (orthorhombic), and M (monoclinic) [38].

³A rough estimation for Ta₂NiSe₅ may be $\gamma \sim 1 \text{ eV/\AA}$, $\delta = \gamma \langle X_{i,\alpha} \rangle \sim 0.02 - 0.04 \text{ eV}$, $K \sim 10 - 30 \text{ eV/\AA}^2$, and $\lambda = \gamma^2/2K \sim 0.02 - 0.05 \text{ eV}$.

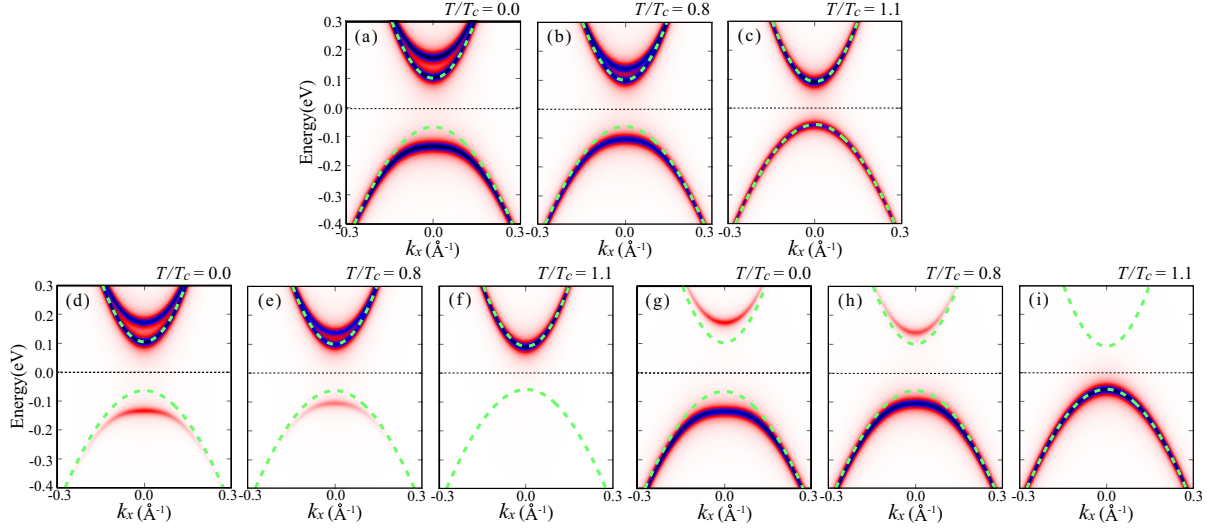


Figure 8.7: Calculated temperature dependence of the single-particle spectra of the three-chain Hubbard model. (a)-(c) Total spectral weight, (d)-(f) spectral weight on the c -orbital, and (g)-(i) spectral weight on the f -orbital. We assume $V = 0.55$ eV and $\lambda = 0.04$ eV. The calculated transition temperature is $k_{\text{B}}T_c = 0.0722$ eV. The Lorentzian broadening of the spectra of 0.01 eV is applied for comparison with the experimental ARPES spectra [36,37]. The band dispersion without condensation $\Delta = \delta = 0$ is given by the dashed curves. The Fermi level is indicated by the horizontal line [38].

The temperature dependence of the EI phase is given in Fig. 8.6(d), where we find that by lowering temperature the BI state with the undistorted (orthorhombic) structure changes into the EI state with the distorted (monoclinic) structure and the transition is of the second order. Thus, the experimental situations are correctly reproduced.

8.3.4 Single-particle Spectra

The single-particle spectra for the c - and f -electrons are calculated as

$$A^c(k, \omega) = \frac{1}{2}u_k^2\delta(\omega - E_{k,+}) + \frac{1}{2}v_k^2\delta(\omega - E_{k,-}) + \frac{1}{2}\delta(\omega - E_{k,c}), \quad (8.25)$$

$$A^f(k, \omega) = v_k^2\delta(\omega - E_{k,+}) + u_k^2\delta(\omega - E_{k,-}), \quad (8.26)$$

respectively, and the total single-particle spectrum is given as $A(k, \omega) = 2A^c(k, \omega) + A^f(k, \omega)$. The calculated temperature dependence of the single-particle spectra is shown in Fig. 8.7, where we find the large deformation of the top of the valence band occurs by the spontaneous c - f hybridization in the EI state formation by lowering temperature: the flattening of the band dispersion is evident and the shift of the top of the valence band away from the Fermi level is noticed, both of which are consistent with experimental ARPES results [36,37]. The hybridization can be seen in the c -orbital spectral weight below the Fermi level (see Figs. 8.7 (d) and 8.7 (e)) and f -orbital spectral weight above the Fermi level (see Figs. 8.7 (g) and 8.7 (h)). Splitting of the c -bands into two is also noticed, where the lower “nonbonding” band remains unaffected in the presence of Δ and δ .

Note that the c - f hybridization is absent above the transition temperature (T_c) in our mean-field calculations (see Figs. 8.7 (c), 8.7 (f), and 8.7(i)). However, the characteristic temperature scale associated with the formation of preformed excitons should be present [23]. In the experimental ARPES spectrum on Ta₂NiSe₅, the band dispersion approaches to the parabolic behavior with increasing temperature, but the flattening of the valence band top remains even above T_c [37,39]. Seki *et al.* showed that the ARPES results around T_c can be well reproduced by the finite temperature variational cluster approximation (VCA) calculations for an extended Falicov-Kimball model, which can take into account the quantum fluctuations beyond the mean-field approximation [39]. The VCA calculations show that the band flattening above T_c is derived from the strong excitonic fluctuation in the preformed exciton region [39].

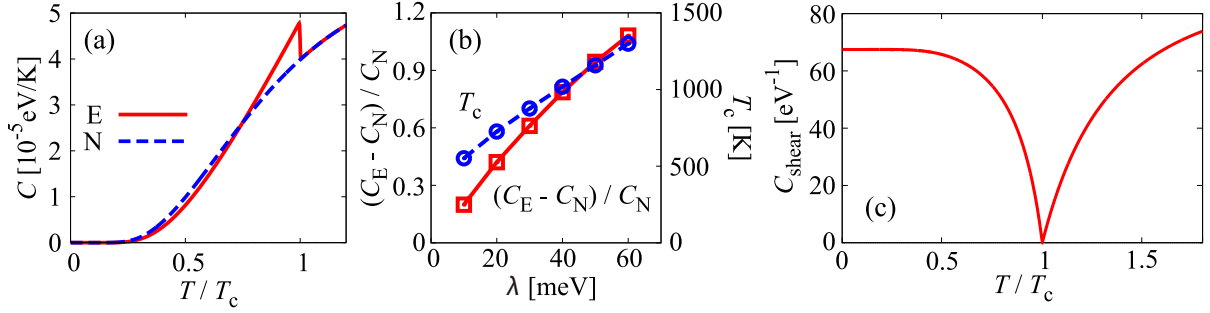


Figure 8.8: (a) Calculated temperature dependence of the heat capacity per unit cell, where the red solid line is for the excitonic phase and the blue dashed line is for the normal phase. (b) Calculated λ dependence of the jump in the heat capacity (red squares) and T_c (blue circles). (c) Calculated temperature dependence of the elastic shear constant per unit cell. We assume $V = 0.6$ eV and $\lambda = 0.01$ eV in (a) and (c) [40].

8.3.5 Heat Capacity

We also evaluate the heat capacity of the model, which may be calculated from the free energy in Eq. (8.19) as

$$C = -T \frac{\partial^2 F}{\partial T^2} = \sum_{k, \epsilon, \sigma} E_{k, \epsilon} \frac{\partial f(E_{k, \epsilon})}{\partial T}. \quad (8.27)$$

Note that, from here, we assume $\Delta_{1,1} \neq \Delta_{1,2}$ and $\Delta_{2,1} \neq \Delta_{2,2}$ in the mean-field calculation⁴ and we set $V = 0.6$ eV and $\lambda = 0.01$ eV unless otherwise stated [40]. The calculated result is shown in Fig. 8.8(a), where we find that the jump at T_c associated with the second-order phase transition is clearly visible, satisfying the entropy balance. The jump is given by $(C_E - C_N)/C_N \simeq 0.20$ for the parameter values appropriate for Ta₂NiSe₅, where C_E and C_N are the heat capacities in the excitonic and normal phases, respectively, at T_c . This value is much smaller than the value 1.43 (a universal constant) in the BCS superconductivity and depends strongly on the model parameters used; its λ dependence, e.g., is shown in Fig. 8.8(b). Such a difference in the magnitude of the jump comes mainly from the difference in the normal phase: It is a band insulator in the present excitonic condensation while it is a metal in superconductivity. We also note in Fig. 8.8(b) that the jump in the heat capacity and the value of T_c increase monotonically as λ increases, indicating that the larger values of the order parameters in the excitonic phase lead to the larger jump in the heat capacity. We point out that a recent specific heat measurement on Ta₂NiSe₅ [152] reveals a behavior consistent with our theoretical prediction. We note that the heat capacity coming from the lattice degrees of freedom should be taken into account when we compare our result with experimental data for Ta₂NiSe₅.

8.3.6 Elastic Constant

Next, we evaluate the elastic constant of the model, which may also be calculated from the mean-field free energy in Eq. (8.19) as

$$C_{\text{shear}} = \frac{\partial^2 F}{\partial \delta^2}, \quad (8.28)$$

where we assume the lattice distortion of the transverse acoustic phonon mode in the long wavelength limit, corresponding to the observed structural phase transition [see Fig. 8.9(d)]. The calculated result is shown in Fig. 8.8(c), where we actually find the elastic softening ($C_{\text{shear}} = 0$) at T_c , leading to the structural phase transition. We observe a Curie-Weiss-like behavior $1/C_{\text{shear}} = 1/C_{\text{shear}}^\infty + A/(T - T_c)$ at $T > T_c$ with $1/C_{\text{shear}}^\infty = 0.094$ eV and $A = 0.546$ eV·K. A recent experimental observation of the diffuse x-ray scattering [153] suggests the presence of the soft phonon mode, which is consistent with our theoretical prediction.

⁴Form here, the calculations were performed by Dr. K. Sugimoto [40].

8.3.7 Ultrasonic Attenuation Rate

Let us discuss the ultrasonic attenuation rate. Defining $A_{q,\alpha} = a_{q,\alpha} + a_{-q,\alpha}^\dagger$ using the phonon annihilation (creation) operator $a_{q,\alpha}$ ($a_{q,\alpha}^\dagger$) on the Ta chain α , we write the Matsubara phonon Green's function as

$$\mathcal{D}_\alpha(q, \tau) = -\langle T_\tau A_{q,\alpha}(\tau) A_{-q,\alpha}(0) \rangle, \quad (8.29)$$

where $A_{q,\alpha}(\tau) = e^{-\omega_q \tau} a_{q,\alpha} + e^{\omega_q \tau} a_{-q,\alpha}^\dagger$ is the Heisenberg representation of $A_{q,\alpha}$ at imaginary time τ and phonon wave number q with a phonon dispersion ω_q . Using the Fourier coefficient $\mathcal{D}_\alpha(q, i\omega_n) = \int_0^{\beta\hbar} d\tau \mathcal{D}_\alpha(q, \tau) e^{i\omega_n \tau}$, the phonon Dyson's equation is given as

$$\mathcal{D}_\alpha(q, i\omega_n) = \mathcal{D}_\alpha^{(0)}(q, i\omega_n) + \mathcal{D}_\alpha^{(0)}(q, i\omega_n) \Pi_\alpha(q, i\omega_n) \mathcal{D}_\alpha(q, i\omega_n), \quad (8.30)$$

where $\Pi_\alpha(q, i\omega_n)$ is the self-energy of the phonon Green's function. The ultrasonic attenuation rate is then given by the imaginary part of the retarded self-energy [154] as

$$\alpha_{q,\alpha} = \frac{1}{\tau_{q,\alpha}} = -2 \text{Im} \Pi_\alpha^R(q, \omega_q + i\eta), \quad (8.31)$$

where $\tau_{q,\alpha}$ is a relaxation time of the phonon and η is an infinitesimal value.

We consider the lattice oscillation corresponding to the distortion in the structural phase transition, i.e., an ultrasonic shear wave for the transverse acoustic mode that propagates along the direction perpendicular to the chains [see Fig. 8.9(d)]. The perturbation Hamiltonian of the phonons coupled with electrons is given by

$$\mathcal{H}' = \sum_{k,q,\sigma} \sum_{\alpha=1}^2 \left\{ M_{-q}^{cc} A_{-q,\alpha} c_{k_-, \alpha, \sigma}^\dagger c_{k_+, \alpha, \sigma} - M_{-q}^{cf} A_{-q,\alpha} \left(c_{k_-, \alpha, \sigma}^\dagger f_{k_+, \sigma} + f_{k_-, \alpha, \sigma}^\dagger c_{k_+, \sigma} \right) \right\}, \quad (8.32)$$

with $k_\pm = k \pm q/2$. The first term represents the coupling between the phonon and charge density of the conduction band electrons with a coupling constant M_{-q}^{cc} , and the second term represents the hybridization between the conduction and valence bands by the phonon with a coupling constant M_{-q}^{cf} . The coupling between the phonon and charge density of the valence band electrons is ignored as being irrelevant to the present instability mode. Eq. (8.32) then reads

$$\mathcal{H}' = \sum_{k,q,\sigma} \sum_{\alpha=1}^2 \sum_{\mu=1}^3 W_{\alpha,\mu}(-q) A_{-q,\alpha} \left(c_{k_-, \alpha, \sigma}^\dagger c_{k_+, \mu, \sigma} + c_{k_-, \mu, \sigma}^\dagger c_{k_+, \alpha, \sigma} \right), \quad (8.33)$$

where $W_{\alpha,\mu}(q) = (\delta_{\alpha,\mu} M_q^{cc}/2 - \delta_{\mu,3} M_q^{cf})$ and we have defined $c_{k,3,\sigma} = f_{k,\sigma}$.

We adopt the second-order perturbation theory for the phonon self-energy. Since the ultrasonic wave number q is small enough, we may assume $q \simeq 0$ in Eq. (8.31). We then obtain

$$\alpha_{q=0,\alpha} = 2\pi\omega_{\text{ph}} \sum_{k,\sigma} \sum_{\epsilon_1, \epsilon_2} \frac{\beta}{4 \cosh^2(\beta E_{k,\epsilon_1}/2)} \delta(E_{k,\epsilon_1} - E_{k,\epsilon_2}) \sum_{\mu,\nu} W_{\alpha,\mu} W_{\alpha,\nu} \times \left\{ 2\Psi_{\alpha,\alpha;\epsilon_1}(k, \sigma) \Psi_{\mu,\nu;\epsilon_2}(k, \sigma) + \Psi_{\nu,\alpha;\epsilon_1}(k, \sigma) \Psi_{\mu,\alpha;\epsilon_2}(k, \sigma) + \Psi_{\alpha,\mu;\epsilon_1}(k, \sigma) \Psi_{\alpha,\nu;\epsilon_2}(k, \sigma) \right\}, \quad (8.34)$$

where ω_{ph} is the ultrasonic frequency and $\Psi_{\mu,\nu;\epsilon}(k, \sigma) = \psi_{k,\sigma;\mu,\epsilon} \psi_{k,\sigma;\nu,\epsilon}^*$ with the Bogoliubov transformation coefficient $\psi_{k,\sigma;\mu,\epsilon}$.

The calculated results for the temperature dependence of the ultrasonic attenuation rate are shown in Figs. 8.9(a)-8.9(c). We find the following: in the normal state (obtained with vanishing order parameters), thermally excited electrons are scattered by phonons via the coupling with charge density of the conduction band electrons, resulting in the behavior $\alpha_{q=0,\alpha} \propto (M_0^{cc})^2$. The M_0^{cf} term does not contribute here. In the excitonic phase, a large coherence peak appears due to the phonon-induced c - f hybridization (M_0^{cf}), which is however overwhelmed by the charge-density term (M_0^{cc}) at $M_0^{cc} \gg M_0^{cf}$, where the increase in the band gap suppresses the thermal excitation of electrons, resulting in a rapid decrease in the rate $\alpha_{q=0,\alpha}$. However, in the ultrasonic attenuation experiment using the transverse sound mode, the coupling between the phonon and charge density of electrons does not contribute to the rate, and therefore we have the situation shown in Fig. 8.9(a). The experimental observation of the coherence peak in the ultrasonic attenuation rate should thus be realizable.

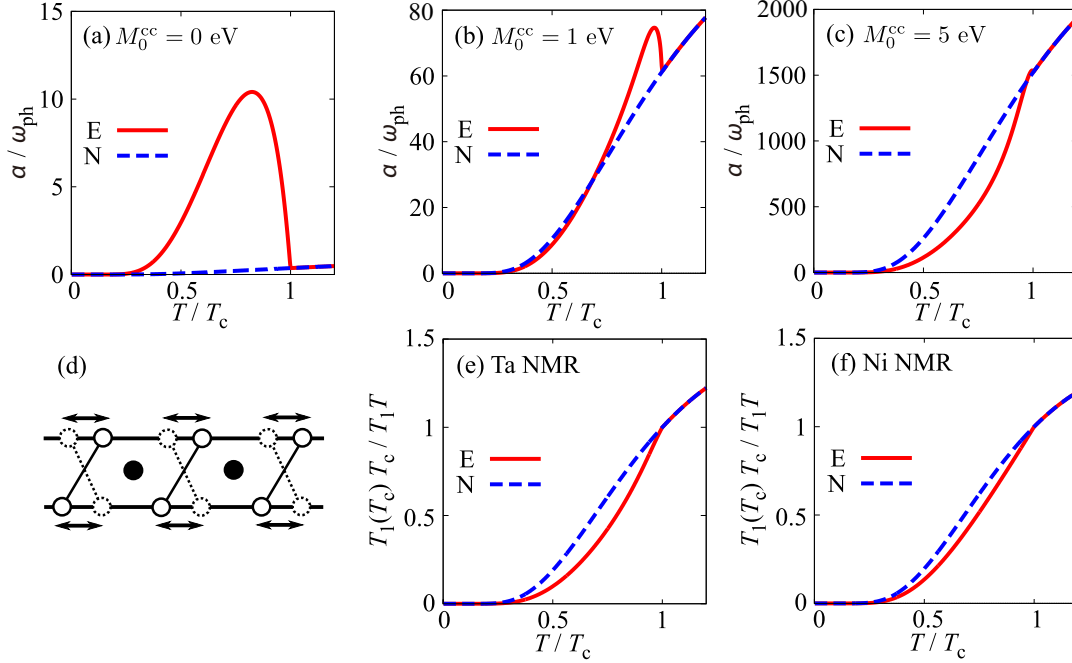


Figure 8.9: Calculated ultrasonic attenuation rate normalized by the ultrasonic frequency ω_{ph} . We assume $M_0^{\text{cf}} = 1$ eV with (a) $M_0^{cc} = 0$ eV, (b) $M_0^{cc} = 1$ eV, and (c) $M_0^{cc} = 5$ eV. (d) Schematic representation of the oscillation of the ultrasonic shear wave that propagates along the direction perpendicular to the chains. Also shown are the calculated NMR relaxation rates at (e) Ta and (f) Ni sites. The red solid line (E) is for the excitonic phase and the blue dashed line (N) is for the normal phase [40].

8.3.8 Nuclear Magnetic Relaxation Rate

Finally, let us discuss the NMR spin-lattice relaxation rate, which may be written [155] as

$$\frac{1}{T_{1,\mu}} \propto -\frac{k_B T}{\hbar \omega_\mu} \sum_q \text{Im} \chi_{+-,\mu}^{\text{R}}(q, \omega_\mu), \quad (8.35)$$

using the transverse dynamical spin susceptibility

$$\chi_{+-,\mu}^{\text{R}}(q, \omega_\mu) = -i \int_{-\infty}^{\infty} dt e^{i\omega_\mu t} \langle [S_{q,\mu}^+(t), S_{-q,\mu}^-(0)] \rangle \theta(t), \quad (8.36)$$

where we define $S_{q,\mu}^+ = \sum_k c_{k_-, \mu, \uparrow}^\dagger c_{k_+, \mu, \downarrow}$ and $S_{q,\mu}^- = \sum_k c_{k_-, \mu, \downarrow}^\dagger c_{k_+, \mu, \uparrow}$, and ω_μ is a resonant frequency of nuclear spins ($\mu = 1, 2$ for Ta and $\mu = 3$ for Ni). Using the mean-field approximation and assuming a small ω_μ value compared to typical energy scales of the system, we may rewrite Eq. (8.35) as

$$\frac{1}{T_{1,\mu}} \propto \pi \sum_{k,q} \sum_{\epsilon_1, \epsilon_2} \Psi_{\mu,\mu;\epsilon_1}(k_-, \uparrow) \Psi_{\mu,\mu;\epsilon_2}(k_+, \downarrow) \frac{1}{4 \cosh^2(\beta E_{k_-, \epsilon_1} / 2)} \delta(E_{k_-, \epsilon_1} - E_{k_+, \epsilon_2}). \quad (8.37)$$

The calculated results for the temperature dependence of the NMR relaxation rate are shown in Figs. 8.9(e) and 8.9(f) for Ta and Ni nuclear spins, respectively. We find that, in contrast to the typical *s*-wave superconducting phase [156], there appear no characteristic peaks in the rate of the excitonic phase but the rate simply drops just below T_c . Thus, the behavior of the NMR relaxation rate in the excitonic phase is similar to that of an ultrasonic attenuation rate in the *s*-wave superconducting phase. We point out that a recent NMR experiment on Ta₂NiSe₅ [157] suggests the behavior of the rate consistent with our theoretical prediction.

8.4 Summary

In summary, we have discussed the origin of the orthorhombic-to-monoclinic phase transition and associated anomalous electronic properties of Ta₂NiSe₅ of the layered chalcogenide Ta₂NiSe₅ using the

band structure calculation and mean-field analysis of the derived three-chain Hubbard model. From the band structure calculation, we have shown that the band structure near the Fermi level is simple; the conduction band has a cosine-like quasi-1D band dispersion coming from the $5d_{xy}$ orbitals of Ta ions arranged along the chain, whereas the top of the valence band has a quasi-1D dispersion coming from the Ni $3d_{xz+yz}$ and Se $4p_{x+y}$ orbitals arranged along the chain. Based on the band structure calculation, we have made the effective three-chain Hubbard model with electron-lattice coupling. We have shown that the BEC of excitonic electron-hole pairs cooperatively induces the instability of the shear lattice distortion in the effective model, resulting in the structural phase transition of the system. We have also shown that the spontaneous c - f hybridization explains the valence states of Ta and Ni ions observed in the XPS experiment and that the calculated single-particle spectra reproduce the flattening and shift of the band structure observed in the ARPES experiment. We have also demonstrated that the heat capacity exhibits a relatively small jump at T_c and the elastic shear constant indicates a softening when the temperature approaches T_c , both of which are consistent with recent experimental observations for Ta₂NiSe₅ [152, 153]. Finally, we have calculated the temperature dependence of the ultrasonic attenuation and NMR relaxation rates and have shown that the coherence peak can appear in the ultrasonic attenuation rate just below T_c . In the NMR relaxation rate, on the other hand, no characteristic peak appears in $1/T_1$ but it simply drops just below T_c , in agreement with recent NMR data for Ta₂NiSe₅ [157]. We therefore hope that our theoretical predictions made here will encourage further experimental studies to provide proof that the excitonic condensation actually occurs in Ta₂NiSe₅.

Chapter 9

Summary

In this thesis, we have presented our theoretical studies of excitonic phases in strongly correlated electron systems. In particular, we have focused on the stability of the excitonic phases as well as on the crossover phenomena between the weak-coupling BCS and strong coupling BEC states in the strongly correlated lattice models. We have also applied the theory of excitonic insulators to the candidate material Ta_2NiSe_5 that has attracted much attention in recent years.

In Chap. 2, we have reviewed the basic theory of excitonic phases. We have discussed the nature of excitonic phases using the simplest spinless model, where we have shown that a lot of similarities with the BCS theory of superconductivity exist in, e.g., the order parameter, gap equation, and its solutions. In contrast to superconductivity, however, we have discussed that the off-diagonal long-range order is absent in the excitonic insulator states, indicating the difficulty in realizing superfluidity in real materials of excitonic insulators. After that, we have described the excitonic phases with spin degrees of freedom. We have introduced two types of the excitonic phases that can be realized when the order parameter has the spin degrees of freedom; i.e., the excitonic charge density wave (CDW) and spin density wave (SDW) states, which are the diagonal long-range orders.

In Chap. 3, we have discussed the numerical methods used in this thesis. First, we have introduced the exact-diagonalization (ED) technique based on the Lanczos algorithm, which can solve the many-body problems in finite-size systems exactly. Next, we have introduced the variational cluster approximation (VCA) based on the self-energy functional theory (SFT), where we can take into account the effects of short-range spatial correlations even in low-dimensional systems in the thermodynamic limit and can discuss the spontaneous symmetry breakings of correlated electron systems beyond the mean-field theory. We have also introduced the cluster perturbation theory (CPT), which is useful for evaluating the single-particle excitation spectrum and their integrated values such as the density of states and momentum distribution function.

In Chap. 4, we have investigated the exciton condensation state in the extended Falicov-Kimball model (EFKM) and have discussed the nature of the BCS-BEC crossover of the condensate. In Sec. 4.2, we have investigated the formation and condensation of excitons in the double-layer EFKM on the square lattice using the ED technique. We have analyzed the nature of the excitonic condensate on the basis of the interband interaction dependence of the anomalous excitation spectrum, condensation amplitude, coherence length, exciton binding energy, and order parameter. We have also investigated the effect of the mass asymmetry of electrons and holes, thereby finding that a mass asymmetry between electrons and holes suppresses the condensation of excitons. In Sec. 4.3, we have examined the one-dimensional EFKM using the density matrix renormalization group (DMRG) technique and have shown that the excitonic insulator state is critical in contrast to that of the higher dimensional systems. We have determined the phase boundary between the band insulator, excitonic insulator, and staggered orbital order, and have presented the complete ground-state phase diagram with high accuracy. Using the anomalous spectral functions, we have also shown that the different nature of the electron-hole pairing and condensation processes occurs in the weak and strong coupling regions.

In Chap. 5, we have studied the stability of the excitonic phases with the spin degrees of freedom in the two-band Hubbard model (TBHM), where we have taken into account the interband Coulomb interaction U' , interband exchange interaction J , pair-hopping interaction J' , as well as the intraband repulsion U . We have rewritten the interband interactions of the Hamiltonian in terms of the creation and annihilation operators of the spin-singlet and spin-triplet excitons and have examined the roles of these interactions, whereby we have shown that the U' term drives the formation of excitons in both

the spin-singlet and spin-triplet channels, and that the J term stabilizes (destabilizes) the formation of the spin-triplet (spin-singlet) exciton. Using the VCA to calculate the grand potential of the system in the thermodynamic limit, we have moreover shown that the exchange interaction always stabilizes the excitonic SDW state and destabilizes the excitonic CDW state, of which the tendencies are enhanced by the pair hopping term. A variety of physical quantities have also been calculated, which include the single-particle spectral function, density of states, anomalous Green's functions, condensation amplitude, and pair coherence length.

In Chap. 6, we have studied the stability of the excitonic states in the TBHM taking into account the electron-phonon coupling, where the static mean-field theory is employed for treating the lattice degrees of freedom and the VCA for the electron-electron correlations. We have shown that both the interband Coulomb interaction U' and the electron-phonon coupling λ tend to stabilize an excitonic CDW state. The CDW typifies predominantly excitonic and phononic states for small and large ratios λ/U' , respectively. Incorporating the interband exchange interactions, we have shown that a spin-triplet excitonic state competes with the spin-singlet excitonic state, and have determined the ground-state phase diagram, where the electron-phonon coupling and interband exchange interactions tend to establish the excitonic CDW and SDW phases, respectively. We have also shown that, while the excitonic insulator state exhibits a gapless acoustic phase mode in the absence of the electron-phonon and pair-hopping couplings, the presence of these couplings fixes the phase of the order parameter and therefore eliminates such a gapless excitation that is related to supertransport properties of the system.

In Chap. 7, we have evaluated the charge and spin densities in the excitonic CDW and SDW states from the local wave functions in the tight-binding approximation. We have shown that, when the valence and conduction bands are composed of different orthogonal orbitals in a single ion, the charge and spin densities of the excitonic phases distribute anisotropically in each unit cell and higher rank electric or magnetic multipole moments become finite, depending on the shapes of the wave functions of the valence and conduction bands. In this case, the excitonic density-wave state is consistent with the multipole density-wave state. In contrast to the conventional CDW and SDW states, the modulation of the total charge or net magnetization in the unit cells does not appear even when the orthogonal two orbitals are hybridized as a result of the excitonic long-range order. However, in the real materials, the energy bands are reconstructed by the hybridization of many orbitals; in such cases, we have shown that the modulation of the net magnetization in each unit cell appears like a conventional SDW (antiferromagnetic) state if the conduction and valence bands include a large amount of the component of the same orbitals. We have also discussed the density of electrons in the excitonic phases when the valence and conduction bands are composed of orbitals located in different ions. In this case, we have shown that the exciton condensation enhances/suppresses the electronic density between the ions, indicating that the excitonic density-wave state corresponds to the bond density-wave state.

In Chap. 8, we have discussed the origin of the phase transition and associated anomalous electronic properties observed in the layered chalcogenide Ta_2NiSe_5 using the band structure calculation and mean-field analysis of the derived three-chain Hubbard model. From the band structure calculation, we have shown that the band structure near the Fermi level is rather simple; the conduction band has a cosine-like quasi-1D band dispersion coming from the orbitals of Ta ions arranged along the chain, whereas the top of the valence band has a quasi-1D dispersion coming from the Ni and Se orbitals arranged along the chain. Based on the results of the band structure calculation, we have constructed the effective three-chain Hubbard model with the electron-lattice coupling. We have shown that the interband Coulomb interaction and electron-lattice coupling cooperatively induce an excitonic and structural phase transition in Ta_2NiSe_5 . The calculated single-particle spectra reproduce the flattening and shift of the band structure observed in the angle-resolved photoemission spectroscopy experiment. We have also demonstrated that the heat capacity exhibits a relatively small jump at T_c and the elastic shear constant indicates a softening when the temperature approaches T_c . Finally, we have calculated the temperature dependence of the ultrasonic attenuation and nuclear-magnetic-resonance (NMR) relaxation rates. We have shown that the coherence peak can appear in the ultrasonic attenuation rate just below T_c , but in the NMR relaxation rate, no characteristic peak appears but the rate simply drops just below T_c .

Future Prospects

It is known that many experimental results so far obtained for the candidate materials of excitonic insulators TiSe_2 and Ta_2NiSe_5 can be explained within the theory of excitonic condensation. However, as we have shown in Chap. 6 and Chap. 8, the electron-phonon coupling may contribute to the formation of the low-temperature ordered phase in these materials, and if this coupling overwhelms the interband

Coulomb interactions in the formation of the order, the phase should not be called the excitonic phase. Therefore, first of all, we point out that it is necessary to quantify experimentally the contributions of the interband Coulomb interaction and electron-phonon coupling in the formation of the low-temperature ordered states of TiSe_2 and Ta_2NiSe_5 . Such experiments would provide us with a solid proof that these materials are indeed excitonic insulators.

Recently, superconductivity in TiSe_2 and Ta_2NiSe_5 has been discovered experimentally under pressure or by intercalation [158–160]. In these materials, the excitonic order expected at ambient pressure vanishes under high pressure (or intercalation) and the superconductivity appears around the point where the ordered state disappears. Therefore, the melting of the excitonic order may contribute to the emergence of the superconductivity; i.e., an exotic electron-electron pairing mediated by excitonic fluctuations may be expected. We point out that the mechanisms of superconductivity in these materials have not been elucidated, which we hope will be explored in near future.

A complicated magnetic multipole order due to excitonic condensation has been predicted theoretically at the spin-state transition in a cobalt oxide with a cubic perovskite structure. However, the electronic structure of this type of excitonic multipole orders has not been identified experimentally. Therefore, we need to study the response of the excitonic magnetic multipole orders to the external fields theoretically and to suggest the way to detect the excitonic order experimentally in such materials. Moreover, when the local wave functions of the valence and conduction bands have different parities (for example s - p , p - d , and d - f orbitals), the excitonic orders become magnetic quadrupole, hexadecapole, or tetrahexacontapole orders, which break the space-inversion and time-reversal symmetries in each unit cell, and thus magnetoelectric effects can be expected in this type of excitonic insulators. Therefore, the magnetic multipole orders caused by the excitonic condensation need to be studied further both experimentally and theoretically.

We can expect a variety of interesting phenomena in (and around) the excitonic phases. However, because the candidate materials of excitonic insulators are not many, one of the most important tasks may be to discover new candidate materials. To realize the excitonic phases, we have to make the band structure located in the vicinity of the semiconductor-semimetal transition. In TiSe_2 and Ta_2NiSe_5 , the valence and conduction bands are composed of the orbitals in different ions. To make materials similar to TiSe_2 and Ta_2NiSe_5 , we have to use ions whose highest occupied and lowest unoccupied energy levels are close to each other. The replacement of chalcogens in large band-gap semiconductors may be a way to realize the band structure around the semiconductor-semimetal transitions; TiO_2 , TiS_2 and Ta_2NiS_5 are large band-gap semiconductors, so that the exciton condensation does not occur here, but replacing the oxygen and sulfur with selenium, the higher energy level of p orbitals of selenium raises the energy of the valence bands, so that the band structures of TiSe_2 and Ta_2NiSe_5 become a small band-overlap semimetal and a small band-gap semiconductor, respectively. When the valence and conduction bands are composed of the orbitals in the same ion, electrons feel the strong interorbital Coulomb repulsion and interorbital exchange interaction such as the Hund's rule coupling, stabilizing a magnetic multipole order as a result of the condensation of atomic size, spin-triplet excitons, as in the cobalt oxide. In this case, the crystal field splitting of orbitals makes the band structure located in the vicinity of the semiconductor-semimetal transition. We have not considered the spin-orbit coupling in this thesis, but this coupling may be another way to split the energy levels of an ion and to realize a suitable band structure for the excitonic condensation state. In this respect, the extension of our theory including the spin-orbit coupling may be necessary in the future.

Appendix A

BCS-BEC Crossover in the Attractive Hubbard Model

A.1 Introduction

Crossover between the Bardeen-Cooper-Schrieffer (BCS) state and the Bose-Einstein condensed (BEC) state, i.e., the BCS-BEC crossover, is the major issues in the physics of exciton condensation or excitonic phase, as well as in the physics of superconductivity. The idea of a continuous crossover between the BCS and BEC limits first arose in the 1960s as a problem of exciton condensation near the semimetal-semiconductor transition [3, 5, 14]. The BCS-BEC crossover also attracted attention from the early stages of the theory of superconductivity, where Eagles first addressed this issue in metals with a very low electron density [161]. In 1980, using a variational approach, Leggett showed a smooth crossover from the weak-coupling BCS state to the strong-coupling BEC state at zero temperature [162]. The critical temperature T_c across the BCS-BEC crossover was first evaluated by Nozières and Schmitt-Rink [22]. In 1986, the discovery of high- T_c cuprate materials, where the coherence length is only a few times larger than the lattice spacing, led to intensive discussion on the possible realization of the BCS-BEC crossover in cuprate superconductors [163]. In systems of ultracold fermionic atoms, the crossover between the BCS-type and BEC-type superfluid states has also been observed [164–171], where the interaction strength is controlled through a magnetically tuned Feshbach resonance.

In this Appendix, we study the BCS-BEC crossover of the superconducting (superfluid) ground state in the attractive Hubbard model by means of the variational cluster approximation (VCA)¹ [77, 78, 80, 82]. We will show that the order parameter is suppressed in comparison with that obtained using the mean-field theory owing to the effects of spatial fluctuations in low-dimensional systems. In order to show the dynamics of the BCS-BEC crossover, we will then use the cluster perturbation theory (CPT) [83] to calculate the single-particle and anomalous Green's functions. We will present the single-particle spectra and densities of states to clarify the behavior of the superconducting (superfluid) gap. We will also present the Bogoliubov quasiparticle spectra and condensation amplitude to discuss the character of the Cooper pairs in the BCS and BEC states. In particular, we will evaluate the pair coherence length ξ from the condensation amplitude and demonstrate the smooth crossover from a weakly paired BCS state ($\xi \gg a$) to a BEC state of tightly bound pairs ($\xi \ll a$), where a is the lattice constant. We will finally calculate the kinetic and potential energies in the superconducting (superfluid) and normal ground states and show that the superconducting (superfluid) state is driven by the gain in potential energy in the BCS state, but by the gain in kinetic energy in the BEC state.

A.2 Model and Method

A.2.1 Attractive Hubbard Model

To discuss the BCS-BEC crossover, we use the attractive Hubbard model defined as

$$\mathcal{H} = -t \sum_{\langle i,j \rangle, \sigma} c_{i\sigma}^\dagger c_{j\sigma} - U \sum_i n_{i\uparrow} n_{i\downarrow} - \mu \sum_{i,\sigma} n_{i\sigma}, \quad (\text{A.1})$$

¹Appendix A is based on T. Kaneko and Y. Ohta, J. Phys. Soc. Jpn. **83**, 024711 (2014).

where $c_{i\sigma}^\dagger$ ($c_{i\sigma}$) is the fermion creation (annihilation) operator with spin $\sigma(=\uparrow, \downarrow)$ at site i and $n_{i\sigma} = c_{i\sigma}^\dagger c_{i\sigma}$. t is the hopping integral between nearest-neighbor sites, $U (> 0)$ is the on-site attractive interaction, and μ is the chemical potential for maintaining the number of particles in the system.

It is known that the superconducting (superfluid) state is always realized in two and higher dimensions at $T = 0$ K for all values of $U (> 0)$ and in the entire particle density range, except at half filling where the superconducting (superfluid) and density-wave states are degenerate [119, 172, 173]. Thus far, focusing on numerical studies, the BCS-BEC crossover of this model has been explored mostly using the dynamical mean-field theory (DMFT) [174–178], where the correlation effects can be taken into account only in the infinite dimension. The cellular DMFT somehow improves the effects of finite dimensionality [179].

A.2.2 Variational Cluster Approximation for Superconductivity

We here employ the VCA based on the SFT [77, 78], where we can take into account the effects of short-range spatial correlations even in low-dimensional systems, thereby reproducing the momentum dependences of physical quantities precisely. This method has been shown to be useful for discussing the spontaneous symmetry breaking of correlated electron models beyond the mean-field theory [82, 99, 128]. Details of the SFT and techniques of the VCA is written in Sec. 3.3 and Sec. 3.4.

Within the VCA, we can take into account the spontaneous symmetry breakings just by adding appropriate Weiss fields to the reference system and taking these fields as variational parameters. The Weiss fields for the superconducting (superfluid) state is given as

$$\mathcal{H}_{\text{pair}} = \Delta' \sum_i c_{i\uparrow}^\dagger c_{i\downarrow}^\dagger + \text{H.c.}, \quad (\text{A.2})$$

where Δ' is the Weiss field for the s -wave pairing. In order to calculate the particle density n correctly [82], we also introduce the on-site potential defined as

$$\mathcal{H}_{\text{local}} = \varepsilon' \sum_{i,\sigma} n_{i\sigma}, \quad (\text{A.3})$$

where ε' is the variational on-site potential. Therefore, the Hamiltonian for the reference system is given by

$$\mathcal{H}' = \mathcal{H} + \mathcal{H}_{\text{pair}} + \mathcal{H}_{\text{local}}. \quad (\text{A.4})$$

Then, we solve the ground-state eigenvalue problem $\mathcal{H}'|\psi_0\rangle = E_0|\psi_0\rangle$ of a finite-size (L_c sites) cluster and calculate the trial Green's function by the Lanczos exact-diagonalization method. In our calculation, a cluster of size $L_c = 2 \times 2 = 4$ is used as a reference system; the effects of on-site correlations within this cluster are taken into account exactly. We use the Nambu formalism $\Psi_i^\dagger = (c_{i\uparrow}^\dagger, c_{i\downarrow})$ to solve the eigenvalue problem of Eq. (A.4); the Green's function matrix is then defined as

$$\hat{\mathbf{G}}'(\omega) = \begin{pmatrix} \mathbf{G}'(\omega) & \mathbf{F}'(\omega) \\ \mathbf{F}'^\dagger(\omega) & -\mathbf{G}'(-\omega) \end{pmatrix}, \quad (\text{A.5})$$

where \mathbf{G}' and \mathbf{F}' are the $L_c \times L_c$ matrices, and each matrix element is defined as $G'_{ij}(\omega) = \langle\langle c_{i\uparrow}; c_{j\uparrow}^\dagger \rangle\rangle_\omega$ and $F'_{ij}(\omega) = \langle\langle c_{i\uparrow}; c_{j\downarrow} \rangle\rangle_\omega$, respectively. We will denote all the Nambu matrices by a ‘hat’ on top. The matrix \mathbf{V} is given as

$$\hat{\mathbf{V}}(\mathbf{K}) = \begin{pmatrix} \mathbf{T}(\mathbf{K}) - \varepsilon' \mathbf{I} & -\Delta' \mathbf{I} \\ -\Delta' \mathbf{I} & -\mathbf{T}(\mathbf{K}) + \varepsilon' \mathbf{I} \end{pmatrix}, \quad (\text{A.6})$$

where $\mathbf{T}(\mathbf{K})$ is the intercluster hopping matrix with $T_{ij}(\mathbf{K}) = -t \sum_{\mathbf{X},x} e^{i\mathbf{K}\cdot\mathbf{X}} \delta_{i+x,j} \delta_{\mathbf{R}+\mathbf{X},\mathbf{R}'}$, where x denotes the neighboring site of the i -th site and \mathbf{X} denotes the neighboring cluster of the \mathbf{R} -th cluster.

Using the matrices $\hat{\mathbf{G}}$ and $\hat{\mathbf{V}}$, we can evaluate the functional

$$\Omega = \Omega' - \frac{1}{N} \oint_C \frac{dz}{2\pi i} \sum_{\mathbf{K}} \ln \det \left[\hat{\mathbf{I}} - \hat{\mathbf{V}}(\mathbf{K}) \hat{\mathbf{G}}'(z) \right], \quad (\text{A.7})$$

where the \mathbf{K} -summation is performed in the reduced Brillouin zone of the superlattice and the contour C of the frequency integral encloses the negative real axis. The variational parameters Δ' and ε' are

optimized on the basis of the variational principle, i.e., $(\partial\Omega/\partial\Delta', \partial\Omega/\partial\varepsilon') = (0, 0)$. The solution with $\Delta' \neq 0$ corresponds to the superconducting state. The average particle density n ($= \langle n_{i\sigma} \rangle$) is expressed as

$$n = \frac{1}{NL_c} \oint_C \frac{dz}{2\pi i} \sum_{\mathbf{K}} \sum_{i=1}^{L_c} \mathcal{G}_{ii}(\mathbf{K}, z), \quad (\text{A.8})$$

whereby the chemical potential μ is determined to maintain the particle density n at quarter filling, $2n = \langle n_{i\uparrow} \rangle + \langle n_{i\downarrow} \rangle = 0.5$. \mathcal{G} in Eq. (A.8) is the diagonal term ($L_c \times L_c$ matrix) of $\hat{\mathcal{G}}(\mathbf{K}, \omega) = [\hat{\mathcal{G}}'^{-1}(\omega) - \hat{\mathcal{V}}(\mathbf{K})]^{-1}$.

A.3 Results

A.3.1 Order Parameter

We first calculate the U dependence of the superconducting order parameter $\Delta = U \langle c_{i\downarrow} c_{i\uparrow} \rangle$. Within the framework of the VCA, the anomalous expectation value $\Phi = \langle c_{i\downarrow} c_{i\uparrow} \rangle$ is defined as

$$\Phi = \frac{1}{NL_c} \oint_C \frac{dz}{2\pi i} \sum_{\mathbf{K}} \sum_{i=1}^{L_c} \mathcal{F}_{ii}(\mathbf{K}, z), \quad (\text{A.9})$$

where \mathcal{F} is the off-diagonal term of the Green's function $\hat{\mathcal{G}}(\mathbf{K}, \omega)$. We also evaluate the binding energy of the pair E_B from the single-particle excitation gap. For comparison with the results of the VCA, we also evaluate the order parameter in the mean-field (MF) theory, which gives Δ as a solution of the self-consistent equations.

The results for Φ and E_B calculated using the VCA and MF theory are shown in Fig. A.1. In the MF theory, the order parameter Δ^{MF} increases exponentially with U , thereby satisfying the relation $E_B^{\text{MF}} = 2\Delta^{\text{MF}}$ in the weak-coupling limit. In the strong-coupling limit, on the other hand, $\Delta^{\text{MF}} = U\sqrt{n(1-n)} = \sqrt{3}U/4$ ($\Phi^{\text{MF}} = \sqrt{3}/4$) and $E_B^{\text{MF}} = U$ at $n = 0.25$, regardless of the spatial dimension. We find that the result of the VCA exhibits the same behavior as that of the MF theory in the weak-coupling limit: Δ increases exponentially with U , satisfying the relation $E_B = 2\Delta$, which recovers the exponential behavior of the BCS mean-field theory. In the intermediate-coupling region, we find that

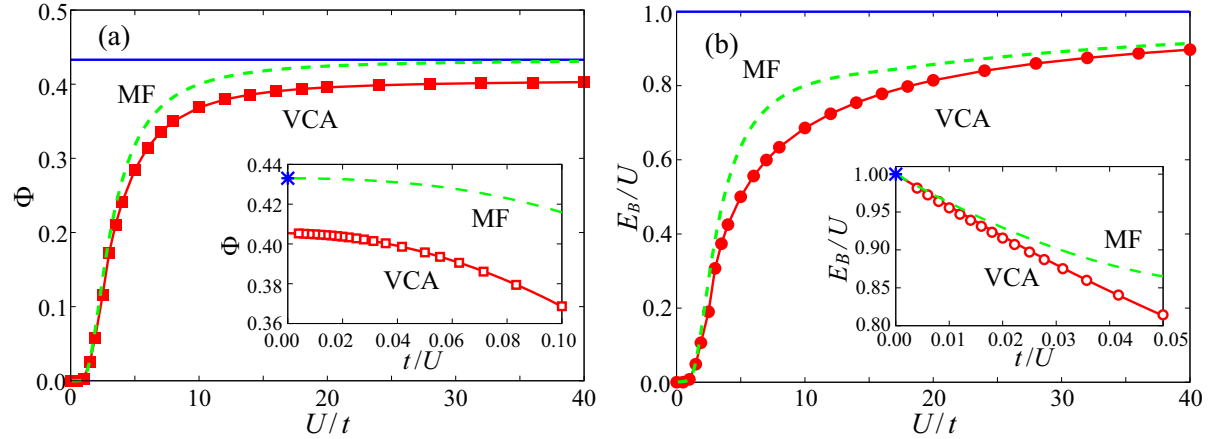


Figure A.1: (a) Anomalous expectation values $\Phi = \langle c_{i\downarrow} c_{i\uparrow} \rangle$ calculated using the VCA (squares) and MF theory (dashed line) as a function of U/t at quarter filling ($n = 0.25$). The horizontal line indicates the Φ in the MF theory in the strong-coupling limit, $\Phi_{\text{MF}} = \sqrt{3}/4$. The inset shows the Φ values calculated using the VCA (open squares) and MF theory (dashed line) in the strong-coupling region as a function of t/U . (b) Binding energies of a pair E_B/U calculated using the VCA (circles) and MF theory (dashed line) as a function of U/t at quarter filling ($n = 0.25$). The horizontal line indicates the E_B/U in the MF theory in the strong-coupling limit, $E_B = U$. The inset shows the E_B/U values calculated using the VCA (open circles) and MF theory (dashed line) in the strong-coupling region as a function of t/U [117].

Φ and E_B are significantly suppressed in comparison with those of the MF theory, which is due to the quantum fluctuations of the system. In the strong-coupling limit, E_B converges to the result of the MF theory, $E_B = E_B^{\text{MF}} = U$ [see the inset of Fig. A.1 (b)], but Φ is suppressed in comparison with the result of the MF theory, $\Phi \sim 0.405 < \Phi^{\text{MF}}$ at $U \rightarrow \infty$ [see the inset of Fig. A.1 (a)].

In the strong-coupling limit, the attractive Hubbard model can be mapped onto the spin-1/2 Heisenberg model in a magnetic field,

$$\mathcal{H}_{\text{eff}} = J \sum_{\langle i,j \rangle} \mathbf{S}_i \cdot \mathbf{S}_j - h \sum_i S_i^z, \quad (\text{A.10})$$

where we use the particle-hole transformation $a_{i\uparrow} = c_{i\uparrow}$ and $a_{i\downarrow} = (-1)^i c_{i\downarrow}^\dagger$ [180], and define $\mathbf{S}_i = \frac{1}{2} \sum_{\alpha\beta} a_{i\alpha}^\dagger \boldsymbol{\sigma}_{\alpha\beta} a_{i\beta}$, $J = 4t^2/|U|$, and $h = 2\mu + |U|$. The superconducting state in the original model at quarter filling ($n = 0.25$) corresponds to the antiferromagnetic state in the xy plane in the effective model with the magnetization $m = \sum \langle S_i^z \rangle / N = 0.25$. It is known that, in the two-dimensional square lattice, strong quantum fluctuations caused by the low dimensionality of the system suppress the long-range staggered magnetic order in the xy plane in comparison with those of classical approximation [172, 181]. Therefore, because the VCA takes into account the short-range spatial correlations and quantum fluctuations in the low-dimensional systems, it is reasonable that the order parameter Φ obtained using the VCA is significantly suppressed in comparison with the result of the MF theory.

To compare the result of the VCA with those of the DMFT calculations, which are justified in the infinite dimension, we notice that our result for Φ in the strong-coupling limit is quite different: Φ in the DMFT increases to the constant value obtained in the MF theory [175, 177], whereas in the VCA, it converges to a significantly smaller value, as shown in Fig. A.1 (a). The MF theory for the Heisenberg model is exact in the infinite dimension. Therefore, the results of the DMFT calculations are consistent with the results of the MF theory in the strong-coupling limit. The difference between the DMFT and the VCA results is thus caused by the effects of spatial quantum fluctuations in low-dimensional systems, which the DMFT cannot take into account.

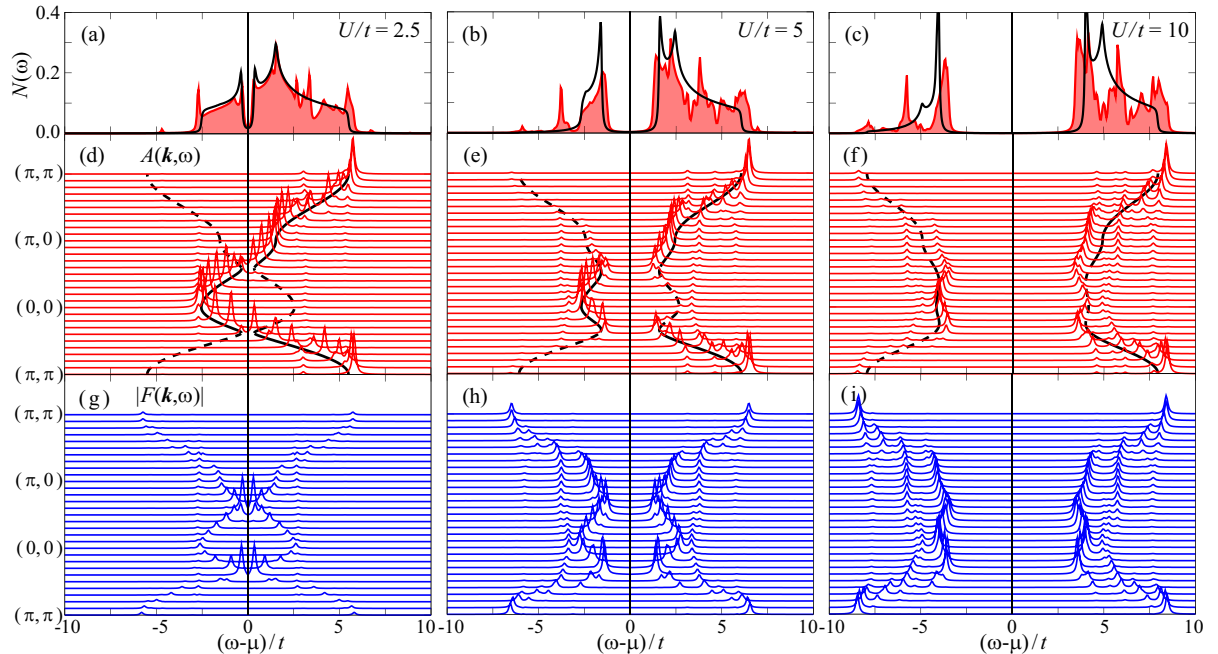


Figure A.2: (a)-(c) Densities of states $N(\omega)$, (d)-(f) single-particle spectra $A(\mathbf{k}, \omega)$, and (g)-(i) Bogoliubov quasiparticle spectra $F(\mathbf{k}, \omega)$ calculated at $U/t = 2.5$ (left), $U/t = 5$ (center), and $U/t = 10$ (right) at quarter filling ($n = 0.25$). The densities of state and quasiparticle dispersions evaluated in the MF theory (solid and dashed lines) are also shown in (a)-(c) and (d)-(f), respectively. The Lorentzian broadening of $\eta/t = 0.05$ is used for $N(\omega)$, and $\eta/t = 0.1$ is used for $A(\mathbf{k}, \omega)$ and $F(\mathbf{k}, \omega)$ [117].

A.3.2 Spectra and Momentum Distributions

The single-particle and anomalous Green's functions are calculated using the CPT with the optimized variational parameters, which are defined as

$$\mathcal{G}_{\text{cpt}}(\mathbf{k}, \omega) = \frac{1}{L_c} \sum_{i,j=1}^{L_c} \mathcal{G}_{ij}(\mathbf{k}, \omega) e^{-i\mathbf{k} \cdot (\mathbf{r}_i - \mathbf{r}_j)}, \quad (\text{A.11})$$

$$\mathcal{F}_{\text{cpt}}(\mathbf{k}, \omega) = \frac{1}{L_c} \sum_{i,j=1}^{L_c} \mathcal{F}_{ij}(\mathbf{k}, \omega) e^{-i\mathbf{k} \cdot (\mathbf{r}_i - \mathbf{r}_j)}, \quad (\text{A.12})$$

from which we calculate the single-particle and Bogoliubov quasiparticle spectra defined respectively as

$$A(\mathbf{k}, \omega) = -\frac{1}{\pi} \text{Im} \mathcal{G}_{\text{cpt}}(\mathbf{k}, \omega + i\eta), \quad (\text{A.13})$$

$$F(\mathbf{k}, \omega) = -\frac{1}{\pi} \text{Im} \mathcal{F}_{\text{cpt}}(\mathbf{k}, \omega + i\eta), \quad (\text{A.14})$$

where η is the artificial Lorentzian broadening. We also calculate the density of states defined as

$$N(\omega) = \frac{1}{N} \sum_{\mathbf{k}} A(\mathbf{k}, \omega). \quad (\text{A.15})$$

In Fig. A.2, we show the calculated results for $A(\mathbf{k}, \omega)$, $F(\mathbf{k}, \omega)$, and $N(\omega)$ from the weak-coupling region to the strong-coupling region. In the weak-coupling region (at $U/t = 2.5$), $A(\mathbf{k}, \omega)$ [or $N(\omega)$] shows a tiny superconducting gap at the Fermi momentum \mathbf{k}_F , together with coherence peaks at the edges of the gap, indicating the existence of weakly bound Cooper pairs. The gap width and peaks of $A(\mathbf{k}, \omega)$ are consistent with quasiparticle spectra in the MF theory. Note that the Fermi momentum \mathbf{k}_F is defined as $\varepsilon_{\mathbf{k}_F} = \mu$ (at $U = 0$), where $\varepsilon_{\mathbf{k}} = -2t(\cos k_x + \cos k_y)$. $F(\mathbf{k}, \omega)$ has a sharp peak at \mathbf{k}_F and its intensity rapidly decreases as the momentum goes away from \mathbf{k}_F . With increasing U , each of the pairs becomes more strongly bound and the superconducting gap becomes larger. In accordance with the E_B shown Fig. A.1 (b), $N(\omega)$ exhibits a spectral gap that is suppressed in comparison with the results of the MF theory, as shown in Figs. A.2 (b) and A.2 (c). At $U/t = 5$, $F(\mathbf{k}, \omega)$ still has a strong

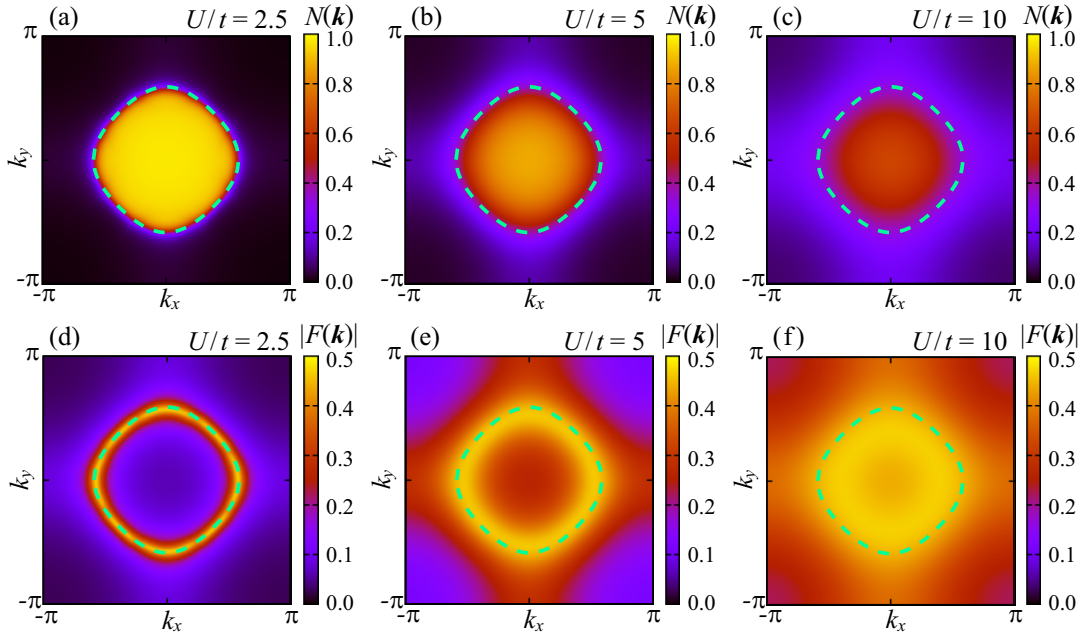


Figure A.3: (a)-(c) Fermion momentum distribution function $N(\mathbf{k})$ and (d)-(f) condensation amplitude $F(\mathbf{k})$ calculated at $U/t = 2.5$ (left), $U/t = 5$ (center), and $U/t = 10$ (right) at quarter filling ($n = 0.25$). The dashed line indicates the Fermi momentum [117].

peak at approximately \mathbf{k}_F . In comparison with the spectra at $U/t = 2.5$, $F(\mathbf{k}, \omega)$ has strong peaks even as the momentum goes away from \mathbf{k}_F . In the strong-coupling region (at $U/t = 10$), the spectra show a large superconducting gap, and the peaks of $F(\mathbf{k}, \omega)$ spread out over the entire Brillouin zone.

In order to see the character of the Cooper pairs in more detail in momentum space, we also calculate the fermion momentum distribution function and condensation amplitude, which are defined respectively as

$$N(\mathbf{k}) = \oint_C \frac{dz}{2\pi i} \mathcal{G}_{\text{cpt}}(\mathbf{k}, z), \quad (\text{A.16})$$

$$F(\mathbf{k}) = \oint_C \frac{dz}{2\pi i} \mathcal{F}_{\text{cpt}}(\mathbf{k}, z). \quad (\text{A.17})$$

The calculated results for $N(\mathbf{k})$ and $F(\mathbf{k})$ are shown in Fig. A.3. In the weak-coupling region (at $U/t = 2.5$), $N(\mathbf{k})$ shows the typical form known from the BCS theory, i.e., momenta inside of \mathbf{k}_F are mostly occupied ($N(\mathbf{k}) \simeq 1$) and $N(\mathbf{k})$ slightly broadens at \mathbf{k}_F , dropping from 1 to 0 over the energy scale of the order parameter. Corresponding to $N(\mathbf{k})$, $F(\mathbf{k})$ exhibits a sharp peak at \mathbf{k}_F ($|F(\mathbf{k}_F)| \simeq 0.5$) and decreases rapidly as the momentum goes away from \mathbf{k}_F . The sharp peak of $F(\mathbf{k})$ in the \mathbf{k} -space indicates that the radius of the pair is large in real space (weakly bound pairs). With increasing U , $N(\mathbf{k})$ and $F(\mathbf{k})$ become broader in momentum space, indicating that the radius of the pair becomes smaller in real space. In the strong-coupling region (at $U/t = 10$), $F(\mathbf{k})$ is spread out over the Brillouin zone; therefore, the pairs are tightly bound in real space.

A.3.3 Pair Coherence Length

In order to see the spatial extension of the Cooper pair directly, we evaluate the pair coherence length ξ defined as

$$\xi^2 = \frac{\sum_{\mathbf{r}} r^2 |F(\mathbf{r})|^2}{\sum_{\mathbf{r}} |F(\mathbf{r})|^2} = \frac{\sum_{\mathbf{k}} |\nabla_{\mathbf{k}} F(\mathbf{k})|^2}{\sum_{\mathbf{k}} |F(\mathbf{k})|^2}, \quad (\text{A.18})$$

where $F(\mathbf{r}) = \frac{1}{\sqrt{L}} \sum_{\mathbf{r}'} \langle c_{\mathbf{r}'+\mathbf{r}\downarrow} c_{\mathbf{r}'\uparrow} \rangle$ is the condensation amplitude for a Cooper pair with a distance \mathbf{r} in real space [116]. The \mathbf{k} -summation was performed with 500×500 \mathbf{k} points in the first Brillouin zone.

In Fig. A.4, we show the results for ξ calculated using the VCA and MF theory. We find that, corresponding to the calculated results for $F(\mathbf{k})$ [see Figs. A.3 (d)-A.3 (f)], the pair coherence length ξ is much larger than the lattice constant a in the weak-coupling region. With increasing U , ξ decreases smoothly to much smaller values than the lattice constant in the strong-coupling region, indicating

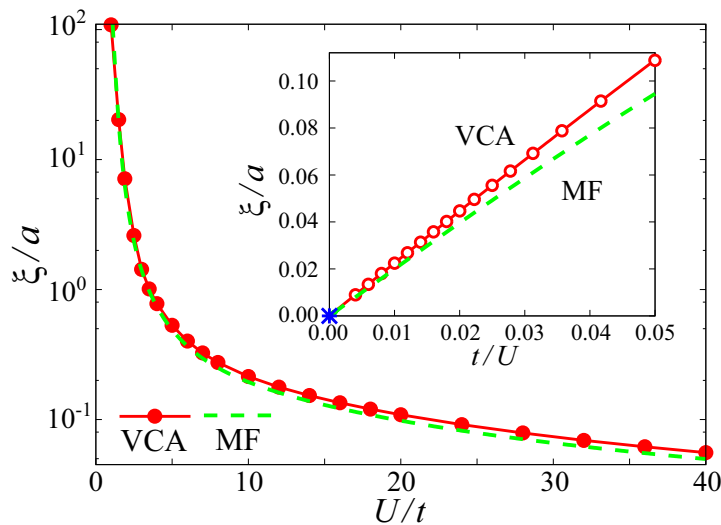


Figure A.4: Pair coherence length ξ/a calculated using the VCA (circles) and MF theory (dashed line) as a function of U/t for quarter filling ($n = 0.25$). The inset shows ξ/a calculated using the VCA (open circles) and MF theory (dashed line) in the strong-coupling limit [117].

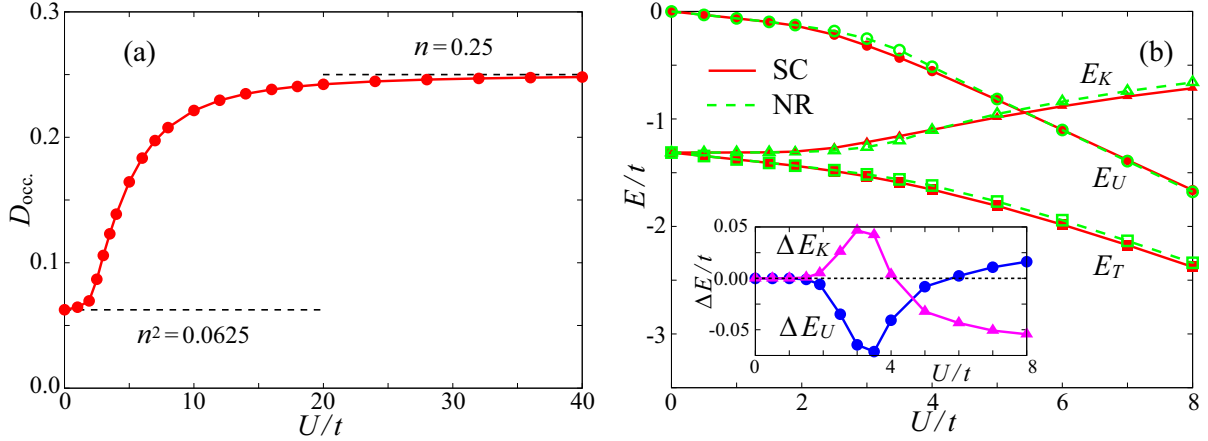


Figure A.5: (a) Double occupancy $D_{\text{occ.}} = \langle n_{i\uparrow} n_{i\downarrow} \rangle$ calculated using the VCA as a function of U/t for quarter filling ($n = 0.25$). (b) Calculated total energy E_T (squares), kinetic energy E_K (triangles), and potential energy E_U (circles) of the superconducting (SC) and normal (NR) ground states as a function of U/t at quarter filling ($n = 0.25$). The inset shows the energy differences between the superconducting and normal ground states [117].

that a smooth crossover occurs from the weakly paired BCS-like state ($\xi \gg a$) to the BEC state of tightly bound pairs ($\xi \ll a$). Note that ξ is already of the size of the lattice constant at $U/t \sim 3.5$. In comparison with the results of the VCA and MF theory, ξ evaluated by the VCA is significantly larger than the results of the MF theory, which is due again to the quantum fluctuations of the system, just as in E_B shown in Fig. A.1 (b). In the strong-coupling limit ($U \rightarrow \infty$), ξ evaluated using the VCA and MF theory converges to 0 ($\xi \rightarrow 0$).

A.3.4 Ground State Energy

Finally, we calculate the ground-state energies of the attractive Hubbard model in the superconducting and normal states. The total ground-state energy E_T is given as $E_T = \Omega + 2\mu n$. Using the double occupancy defined as $D_{\text{occ.}} = \langle n_{i\uparrow} n_{i\downarrow} \rangle = dE_T/dU$, we obtain the potential energy E_U as $E_U = -UD_{\text{occ.}}$ and the kinetic energy E_K as $E_K = E_T - E_U$. The calculated results are shown in Fig. A.5, where the difference ΔE denotes the energy of the superconducting state minus the energy of the normal state.

First, let us consider the behavior of E_U and E_K . In Fig. A.5 (a), we show the calculated double occupancy $D_{\text{occ.}}$. In the noninteracting limit, $D_{\text{occ.}}$ is given by $n^2 = 0.0625$ since $\langle n_{i\uparrow} n_{i\downarrow} \rangle = \langle n_{i\uparrow} \rangle \langle n_{i\downarrow} \rangle = n^2$ in the uncorrelated fermion systems. In the strong-coupling limit, on the other hand, all the fermions are tightly bound to form composite bosons and hence $D_{\text{occ.}}$ is given by the particle density as $D_{\text{occ.}} = n = 0.25$. The calculated result for $D_{\text{occ.}}$ shows a smooth crossover from the weakly paired BCS state ($D_{\text{occ.}} \simeq n^2$) to the tightly paired BEC state ($D_{\text{occ.}} \simeq n$). Therefore, with increasing U , E_U decreases owing to the pair formation and E_K increases owing to the gap opening, resulting in a gradual decrease in E_T , irrespective of whether the ground state is superconducting or normal; the effects of the presence of the order parameter are found to be rather small.

Then, let us see the effects of the order parameter, the results of which are shown in the inset of Fig. A.5 (b). In the weak-coupling region, we find that the superconducting state occurs owing to the loss of kinetic energy ($\Delta E_K > 0$) and gain in potential energy ($\Delta E_U < 0$). This means that, in the BCS weak-coupling limit, the decrease in the potential energy due to the Cooper pair formation overwhelms the loss of kinetic energy due to the broadening of the Fermi edge. Thus, in the weak-coupling region, the superconducting state is driven by the gain in potential energy. In our calculation, the BCS features ($\Delta E_K > 0$ and $\Delta E_U < 0$) vanish at $U/t \sim 4$.

In the strong-coupling region, on the other hand, the roles are interchanged, i.e., the superconducting state is characterized by $\Delta E_K < 0$ and $\Delta E_U > 0$. This means that, in the BEC strong-coupling limit, tightly bound composite bosons gain in kinetic energy because they condense at $\mathbf{k} = 0$ in momentum space, simultaneously when the order parameter becomes nonzero. The loss of the potential energy arises because the motion of composite bosons is accompanied necessarily by the breaking of on-site pairs. Thus, in the strong-coupling region, the superconducting state is driven by the gain in kinetic energy.

In our calculation, the BEC features ($\Delta E_K < 0$ and $\Delta E_U > 0$) appear at $U/t \sim 6$. These behaviors of the kinetic and potential energies in the attractive Hubbard model are qualitatively consistent with the results of the previous DMFT calculations [176, 179].

A.4 Summary

We have studied the superconducting ground state in the two-dimensional attractive Hubbard model by the VCA. We have calculated the U dependence of the order parameter and have shown that the order parameter is suppressed in comparison with that obtained using the MF theory owing to spatial fluctuations in the low-dimensional system. In order to discuss the character of the BCS-BEC crossover, the CPT has been used to calculate the single-particle and anomalous Green's functions. We have shown that the single-particle spectra and densities of states clearly exhibit the behavior of the superconducting gap and that the Bogoliubov quasiparticle spectra and condensation amplitude characterize the Cooper pairs in momentum space that changes continuously from the BCS state to the BEC state. From the calculated condensation amplitude, we have evaluated the pair coherence length ξ , which demonstrates the smooth crossover in real space from the weakly paired BCS state ($\xi \gg a$) to the BEC state of tightly bound pairs ($\xi \ll a$). We have also calculated the kinetic and potential energies in the superconducting and normal ground states and have shown that the superconducting state is driven by the gain in potential energy in the BCS state, but by the gain in kinetic energy in the BEC state.

Appendix B

Description of Multipoles in Excitonic Insulators

In Chap. 7, we discussed the charge and spin density distributions in excitonic phases. In this Appendix, we consider the electronic density distribution of the excitonic phases when the valence and conduction bands are composed of the orbitals in a single ion. In particular, we present on the multipole expansion of the electronic density in excitonic insulators.

The field operator of a multi-orbital system in a single ion is given by

$$\Psi(\mathbf{r}) = \sum_{\alpha} \phi_{\alpha}(\mathbf{r})c_{\alpha}, \quad \Psi^{\dagger}(\mathbf{r}) = \sum_{\alpha} \phi_{\alpha}^{*}(\mathbf{r})c_{\alpha}^{\dagger}, \quad (\text{B.1})$$

where $\phi_{\alpha}(\mathbf{r})$ is the wave function and c_{α} (c_{α}^{\dagger}) is the annihilation (creation) operator of an electron in the α orbital [60, 138]. In this Appendix, we consider the wave functions of the orbitals in a single unit cell and therefore we omit the site and spin indices for simplicity. The wave function of the α orbital is then given by

$$\phi_{\alpha}(\mathbf{r}) = \phi_{n_{\alpha}l_{\alpha}m_{\alpha}}(\mathbf{r}) = R_{n_{\alpha}l_{\alpha}}(r)Y_{l_{\alpha}m_{\alpha}}(\hat{\mathbf{r}}), \quad (\text{B.2})$$

where $R_{nl}(r)$ is the radial wave function and $Y_{lm}(\hat{\mathbf{r}}) = Y_{lm}(\theta, \varphi)$ is the spherical harmonics. n_{α} , l_{α} , and m_{α} are the principal, azimuthal, magnetic quantum numbers of the α orbital, respectively. Using the field operator in Eq. (B.1), the electronic density is given by

$$\rho(\mathbf{r}) \equiv \langle \Psi^{\dagger}(\mathbf{r})\Psi(\mathbf{r}) \rangle = \sum_{\alpha, \beta} \phi_{\alpha}^{*}(\mathbf{r})\phi_{\beta}(\mathbf{r})\langle c_{\alpha}^{\dagger}c_{\beta} \rangle. \quad (\text{B.3})$$

From this equation, we find that the modification of the electronic density $\rho(\mathbf{r})$ is given by the spontaneous orbital hybridizations $\langle c_{\alpha}^{\dagger}c_{\beta} \rangle \neq 0$ due to the excitonic ordering.

Now, let us describe the character of the excitonic phases in terms of the multipole moments. In general, the multipole moments are characterized by the projection onto the spherical harmonics [139–141]. Using the spherical harmonics, the multipole moment is defined as

$$Q_{lm} \equiv \int d\mathbf{r} r^l Z_{lm}^{*}(\hat{\mathbf{r}})\rho(\mathbf{r}), \quad (\text{B.4})$$

where we define $Z_{lm}(\hat{\mathbf{r}}) \equiv \sqrt{4\pi/(2l+1)}Y_{lm}(\hat{\mathbf{r}})$ and $Z_{lm}^{*}(\hat{\mathbf{r}}) = (-1)^m Z_{l-m}(\hat{\mathbf{r}})$. l is the rank of the multipole moments, and the moment of each rank is called the monopole ($l = 0$), dipole ($l = 1$), quadrupole ($l = 2$), octupole ($l = 3$), hexadecapole ($l = 4$), dotriacontapole ($l = 5$), etc. Using the density in Eq. (B.3), the multipole moment is given by

$$Q_{lm} = \sum_{\alpha, \beta} \left[\int d\mathbf{r} \phi_{\alpha}^{*}(\mathbf{r})r^l Z_{lm}^{*}(\hat{\mathbf{r}})\phi_{\beta}(\mathbf{r}) \right] \langle c_{\alpha}^{\dagger}c_{\beta} \rangle = \sum_{\alpha, \beta} \Gamma_{lm}^{\alpha\beta} \langle c_{\alpha}^{\dagger}c_{\beta} \rangle, \quad (\text{B.5})$$

where we define the integral part of the wave functions as

$$\Gamma_{lm}^{\alpha\beta} \equiv \int d\mathbf{r} \phi_{\alpha}^{*}(\mathbf{r})r^l Z_{lm}^{*}(\hat{\mathbf{r}})\phi_{\beta}(\mathbf{r}). \quad (\text{B.6})$$

From Eq. (B.5), we find that the multipole moment becomes finite, $Q_{lm} \neq 0$, when both the integral part of the wave functions $\Gamma_{lm}^{\alpha\beta}$ and the expectation value $\langle c_\alpha^\dagger c_\beta \rangle$ satisfy $\Gamma_{lm}^{\alpha\beta} \neq 0$ and $\langle c_\alpha^\dagger c_\beta \rangle \neq 0$. The expectation value $\langle c_\alpha^\dagger c_\beta \rangle$ is given by the symmetry-broken solution of the effective multi-orbital models, but $\Gamma_{lm}^{\alpha\beta}$ depends on the character of the wave functions of the orbitals in the valence and conduction bands.

In this Appendix, we investigate the integral part $\Gamma_{lm}^{\alpha\beta}$ in detail and we evaluate which rank of multipole moments becomes finite when the orbitals are hybridized. Using Eq. (B.2), $\Gamma_{lm}^{\alpha\beta}$ becomes

$$\Gamma_{lm}^{\alpha\beta} = \left[\int r^2 dr R_{n_\alpha l_\alpha}(r) r^l R_{n_\beta l_\beta}(r) \right] \left[\int d\Omega Y_{l_\alpha m_\alpha}^*(\hat{\mathbf{r}}) Z_{lm}^*(\hat{\mathbf{r}}) Y_{l_\beta m_\beta}(\hat{\mathbf{r}}) \right], \quad (\text{B.7})$$

where $d\Omega = \sin\theta d\theta d\varphi$. Defining the integrals of the radial and angular parts respectively as

$$\Lambda_l(n_\alpha l_\alpha, n_\beta l_\beta) \equiv \int r^2 dr R_{n_\alpha l_\alpha}(r) r^l R_{n_\beta l_\beta}(r), \quad (\text{B.8})$$

$$\Theta_{lm}(l_\alpha m_\alpha, l_\beta m_\beta) \equiv \int d\Omega Y_{l_\alpha m_\alpha}^*(\hat{\mathbf{r}}) Z_{lm}^*(\hat{\mathbf{r}}) Y_{l_\beta m_\beta}(\hat{\mathbf{r}}), \quad (\text{B.9})$$

we can divide the integral $\Gamma_{lm}^{\alpha\beta}$ into the radial and angular parts as

$$\Gamma_{lm}^{\alpha\beta} = \Lambda_l(n_\alpha l_\alpha, n_\beta l_\beta) \Theta_{lm}(l_\alpha m_\alpha, l_\beta m_\beta). \quad (\text{B.10})$$

The radial part is always nonzero, $\Lambda_l(n_\alpha l_\alpha, n_\beta l_\beta) \neq 0$, and thus we can classify whether $\Gamma_{lm}^{\alpha\beta}$ is finite or not from the angular part $\Theta_{lm}(l_\alpha m_\alpha, l_\beta m_\beta)$. The integral of the angular part is given as

$$\Theta_{lm}(l_\alpha m_\alpha, l_\beta m_\beta) = \int d\Omega Y_{l_\alpha m_\alpha}^*(\hat{\mathbf{r}}) Z_{lm}^*(\hat{\mathbf{r}}) Y_{l_\beta m_\beta}(\hat{\mathbf{r}}) = (-1)^m \int d\Omega Y_{l_\alpha m_\alpha}^*(\hat{\mathbf{r}}) Z_{l-m}(\hat{\mathbf{r}}) Y_{l_\beta m_\beta}(\hat{\mathbf{r}}). \quad (\text{B.11})$$

From $Y_{lm}(\hat{\mathbf{r}}) \propto e^{im\varphi}$ and the integral over φ , we find $\Theta_{lm}(l_\alpha m_\alpha, l_\beta m_\beta)$ is nonzero when m , m_α , and m_β satisfy the following relation [182],

$$-m = m_\alpha - m_\beta. \quad (\text{B.12})$$

Using the relation in Eq. (B.12), we define the integral of the spherical harmonics as

$$c^l(l_\alpha m_\alpha, l_\beta m_\beta) \equiv \int d\Omega Y_{l_\alpha m_\alpha}^*(\hat{\mathbf{r}}) Z_{lm_\alpha - m_\beta}(\hat{\mathbf{r}}) Y_{l_\beta m_\beta}(\hat{\mathbf{r}}), \quad (\text{B.13})$$

and $\Theta_{lm}(l_\alpha m_\alpha, l_\beta m_\beta)$ becomes

$$\Theta_{lm}(l_\alpha m_\alpha, l_\beta m_\beta) = (-1)^{m_\beta - m_\alpha} c^l(l_\alpha m_\alpha, l_\beta m_\beta) \delta_{m, m_\beta - m_\alpha}. \quad (\text{B.14})$$

The calculated $c^l(l_\alpha m_\alpha, l_\beta m_\beta)$ are summarized in the text book written by Kamimura *et al.* [182], where we know that $c^l(l_\alpha m_\alpha, l_\beta m_\beta)$ is nonzero when l , l_α , and l_β satisfy the following relations [182],

$$l + l_\alpha + l_\beta = (\text{even}), \quad |l_\alpha - l_\beta| \leq l \leq l_\alpha + l_\beta. \quad (\text{B.15})$$

$Y_{lm}(\hat{\mathbf{r}})$ and $Z_{lm}(\hat{\mathbf{r}})$ are complex for $|m| > 0$ and it is useful to apply the real spherical harmonics, which are sometimes called the tesseral harmonics, when the wave functions $\phi_\alpha(\mathbf{r})$ are real. The spherical harmonics with $m = 0$ are real. For $|m| > 0$, the spherical harmonics can be taken to be real with¹

$$Y_{lm}^{(c)}(\hat{\mathbf{r}}) = \frac{1}{\sqrt{2}} [Y_{l-m}(\hat{\mathbf{r}}) + (-1)^m Y_{lm}(\hat{\mathbf{r}})], \quad (\text{B.16})$$

$$Y_{lm}^{(s)}(\hat{\mathbf{r}}) = \frac{i}{\sqrt{2}} [Y_{l-m}(\hat{\mathbf{r}}) - (-1)^m Y_{lm}(\hat{\mathbf{r}})]. \quad (\text{B.17})$$

For example, $Y_{11}^{(c)}(\hat{\mathbf{r}})$ corresponds to p_x orbital and $Y_{22}^{(s)}(\hat{\mathbf{r}})$ corresponds to d_{xy} orbital. We summarize the correspondence between the tesseral representation and the orthogonal coordinate representation in Table B.1.

¹ Θ_{lm} can be taken to be real with $\Theta_{lm}^{(c)} = [\Theta_{l-m} + (-1)^m \Theta_{lm}] / \sqrt{2}$ and $\Theta_{lm}^{(s)} = [\Theta_{l-m} - (-1)^m \Theta_{lm}] / (\sqrt{2}i)$.

l	m	(c) and 0	(s)
0	0	1	–
1	0	z	
	1	x	y
2	0	$3z^2 - r^2$	–
	1	zx	yz
	2	$x^2 - y^2$	xy
3	0	$z(5z^2 - 3r^2)$	–
	1	$x(5z^2 - r^2)$	$y(5z^2 - r^2)$
	2	$z(x^2 - y^2)$	xyz
	3	$x(x^2 - 3y^2)$	$y(3x^2 - y^2)$
4	0	$35z^4 - 30z^2r^2 + 3r^4$	–
	1	$zx(7z^2 - 3r^2)$	$yz(7z^2 - 3r^2)$
	2	$(x^2 - y^2)(7z^2 - r^2)$	$xy(7z^2 - r^2)$
	3	$zx(x^2 - 3y^2)$	$yz(3x^2 - y^2)$
	4	$x^4 - 6x^2y^2 + y^4$	$xy(x^2 - y^2)$

Table B.1: Correspondence between the tesseral representation and the orthogonal coordinate representation.

Next, let us evaluate Θ_{lm} in the tesseral representation. Here, we consider an example where α is the $d_{3z^2-r^2}$ ($[l_\alpha m_\alpha] = [20]$) orbital and β is the $d_{x^2-y^2}$ ($[l_\beta m_\beta] = [22_c]$) orbital. Using $l_\alpha = l_\beta = 2$ and the relation in Eq. (B.15), we find that possible ranks of the multipoles are $l = 0, 2, 4$ in this example. Using the tesseral harmonics, $\Theta_{lm}(d_{3z^2-r^2}, d_{x^2-y^2})$ becomes²

$$\Theta_{lm}(d_{3z^2-r^2}, d_{x^2-y^2}) = (-1)^m \int d\Omega Y_{20} Z_{l-m} Y_{22}^{(c)} = \frac{1}{\sqrt{2}} c^l (20, 2 \pm 2) \delta_{m, \pm 2}. \quad (\text{B.18})$$

We find that $\Theta_{lm} \neq 0$ at $m = \pm 2$. Therefore, $l = 2, 4$ are possible and $\Theta_{2\pm 2}$ and $\Theta_{4\pm 2}$ are given as³,

$$\Theta_{2\pm 2}(d_{3z^2-r^2}, d_{x^2-y^2}) = \frac{1}{\sqrt{2}} c^2 (20, 2 \pm 2) = -\frac{\sqrt{2}}{7}, \quad (\text{B.19})$$

$$\Theta_{4\pm 2}(d_{3z^2-r^2}, d_{x^2-y^2}) = \frac{1}{\sqrt{2}} c^4 (20, 2 \pm 2) = \frac{\sqrt{15}}{21\sqrt{2}}. \quad (\text{B.20})$$

Applying the tesseral representation to $\Theta_{l\pm 2}$, we find $\Theta_{l2}^{(s)}(d_{3z^2-r^2}, d_{x^2-y^2}) \propto [\Theta_{l-2} - \Theta_{l2}] = 0$ and

$$\Theta_{22}^{(c)}(d_{3z^2-r^2}, d_{x^2-y^2}) = \frac{1}{\sqrt{2}} [\Theta_{2-2} + \Theta_{22}] = -\frac{2}{7}, \quad (\text{B.21})$$

$$\Theta_{42}^{(c)}(d_{3z^2-r^2}, d_{x^2-y^2}) = \frac{1}{\sqrt{2}} [\Theta_{4-2} + \Theta_{42}] = \frac{\sqrt{15}}{21}. \quad (\text{B.22})$$

Due to $\Theta_{22}^{(c)} \neq 0$ and $\Theta_{42}^{(c)} \neq 0$, the quadrupole moment $Q_{22}^{(c)} = Q_{x^2-y^2}$ and the hexadecapole moment $Q_{42}^{(c)} = Q_{(x^2-y^2)(7z^2-r^2)}$ become finite when the $d_{3z^2-r^2}$ and $d_{x^2-y^2}$ orbitals are hybridized spontaneously due to excitonic ordering. In the same way, we evaluate the relations between the orbitals and multipole moments from s ($l = 0$) to d ($l = 2$) orbitals, which are summarized in Table. B.2.

Finally, let us consider the multipole expansion for the product of the wave functions in the electronic density given in Eq. (B.3),

$$F_{\alpha\beta}(\mathbf{r}) = \phi_\alpha^*(\mathbf{r}) \phi_\beta(\mathbf{r}). \quad (\text{B.23})$$

²In Eq. (B.18), we have

$$\int d\Omega Y_{20} Z_{l-m} Y_{22}^{(c)} = \frac{1}{\sqrt{2}} \int d\Omega [Y_{20} Z_{l-m} Y_{2-2} + Y_{20} Z_{l-m} Y_{22}] = \frac{1}{\sqrt{2}} [c^l (20, 2-2) \delta_{m,-2} + c^l (20, 22) \delta_{m,2}].$$

³We use $c^2(20, 2 \pm 2) = -2/7$, $c^4(20, 2 \pm 2) = \sqrt{15}/21$ in Eq. (B.20) [182].

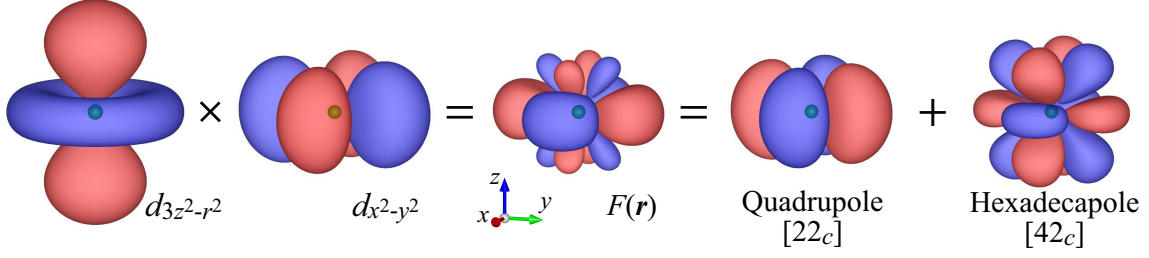


Figure B.1: Schematic picture of the multipole expansion of the product of the wave functions $F_{\alpha\beta}(\mathbf{r}) = \phi_{\alpha}(\mathbf{r})\phi_{\beta}(\mathbf{r})$, where we assume $\alpha = d_{3z^2-r^2}$ and $\beta = d_{x^2-y^2}$.

Using the relation $\sum_{l,m} (2l+1) Z_{lm}^*(\hat{\mathbf{r}}') Z_{lm}(\hat{\mathbf{r}}) = 4\pi\delta(\hat{\mathbf{r}} - \hat{\mathbf{r}}')$, we have⁴

$$Y_{l_{\alpha}m_{\alpha}}^*(\hat{\mathbf{r}}) Y_{l_{\beta}m_{\beta}}(\hat{\mathbf{r}}) = \sum_{l,m} \left(\frac{2l+1}{4\pi} \right) \Theta_{lm}(l_{\alpha}m_{\alpha}, l_{\beta}m_{\beta}) Z_{lm}(\hat{\mathbf{r}}). \quad (\text{B.24})$$

Therefore, from Eqs. (B.2) and Eq. (B.24), the multipole expansion of $F_{\alpha\beta}(\mathbf{r})$ is given by

$$F_{\alpha\beta}(\mathbf{r}) = R_{n_{\alpha}l_{\alpha}}(r) R_{n_{\beta}l_{\beta}}(r) \sum_{l,m} \left(\frac{2l+1}{4\pi} \right) \Theta_{lm}(l_{\alpha}m_{\alpha}, l_{\beta}m_{\beta}) Z_{lm}(\hat{\mathbf{r}}). \quad (\text{B.25})$$

Using the multipole expansion in Eq. (B.25), the electronic density in Eq. (B.3) is given by

$$\rho(\mathbf{r}) = \sum_{\alpha,\beta} R_{n_{\alpha}l_{\alpha}}(r) R_{n_{\beta}l_{\beta}}(r) \left[\sum_{l,m} \left(\frac{2l+1}{4\pi} \right) \Theta_{lm}(l_{\alpha}m_{\alpha}, l_{\beta}m_{\beta}) Z_{lm}(\hat{\mathbf{r}}) \right] \langle c_{\alpha}^{\dagger} c_{\beta} \rangle. \quad (\text{B.26})$$

In the previous example with $\alpha = d_{3z^2-r^2}$ and $\beta = d_{x^2-y^2}$, we note $\Theta_{22}^{(c)} \neq 0$ and $\Theta_{42}^{(c)} \neq 0$, so that we can expand $F_{\alpha\beta}(\mathbf{r})$ into the quadrupole and hexadecapole as

$$F_{\alpha\beta}(\mathbf{r}) = \frac{5}{4\pi} R_{32}^2(r) \Theta_{22}^{(c)}(d_{3z^2-r^2}, d_{x^2-y^2}) Z_{22}^{(c)}(\hat{\mathbf{r}}) + \frac{9}{4\pi} R_{32}^2(r) \Theta_{42}^{(c)}(d_{3z^2-r^2}, d_{x^2-y^2}) Z_{42}^{(c)}(\hat{\mathbf{r}}). \quad (\text{B.27})$$

In Fig. B.1, we show the schematic picture of the multipole expansion in this example. As in Fig. B.1, the product of the wave functions $F_{\alpha\beta}(\mathbf{r})$ is generally given by the sum of the multipoles.

⁴In Eq. (B.24), we have

$$\begin{aligned} Y_{l_{\alpha}m_{\alpha}}^*(\hat{\mathbf{r}}) Y_{l_{\beta}m_{\beta}}(\hat{\mathbf{r}}) &= \int d\Omega' \left[\sum_{l,m} \left(\frac{2l+1}{4\pi} \right) Z_{lm}^*(\hat{\mathbf{r}}') Z_{lm}(\hat{\mathbf{r}}) \right] Y_{l_{\alpha}m_{\alpha}}^*(\hat{\mathbf{r}}') Y_{l_{\beta}m_{\beta}}(\hat{\mathbf{r}}') \\ &= \sum_{l,m} \left(\frac{2l+1}{4\pi} \right) \left[\int d\Omega' Y_{l_{\alpha}m_{\alpha}}^*(\hat{\mathbf{r}}') Z_{lm}^*(\hat{\mathbf{r}}') Y_{l_{\beta}m_{\beta}}(\hat{\mathbf{r}}') \right] Z_{lm}(\hat{\mathbf{r}}) = \sum_{l,m} \left(\frac{2l+1}{4\pi} \right) \Theta_{lm}(l_{\alpha}m_{\alpha}, l_{\beta}m_{\beta}) Z_{lm}(\hat{\mathbf{r}}). \end{aligned}$$

α	$[l_\alpha m_\alpha]$	β	$[l_\beta m_\beta]$	$l = 0$	$l = 1$	$l = 2$	$l = 3$	$l = 4$
s	[00]	s	[00]	[00]	–	–	–	–
s	[00]	p_z	[10]	–	[10]	–	–	–
		p_x	[11 _c]	–	[11 _c]	–	–	–
		p_y	[11 _s]	–	[11 _s]	–	–	–
s	[00]	$d_{3z^2-r^2}$	[20]	–	–	[20]	–	–
		d_{zx}	[21 _c]	–	–	[21 _c]	–	–
		d_{yz}	[21 _s]	–	–	[21 _s]	–	–
		$d_{x^2-y^2}$	[22 _c]	–	–	[22 _c]	–	–
		d_{xy}	[22 _s]	–	–	[22 _s]	–	–
p_z	[10]	p_z	[10]	[00]	–	[20]	–	–
		p_x	[11 _c]	–	–	[21 _c]	–	–
		p_y	[11 _s]	–	–	[21 _s]	–	–
p_x	[11 _c]	p_x	[11 _c]	[00]	–	[20], [22 _c]	–	–
		p_y	[11 _s]	–	–	[22 _s]	–	–
p_y	[11 _s]	p_y	[11 _s]	[00]	–	[20], [22 _c]	–	–
p_z	[10]	$d_{3z^2-r^2}$	[20]	–	[10]	–	[30]	–
		d_{zx}	[21 _c]	–	[11 _c]	–	[31 _c]	–
		d_{yz}	[21 _s]	–	[11 _s]	–	[31 _s]	–
		$d_{x^2-y^2}$	[22 _c]	–	–	–	[32 _c]	–
		d_{xy}	[22 _s]	–	–	–	[32 _s]	–
p_x	[11 _c]	$d_{3z^2-r^2}$	[20]	–	[11 _c]	–	[31 _c]	–
		d_{zx}	[21 _c]	–	[10]	–	[30], [32 _c]	–
		d_{yz}	[21 _s]	–	–	–	[32 _s]	–
		$d_{x^2-y^2}$	[22 _c]	–	[11 _c]	–	[31 _c], [33 _c]	–
		d_{xy}	[22 _s]	–	[11 _s]	–	[31 _s], [33 _s]	–
p_y	[11 _s]	$d_{3z^2-r^2}$	[20]	–	[11 _s]	–	[31 _s]	–
		d_{zx}	[21 _c]	–	–	–	[32 _s]	–
		d_{yz}	[21 _s]	–	[10]	–	[30], [32 _c]	–
		$d_{x^2-y^2}$	[22 _c]	–	[11 _s]	–	[31 _s], [33 _s]	–
		d_{xy}	[22 _s]	–	[11 _c]	–	[31 _c], [33 _c]	–
$d_{3z^2-r^2}$	[20]	$d_{3z^2-r^2}$	[20]	[00]	–	[20]	–	[40]
		d_{zx}	[21 _c]	–	–	[21 _c]	–	[41 _c]
		d_{yz}	[21 _s]	–	–	[21 _s]	–	[41 _s]
		$d_{x^2-y^2}$	[22 _c]	–	–	[22 _c]	–	[42 _c]
		d_{xy}	[22 _s]	–	–	[22 _s]	–	[42 _s]
d_{zx}	[21 _c]	d_{zx}	[21 _c]	[00]	–	[20], [22 _c]	–	[40], [42 _c]
		d_{yz}	[21 _s]	–	–	[22 _s]	–	[42 _s]
		$d_{x^2-y^2}$	[22 _c]	–	–	[21 _c]	–	[41 _c], [43 _c]
		d_{xy}	[22 _s]	–	–	[21 _s]	–	[41 _s], [43 _s]
d_{yz}	[21 _s]	d_{yz}	[21 _s]	[00]	–	[20], [22 _c]	–	[40], [42 _c]
		$d_{x^2-y^2}$	[22 _c]	–	–	[21 _s]	–	[41 _s], [43 _s]
		d_{xy}	[22 _s]	–	–	[21 _c]	–	[41 _c], [43 _c]
$d_{x^2-y^2}$	[22 _c]	$d_{x^2-y^2}$	[22 _c]	[00]	–	[20]	–	[40], [44 _c]
		d_{xy}	[22 _s]	–	–	–	–	[44 _s]
d_{xy}	[22 _s]	d_{xy}	[22 _s]	[00]	–	[20]	–	[40], [44 _c]

Table B.2: Correspondence between the orbitals and nonvanishing multipole moments. $[lm_c]$ and $[lm_s]$ indicate $Y_{lm}^{(c)}(\hat{\mathbf{r}})$ ($Z_{lm}^{(c)}(\hat{\mathbf{r}})$) and $Y_{lm}^{(s)}(\hat{\mathbf{r}})$ ($Z_{lm}^{(s)}(\hat{\mathbf{r}})$), respectively.

Acknowledgements

First, I would like to express my sincere gratitude to Prof. Y. Ohta for his enormous support, advice and encouragement during the course of my study. During my Doctoral and Master courses, he supported my study in all the aspects such as suggestions of the research tasks, discussion about the results, and how to give a presentation and write in English. I would like to show my appreciation to Dr. S. Ejima, Prof. H. Fehske, and Dr. B. Zenker. My studies were inspired by the discussions with them during my stay in Greifswald, where they gave me insightful comments and suggestions. I am indebted to Dr. K. Seki for his guidance and advices in the numerical calculation techniques. I am very much grateful to Prof. T. Konishi and Dr. T. Toriyama for their guidance and persistent helps in the density-functional-theory based electronic structure calculations of Ta_2NiSe_5 . I would like to thank Dr. K. Sugimoto for extending the theoretical study of Ta_2NiSe_5 . I would like to thank Dr. N. Katayama, Dr. Y. F. Lu, Prof. K. Matsubayashi, Prof. T. Mizokawa, Prof. H. Sawa, Prof. H. Takagi, Prof. Y. Uwatoko, and Dr. Y. Wakisaka for discussing experimental aspects of Ta_2NiSe_5 . I would like to thank Prof. K. Oto, Prof. T. Hanawa, Prof. Y. Ohta, and Dr. S. Yunoki for giving me insightful comments and advices on my thesis and in the defense talk. I would greatly appreciate the cooperative studies with Mr. K. Misumi, Mr. S. Miyakoshi, Mr. M. Ebato, Mr. N. Ogawa, Mr. T. Hasunuma, Mr. H. Nishida, and Mr. K. Hamada. I could not include their studies in this thesis but I am very happy to collaborate and to publish some of them. I would thank many students for discussion and refreshment, who include Dr. K. Nakano, Mr. D. Katagiri, Dr. Y. Fuji, Mr. M. Kobori, Mr. S. Yamaki, Mr. M. Watanabe, Ms. A. Shimoi, Mr. T. Nakayama, Mr. T. Ishikawa, and Mr. H. Goto. I would like to express my gratitude to a JSPS Research Fellowship for Young Scientists for financial support for three years in my Doctoral course. Finally, I would like to thank my parents for their support and encouragement during my Master and Doctoral courses.

Bibliography

- [1] N. F. Mott, *Philos. Mag.* **6**, 287 (1961).
- [2] R. Knox, in *Solid State Physics* (Academic, New York, 1963), Vol. 5, p. 100.
- [3] L. V. Keldysh and Y. V. Kopeav, *Sov. Phys. Solid state* **6**, 2219 (1965).
- [4] J. Des Cloizeaux, *J. Phys. Chem. Solids* **26**, 259 (1965).
- [5] A. N. Kozolov and L. A. Maksimov, *Sov. Phys. JETP* **21**, 790 (1965).
- [6] A. N. Kozlov and L. A. Maksimov, *Sov. Phys. JETP* **22**, 889 (1966).
- [7] A. N. Kozlov and L. A. Maksimov, *Sov. Phys. JETP* **23**, 88 (1966).
- [8] W. Kohn, *Phys. Rev. Lett.* **19**, 439 (1967).
- [9] D. Jérôme, T. M. Rice, and W. Kohn, *Phys. Rev.* **158**, 462 (1967).
- [10] J. Zittartz, *Phys. Rev.* **162**, 752 (1967).
- [11] J. Zittartz, *Phys. Rev.* **164**, 575 (1967).
- [12] J. Zittartz, *Phys. Rev.* **165**, 605 (1968).
- [13] J. Zittartz, *Phys. Rev.* **165**, 612 (1968).
- [14] B. I. Halperin and T. M. Rice, *Rev. Mod. Phys.* **40**, 755 (1968).
- [15] B. I. Halperin and T. M. Rice, in *Solid State Physics* (Academic, New York, 1968), Vol. 21, p. 115.
- [16] L. V. Keldysh and A. N. Kozlov, *Sov. Phys. JETP* **27**, 521 (1968).
- [17] W. Kohn and D. Sherrington, *Rev. Mod. Phys.* **42**, 1 (1970).
- [18] R. R. Guseinov and L. V. Keldysh, *Sov. Phys. JETP* **36**, 1193 (1973).
- [19] B. A. Volkov, Y. V. Kopaev, and A. I. Rusinov, *Sov. Phys. JETP* **41**, 952 (1975).
- [20] C. Comte and P. Nozieres, *J. Phys. (France)* **43**, 1069 (1982).
- [21] P. Nozieres and C. Comte, *J. Phys. (France)* **43**, 1083 (1982).
- [22] P. Nozières and S. Schmitt-Rink, *J. Low Temp. Phys.* **59**, 195 (1985).
- [23] F. X. Bronold and H. Fehske, *Phys. Rev. B* **74**, 165107 (2006).
- [24] B. Bucher, P. Steiner, and P. Wachter, *Phys. Rev. Lett.* **67**, 2717 (1991).
- [25] D. Young, D. Hall, M. Torelli, Z. Fisk, J. Sarrao, J. Thompson, H.-R. Ott, S. Oseroff, R. Goodrich, and R. Zysler, *Nature* **397**, 412 (1999).
- [26] M. Zhitomirsky, T. Rice, and V. Anisimov, *Nature* **402**, 251 (1999).
- [27] L. Balents and C. M. Varma, *Phys. Rev. Lett.* **84**, 1264 (2000).

-
- [28] H. Cercellier, C. Monney, F. Clerc, C. Battaglia, L. Despont, M. G. Garnier, H. Beck, P. Aebi, L. Patthey, H. Berger, and L. Forró, *Phys. Rev. Lett.* **99**, 146403 (2007).
- [29] C. Monney, H. Cercellier, F. Clerc, C. Battaglia, E. F. Schwier, C. Didiot, M. G. Garnier, H. Beck, P. Aebi, H. Berger, L. Forró, and L. Patthey, *Phys. Rev. B* **79**, 045116 (2009).
- [30] C. Monney, E. F. Schwier, M. G. Garnier, N. Mariotti, C. Didiot, H. Beck, P. Aebi, H. Cercellier, J. Marcus, C. Battaglia, H. Berger, and A. N. Titov, *Phys. Rev. B* **81**, 155104 (2010).
- [31] C. Monney, C. Battaglia, H. Cercellier, P. Aebi, and H. Beck, *Phys. Rev. Lett.* **106**, 106404 (2011).
- [32] C. Monney, G. Monney, P. Aebi, and H. Beck, *Phys. Rev. B* **85**, 235150 (2012).
- [33] B. Zenker, H. Fehske, H. Beck, C. Monney, and A. R. Bishop, *Phys. Rev. B* **88**, 075138 (2013).
- [34] G. Monney, C. Monney, B. Hildebrand, P. Aebi, and H. Beck, *Phys. Rev. Lett.* **114**, 086402 (2015).
- [35] H. Watanabe, K. Seki, and S. Yunoki, *Phys. Rev. B* **91**, 205135 (2015).
- [36] Y. Wakisaka, T. Sudayama, K. Takubo, T. Mizokawa, M. Arita, H. Namatame, M. Taniguchi, N. Katayama, M. Nohara, and H. Takagi, *Phys. Rev. Lett.* **103**, 026402 (2009).
- [37] Y. Wakisaka, T. Sudayama, K. Takubo, T. Mizokawa, N. Saini, M. Arita, H. Namatame, M. Taniguchi, N. Katayama, M. Nohara, and H. Takagi, *J. Supercond. Nov. Magn.* **25**, 1231 (2012).
- [38] T. Kaneko, T. Toriyama, T. Konishi, and Y. Ohta, *Phys. Rev. B* **87**, 035121 (2013); **87**, 199902(E) (2013).
- [39] K. Seki, Y. Wakisaka, T. Kaneko, T. Toriyama, T. Konishi, T. Sudayama, N. L. Saini, M. Arita, H. Namatame, M. Taniguchi, N. Katayama, M. Nohara, H. Takagi, T. Mizokawa, and Y. Ohta, *Phys. Rev. B* **90**, 155116 (2014).
- [40] K. Sugimoto, T. Kaneko, and Y. Ohta, *Phys. Rev. B* **93**, 041105(R) (2016).
- [41] T. Yamada, K. Domon, and Y. Ōno, arXiv:1602.03248 (2016).
- [42] T. M. Rice, *Phys. Rev. B* **2**, 3619 (1970).
- [43] E. Sonin, *Solid State Commun.* **25**, 253 (1978).
- [44] E. Fawcett, *Rev. Mod. Phys.* **60**, 209 (1988).
- [45] A. Gabovich, A. Voitenko, and M. Ausloos, *Phys. Rep.* **367**, 583 (2002).
- [46] T. Mizokawa, T. Sudayama, and Y. Wakisaka, *J. Phy. Soc. Jpn.* **77**, 158 (2008).
- [47] A. V. Chubukov, D. V. Efremov, and I. Eremin, *Phys. Rev. B* **78**, 134512 (2008).
- [48] M. M. Korshunov and I. Eremin, *Phys. Rev. B* **78**, 140509 (2008).
- [49] Q. Han, Y. Chen, and Z. D. Wang, *Europhys. Lett.* **82**, 37007 (2008).
- [50] A. B. Vorontsov, M. G. Vavilov, and A. V. Chubukov, *Phys. Rev. B* **79**, 060508 (2009).
- [51] P. M. R. Brydon and C. Timm, *Phys. Rev. B* **79**, 180504 (2009).
- [52] P. M. R. Brydon and C. Timm, *Phys. Rev. B* **80**, 174401 (2009).
- [53] I. Eremin and A. V. Chubukov, *Phys. Rev. B* **81**, 024511 (2010).
- [54] A. B. Vorontsov, M. G. Vavilov, and A. V. Chubukov, *Phys. Rev. B* **81**, 174538 (2010).
- [55] R. M. Fernandes and J. Schmalian, *Phys. Rev. B* **82**, 014521 (2010).
- [56] J. Knolle, I. Eremin, and R. Moessner, *Phys. Rev. B* **83**, 224503 (2011).
- [57] B. Zocher, C. Timm, and P. M. R. Brydon, *Phys. Rev. B* **84**, 144425 (2011).

-
- [58] R. M. Fernandes, A. V. Chubukov, J. Knolle, I. Eremin, and J. Schmalian, *Phys. Rev. B* **85**, 024534 (2012).
- [59] J. Schmiedt, P. M. R. Brydon, and C. Timm, *Phys. Rev. B* **89**, 054515 (2014).
- [60] J. Kuneš and P. Augustinský, *Phys. Rev. B* **89**, 115134 (2014).
- [61] J. Kuneš and P. Augustinský, *Phys. Rev. B* **90**, 235112 (2014).
- [62] J. Kuneš, *Phys. Rev. B* **90**, 235140 (2014).
- [63] S. R. White, *Phys. Rev. Lett.* **69**, 2863 (1992).
- [64] S. A. Moskalenko and D. W. Snoke, *Bose-Einstein Condensation of Excitons and Biexcitons* (Cambridge University Press, Cambridge, 2000).
- [65] O. Penrose and L. Onsager, *Phys. Rev.* **104**, 576 (1956).
- [66] C. N. Yang, *Rev. Mod. Phys.* **34**, 694 (1962).
- [67] Y. Nagaoka, *Bussei Kenkyu* **23**, 257 (1975).
- [68] H. Fröhlich, *Proc. R. Soc. A* **223**, 296 (1954).
- [69] P. Lee, T. Rice, and P. Anderson, *Solid State Commun.* **14**, 703 (1974).
- [70] L. V. Keldysh, *Problems of Theoretical Physics* (Nauka, Moscow, 1972), p. 433.
- [71] Y. Nagaoka, *Bussei Kenkyu* **24**, 55 (1975).
- [72] E. Dagotto, *Rev. Mod. Phys.* **66**, 763 (1994).
- [73] T. Shirakawa, Ph.D. thesis, Chiba University, 2008.
- [74] A. Weisse and H. Fehske, in *Computational Many-Particle Physics*, Vol. 739 of *Lecture Notes in Physics* (Springer-Verlag, Berlin Heidelberg, 2008), Chap. 18, pp. 529–544.
- [75] M. Potthoff, in *Strongly Correlated Systems — Theoretical Methods*, Vol. 171 of *Springer Series in Solid-State Sciences* (Springer-Verlag, Berlin Heidelberg, 2012), Chap. 10, pp. 303–339.
- [76] J. M. Luttinger and J. C. Ward, *Phys. Rev.* **118**, 1417 (1960).
- [77] M. Potthoff, *Eur. Phys. J. B* **32**, 429 (2003).
- [78] M. Potthoff, *Eur. Phys. J. B* **36**, 335 (2003).
- [79] K. Seki, Ph.D. thesis, Chiba University, 2013.
- [80] M. Potthoff, M. Aichhorn, and C. Dahnken, *Phys. Rev. Lett.* **91**, 206402 (2003).
- [81] D. Sénéchal, arXiv:0806.2690 (2008).
- [82] C. Dahnken, M. Aichhorn, W. Hanke, E. Arrigoni, and M. Potthoff, *Phys. Rev. B* **70**, 245110 (2004).
- [83] D. Sénéchal, D. Perez, and M. Pioro-Ladrière, *Phys. Rev. Lett.* **84**, 522 (2000).
- [84] D. Sénéchal, in *Strongly Correlated Systems — Theoretical Methods*, Vol. 171 of *Springer Series in Solid-State Sciences* (Springer-Verlag, Berlin Heidelberg, 2012), Chap. 8, pp. 237–270.
- [85] L. M. Falicov and J. C. Kimball, *Phys. Rev. Lett.* **22**, 997 (1969).
- [86] P. Farkašovský, *Eur. Phys. J. B* **20**, 209 (2001).
- [87] C. D. Batista, *Phys. Rev. Lett.* **89**, 166403 (2002).
- [88] C. D. Batista, J. E. Gubernatis, J. Bonča, and H. Q. Lin, *Phys. Rev. Lett.* **92**, 187601 (2004).
- [89] P. Farkašovský, *Phys. Rev. B* **77**, 155130 (2008).

- [90] C. Schneider and G. Czycholl, *Eur. Phys. J. B* **64**, 43 (2008).
- [91] B. Zenker, H. Fehske, and C. D. Batista, *Phys. Rev. B* **82**, 165110 (2010).
- [92] D. Ihle, M. Pfafferoth, E. Burovski, F. X. Bronold, and H. Fehske, *Phys. Rev. B* **78**, 193103 (2008).
- [93] P. M. R. Brydon, *Phys. Rev. B* **77**, 045109 (2008).
- [94] B. Zenker, D. Ihle, F. X. Bronold, and H. Fehske, *Phys. Rev. B* **81**, 115122 (2010).
- [95] B. Zenker, D. Ihle, F. X. Bronold, and H. Fehske, *Phys. Rev. B* **83**, 235123 (2011).
- [96] B. Zenker, D. Ihle, F. X. Bronold, and H. Fehske, *Phys. Rev. B* **85**, 121102 (2012).
- [97] V.-N. Phan, K. W. Becker, and H. Fehske, *Phys. Rev. B* **81**, 205117 (2010).
- [98] V.-N. Phan, H. Fehske, and K. W. Becker, *Europhys. Lett.* **95**, 17006 (2011).
- [99] K. Seki, R. Eder, and Y. Ohta, *Phys. Rev. B* **84**, 245106 (2011).
- [100] J. P. Eisenstein and A. H. MacDonald, *Nature (London)* **432**, 691 (2004).
- [101] X. Zhu, P. B. Littlewood, M. S. Hybertsen, and T. M. Rice, *Phys. Rev. Lett.* **74**, 1633 (1995).
- [102] J. A. Seamons, C. P. Morath, J. L. Reno, and M. P. Lilly, *Phys. Rev. Lett.* **102**, 026804 (2009).
- [103] H. Min, R. Bistritzer, J.-J. Su, and A. H. MacDonald, *Phys. Rev. B* **78**, 121401 (2008).
- [104] V.-N. Phan and H. Fehske, *New J. Phys.* **14**, 075007 (2012).
- [105] A. Perali, D. Neilson, and A. R. Hamilton, *Phys. Rev. Lett.* **110**, 146803 (2013).
- [106] D. W. Snoke, J. P. Wolfe, and A. Mysyrowicz, *Phys. Rev. B* **41**, 11171 (1990).
- [107] N. Naka and N. Nagasawa, *J. Lumin.* **112**, 11 (2005).
- [108] K. Yoshioka, E. Chae, and M. Kuwata-Gonokami, *Nat. Commun.* **2**, 328 (2011).
- [109] H. Stolz, R. Schwartz, F. Kieseling, S. Som, M. Kaupsch, S. Sobkowiak, D. Semkat, N. Naka, T. Koch, and H. Fehske, *New J. Phys.* **14**, 105007 (2012).
- [110] L. V. Butov, A. C. Gossard, and D. S. Chemla, *Nature (London)* **418**, 751 (2002).
- [111] D. Snoke, S. Denev, Y. Liu, L. Pfeiffer, and K. West, *Nature (London)* **418**, 754 (2002).
- [112] A. H. Castro Neto, F. Guinea, N. M. R. Peres, K. S. Novoselov, and A. K. Geim, *Rev. Mod. Phys.* **81**, 109 (2009).
- [113] J. Schleede, A. Filinov, M. Bonitz, and H. Fehske, *Contrib. Plasma Phys.* **52**, 819 (2012).
- [114] T. Kaneko, S. Ejima, H. Fehske, and Y. Ohta, *Phys. Rev. B* **88**, 035312 (2013).
- [115] Y. Ohta, T. Shimozato, R. Eder, and S. Maekawa, *Phys. Rev. Lett.* **73**, 324 (1994).
- [116] Y. Ohta, A. Nakauchi, R. Eder, K. Tsutsui, and S. Maekawa, *Phys. Rev. B* **52**, 15617 (1995).
- [117] T. Kaneko and Y. Ohta, *J. Phys. Soc. Jpn.* **83**, 024711 (2014).
- [118] T. Kaneko, S. Ejima, H. Fehske, and Y. Ohta, *JPS Conf. Proc.* **3**, 017006 (2014).
- [119] R. Micnas, J. Ranninger, and S. Robaszkiewicz, *Rev. Mod. Phys.* **62**, 113 (1990).
- [120] K. Mizoo, T. J. Inagaki, Y. Ueshima, and M. Aihara, *J. Phys. Soc. Jpn.* **74**, 1745 (2005).
- [121] G. Fáth, Z. Domański, and R. Lemański, *Phys. Rev. B* **52**, 13910 (1995).
- [122] J. Des Cloizeaux and M. Gaudin, *Journal of Mathematical Physics* **7**, 1384 (1966).
- [123] M. Takahashi, *Thermodynamics of One Dimensional Solvable Models* (Cambridge University Press, Cambridge, 1999).

- [124] A. N. Kocharian and J. H. Sebold, Phys. Rev. B **53**, 12804 (1996).
- [125] S. Ejima, T. Kaneko, Y. Ohta, and H. Fehske, Phys. Rev. Lett. **112**, 026401 (2014).
- [126] P. Calabrese and J. Cardy, J. Stat. Mech. **2004**, P06002 (2004).
- [127] S. Nishimoto, Phys. Rev. B **84**, 195108 (2011).
- [128] T. Kaneko, K. Seki, and Y. Ohta, Phys. Rev. B **85**, 165135 (2012).
- [129] T. Kaneko and Y. Ohta, Phys. Rev. B **90**, 245144 (2014).
- [130] J. S. Griffith, *The Theory of Transition-Metal Ions* (Cambridge University Press, Cambridge, U.K., 1961).
- [131] B. H. Brandow, Adv. Phys. **26**, 651 (1977).
- [132] A. M. Olés, Phys. Rev. B **28**, 327 (1983).
- [133] V.-N. Phan, K. W. Becker, and H. Fehske, Phys. Rev. B **88**, 205123 (2013).
- [134] B. Zenker, H. Fehske, and H. Beck, Phys. Rev. B **90**, 195118 (2014).
- [135] T. Kaneko, B. Zenker, H. Fehske, and Y. Ohta, Phys. Rev. B **92**, 115106 (2015).
- [136] P. B. Littlewood and X. Zhu, Phys. Scr. **T68**, 56 (1996).
- [137] G. Grüner, *Density Waves in Solids* (Perseus, New York, 2000).
- [138] L. Balents, Phys. Rev. B **62**, 2346 (2000).
- [139] H. Kusunose, J. Phys. Soc. Jpn. **77**, 064710 (2008).
- [140] Y. Kuramoto, H. Kusunose, and A. Kiss, J. Phys. Soc. Jpn. **78**, 072001 (2009).
- [141] H. Kusunose, Bussei Kenkyu **97**, 730 (2012).
- [142] A. Zunger and A. J. Freeman, Phys. Rev. B **17**, 1839 (1978).
- [143] C. M. Fang, R. A. d. Groot, and C. Haas, Phys. Rev. B **56**, 4455 (1997).
- [144] S. A. Sunshine and J. A. Ibers, Inorg. Chem. **24**, 3611 (1985).
- [145] F. Di Salvo, C. Chen, R. Fleming, J. Waszczak, R. Dunn, S. Sunshine, and J. A. Ibers, J. Less-Common Met. **116**, 51 (1986).
- [146] E. Canadell and M. H. Whangbo, Inorg. Chem. **26**, 3974 (1987).
- [147] P. Blaha, K. Schwarz, G. Madsen, D. Kvasnicka, and J. Luitz, *WIEN2K*, Technical Universität Wien, Austria, 2001.
- [148] J. P. Perdew, K. Burke, and M. Ernzerhof, Phys. Rev. Lett. **77**, 3865 (1996).
- [149] H. Lin, R. S. Markiewicz, L. A. Wray, L. Fu, M. Z. Hasan, and A. Bansil, Phys. Rev. Lett. **105**, 036404 (2010).
- [150] S.-G. Park, B. Magyari-Köpe, and Y. Nishi, Phys. Rev. B **82**, 115109 (2010).
- [151] W. P. Su, J. R. Schrieffer, and A. J. Heeger, Phys. Rev. B **22**, 2099 (1980).
- [152] Y. F. Lu, and H. Takagi *et al.*, unpublished.
- [153] N. Katayama and H. Sawa, private communication.
- [154] S. Hershfield and M. Y. Reizer, Phys. Rev. B **43**, 9475 (1991).
- [155] T. Moriya, J. Phys. Soc. Jpn. **18**, 516 (1963).
- [156] L. C. Hebel and C. P. Slichter, Phys. Rev. **113**, 1504 (1959).

- [157] S. Lee, Y. Kobayashi, and M. Itoh, unpublished.
- [158] E. Morosan, H. Zandbergen, B. Dennis, J. Bos, Y. Onose, T. Klimczuk, A. Ramirez, N. Ong, and R. Cava, *Nature Phys.* **2**, 544 (2006).
- [159] A. F. Kusmartseva, B. Sipos, H. Berger, L. Forró, and E. Tutiš, *Phys. Rev. Lett.* **103**, 236401 (2009).
- [160] K. Matsubayashi *et al.*, unpublished.
- [161] D. M. Eagles, *Phys. Rev.* **186**, 456 (1969).
- [162] A. J. Leggett, in *Modern Trends in the Theory of Condensed Matter*, Vol. 115 of *Lecture Notes in Physics*, edited by A. Pekalski and J. Przystawa (Springer Berlin Heidelberg, ADDRESS, 1980), pp. 13–27.
- [163] A. J. Leggett, *Nat. Phys.* **2**, 134 (2006).
- [164] S. Jochim, M. Bartenstein, A. Altmeyer, G. Hendl, S. Riedl, C. Chin, J. H. Denschlag, and R. Grimm, *Science* **302**, 2101 (2003).
- [165] M. W. Zwierlein, C. A. Stan, C. H. Schunck, S. M. F. Raupach, S. Gupta, Z. Hadzibabic, and W. Ketterle, *Phys. Rev. Lett.* **91**, 250401 (2003).
- [166] M. Greiner, C. A. Regal, and D. S. Jin, *Nature* **426**, 537 (2003).
- [167] T. Bourdel, L. Khaykovich, J. Cubizolles, J. Zhang, F. Chevy, M. Teichmann, L. Tarruell, S. J. J. M. F. Kokkelmans, and C. Salomon, *Phys. Rev. Lett.* **93**, 050401 (2004).
- [168] C. A. Regal, M. Greiner, and D. S. Jin, *Phys. Rev. Lett.* **92**, 040403 (2004).
- [169] M. Bartenstein, A. Altmeyer, S. Riedl, S. Jochim, C. Chin, J. H. Denschlag, and R. Grimm, *Phys. Rev. Lett.* **92**, 120401 (2004).
- [170] M. W. Zwierlein, C. A. Stan, C. H. Schunck, S. M. F. Raupach, A. J. Kerman, and W. Ketterle, *Phys. Rev. Lett.* **92**, 120403 (2004).
- [171] I. Bloch, J. Dalibard, and W. Zwerger, *Rev. Mod. Phys.* **80**, 885 (2008).
- [172] R. T. Scalettar, E. Y. Loh, J. E. Gubernatis, A. Moreo, S. R. White, D. J. Scalapino, R. L. Sugar, and E. Dagotto, *Phys. Rev. Lett.* **62**, 1407 (1989).
- [173] A. Moreo and D. J. Scalapino, *Phys. Rev. Lett.* **66**, 946 (1991).
- [174] M. Capone, C. Castellani, and M. Grilli, *Phys. Rev. Lett.* **88**, 126403 (2002).
- [175] A. Garg, H. R. Krishnamurthy, and M. Randeria, *Phys. Rev. B* **72**, 024517 (2005).
- [176] A. Toschi, M. Capone, and C. Castellani, *Phys. Rev. B* **72**, 235118 (2005).
- [177] J. Bauer, A. C. Hewson, and N. Dupuis, *Phys. Rev. B* **79**, 214518 (2009).
- [178] A. Koga and P. Werner, *Phys. Rev. A* **84**, 023638 (2011).
- [179] B. Kyung, A. Georges, and A.-M. S. Tremblay, *Phys. Rev. B* **74**, 024501 (2006).
- [180] H. Shiba, *Progress of Theoretical Physics* **48**, 2171 (1972).
- [181] A. Lüscher and A. M. Läuchli, *Phys. Rev. B* **79**, 195102 (2009).
- [182] H. Kamimura, S. Sugano, and Y. Tanabe, *Ligand Field Theory and Its Applications* (Syokabo, Tokyo, 1969).